AWARD NUMBER: W81XWH-19-1-0004

TITLE: Long-Term Wearable Touchless Radiofrequency Sensors for Cardiopulmonary Functions

PRINCIPAL INVESTIGATOR: Edwin C. Kan

CONTRACTING ORGANIZATION: Cornell University, Ithaca, NY

REPORT DATE: November 2020

TYPE OF REPORT: Final Report

PREPARED FOR: U.S. Army Medical Research and Development Command
Fort Detrick, Maryland 21702-5012

DISTRIBUTION STATEMENT: Approved for Public Release;
Distribution Unlimited

The views, opinions and/or findings contained in this report are those of the author(s) and should not be construed as an official Department of the Army position, policy or decision unless so designated by other documentation.

REPORT DOCUMENTATION PAGE

Form Approved
OMB No. 0704-0188

Public reporting burden for this collection of information is estimated to average 1 hour per response, including the time for reviewing instructions, searching existing data sources, gathering and maintaining the data needed, and completing and reviewing this collection of information. Send comments regarding this burden estimate or any other aspect of this collection of information, including suggestions for reducing this burden to Department of Defense, Washington Headquarters Services, Directorate for Information Operations and Reports (0704-0188), 1215 Jefferson Davis Highway, Suite 1204, Arlington, VA 22202-4302. Respondents should be aware that notwithstanding any other provision of law, no person shall be subject to any penalty for failing to comply with a collection of information if it does not display a currently valid OMB control number. **PLEASE DO NOT RETURN YOUR FORM TO THE ABOVE ADDRESS.**

1. REPORT DATE	2. REPORT TYPE	3. DATES COVERED
November 2020	Final Report	01Feb2019-31Jul2020

4. TITLE AND SUBTITLE

Long-Term Wearable Touchless Radiofrequency Sensors for Cardiopulmonary Functions

5a. CONTRACT NUMBER
PR182496

5b. GRANT NUMBER
W81XWH-19-1-0004

5c. PROGRAM ELEMENT NUMBER

6. AUTHOR(S)

Edwin C. Kan

E-Mail: kan@ece.cornell.edu; Phone: 1-607-255-3998

5d. PROJECT NUMBER

5e. TASK NUMBER

5f. WORK UNIT NUMBER

7. PERFORMING ORGANIZATION NAME(S) AND ADDRESS(ES)

325 Phillips Hall,
Cornell University,
Ithaca, NY

8. PERFORMING ORGANIZATION REPORT NUMBER

9. SPONSORING / MONITORING AGENCY NAME(S) AND ADDRESS(ES)

U.S. Army Medical Research and Development Command
Fort Detrick, Maryland 21702-5012

10. SPONSOR/MONITOR'S ACRONYM(S)

11. SPONSOR/MONITOR'S REPORT NUMBER(S)

12. DISTRIBUTION / AVAILABILITY STATEMENT

Approved for Public Release; Distribution Unlimited

13. SUPPLEMENTARY NOTES

14. ABSTRACT

In the research efforts, we aim to improve the passive and active RF near-field coherent sensing (NCS) system design, and establish the feasibility for detailed and robust cardiopulmonary function recognition as well as long-term wellness, diagnostic, pathological, behavioral and emotional studies. We have benchmarked the NCS features with synchronous electrocardiogram (ECG), respiratory inductance plethysmography (RIP) and oximetry SpO2 measurements, not only for calibration but also for collaborative functions by correlating feature points among these methods. For example, ECG measures the nerve stimulation while NCS the resulting heart and valve motion. The successive blood flow from pulmonary circulation to systemic circulation then results in the SpO2 measured in the branchial vessels. Comparison of aligned waveform features can bring forth new information not available in individual methods. Due to the much lower noise floor in NCS due to direct motion modulation, we also aim to extract detailed cardiomyopathy and respiration dynamics from NCS by nonlinear adaptive filtering for further wellness and pathological evaluation. Accurate heart rate variation (HRV) extracted from NCS can also be used in stress and emotion estimation. NCS is a wearable touchless method, uniquely suited for animals with various surface coverings. This opens up new opportunities to monitor vital signs and stress levels in lab animals.

15. SUBJECT TERMS
None listed.

16. SECURITY CLASSIFICATION OF:			17. LIMITATION OF ABSTRACT	18. NUMBER OF PAGES	19a. NAME OF RESPONSIBLE PERSON
a. REPORT	b. ABSTRACT	c. THIS PAGE			19b. TELEPHONE NUMBER *(include area code)*
Unclassified	Unclassified	Unclassified	Unclassified	147	USAMRMC

Standard Form 298 (Rev. 8-98)
Prescribed by ANSI Std. Z39.18

TABLE OF CONTENTS

	Page
1. Introduction	4
2. Keywords	5
3. Accomplishments	5
4. Impact	7
5. Changes/Problems	8
6. Products	8
7. Participants & Other Collaborating Organizations	8
8. Special Reporting Requirements	9
9. Appendices	9

1. Introduction

In the CDMRP effort, we have proposed three specific aims for the 18-month effort. We have achieved all aims in vital-sign monitoring, as well as extensive benchmarks with existing sensors of ECG, chest belts and oximetry. Due to the touchless sensing over clothing and various surface coverings, the NCS sensor has been extended to monitor vital signs of small animals. This unprecedented capability not only extends the basic scientific capability to understand animals, but also can be of great values to United States Army Medical Research Institute of Infectious Diseases (USAMRIID) where animal models are extensively used for drug and vaccine development.

We will first give a summary of the achievement in the proposed three aims, and then present the details in the Section of Accomplishment with references to the publications under this CDMRP effort.

AIM 1. ACTIVE AND PASSIVE TAG CONSTRUCTION FOR RELIABLE OPERATION. We have made both active and passive NCS tags, as shown in Fig. 1. Both tags have been benchmarked for long-term recording in realistic protocols. The active tag can have body motion interference if the tag is not firmly fixed on the snug wearing. The passive tag can be additionally interfered with large motion in the ambient. Both passive and active tags are readily multiplexed for multi-tag operations.

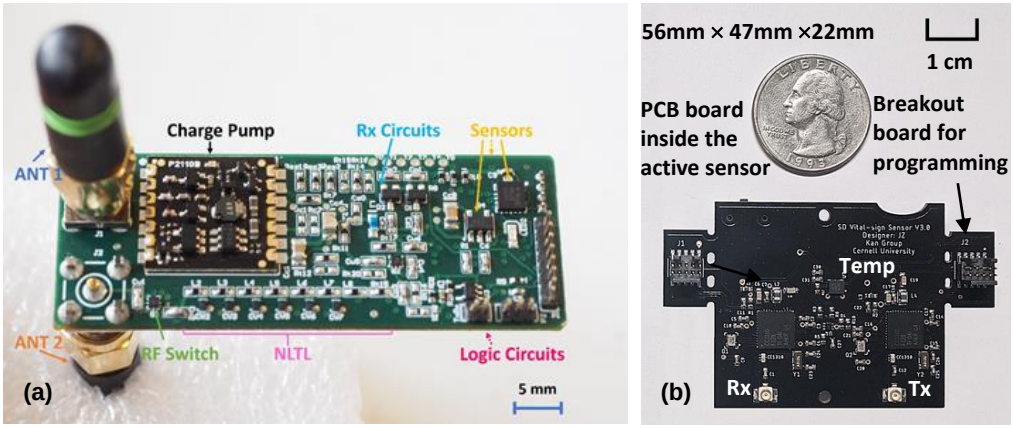

Fig. 1. RF NCS sensing tag. (a) Passive tags integrated on the WISP platform for tag multiplexing. Notice that the vital-sign reading operation by a remote reader does not require a battery on the sensing tag. (b) The active NCS tag with a built-in temperature sensor, microphone, battery and Bluetooth connection. The unit weight is 44 g. The sensor can be covered in fabric material and placed onto clothing to record cardiopulmonary waveforms.

AIM 2. CHARACTERIZATION OF CARDIOVASCULAR AND CARDIOVAVULAR FUNCTIONS. We have demonstrated detailed cardiovascular function monitoring from multiple NCS tags as shown in Fig. 2, and benchmarked against ECG, phonocardiogram (PCG) and cuff-based blood pressure measurements under known cardiopulmonary stimulation conditions. For the first time, we are able to derive the four central blood pressures (systolic and diastolic blood pressures in the systemic and pulmonary circulations) in a non-invasive manner, which was only possible before with catheter-based measurements. The detailed cardiovascular physiological information can be derived from the higher characteristic frequency directly from NCS, which was not possible by ECG, cuff-based sphygmomanometers, or pulse-transit time (PTT) methods. The broad spectrum of tissue vibration can be applied to indicate heart murmur, stenosis and regurgitation. The audible band (20 Hz – 2,000 Hz) was compared with the heart sound from acoustic stethoscopes recording of heart valve closure, and the timing and waveforms are reasonably matched.

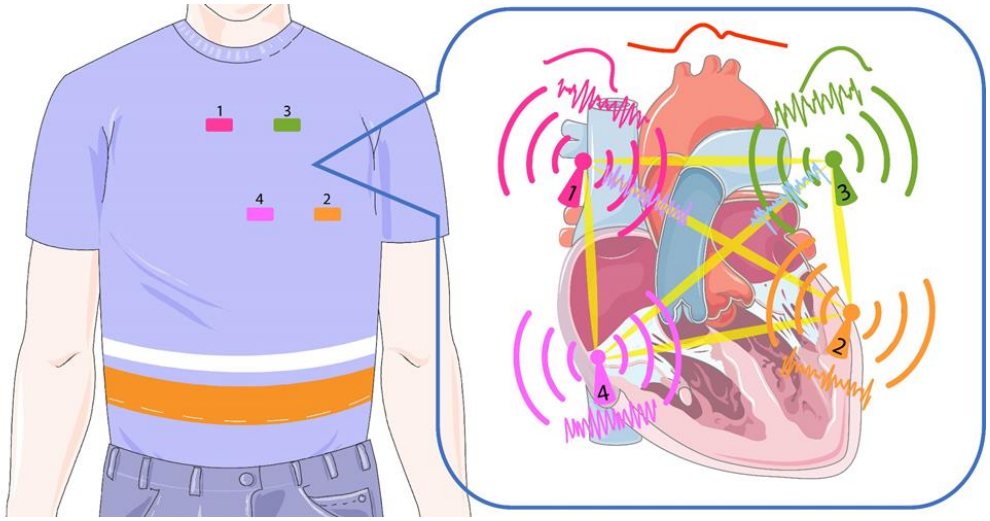

Fig. 2. Monitoring complex heartbeat dynamics by the multi-point NCS system from the tissue vibration information. The wave propagation symbol depicts the backscattering channels for local observation, while the yellow path indicates cross-point channels. The representative heartbeat cyclic waveform is shown accordingly for each channel. Transient pressure traces in the systole phase by Hilbert-Huang analyses at Points 1 and 3 are also shown. The transient pressure waveforms can be used to derive four blood pressures and biometrics from heartbeats.

AIM 3. BENCHMARKING RESPIRATION CHARACTERISTICS. Although the NCS signal from thorax and diaphragm breathing motion is much stronger than the heartbeat, characterization of respiration rhythms and air flow remains challenging due to the mixed spontaneous and autonomous nature of breathing as well as the need to differentiate important anomaly

from apnea, dyspnea, asthma, coughing and sneezing. By employing two NCS tags on thorax and abdomen, we are able to retrieve the breath rate and respiratory volume by body or furniture placement of sensors, as shown in Fig. 3. Long-term continuous monitoring has been compared with chest belts based on strain or respiratory inductance plethysmography (RIP). Various respiration characteristics can be captured by NCS for free-motion wearers during normal spontaneous breathing; breathing exercises with speaking; isovolumetric breathing when the air duct is blocked; mock apnea, dyspnea, coughing, sneezing, Cheyne-Stokes and depression. The cardiopulmonary characteristics captured by NCS can also be used to derive stress and emotion from variability in heart rates, breath intervals and respiratory volumes.

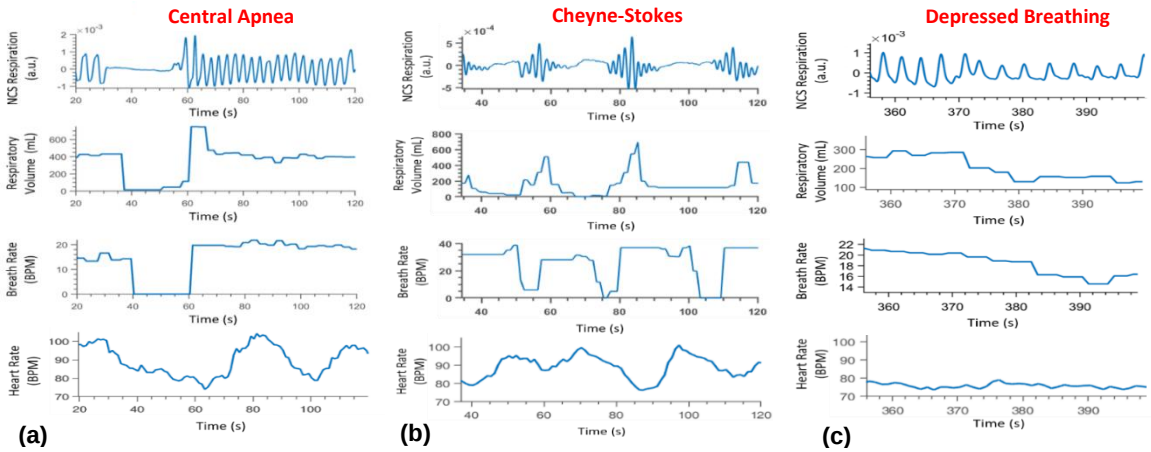

Fig. 3. Respiratory volume, breathing rate and heart rate collected in various simulated breathing disorders using the NCS device: (a) Central apnea: Both respiratory volume and breath rate decrease to nearly 0; (b) Cheyne-Stokes: Apnea followed by fast breathing; (c) Depressed breathing: Gradual decrease in volume and rate.

2. Keywords

Wearable RF sensors; continuous vital-sign monitoring; cardiopulmonary functions; central blood pressures; animal vital signs; stress and emotion evaluation

3. Accomplishments

3.1 Cardiovascular monitoring

Systolic and diastolic blood pressure estimation using arm-cuff monitors is one of the most common cardiovascular evaluation criteria in healthcare today, however these measures lack critical heartbeat and pressure dynamics. Pulse-transit time can be used as an alternative for arm-cuff monitors, but gives only one parameter for two pressure quantities. Ultrasound, computed tomography scan, and magnetic resonance imaging can retrieve geometrical features of the heart, but cannot directly estimate vascular pressures. Here we show a novel radio-frequency heartbeat sensor based on multi-point near-field observation. By comparing to synchronized electrocardiogram and auscultation, the multi-point sensor can assess motion and pressure in different parts of the heart following the Wiggers diagram. By applying the Hilbert-Huang frequency-time transform, the central blood pressure can be derived from the vascular vibration characteristics as continuous transients, including during the pulmonary cycle which is previously inaccessible from branchial measurements. Our scheme can be further extended to a full multiple-input-multiple-output (MIMO) channel arrangement, producing rich content for diagnostic and biometric applications. We employ dynamic time warping analyses to illustrate the sensor's wealth of diversified information across different channels and persons. This new multi-point sensor, which can be worn conveniently over clothing, enables unprecedented monitoring capabilities of detailed central blood pressure transients and heartbeat dynamics under the given measurement instructions for at-home and clinical cardiovascular diagnostics.

See details in Appendix A (IEEE Access 2020).

3.2 Respiration monitoring

Many health diagnostic systems demand non-invasive sensing of respiratory rate, respiratory volume and heart rate with high user comfort. Previous methods often require multiple sensors including skin-touch electrodes, tension belts, or nearby off-the-body readers, and hence are uncomfortable or inconvenient. Here we show an over-clothing wearable radio-frequency sensor study, conducted on 20 healthy participants (14 females) performing voluntary breathing exercises in various postures. Two prototype sensors were placed on the participants, one close to the heart and the other below the xiphoid process to couple to the motion from heart, lungs and diaphragm, by the near-field coherent sensing principle. We can achieve satisfactory correlation of our sensor with the reference devices for the three vital signs: heart rate

($r = 0.95$), respiratory rate ($r = 0.93$) and respiratory volume ($r = 0.84$). We also detected voluntary breath-hold periods with an accuracy of 96%. Further, the participants performed a breathing exercise by contracting abdomen inwards while holding breath, leading to paradoxical outward thorax motion under the isovolumetric condition, which was detected with an accuracy of 83%.

See details in Appendix B (EMBC 2019) and Appendix C (NPJ Digital Medicine 2020).

3.3 Tissue vibration monitoring

The NCS system can detect weak cyclic motion inside living bodies, such as human wrist pulses and the heartbeat of small animals. To couple significant energy to the motion source, a GHz RF carrier was employed, where the vibration amplitude is often much smaller than the wavelength. To optimize the signal quality, we presented a small-signal model with nonlinearity analysis by Jacobi-Anger expansion. The quiescent-point determination and signal composition were then discussed to guide the hardware and algorithm design. The model was validated by electromagnetic simulation in CST Studio and a simple robotic platform. A novel algorithm of adaptive control by signal injection can boost the signal magnitude and data converter utilization. The signal-to-quantization-noise ratio (SQNR) is improved by 35 dB and signal-to-noise ratio (SNR) by more than 10 dB. Sensing of vocal cord vibration was demonstrated as a potential application, where the harmonic radio frequency identification (RFID) system was chosen for its low noise floor to achieve high-fidelity recording of music scales and procedure words.

See details in Appendix D (IMS 2019) and Appendix E (IEEE MTT preprint).

3.4 Covert vital-sign sensing with furniture integration

Non-invasive respiration sensors integrated into furniture can be invisible to the user and greatly enhance comfort and convenience to facilitate many applications. Current sensors often require user cooperation or fitting, which discourages frequent usage. We present a new respiration sensor integrated into a bed or a chair by modifying a radio-frequency (RF) coaxial cable structure with a designed notch. The lung motion is coupled to the electromagnetic leakage at the notch through near-field coherent sensing (NCS). The sensors, covered with fabrics and positioned under the abdomen and thorax, can capture the respiratory waveforms and derive the breath rate. The heart rate can also be evaluated in the same setup with proper filtering. The sensor design can tolerate large position variation to accommodate user uncertainties. Various voluntary exercises of normal, deep, fast, held and blocked breathing were measured under different postures of supine, recumbent and sitting by the carrier frequency range between 900MHz and 2.4GHz. The breath rate from 10 participants compare well with the synchronous commercial chest-belt sensors in all breathing routines.

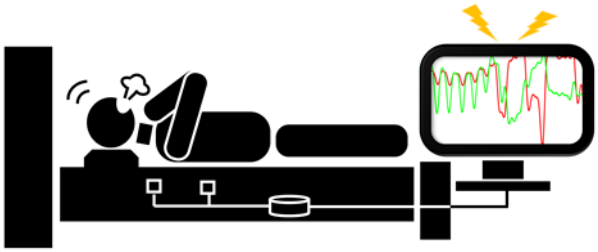

Fig. 4. Illustration of covert vital-sign sensing with bed-integrated NCS sensors.

See details in Appendix F (IMBioC 2019) and Appendix G (IEEE Sensor preprint).

3.5 Stress and attention derivation

The provision of individually tailored sensory response systems has been of increasing importance in recent years. Using emotion recognition has been an important part of the human-machine interaction system by teaching a robot to give appropriate facial and speech responses. Smart buildings can be enabled to adjust lighting according to the emotional state and keep track of mental health, including depression and anxiety monitoring and alert family when required. With increasing work-from-home jobs, forced by the COVID-19 pandemic, such systems are even more important to monitor work fatigue. Keeping track of fatigue or the opposite, attention, is even more important for people working in critical conditions like soldiers in action, heavy machine operators, air traffic controllers, and drivers. With accurate knowledge of the attention state, actions in form of visual or sound stimuli can be provided if a person is slipping into drowsiness or a less attentive state. The capability of an intelligent machine response requires an understanding of human emotional and cognitive reactions. There has been a debate starting from the early philosophers if reason and emotion are two opposite or related concepts, with recent research demonstrating a high level of interdependence. When people perceive a vast amount of information, a subset processing is prioritized and extraneous irrelevant information filtered out, to access the conscious awareness, which can be termed as attention. Thus, attention is a basic function that controls focus, vigilance, and response simultaneously. It can be classified as two types: exogenous attention is sensory-driven, involuntary response, while endogenous attention is a voluntary process with the conscious expectation of events. There is another state called *emotional attention*, which is involuntary similar to exogenous attention but has been suggested to rely on special neural circuitry involving the amygdala. Here we have focused primarily on attention versus relaxation

classification. The attention under this study is endogenous, in response to certain events that the user interacts with during a specific task. The relaxation has been loosely defined as a state similar to drowsiness or fatigue but covers a broader aspect of user inattentiveness including the meditative state. This is an important factor, as the user needs to be attentive even though no harmful activity has been perceived for a long period, such as in driving or guarding. A study on 25 healthy participants sitting on the chair was performed while wearing NCS RF sensors on the thorax and abdomen with routines involving neutral, relaxation, and attention states while sitting in a chair.

See details in Appendix H (Manuscript under preparation).

3.6 Animal monitoring

Measuring the heartbeat and respiration of small conscious animals is important for assessing their health and behavior, but present techniques such as ECG, ultrasound and auscultation rely on close skin contact with the animal. These methods can also require surface preparation, cause discomfort or stress to animals, and even require anesthetic administration, especially for birds, reptiles and fish. Here we show that the RF NCS method can provide a new solution to balance the benefit of animal monitoring while ensuring minimal pain and distress. We first benchmarked NCS with synchronous ECG on an anesthetized rat. NCS is then applied to monitor a conscious hamster from outside its cage, which was further extended to collect vital signs from a parakeet, Russian tortoise, and betta fish non-invasively. Our system can revolutionize vital-sign monitoring of small conscious animals in their lab living quarters or natural habitats.

Mouse vital signs such as the heartbeat and respiration rates are critical observables for the current biomedical and pharmaceutical researches. The number of mice going through the measurement pipeline often needs to be massive to derive statistically significant correlation. However, present mouse vital-sign monitoring methods require substantial individual handling and have limited throughput per setup. Here we demonstrated for the first time a parallel mouse vital-sign reading system, which can simultaneously retrieve the respiration and heartbeat rates for multiple mice in individual chambers with minimal non-invasive handling. The cardio signal quality is high enough to estimate the stress states by the heart rate variation analyses. Our system utilizes the multiplexed RF signal around 1.8 GHz to detect the vital signs by NCS. The cross-chamber interference is minimized by the locality of near fields, frequency division and radar absorbing materials. The isolation can be readily more than 20 dB within a compact system volume. Our scalable design clearly shows how to achieve a high-throughput system for mouse vital-sign monitoring.

See details in Appendix I (Science Advances 2019), Appendix J (IEEE J. Electromagnetics, RF and Microwaves in Medicine and Biology 2020) and Appendix K (IEEE Antenna and Propagation Letters 2020)

4. Impact

We will list the major impacts in the research efforts that are first-time demonstration in the literature and have broad and deep impacts to enable new applications. Additional intellectual impacts on smart buildings, assisted living, effective emergency room management, car seat, wellness evaluation, and digital medicine can be found in the previous section of Achievement.

4.1 Cardiopulmonary health

NCS measures the actual muscle and tissue motion, in comparison to the electrical polarization/depolarization of ECG and SpO2 in oximeter. NCS has unprecedented sensitivity a local specificity that can be broadly applied to monitoring heartbeat, pulses and respiration with multi-point sensor to provide rich information. For cardiac health, NCS can provide continuous transients of four blood pressures (systolic and diastolic blood pressures in the systemic and pulmonary circulations) in every heartbeat. This new cardiovascular information was only possible by invasive catheter methods before. For respiration, NCS offers accurate respiratory volume and detailed breathing waveforms, which was not available previously without employing chest belts with tight tension or facemask or nasal cannula, all of which are uncomfortable for long-term monitoring or need user attention. In comparison, NCS can be a wearable device over clothing or integrated in furniture that can be employed over a long term.

4.2 Comfortable or covert sensing of wellness and stress

Due to the use of UHF RF signals that can penetrate clothing, surface covering and tissues to a controllable depth, NCS can be implemented with great flexibility and various packaging to improve the wearer comfort and even to hide the sensor from the user during monitoring. Passive tags can be embedded into clothing, not necessarily underwear, and can go through laundry as there is no electrical connections. Active tags can be packaged as wearables such as in wristwatch, necklace and lanyards. Alternatively, active tags can be embedded inside beds or chairs, providing on-demand monitoring of vital signs in a covert manner.

4.3 High-throughput covert animal monitoring

Present animal vital-sign monitoring methods require laborious and invasive surface preparation, and are not feasible for animals with shells or thick blubber. Due to the RF signal penetration over various surface coverings of furs, hair, scales, scutes, shells and feathers, NCS can be applied to animal vital-sign monitoring without surface preparation. Similar to furniture integration, NCS sensors can be installed on cages and habitats, and most animals have no awareness or stress during the monitoring of their vital signs.

5. Changes/Problems

We have executed the CDMRP efforts reasonably close to the proposed aims and tasks, as described in Sec. 1. NCS can obtain accurate cardiopulmonary waveforms through clothing and various surface coverings, as the UHF band RF signals can couple deeply into tissues by the near fields. This is a unique technology to be applied to small conscious animals. We therefore expand our investigation to various animals including mice, rats, hamsters, birds, tortoises, fish, lemurs (primates), dogs, cows and even elephant seals, based on the availability of animal models that we have access.

6. Products

6.1 Bibliography of Publications

[1] X. Hui and E. C. Kan, "No-touch measurements of vital signs in small conscious animals", *Science Advances*, vol. 5, art: eaau0169, Feb. 2019. (Featured in *AAAS News*)

[2] X. Hui and E. C. Kan, "Seat integration of RF vital-sign monitoring", *International Microwave Biomedical Conf. (IMBioC)*, Nanjing, China, May 6 – 8, 2019.

[3] X. Hui, P. Sharma and E. C. Kan, "Microwave stethoscope for heart sound by near-field coherent sensing", *International Microwave Symposium*, Boston, MA, June 2 – 7, 2019.

[4] P. Sharma, X. Hui and E. C. Kan, "An RF sensor for monitoring respiratory patterns", *41st Annual Intl. Conf. IEEE Engineering in Medicine and Biology Society (EMBC'19)*, Berlin Germany, July 23 – 27, 2019.

[5] X. Hui, T. B. Conroy and E. C. Kan, "Multi-point near-field RF sensing of blood pressures and heartbeat dynamics", *IEEE Access,* doi: 10.1109/ACCESS.2020.2993994, 2020.

[6] J. Zhou, P. Sharma, X. Hui and E. C. Kan, "Wireless wearable RF sensor for long-term vital-sign monitoring on chelonians", *IEEE J. Electromagnetics, RF and Microwaves in Medicine and Biology*, doi: 10.1109/JERM.2020.2998761, 2020.

[7] X. Hui, J. Zhou and E. C. Kan, "High-volume parallel mouse vital-sign monitoring with near-field coherent sensing", *IEEE Antenna and Wireless Propagation Letters*, doi: 10.1109/ LAWP.2020.2992055, 2020.

[8] P. Sharma, X. Hui, J. Zhou, T. B. Conroy and E. C. Kan, "Robust cardiopulmonary monitoring using wearable radio-frequency sensors", *Nature Partner Journal (NPJ), Digital Medicine*, doi: 10.1038/s41746-020-0307-6, July 2020.

[9] Z. Zhang, P. Sharma, J. Zhou, X. Hui and E. C. Kan, "Furniture-integrated respiration sensors by notched transmission lines", accepted by *IEEE Sensor J*., 2020.

[10] X. Hui, T. B. Conroy and E. C. Kan, "Near-field coherent sensing with harmonic analysis and balance signal injection", accepted by *IEEE Trans. MTT*.

6.2 List of Available Hardware and Software

- Active NCS sensors by Ettus software-defined radios (SDR)
- Active NCS sensors by custom PCB and 3D-printed packages
- Passive NCS sensors based on WISP 5.0
- Passive NCS sensors based on custom PCB with commercial antennas
- Passive NCS sensor readers by Ettus SDR
- Control software for Ettus SDR by Labview
- Control software for custom PCB on Windows and Android
- Signal processing software based on adaptive filtering and conditioning by Matlab
- Signal processing software for waveform processing and peak detection by Matlab
- Signal processing software based on Hilbert-Huang time-frequency transforms by Matlab

7. Participants & Other Collaborating Organizations

7.1 Participating Personnel

PI: Edwin Kan
Ph.D. student: Xiaonan Hui

Ph.D. student: Pragya Sharma
Ph.D. student: Jianlin Zhou
Ph.D. student: Zijing Zhang
M.Eng. student: Tejas Advait

7.2 Collaborating Organizations

Mukesh Bansal, Psychogenics, Paramus NJ: On large-scale vital-sign monitoring for lab mice.

Marina Blanko, Duke Lemur Center, Duke University: On torpor behavior study for lemurs.

These two organizations have NOT used any of the CDMRP funding, but are collaborators in using the developed vital-sign sensor, providing the animal models for experimental demonstration and sensor validation. The experimental results were successful, but have not been put into publication submission.

8. Special Reporting Requirements

N/A.

9. Appendices

The ten publications under the support of the CDMRP effort are attached as appendices, which include 5 published journal papers, 3 published conference papers and 2 journal paper preprints. An additional manuscript under preparation is also attached as Appendix K, which deals with the stress derivation from vital signs. The main theme of each paper is summarized in Sec. 3: Accomplishment.

A. (PDF downloaded from IEEE) X. Hui, T. B. Conroy and E. C. Kan, "Multi-point near-field RF sensing of blood pressures and heartbeat dynamics", *IEEE Access,* doi: 10.1109/ACCESS.2020.2993994, 2020.
B. (PDF downloaded from IEEE) P. Sharma, X. Hui and E. C. Kan, "An RF sensor for monitoring respiratory patterns", *41st Annual Intl. Conf. IEEE Engineering in Medicine and Biology Society (EMBC'19)*, Berlin Germany, July 23 – 27, 2019.
C. (PDF downloaded from Nature) P. Sharma, X. Hui, J. Zhou, T. B. Conroy and E. C. Kan, "Robust cardiopulmonary monitoring using wearable radio-frequency sensors", *Nature Partner Journal (NPJ), Digital Medicine*, doi: 10.1038/s41746-020-0307-6, July 2020.
D. (PDF downloaded from IEEE) X. Hui, P. Sharma and E. C. Kan, "Microwave stethoscope for heart sound by near-field coherent sensing", *International Microwave Symposium (IMS)*, Boston, MA, June 2 – 7, 2019.
E. (PDF preprint) X. Hui, T. B. Conroy and E. C. Kan, "Near-field coherent sensing with harmonic analysis and balance signal injection", accepted in *IEEE Trans. MTT*.
F. (PDF downloaded from IEEE) X. Hui and E. C. Kan, "Seat integration of RF vital-sign monitoring", *International Microwave Biomedical Conf. (IMBioC)*, Nanjing, China, May 6 – 8, 2019.
G. (PDF preprint) Z. Zhang, P. Sharma, J. Zhou, X. Hui and E. C. Kan, "Furniture-integrated respiration sensors by notched transmission lines", accepted in *IEEE Sensor J*., 2020.
H. (PDF manuscript under preparation) P. Sharma, Z. Zhang, X. Hui and E. C. Kan, "Attention monitoring using non-invasive vital-sign features", manuscript under preparation.
I. (PDF downloaded from Science) X. Hui and E. C. Kan, "No-touch measurements of vital signs in small conscious animals", *Science Advances*, vol. 5, art: eaau0169, Feb. 2019. (Featured in *AAAS News*)
J. (PDF downloaded from IEEE) J. Zhou, P. Sharma, X. Hui and E. C. Kan, "Wireless wearable RF sensor for long-term vital-sign monitoring on chelonians", *IEEE J. Electromagnetics, RF and Microwaves in Medicine and Biology*, doi: 10.1109/JERM.2020.2998761, 2020.
K. (PDF downloaded from IEEE) X. Hui, J. Zhou and E. C. Kan, "High-volume parallel mouse vital-sign monitoring with near-field coherent sensing", *IEEE Antenna and Wireless Propagation Letters*, doi: 10.1109/ LAWP.2020.2992055, 2020.

Appendix A

(PDF downloaded from IEEE) X. Hui, T. B. Conroy and E. C. Kan, “Multi-point near-field RF sensing of blood pressures and heartbeat dynamics”, *IEEE Access,* doi: 10.1109/ACCESS.2020.2993994, 2020.

IEEE Access
Multidisciplinary | Rapid Review | Open Access Journal

Received April 16, 2020, accepted May 4, 2020, date of publication May 12, 2020, date of current version May 26, 2020.

Digital Object Identifier 10.1109/ACCESS.2020.2993994

Multi-Point Near-Field RF Sensing of Blood Pressures and Heartbeat Dynamics

XIAONAN HUI, (Student Member, IEEE), THOMAS B. CONROY, AND EDWIN C. KAN, (Senior Member, IEEE)
School of Electrical and Computer Engineering, Cornell University, Ithaca, NY 14853, USA

Corresponding author: Xiaonan Hui (xh273@cornell.edu)

This work was supported in part by the Department of Energy (DoE) of United States through the Advanced Research Projects Agency-Energy (ARPA-E) under Project DE-AR0000946, and in part by the Department of Defense of United States through the Office of the Congressionally Directed Medical Research Programs (CDMRP) Discovery under Award PR-182496.

ABSTRACT Systolic and diastolic blood pressure estimation using arm-cuff monitors is one of the most common cardiovascular evaluation criteria in healthcare today, however these measures lack critical heartbeat and pressure dynamics. Pulse-transit time can be used as an alternative for arm-cuff monitors, but gives only one parameter for two pressure quantities. Ultrasound, computed tomography scan, and magnetic resonance imaging can retrieve geometrical features of the heart, but cannot directly estimate vascular pressures. Here we show a novel radio-frequency heartbeat sensor based on multi-point near-field observation. By comparing to synchronized electrocardiogram and auscultation, the multi-point sensor can assess motion and pressure in different parts of the heart following the Wiggers diagram. By applying the Hilbert-Huang frequency-time transform, the central blood pressure can be derived from the vascular vibration characteristics as continuous transients, including during the pulmonary cycle which is previously inaccessible from branchial measurements. Our scheme can be further extended to a full multiple-input-multiple-output (MIMO) channel arrangement, producing rich content for diagnostic and biometric applications. We employ dynamic time warping analyses to illustrate the sensor's wealth of diversified information across different channels and persons. This new multi-point sensor, which can be worn conveniently over clothing, enables unprecedented monitoring capabilities of detailed central blood pressure transients and heartbeat dynamics under the given measurement instructions for at-home and clinical cardiovascular diagnostics.

INDEX TERMS Biomedical signal processing, cardiography, microwave sensors, MIMO, stethoscope, wearable sensors.

I. INTRODUCTION

Arm-cuff sphygmomanometers for blood pressure (BP) measurements are universally employed in modern at-home and in-patient healthcare practices. Systolic and diastolic BPs are estimated by branchial vascular occlusion once within a period of many pulses. However, the intrusive cuff inflation can disturb sleep as well as interrupt circadian rhythms and vigilance. In addition, continuous heartbeat dynamics during central aortic and atrioventricular cycles remain unavailable, and the characteristics of the pulmonary circulation are entirely missing. Monitoring central aortic and pulmonary artery pressure transients results in more accurate evaluation of cardiovascular risk factors than the branchial BPs, however these crucial metrics can previously only be measured by invasive catheters [1], [2]. To reduce disturbance to patients, BP can be indirectly derived from the pulse-transit time (PTT) [3], [4], which is defined as the transit delay between two chosen proximal and distal points. PTT can be measured by either photo-plethysmography (PPG) [5], [6] or radio-frequency (RF) [7] methods to estimate the systolic pressure with personal calibration, while the diastolic pressure is derived from a fitting ratio. PTT sensors must be placed on two disjoint body positions and require synchronization with sub-millisecond precision, making PTT a cumbersome method for long-term ambulatory monitoring. Notice that PTT derives both systolic and diastolic pressures from a single measurement parameter, which is non-ideal for pathological evaluation, even with personal calibration. Alternatively, heartbeat geometrical features can be

The associate editor coordinating the review of this manuscript and approving it for publication was Zesong Fei.

This work is licensed under a Creative Commons Attribution 4.0 License. For more information, see https://creativecommons.org/licenses/by/4.0/

recovered by ultrasound, computed tomography (CT) scan, and magnetic resonance imaging (MRI) [8], each of which often require professional operators and extensive lab setup, and are hence infeasible for long-term or at-home monitoring. BP cannot be directly measured with these methods but can be estimated with personal calibration. Ultrasound has limited spatial resolution for accurate extraction of detailed valve dynamics, although the blood velocity and systolic BP can be derived from the Doppler effect [9]. CT scans and MRI have limited time resolution, and the heart valve timing and pressure dynamics are subject to large uncertainties.

Electromagnetic heartbeat sensing has been investigated for many years as well [10], [11]. Microwave radar-based approaches, by either the Doppler effect or the frequency-modulation chirps [12], [13], require the line-of-sight (LoS) alignment to the chest area by an off-body reader, although no wearable body tag is needed. As the minute chest movement caused by heartbeats is read at a distance, the signal is often weak and the spatial resolution of the different heart areas is low. Alternatively, notched or resonator-loaded transmission lines can be employed to sense the local dielectric properties [14], [15], which had been extended to vital-sign monitoring [7]. However, the blood pressure estimation has been restricted to PTT, and no multi-point observation on the heart had been attempted.

In this paper, we present a new RF-based method for tracking heart dynamics and central blood pressure based on the near-field coherent sensing (NCS) principle [4]. This method enables convenient and comfortable cardiac monitoring by placing multiple sensing antennas over clothing on top of the heart, allowing for heartbeat dynamics to be directly modulated onto the received RF signal. Due to the high sensitivity and broadband coupling of NCS, both large cardiovascular motion and minute cardiac vibration characteristics can be retrieved. When these cardiac vibrations are processed using the Hilbert-Huang frequency-time transform, beat-to-beat blood pressure transients can be derived by matching the frequency-time signal to the Wiggers diagram [16]. The multi-point NCS method enables position-specific sensing, in which multiple antennas provide a wealth of diversified information to analyze complex heartbeat motion dynamics, including both systemic and pulmonary circulation when the subjects sit still and control their breathing rhythm. The new multi-point NCS system in this paper is the first long-term wearable technology that can provide such detailed central blood pressure transients and heartbeat dynamics, and can offer unparalleled monitoring capabilities under the given measurement condition for clinical and at-home cardiovascular diagnostics.

II. THE MULTI-POINT NCS SYSTEM SETUP

The NCS principle states that when a dielectric boundary moves in the near-field region of a transmitting or backscattering antenna, its motion becomes part of the antenna characteristics that can be evaluated after carrier demodulation and baseband filtering [4], [17]. Both carrier and baseband injection in NCS contributes to channel isolation and eventual multiplexing, and the near-field coupling provides the sensing locality. Dielectric boundary motion relative to the antenna will be mainly captured by the received NCS magnitude, from the interferometer-like structure as a differential mode, while boundary motion occurring together with the antenna will be captured by the NCS phase as a common mode [4]. The NCS system couples significant RF energy in the ultra-high frequency (UHF) band (300 MHz – 3 GHz) into the entire heart region, allowing for the complex dielectric boundary motion of the heart to be directly modulated onto our received signal magnitude and phase. The radiation level is very low and well under the safety standard prescribed by OSHA (Occupational Safety and Health Administration) [18]. To study the complex heartbeat dynamics from different angles, multiple observation points are helpful, as the received signal at each point is dominated by the local dielectric boundary motion.

The new multi-point NCS system is shown in Fig. 1(a), which consisted of two software defined radios (SDR, National Instrument Ettus Research B210), denoted as SDR1 and SDR2. The two SDRs are synchronized by an external local oscillator (LO) with 10 MHz reference and 1 PPS (pulse per second) baseband synchronization (BG7TBL-GPSDO). The SDRs were connected to a host computer through USB cables. The control software was implemented in LabVIEW.

Each port of the NCS system consists of one RF transmitter (Tx) and one receiver (Rx). For Port 1 (Po1) in SDR1, the first NCS sensing antenna pair is connected to Tx1 (blue triangle) and Rx1 (red triangle). The field programmable gate array (FPGA) prepares the baseband signal to be fed to the Tx1 chain, and the received RF signal modulated by the heartbeat is fed to Rx1 and demodulated by the FPGA. The other three ports (Po2 to Po4) are similarly configured with Tx2 and Rx2 to Po2 in SDR1, Tx3 and Rx3 to Po3 in SDR2, and Tx4 and Rx4 to Po4 in SDR2. The RF signal at each Tx can be multiplexed with time-division multiple access (TDMA) [19], code division multiple access (CDMA) [20], [21] or, in the case of this work, frequency division multiple access (FDMA) [17], [22]. The carrier frequency is 1.82 GHz with 0.71 MHz, 1.22 MHz, 1.71 MHz and 2.33 MHz baseband offsets for Tx1 –Tx4, respectively. The four sensing antenna pairs were placed at Points $1-4$ in Fig. 1(b), which were chosen to mimic the conventional auscultatory stethoscope for listening to the aortic, mitral, pulmonary and tricuspid valves. Point 0 was chosen as Erb's point, a central area of the chest used as a reference NCS position for timing comparison. The electrodes of the electrocardiogram (ECG, NeuroSky BMD101) were pasted on the torso at Points LL (left leg) and RA (right arm) and connected to the host computer by USB. The ECG signal was used as a timing reference to highlight the feature points in the cardiac cycle. A digital stethoscope (Thinklabs One) was placed at Point ST to record the S1 and S2 heart sounds. The SDR sampling rates of the data converter were set as 5 MSps, which is above the Nyquist rate of 2 times of the highest

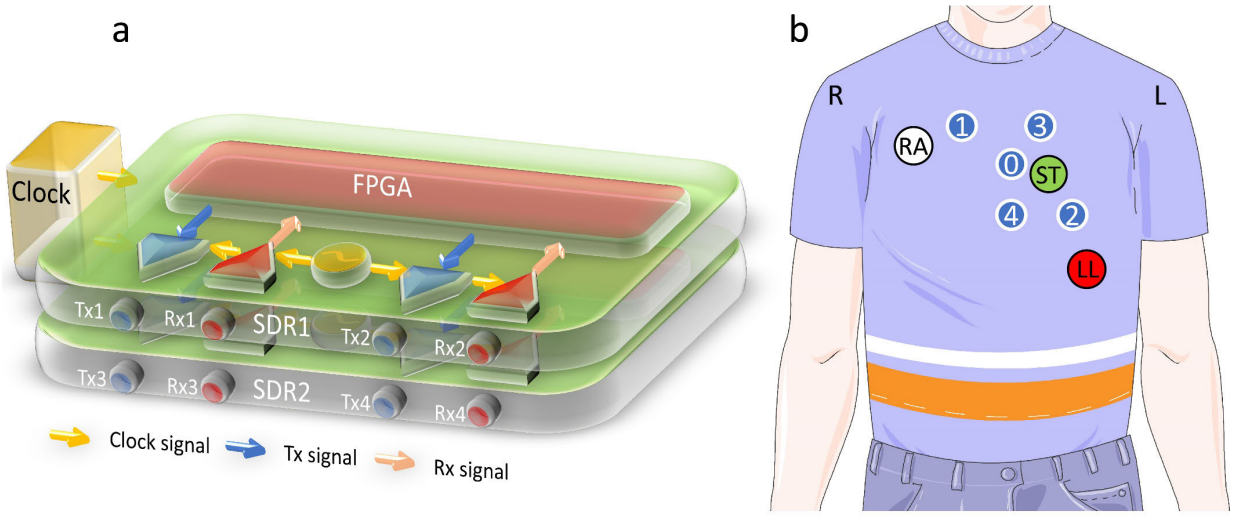

FIGURE 1. The multi-point RF system for near-field coherent sensing (NCS). (a) Electronic hardware: The cardio reader constructed by two SDRs and an external reference clock source for synchronization. (b) Body placement: The location of the sensing points: Points 0 to 4 are for NCS, ST is the stethoscope drum placement, and the ECG electrodes are pasted at LL and RA. The letters "L" and "R" in the deltoid area indicate body left and right. FPGA denotes the field-programmable gate array; Tx the transmitter; Rx the receiver.

baseband offset at 2.33 MHz. After channel demodulation, the NCS signal was down-sampled to 50 kSps, which is slightly higher than 44.1 kSps of the digital stethoscope so that NCS can contain all information from the audible signal. The NCS, ECG, and stethoscope signals were synchronized in LabVIEW. A detailed system schematic is shown in Supplementary Fig. 1.

The picture of the fully coherent system is shown in Fig. 2(a). In Figs. 2(b) and (c), two kinds of NCS antenna pairs are shown. In Fig. 2(b), two monopole antennas (black whips, Taoglas TG.19.0112) are mounted on a 3D-printed holder. The overall dimensions are 69 × 17 × 11 mm (W × L × D). The operating frequency is around 1.82 GHz with a bandwidth of 40 MHz. A smaller NCS sensing antenna pair by two ceramic patch antennas (Taoglas WLP.12C) is shown in Fig. 2(c). The overall dimension is reduced to 32 × 14 × 5 mm. The operating frequencies are around 900 MHz and 5 GHz. For the commercial antennas used here, the operational bands are chosen by the reflection coefficient S_{11} when the NCS antenna pair is placed on the human chest area [23]. In general, the lower frequency provides better penetration into the body and stronger signal coupling. The carrier frequency selection should also comply with the government regulation in the future when custom antennas are deployed.

To extend the system to full multiple-input-multiple-output (MIMO) capability, we configured the dual SDR system to implement cross-point channels. This enabled, for example, Tx1 to be received by Rx1, Rx2, Rx3 and Rx4, for greater signal diversity and measurement opportunities. The ECG electrodes and the stethoscope drum require direct skin contact to acquire clear signal, yet the NCS sensing antennas can be placed outside the clothing as shown in Fig. 2(d) due to the effective RF penetration in the UHF band [4], [22]. All NCS, ECG and stethoscope recordings were synchronized in the host computer. An illustration of the MIMO NCS coverage is shown in Supplementary Fig. 2.

III. SYNCHRONIZED NCS, ECG AND STETHOSCOPE

The timing relation among the synchronized ECG, stethoscope and single-channel NCS signals is shown in Fig. 3(a), where the NCS antenna pair was put on Point 0 (Erb's point) in Fig. 1(b). The demodulated NCS raw recording is shown as the green curve in Fig. 3(a), and its zero-phase bandpass filtered (7 –20 Hz) waveform is the purple curve to highlight the high-frequency vibration components. The synchronized ECG and stethoscope waveforms are shown as the blue and pink curves. The first heart sound (S1) happens around the R-S period of the ECG caused by the closure turbulence or claps of the atrioventricular (AV) valves, and the second heart sound (S2) is at the end of the T wave generated by that of the semilunar (SL) valves. These timing features will be aligned according to the physiological Wiggers diagram [1], [16] in later analyses.

As the NCS signal is modulated by the mechanical motion of the dielectric boundaries in its proximity, the received raw waveform is dominated by the strong fundamental heartbeat tone. In addition to this tone, the details of the internal motion of the atria, ventricles, valves and artery are also coupled to the NCS signal and each motion has its frequency features and timing. Because all physiological frequencies are much lower than the impinging RF carrier, they will all be captured in the demodulated NCS signal, constrained only by the signal-to-noise ratio (SNR). Similar to audible sound analysis, higher frequency components will have lower amplitude for the same spectral energy. The high-frequency information of the heartbeat is thus visually overwhelmed by the low-frequency component in the time domain. After proper bandpass

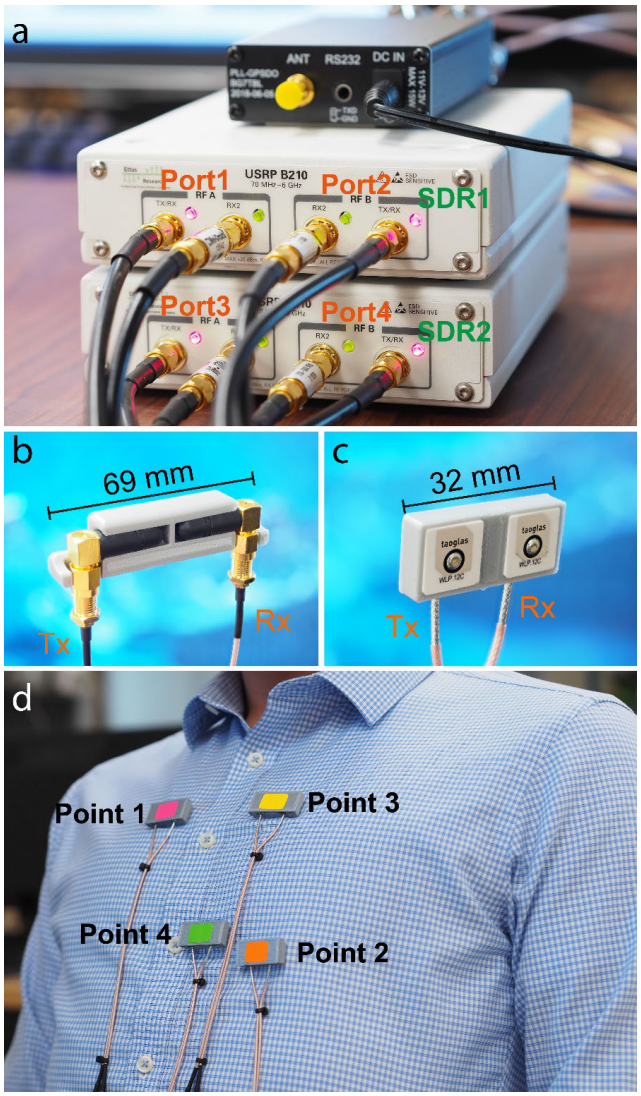

FIGURE 2. The multi-point NCS system photos. (a) The transceiver by two coherent software-defined radios (SDR1 and SDR2). (b) The sensing antenna pair at 1.8 GHz band; (c) at the 900 MHz and 5 GHz bands. (d) The sensing antenna placement when 4 antenna pairs are deployed to Points 1 – 4 in Fig. 1(b). The sensing antenna pairs are placed over the shirt.

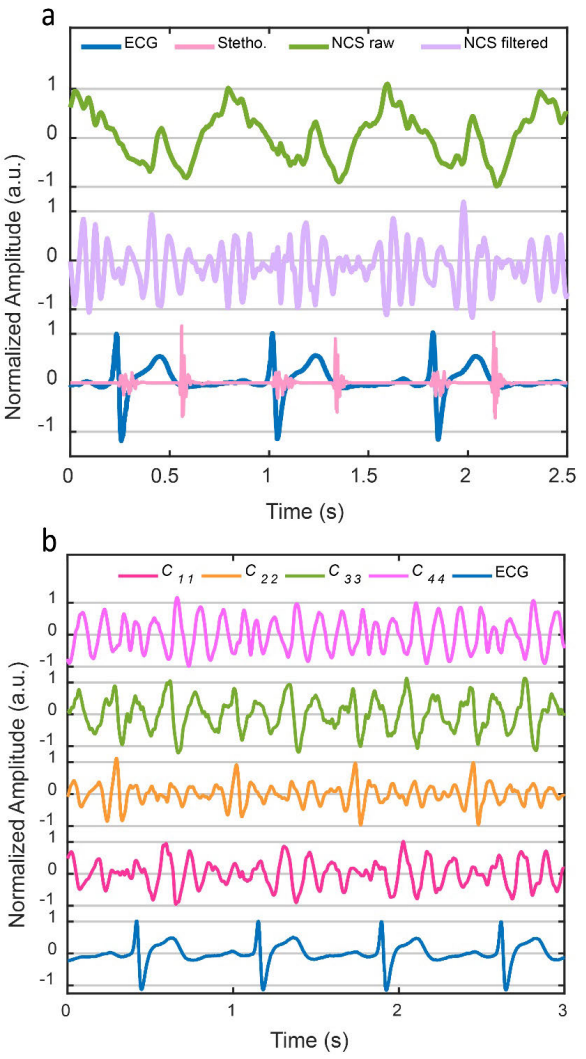

FIGURE 3. Comparison of the synchronized NCS, ECG and stethoscope waveforms. (a) The single-channel NCS at Point 0 is shown in green. The purple waveform is the high-frequency NCS waveform after bandpass filtering of 7-20Hz, while the blue and pink curves are the ECG and the stethoscope signals. (b) The synchronized four-point NCS backscattering channels. The waveforms from C_{11} to C_{44} (red, yellow, green, pink) are from Points 1 – 4 in Fig. 1(b), respectively. The synchronized ECG curve (blue) is shown for timing reference.

filtering is applied to the raw NCS signal, the high-frequency features can be more clearly viewed in the systole and diastole phases. Notice that some NCS features are not included in either ECG or stethoscope. ECG measures the electrical activity started from the sinoatrial node, which does not carry the direct information of the mechanical motion. Stethoscope, on the other hand, can only capture vibration in the audible range as determined by the acoustic impedance matching of the drum, and will likely attenuate low-frequency parts of the auditory signal. From Fig. 3(a), we can clearly observe that no clear stethoscope signal is present between S1 and S2, but the bandpass filtered NCS signal still contains many features, which are likely from atrial and ventricular chamber movement with spectral features lower than the audible frequencies in stethoscopes. For a direct comparison, the NCS signal after bandpass filtering of 16 – 120 Hz is compared to the synchronized waveforms in the acoustic stethoscope [23], as illustrated in the Supplementary Fig. 3 and Supplementary Movie 1.

We will now use the four-point NCS system shown as Points 1 – 4 in Fig. 1(b). In Fig. 3(b), the backscattering channels of Tx1-to-Rx1 (C_{11}), Tx2-to-Rx2 (C_{22}), Tx3-to-Rx3 (C_{33}) and Tx4-to-Rx4 (C_{44}) after the same zero-phase bandpass filtering (7 – 20 Hz) are presented as red, yellow, green and pink curves, respectively. The synchronized ECG in the blue curve is added for timing reference. The system setups of C_{11} to C_{44} are the same, but each antenna pair demonstrates its unique weighted coupling to the different parts of the heartbeat. C_{11} and C_{33} have stronger signals just

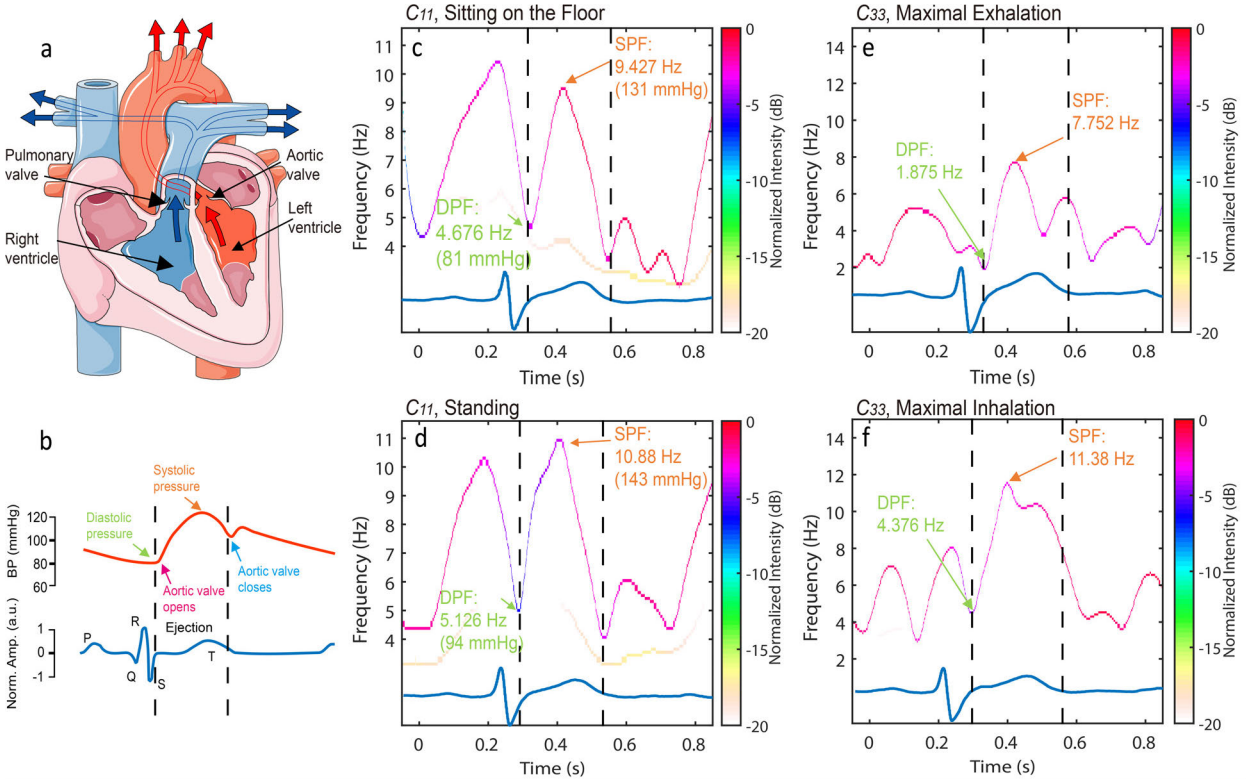

FIGURE 4. BP analyses based on the NCS backscattering channel during the systole phase. (a) The cross section of the heart ejecting blood from left and right ventricles. (b) The Wiggers diagram shows the expected timing relation between ECG (blue) and the aortic pressure (red). (c) The HHT frequency-time analysis of C_{11} when the person sat on the floor. The synchronized ECG signal (blue) indicates the timing. (d) C_{11} HHT when the person took a standing posture. (e) C_{33} HHT for the pulmonary cycle when the person held breath after maximum exhalation. (f) C_{33} HHT when the person held breath after maximum inhalation.

after the QRS complex when the heart ejects the blood from the ventricles to the artery through the SL valves. Analogous to the auscultation position, C_{11} will have more emphasis on the aortic valve and artery, while C_{33} will emphasize the pulmonary valve and artery. Similarly, C_{22} contains more mitral valve motion during the P-R period, and C_{44} contains more tricuspid valve information although it also couples in the strong left ventricular motion during the T wave. The aortic circulation usually has larger motion and higher pressure than the pulmonary circulation due to the higher vascular resistance. This cannot be directly observed from Fig. 3, as the NCS magnitude is normalized to its respective highest peak during the recording to visualize each channel more clearly.

IV. BLOOD PRESSURE EXTRACTION

During the systole phase, the C_{11} waveform is dominated by the aortic movement and can be used for BP derivation through the vessel vibration characteristics. Notice that C_{11} is related to the central BP of the aortic artery instead of the branchial BP given by the arm cuff, although the two values are often reasonably correlated when the cuff is at the same height of the heart [1]. At the end of the diastole phase, left and right ventricles are at their largest volume filled with blood. Then the ventricular contraction is triggered by the QRS signals into the systole phase. Fig. 4(a) shows the cross section of the heart ejecting blood from both ventricles into the aorta and pulmonary arteries. Fig. 4(b) shows the corresponding part of the Wiggers diagram [16] for the timing relation between ECG (blue) and the aortic pressure (red). The systole period is between the black dashed lines, where the tricuspid and the mitral valves are closed to inhibit regurgitation and thus the atria have no significant motion during systole. When the BP in the ventricles are higher than those in aorta and pulmonary arteries, the aortic and pulmonary valves will open, which is indicated by the magenta arrow in Fig. 4(b). The ventricular contraction makes the aortic pressure reach its peak value, which is defined as the central systolic BP indicated by the orange arrow around the T wave. Afterwards the aortic pressure begins to drop due to blood flow to branchial vessels until the aortic and left ventricle pressures are equal, then the aortic valve closes to form a small cusp in the aortic pressure generating the S2 heart sound, as indicated by the cyan arrow. The aortic pressure keeps dropping in the next diastole phase when the AV valves are open for blood to flow from atria to ventricles. Immediately after the QRS complex, the aortic pressure reaches its minimum value, which is defined as the central diastolic BP indicated by the green arrow, where the AV valves close to make the S1 heart sound. As the fluid pressure is positively correlated to the vibration characteristics of the containing viscoelastic vessel and valve [9], [24], the high-frequency

components in C_{11} during systole would contain the aorta vibration features, which can be used to estimate the central systolic and diastolic BP.

Therefore, NCS BP derivation requires high resolution in both frequency and time with a broad base bandwidth. Frequency and time are the Fourier transform pair, and hence frequency and time resolutions are limited by the Uncertainty Principle model [25], [26]. A simplest way to observe this limitation is by the short-time Fourier transform (STFT) [27] where a time window is applied to compute the spectrum of an infinite time series. To obtain high time resolution in STFT, we need to reduce the time window length, which causes the spectrum within the time window to spread out, and thus high frequency resolution cannot be simultaneously achieved by Fourier transform. Other methods such as wavelet transform and windowed Fourier transform [28] can mitigate this deficiency to some extent, but the tradeoff between the time and frequency resolutions remains.

To minimize the frequency-time resolution contradiction, we opted to use the Hilbert-Huang transform (HHT) to obtain the frequency-time spectrum [29], [30], where the instantaneous frequency is calculated at each sampling time point for the nonstationary oscillation analysis. The time resolution depends on the sampling rate in the time domain, which can be easily above 10^6 samples per second (Sps) by the analog-to-digital converter (ADC) in the chosen SDR. The high ADC sampling rate can also spread the noise over a larger spectrum to reduce the noise floor and increase SNR. This frequency resolution was chosen to facilitate reasonable computation time. C_{11} represents observation from Point 1, which mimics the stethoscope position for the aortic valve murmur. Fig. 4(c) is the HHT frequency-time analysis of a single heartbeat obtained from C_{11} when the person under test sat on the floor. The blue curve is the synchronized ECG signal to show timing, and the ventricular ejection period is between the dashed lines. The sampling rate for the waveform is 10^3 Sps, producing a 1 ms time resolution. The highest frequency response is half of the sampling rate at 500 Hz. The frequency resolution is set to 0.125 Hz, 1/8000 of the sampling rate.

All post processing was performed in MATLAB. All filtering used zero-phase FIR (finite impulse response) filters to cancel the phase shift and maintain the linear phase response. The down-sampled signal was further bandpass-filtered (1.5–16 Hz) to attenuate the fundamental heartbeat tone, high-frequency heart sounds, and noises. The filter frequencies are selected based on the signal characteristics [23]. The resulting waveform $x(t)$ was then processed by empirical mode decomposition (EMD) [29] as a part of the HHT algorithm, where several intrinsic mode functions (IMF) $c_j(t)$ represent the simple nonstationary oscillatory modes and can be extracted as:

$$x(t) = \sum_{j=1}^{n} c_j(t) + r_n \tag{1}$$

where the final residue r_n is either the mean trend or a constant. We extracted the first seven IMF $c_1(t)$ to $c_7(t)$ for $x(t) = C_{11}$ in Supplementary Fig. 4, where we can see most features are captured in $c_1(t)$ and $c_2(t)$. The signal is further processed by the Hilbert spectral analysis (HSA).

$$y_j(t) = H[c_j(t)] = \frac{1}{\pi} PV \int_{-\infty}^{\infty} \frac{c_j(\tau)}{t-\tau} d\tau \tag{2}$$

where $H[\cdot]$ and PV represent the Hilbert transform and the Cauchy principal value. Then the analytic signal $z_j(t)$, which comprises the original signal and its Hilbert transform, can be defined as

$$z_j(t) = c_j(t) + iy_j(t) = a_j(t)\exp[i\theta_j(t)] \tag{3}$$

where i is the imaginary unit, $a(t)$ is the instantaneous amplitude, and $\theta(t)$ is the phase function. The analytic signal $z_j(t)$ is a complex-valued function that has no negative frequency component, and can be considered as a generalized time-varying phasor. The instantaneous frequency can then be extracted as

$$\omega_j = \frac{d\theta_j}{dt} \tag{4}$$

We only kept the first two IMFs with the highest magnitude here. The IMF distribution is shown in Supplementary Fig. 4 for illustration. This procedure can be considered as an additional filtering which is not based on the pass-stop band, but by the oscillatory modes. The real part ($\Re\{\cdot\}$) of the processed signal can be expressed as

$$x'(t) = \Re\{\sum_{j=1}^{2} a_j(t)\exp[i\int \omega_j(t)dt]\} \tag{5}$$

In Fig. 4(c), each point represents the instantaneous frequency ω_1 at the corresponding time, and its color shows the instantaneous amplitude in the dB scale normalized by the respective maximum value. The horizontal and vertical axes are the time and frequency, respectively. During the systole phase, the frequency-time points of ω_1 form a red-pink "curve" with a similar shape of the aortic pressure curve in the Wiggers diagram. The maximum frequency point at 9.427 Hz, denoted as the systolic pressure frequency (SPF), is well aligned with the systolic BP point. The minimum at 4.676 Hz, denoted as the diastolic pressure frequency (DPF), is aligned with the diastolic BP point at the beginning the systole phase. The concurrent brachial BPs measured by an arm-cuff monitor (Omron BP760N) are 131 mmHg and 81 mmHg. We then repeated the experiment when the person stood up. The frequency-time analysis is shown in Fig. 4(d). The SPF and DPF in this case are 10.88 Hz and 5.126 Hz, and the corresponding arm-cuff BPs are 143 mmHg and 94 mmHg. Two-point linear interpolation can transform the two SPFs to systolic BP, and similarly the two DPFs to diastolic BP in Figs. 4(c)(d). This interpolation scheme enable the NCS system to estimate continuous blood pressure transients. The frequency resolution is 0.125 Hz, corresponding to 1.0 mmHg resolution for the systolic BP and 3.6 mmHg

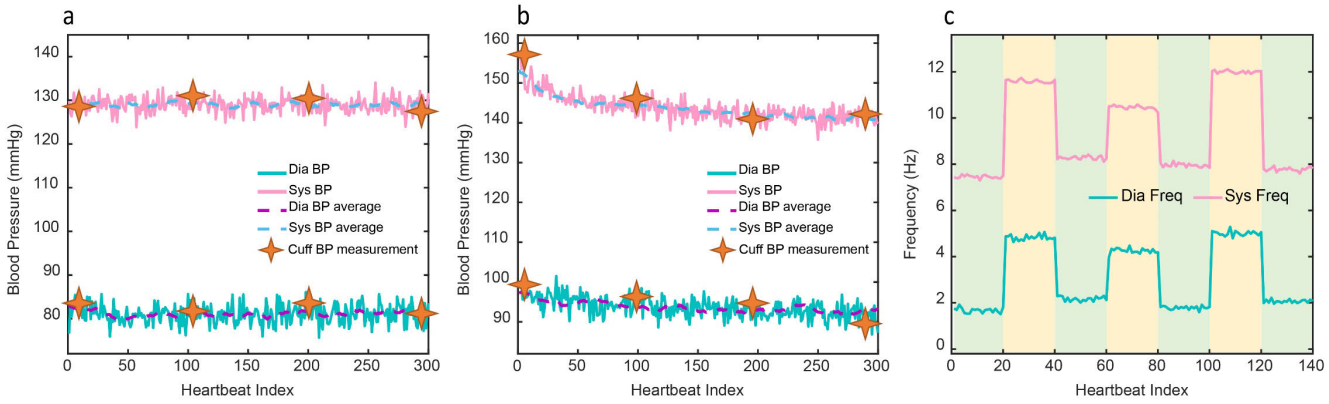

FIGURE 5. The NCS-derived aortic BP and pulmonary cycle dynamics. (a) The systolic (pink) and diastolic BPs (cyan) in the systemic circulation from NCS when the person sat on the chair. The solid line was evaluated from every heartbeat and the dash line from the moving average of 10 heartbeats. Arm-cuff BP are denoted as orange stars. (b) Similar analyses to (a) for the person standing after a mild exercise. (c) The pulmonary SPF (pink) and DPF (cyan). The green shades correspond to holding breath after maximal exhalation and the yellow shades after maximal inhalation.

for the diastolic BP. The frequency resolution can be further improved by adjusting the HHT parameters at the cost of computational time. A measurement from the second person is shown in Supplementary Fig. 5. Due to the chosen HHT calculation, spurious traces of ω_2 with lower frequency were also observed in Figs. 4(c)(d), which can be observed as the faint yellow curves. This ambiguity can be eliminated with the narrower choice of HHT bandwidth or can be simply ignored from its lower magnitude as usually the first IMF $c_1(t)$ is much stronger than the second IMF $c_2(t)$. Notice that the aorta region is the main nonstationary oscillation in C_{11} HHT only for the systole period. During the diastole phase, there can be other vibration in the vicinity of Point 1 such as the right atrium. However, we do not have a direct method to confirm the physiological meaning of diastole C_{11} at the present time. Analogous to the stethoscope recording, the heart sound S2 originated from the aorta region can be listened from Point 1 over the right atrium which does not have significant vibration during the systole phase. The collected heart sound by SL valve closure was mostly in the frequency range of 16 - 120 Hz, which was not included in our HHT.

After calibration, we tested the extracted systemic BP in a longer period. The measurements in Fig. 5(a) were taken when the person sat in a chair. The pink and cyan curves are the systolic and diastolic BP from 300 continuous heartbeats monitored by C_{11} HHT. The dashed curves are the BP moving average with the window of 10 heartbeats. The orange stars are the measurements from the arm-cuff BP monitor. The measurements in Fig. 5(b) were taken after the person did some mild exercises and stood up, where the BP relaxation was traced accurately.

C_{33} at Point 3 in Fig. 1(b) corresponds to the auscultatory position to acquire the pulmonary valve murmurs. Similar to the aortic circulation, the oscillatory characteristics of the pulmonary artery are related to the right ventricular and pulmonary BP [9]. As the pulmonary BP is more affected by the lung volume due to transpulmonary pressure instead of the posture [31]–[33], Fig. 4(e) shows the C_{33} HHT analysis with the synchronized ECG when the person held breath after maximal exhalation. The SPF (orange arrow) and DPF (green arrow) were extracted at 7.752 Hz and 1.875 Hz. We then took the measurement in Fig. 4(f) when the person held breath after maximal inhalation with SPF and DPF now at 11.38 Hz and 4.376 Hz. Both SPF and DPF increased due to the higher transpulmonary pressure. In Figs. 4(e)(f), only one IMF curve was observed. Due to a lack of access to cardiac catheterization, the SPF and DPF frequencies cannot be quantitatively mapped to BP, but are independently useful as they provide a non-invasive method of monitoring pulmonary artery physiology, enabling improved cardiac diagnostics and overall cardiopulmonary health analysis. We analyzed 20 heartbeats for each of the two scenarios and repeated the measurements three times, where the calculated SPF (pink) and DPF (cyan) for the pulmonary cycle are shown in Fig. 5(c). In comparison with the PTT scheme which assumes a fixed ratio between the systolic and diastolic pressures, the calibration method in this work utilizes individual SPF and DPF to interpret the two pressures independently to give a more accurate model.

V. MULTI-STATIC MIMO NCS

The NCS system can observe heartbeat dynamics not only from each sensing antenna pair with collocated Tx and Rx by backscattering, but also from the multi-static MIMO channels. Four cross-point signals are presented in Fig. 6(a). The purple waveform (C_{21}) is the signal transmitted from Tx1 and received by Rx2. The naming order of Tx-Rx ports follows the convention of the multi-port scattering matrix in microwave component testing [34]. The pink (C_{12}), light blue (C_{43}) and green (C_{34}) curves are the signals from Tx2 to Rx1, Tx3 to Rx4 and Tx4 to Rx3, respectively. The ECG waveform (blue) remains as the timing reference. The real-time recording is shown in Supplementary Movie 2 with descriptions in Supplementary Fig. 6. Because the collocated

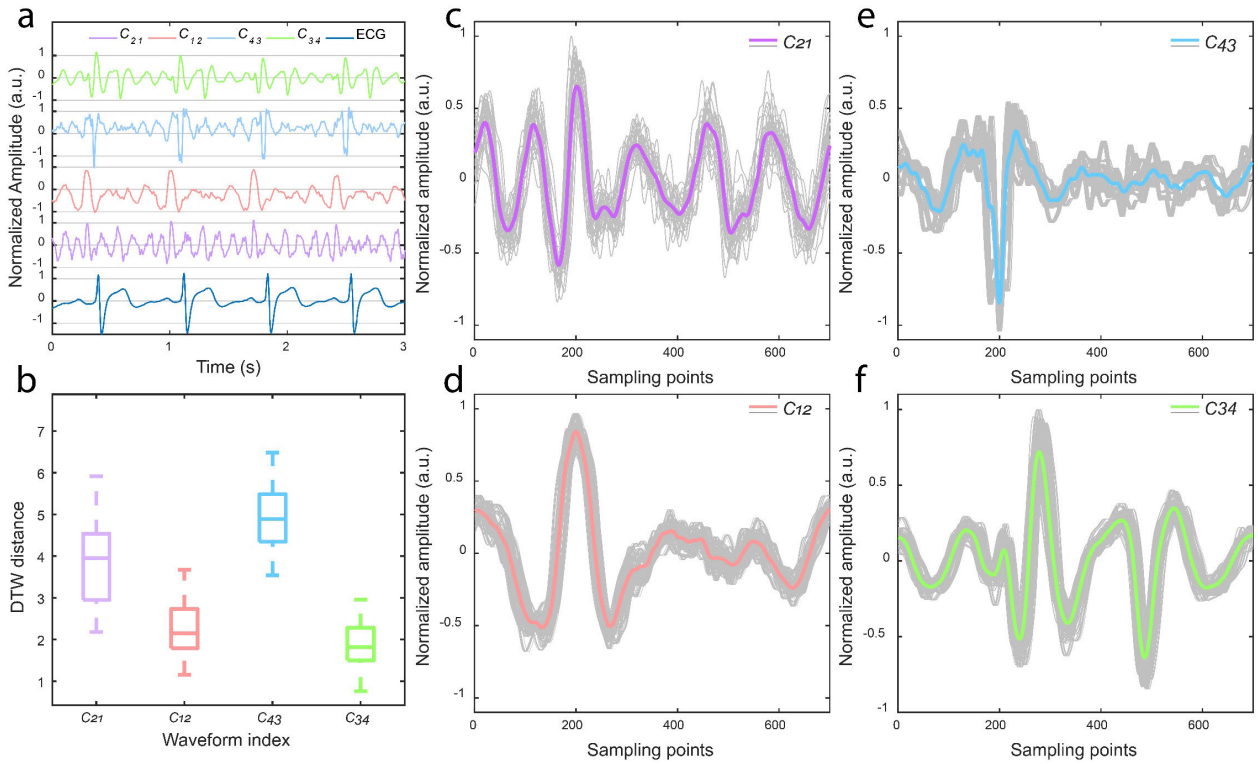

FIGURE 6. The waveform analyses by dynamic time warping (DTW) from NCS cross-point channels. (a) C_{21}, C_{12}, C_{43} and C_{34} (purple, red, light blue and green) are Tx1 to Rx2, Tx2 to Rx1, Tx3 to Rx4, and Tx4 to Rx3. The synchronized ECG (blue) still serves as timing reference. (b) The DTW distances against the corresponding template waveforms. (c) The overlapped C_{21} waveforms from about 300 heartbeat cycles. (d) (e) and (f) are the overlapped C_{12}, C_{43} and C_{34} waveforms, respectively. The purple, red, blue and green curves are the averaged waveforms to serve as the templates.

backscattering channels are more sensitive to the respective local areas, the purpose of the cross-point observation is to expand the sensing path so that extra content of the heartbeat motion can be collected. Notice that this observation mode is not applicable in the passive stethoscope, but is an option for ultrasound imaging. The MIMO observation is also difficult for the conventional RF systems [12], [13], because of the signal reflection on the body surface and low spatial resolution. Each multi-static channel records clear cyclic information. The dynamic-time warping (DTW) [35] algorithm is employed to search for the optimal match among waveforms in each cycle. The Euclidean distance $a_{m,n}$ between a pair of points in the template Γ and the heartbeat h signals is defined as:

$$a_{m,n} = \frac{|\Gamma_m - h_n|}{e + f} \tag{6}$$

where e is the length of the discretized Γ and f is the length of the discretized h. The indices m and n are the time stamps in the waveforms of Γ and h. The distance σ in the warp path P can be calculated as:

$$\sigma(P) = \sum_{k,l} \sigma(p_k, p_l) \tag{7}$$

For a legitimate warp path P, the monotonically increasing k must match with one or more monotonically increasing l, and vice versa. The first and last indices of k must match with the first and last indices of l, respectively. The minimal $\sigma(P)$ from all legitimate paths of P is then defined as the DTW distance, which measures the similarity between the two waveforms. It is noteworthy that the DTW calculation can be performed efficiently by dynamic programming [36], and is often implemented as an on-line method.

With the warping adjustment that gives the minimal $\sigma(P)$, we overlaid the signals of each heartbeat and calculate the averaged waveform as the template of the specific channel. A box-whisker plot displaying the DTW distances of the cross-point waveforms to the corresponding template is shown in Fig. 6(b), and the overlaid waveforms from the 4 channels are shown in Figs. 6(c) to (f). During data collection, the person under test remained as still as possible and controlled their breathing. DTW analysis was performed on recordings during maximum inhalation breath hold. The algorithm first extracted beat segments by identifying peaks and peak-to-peak intervals. Then the averaged peak-to-peak interval was set as the segment length which is around 703 sampling points under the sampling rate of 1 kSps. We see from the DTW analyses that the recorded waveforms are repeatable on the waveform details after periodicity adjustment, and DTW distances stay relatively low for these cross-point signals. The multi-static waveform results from

modulation of the dielectric boundary motion along the cross-point path, which has a nonlinear coupling with stronger weighting towards Tx according to the near-field approximation [37]. C_{21} and C_{12} monitor the heart region in a longer path and are further away from the strong left ventricle and aortic valve than C_{43} and C_{34}. Hence, C_{21} and C_{12} have their largest component during the atrial systole phase around the P-R interval, while C_{43} and C_{34} have larger signals during the isovolumetric contraction around the R-S interval. Cross-point waveforms can be further used to extract the timing and magnitude of detailed heart dynamics by least-square fitting in the future. Similar analyses are conducted with another individual, and the result is shown in Supplementary Fig. 7.

VI. DISCUSSION

The described multi-point NCS system provides a convenient method of acquiring rich cardiac dynamics, including estimation of the central BP. In comparison with the PTT method, which derives both systolic and diastolic BP from one variable, the NCS method can provide SPF and DPF to derive the systolic and diastolic BP independently. Unlike a traditional arm-cuff monitor, the multi-point NCS method enables SPF and DPF to be calculated on each heartbeat. This allows for beat-to-beat BP changes to be estimated; a metric that is unattainable with an arm-cuff. Other approaches analyze the shape of the time-domain waveforms by optical or ultrasound methods to indirectly interpret BP [38], [39], but are often inconsistent due to operation variations. Another advantage of the NCS system is the continuous trace of pressure dynamics instead of just two BP points. Although our present estimation of systemic BP is only derived from C_{11} HHT during the systole phase, multiple channels can provide more reliable parameter extraction for continuous dynamics as well as more features of the heartbeat in the future. As the S1 and S2 heart sounds can be recovered from NCS [23] to provide timing reference, the synchronized ECG is not essential. However, similar to other indirect BP methods, NCS presently needs personal calibration. BP variation between adjacent heartbeats may result from measurement inaccuracy or may have physiological origins similar to heart rate variation. This will need to be investigated in the future. The sensing antennas also need to be carefully deployed at the corresponding positions. The signal should be recorded according to the given instructions in this paper in order to achieve the high-quality data needed for further HHT and DTW analyses.

Prior to this work, critical pulmonary circulation dynamics have few viable measurement methods. The gold standard is cardiac catheterization [40], [41], which requires significant setup and highly trained professionals as well as posing considerable risks. Another method is Doppler echocardiography to derive the pulmonary blood pressure through the velocity of the blood flow [4], [42], similar to our derivation. However, the ultrasound system size is significant, and the broad-spectrum acoustic impedance matching often demands gel application, disabling wearable fitting or long-term usage. The lower sampling rate in Doppler imaging can also reduce its accuracy. On the other hand, NCS can work over clothing and take advantage of the low cost and compact size in modern RF devices such as the smart phone. For various application scenarios, the NCS system can be adapted to the RFID system [4], wearable devices [4], [43], and dedicated in-clinic wired setup [17], [22], [44]. The standard digital filters in the above analyses can be easily realized on various platforms without heavy computational loads. Because HHT is an adaptive algorithm, the computation time depends on the signal complexity and required resolution. Recent heterogeneous computing design [45], [46] can potentially offer online responses.

The multi-point NCS system is the first RF technology achieving rich cardiovascular features and profusion of observation channels. Conventional RF-based heartbeat sensing systems [12], [13] are limited by low SNR, so that the detailed heartbeat dynamics cannot be distinguished. Spatial resolution is also severely limited due to the broad beam coverage. Our demonstrated system has significant mechanical-RF coupling to improve SNR, and the locality nature of NCS enhances the spatial resolution, which provides the signal from different parts of the heart. The information from the MIMO NCS system provides broader application possibilities, including physiological and pathological diagnostic, biometrics recognition, and remote health care. However, the present hardware system and understanding of the signal characteristics are still in the early phase. More efforts on variation studies, signal processing and calibration methods are still needed.

VII. CONCLUSION

In this paper we present a multi-point NCS system to investigate the detailed BP transient and heartbeat motion. Based on the different observation channels, the systolic and diastolic BP in the systemic and pulmonary circulation can be evaluated from HHT analyses. Personal parameter extraction is still needed, but continuous values of independent systolic and diastolic pressures for each heartbeat can be evaluated after calibration. The full MIMO observation from backscattering and cross-channels gives rich information on the various parts of heartbeats. Our proposed approach provides a new diagnostic tool for not only cardiology research but also at-home long-term monitoring.

REFERENCES

[1] A. Avolio, "Central aortic blood pressure and cardiovascular risk: A paradigm shift?" *Hypertension*, vol. 51, no. 6, pp. 1470–1471, Jun. 2008.

[2] B. Williams, "Differential impact of blood pressure-lowering drugs on central aortic pressure and clinical outcomes: Principal results of the conduit artery function evaluation (CAFE) study," *Circulation*, vol. 113, no. 9, pp. 1213–1225, Mar. 2006.

[3] R. Mukkamala, J.-O. Hahn, O. T. Inan, L. K. Mestha, C.-S. Kim, H. Toreyin, and S. Kyal, "Toward ubiquitous blood pressure monitoring via pulse transit time: Theory and practice," *IEEE Trans. Biomed. Eng.*, vol. 62, no. 8, pp. 1879–1901, Aug. 2015.

[4] X. Hui and E. C. Kan, "Monitoring vital signs over multiplexed radio by near-field coherent sensing," *Nature Electron.*, vol. 1, no. 1, pp. 74–78, Jan. 2018.

[5] J. Allen, "Photoplethysmography and its application in clinical physiological measurement," *Physiological Meas.*, vol. 28, no. 3, pp. R1–R39, Mar. 2007.
[6] C. Holz and E. J. Wang, "Glabella: Continuously sensing blood pressure behavior using an unobtrusive wearable device," *Proc. ACM Interact., Mobile, Wearable Ubiquitous Technol.*, vol. 1, no. 3, pp. 1–23, Sep. 2017.
[7] P.-K. Chan, C.-C. Chen, and C.-L. Yang, "Systolic and diastolic blood pressure estimation from pulse transit time using dual split-ring resonators with notch structure," in *IEEE MTT-S Int. Microw. Symp. Dig.*, Boston, MA, USA, Jun. 2019, pp. 361–364.
[8] P. Libby, *Braunwald's Heart Disease: A Textbook of Cardiovascular Medicine*. Amsterdam, The Netherlands: Elsevier, 2007.
[9] P. G. Yock and R. L. Popp, "Noninvasive estimation of right ventricular systolic pressure by Doppler ultrasound in patients with tricuspid regurgitation.," *Circulation*, vol. 70, no. 4, pp. 657–662, Oct. 1984.
[10] J. C. Lin, "Noninvasive microwave measurement of respiration," *Proc. IEEE*, vol. 63, no. 10, p. 1530, Oct. 1975.
[11] J. C. Lin, "Diagnostic applications of electromagnetic fields," in *Review of Radio Science*, W. R. Stone, Ed. Oxford, U.K.: Oxford Univ. Press, 1993, pp. 771–778.
[12] C. Li, V. M. Lubecke, O. Boric-Lubecke, and J. Lin, "A review on recent advances in Doppler radar sensors for noncontact healthcare monitoring," *IEEE Trans. Microw. Theory Techn.*, vol. 61, no. 5, pp. 2046–2060, May 2013.
[13] C. Li, Z. Peng, T.-Y. Huang, T. Fan, F.-K. Wang, T.-S. Horng, J.-M. Munoz-Ferreras, R. Gomez-Garcia, L. Ran, and J. Lin, "A review on recent progress of portable short-range noncontact microwave radar systems," *IEEE Trans. Microw. Theory Techn.*, vol. 65, no. 5, pp. 1692–1706, May 2017.
[14] J. Naqui and F. Martin, "Microwave sensors based on symmetry properties of resonator-loaded transmission lines," *J. Sensors*, vol. 2015, Feb. 2015, Art. no. 741853 , doi: 10.1155/2015/741853.
[15] A. Ebrahimi, J. Scott, and K. Ghorbani, "Differential sensors using microstrip lines loaded with two split-ring resonators," *IEEE Sensors J.*, vol. 18, no. 14, pp. 5786–5793, Jul. 2018.
[16] C. J. Wiggers, *Modern Aspects of the Circulation in Health and Disease*. Philadelphia, PA, USA: Lea & Febiger, 1923.
[17] X. Hui and E. C. Kan, "No-touch measurements of vital signs in small conscious animals," *Sci. Adv.*, vol. 5, no. 2, Feb. 2019, Art. no. eaau0169.
[18] National Research Council, "Animal and human studies addressing health effects," in *An Assessment of Potential Health Effects From Exposure to PAVE PAWS Low-Level Phased-Array Radiofrequency Energy*. Washington, DC, USA: The National Academies Press, 2005, ch. 7.
[19] D. J. Yeager, A. P. Sample, and J. R. Smith, *RFID Handbook: Applications, Technology, Security, and Privacy*, S. I. Ahson and M. Ilyas, Eds. Boca Raton, FL, USA: CRC Press, 2008, pp. 261–278.
[20] X. Hui, Y. Ma, and E. C. Kan, "Code division multiple access in centimeter accuracy harmonic RFID locating system," *IEEE J. Radio Freq. Identificat.*, vol. 1, no. 1, pp. 51–58, Mar. 2017.
[21] X. Hui and E. C. Kan, "Radio ranging with ultrahigh resolution using a harmonic radio-frequency identification system," *Nature Electron.*, vol. 2, no. 3, pp. 125–131, Mar. 2019.
[22] X. Hui and E. C. Kan, "Seat integration of RF vital-sign monitoring," in *IEEE MTT-S Int. Microw. Symp. Dig.*, May 2019, pp. 1–3.
[23] X. Hui, P. Sharma, and E. C. Kan, "Microwave stethoscope for heart sound by near-field coherent sensing," in *IEEE MTT-S Int. Microw. Symp. Dig.*, Boston, MA, USA, Jun. 2019, pp. 365–368.
[24] C. K. Batchelor and G. K. Batchelor, *An Introduction to Fluid Dynamics*. Cambridge, U.K.: Cambridge Univ. Press, 2000.
[25] D. L. Donoho and P. B. Stark, "Uncertainty principles and signal recovery," *SIAM J. Appl. Math.*, vol. 49, no. 3, pp. 906–931, Jun. 1989.
[26] G. B. Folland and A. Sitaram, "The uncertainty principle: A mathematical survey," *J. Fourier Anal. Appl.*, vol. 3, no. 3, pp. 207–238, May 1997.
[27] L. Cohen, "Uncertainty principles of the short-time Fourier transform," *Proc. SPIE*, vol. 2563, pp. 80–90, Jun. 1995.
[28] L. Cohen, *Wavelet Transforms & Time-Frequency Signal Analysis*, L. Debnath, Ed. New York, NY, USA: Springer, 2001, pp. 217–231.
[29] N. E. Huang, *Hilbert-Huang Transform and Its Applications*. Singapore: World Scientific, 2014.
[30] N. E. Huang, M.-L.-C. Wu, S. R. Long, S. S. P. Shen, W. Qu, P. Gloersen, and K. L. Fan, "A confidence limit for the empirical mode decomposition and Hilbert spectral analysis," *Proc. Roy. Soc. London. A, Math., Phys. Eng. Sci.*, vol. 459, no. 2037, pp. 2317–2345, Sep. 2003.
[31] M. R. Grübler, O. Wigger, D. Berger, and S. Blöchlinger, "Basic concepts of heart-lung interactions during mechanical ventilation," *Swiss Med. Weekly*, vol. 147, Sep. 2017, Art. no. w14491.
[32] G. Kovacs, A. Avian, M. Pienn, R. Naeije, and H. Olschewski, "Reading pulmonary vascular pressure tracings how to handle the problems of zero leveling and respiratory swings," *Amer. J. Respiratory Crit. Care Med.*, May 2014, Art. no. 140528122914004.
[33] F. Michard, S. Boussat, D. Chemla, N. Anguel, A. Mercat, Y. Lecarpentier, C. Richard, M. R. Pinsky, and J.-L. Teboul, "Relation between respiratory changes in arterial pulse pressure and fluid responsiveness in septic patients with acute circulatory failure," *Amer. J. Respiratory Crit. Care Med.*, vol. 162, no. 1, pp. 134–138, 2014.
[34] L. Tsang, J. A. Kong, and K. H. Ding, *Scattering of Electromagnetic Waves: Theories and Applications*. Hoboken, NJ, USA: Wiley, 2004.
[35] H. Sakoe and S. Chiba, "Dynamic programming algorithm optimization for spoken word recognition," *IEEE Trans. Acoust. Speech Signal Process*, vol. 26, no. 1, pp. 43–49, Feb. 1978.
[36] Y. Cao, N. Rakhilin, P. H. Gordon, X. Shen, and E. C. Kan, "A real-time spike classification method based on dynamic time warping for extracellular enteric neural recording with large waveform variability," *J. Neurosci. Methods*, vol. 261, pp. 97–109, Dec. 2015, doi: 10.1016/j.jneumeth.2015.12.006.
[37] C. A. Balanis, *Antenna Theory: Analysis and Design*. Hoboken, NJ, USA: Wiley, 2016.
[38] X. Xing and M. Sun, "Optical blood pressure estimation with photoplethysmography and FFT-based neural networks," *Biomed. Opt. Express*, vol. 7, no. 8, pp. 3007–3020, Aug. 2016.
[39] C. Wang *et al.*, "Monitoring of the central blood pressure waveform via a conformal ultrasonic device," *Nature Biomed. Eng.*, vol. 2, no. 9, pp. 687–695, Sep. 2018.
[40] W. Grossman, *Grossman's Cardiac Catheterization, Angiography, and Intervention*. Baltimore, MD, USA: Williams & Wilkins, 2006.
[41] W. Huang, Z. Shen, N. E. Huang, and Y. C. Fung, "Nonlinear indicial response of complex nonstationary oscillations as pulmonary hypertension responding to step hypoxia," *Proc. Nat. Acad. Sci. USA*, vol. 96, no. 5, pp. 1834–1839, Mar. 1999.
[42] L. G. Rudski, W. W. Lai, J. Afilalo, L. Hua, M. D. Handschumacher, K. Chandrasekaran, S. D. Solomon, E. K. Louie, and N. B. Schiller, "Guidelines for the echocardiographic assessment of the right heart in adults: A report from the American society of echocardiography endorsed by the European association of echocardiography, a registered branch of the European society of cardiology, and the Canadian society of echocardiography," *J. Amer. Soc. Echocardiography*, vol. 23, no. 7, pp. 685–713, Jul. 2010.
[43] X. Hui and E. C. Kan, "Mitigation of body movement interference in near-field coherent sensing for heartrate monitoring," in *Proc. IEEE 15th Int. Conf. Wearable Implant. Body Sensor Netw. (BSN)*, Mar. 2018, pp. 156–159.
[44] X. Hui and E. C. Kan, "Accurate extraction of heartbeat intervals with near-field coherent sensing," in *Proc. IEEE Int. Conf. Commun. (ICC)*, May 2018, pp. 1–6.
[45] D. Chen, D. Li, M. Xiong, H. Bao, and X. Li, "GPGPU-aided ensemble empirical-mode decomposition for EEG analysis during anesthesia," *IEEE Trans. Inf. Technol. Biomed.*, vol. 14, no. 6, pp. 1417–1427, Nov. 2010.
[46] N.-F. Chang, T.-C. Chen, C.-Y. Chiang, and L.-G. Chen, "On-line empirical mode decomposition biomedical microprocessor for Hilbert Huang transform," in *Proc. IEEE Biomed. Circuits Syst. Conf. (BioCAS)*, Nov. 2011, pp. 420–423.

XIAONAN HUI (Student Member, IEEE) received the B.S. degree from Northeastern University, China, in 2012, and the M.S. degree from Zhejiang University, China, in 2015, all in electrical engineering. He is currently pursuing the Ph.D. degree in electrical and computer engineering with Cornell University, Ithaca, NY, USA.

THOMAS B. CONROY received the B.S. degree in electrical engineering from Clarkson University, Potsdam, NY, USA, in 2019. He is currently pursuing the Ph.D. degree in electrical and computer engineering with Cornell University, Ithaca, NY, USA.

EDWIN C. KAN (Senior Member, IEEE) received the B.S. degree from National Taiwan University, in 1984, and the M.S. and Ph.D. degrees from the University of Illinois at Urbana–Champaign, in 1988 and 1992, respectively, all in electrical engineering. He was a Second Lieutenant with the Air Force, Taiwan, from 1984 to 1986. In January 1992, he joined Dawn Technologies as a Principal CAD Engineer. He was a Research Associate with Stanford University, from 1994 to 1997. In 1997, he joined the School of Electrical and Computer Engineering, Cornell University, Ithaca, NY, USA, as an Assistant Professor, where he is currently a Professor.

Supplementary Materials

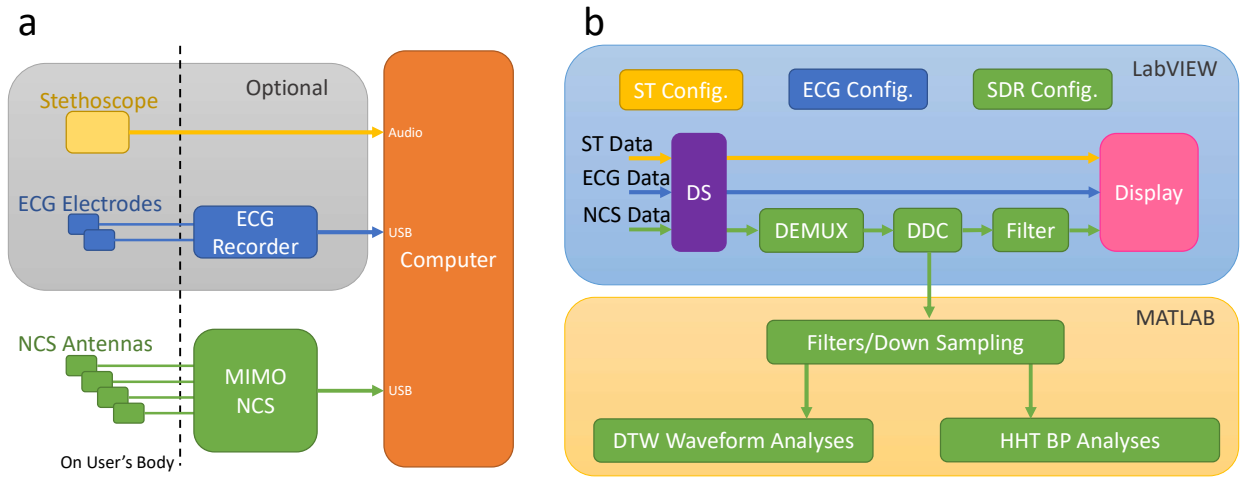

Supplementary Fig. 1. The system schematic of synchronized NCS, ECG and stethoscope. (a) Electronic hardware. (b) Software function blocks and data flow.

Supplementary Fig. 1 (a) shows the electronic hardware schematic. The NCS antennas are attached on the user's clothing, and the ECG electrodes and the digital stethoscope (ST) are pasted on the user's bare skin. The stethoscope is connected to the audio card of the computer. The ECG electrodes are connected to the ECG recorder, and the digitized signal is transferred to the computer through a USB cable. Four NCS antenna pairs are connected to the two SDRs of MIMO NCS as shown in Fig. 1 (a). The SDRs are synchronized and the digitized signal is transferred to the computer also through USB. The stethoscope and ECG subsystems are optional, which are just for the waveform comparison. Supplementary Fig. 1 (b) shows the software function blocks and data flow. Data from the stethoscope data, ECG and NCS are first processed in LabVIEW at the data synchronizer (DS) shown as the purple block. Then the ST and ECG data are fed to the display function directly. The NCS data are piped through the demultiplexer (DEMUX) to sort out the NCS channels (16 channels in the full 4×4 MIMO mode). Each channel signal will go through the digital down-converter (DDC) to formulate the raw NCS signal. After proper filtering, the NCS signals with different emphases are shown on the display. The raw NCS data are also branched from DDC to the MATLAB algorithms where DTW waveform analyses and HHT are performed. The LabVIEW software also provides the configuration functions for stethoscope, ECG and SDR to control the unit operations.

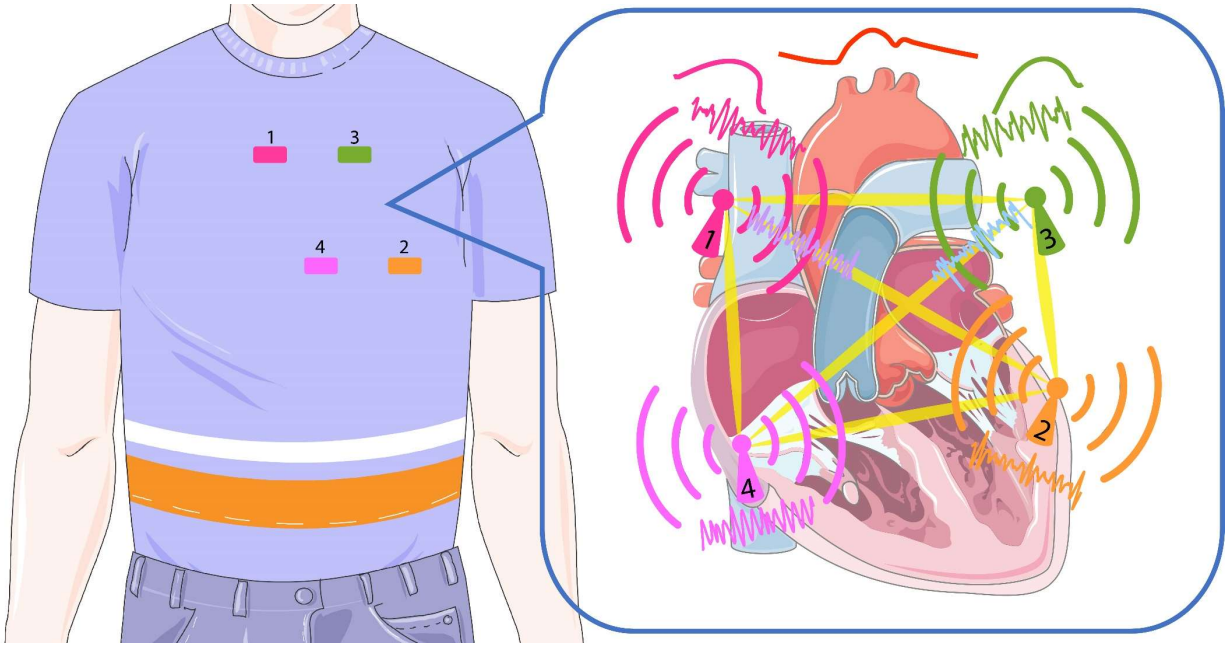

Supplementary Fig. 2. Monitoring complex heartbeat dynamics by the multi-point NCS system. The wave propagation symbol depicts the backscattering channels for local observation, while the yellow path indicates cross-point channels. The representative heartbeat cyclic waveform is shown accordingly for each channel. Transient pressure traces in the systole phase by Hilbert-Huang analyses at Points 1 and 3 are also shown.

Four radio-frequency (RF) antennas represented by the red, yellow, green and pink blocks at the sensing points 1 to 4 are placed over the shirt around the heart area in Supplementary Fig. 2. Based on the principle of near-field coherent sensing (NCS) from multiple-input-multiple-output (MIMO) observation, rich content of pressure dynamics and heartbeat motion can be retrieved. The individual sensing antenna explores the heartbeat in its vicinity, indicated by the wavefront and waveform in the same color of the antenna. The cross-point multi-static channels are shown as the light-yellow paths. The backscattering signals from antennas 1 and 3 can be utilized to evaluate the systolic and diastolic blood pressures in both aortic and pulmonary circulations.

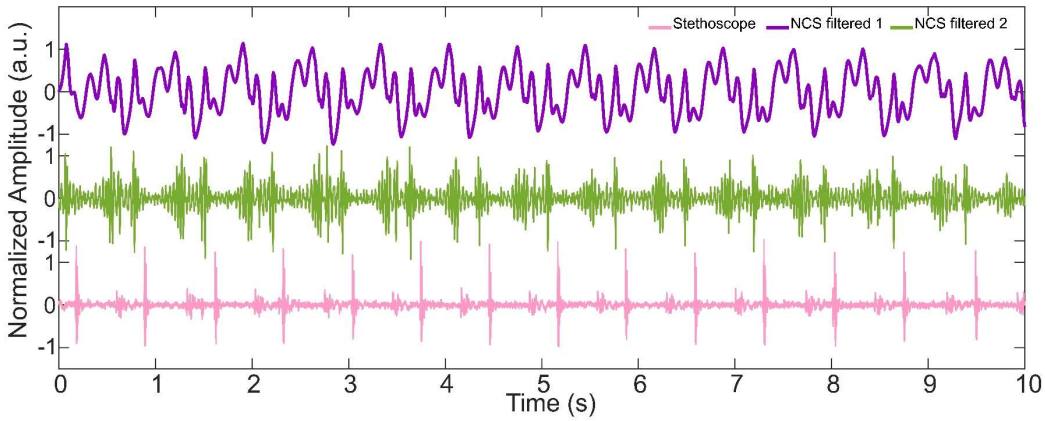

Supplementary Fig. 3. The audible-frequency components filtered from the NCS signal in comparison with the synchronized stethoscope signal.

The NCS signal from Point 0 in Fig. 1 (b) is shown in the purple waveform after a high-pass filter with the cutoff frequency of 1.2 Hz, and in the green waveform after a band-pass filter of 20 – 120 Hz. The pink waveform is the synchronized stethoscope recording. The NCS and stethoscope audio playback can be found in Supplementary Movie 1.

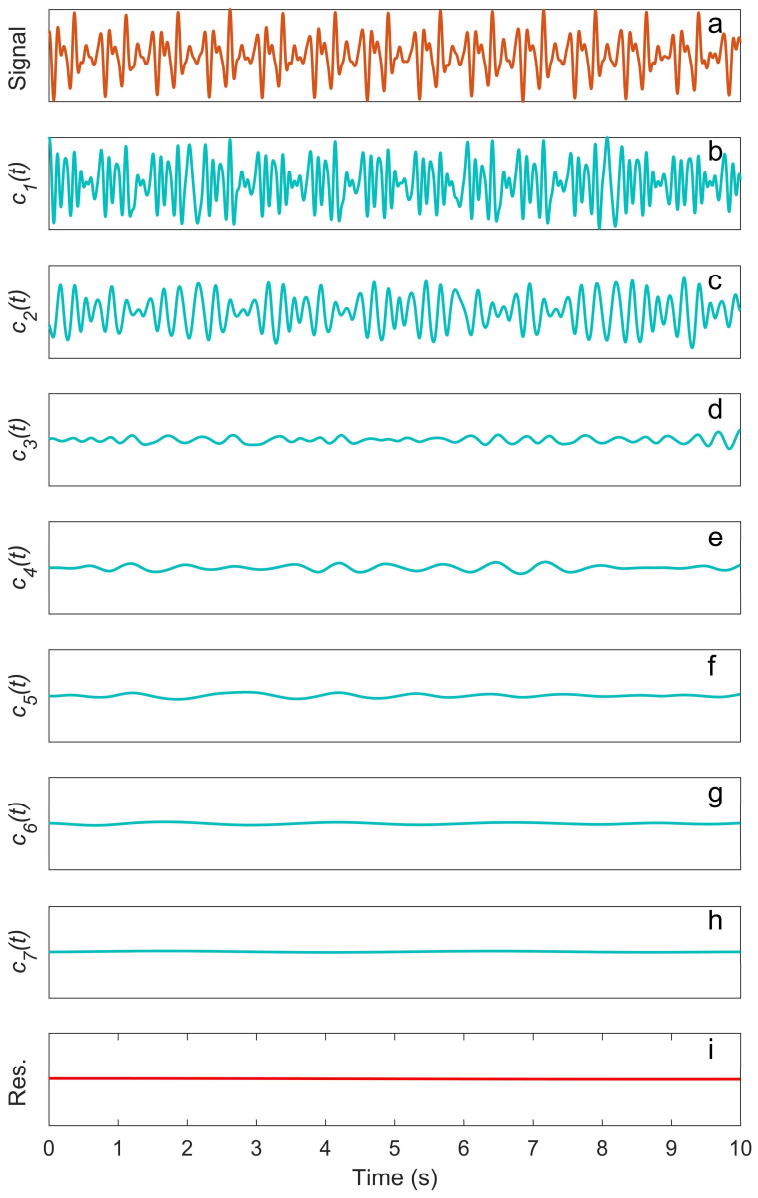

Supplementary Fig. 4. Intrinsic mode functions (IMF) $c_j(t)$ obtained after processing C_{11} by EMD. (a) is the filtered C_{11} NCS signal, (b) to (h) are the $c_1(t)$ to $c_7(t)$, and (i) is the residue function after the decomposition.

The IMFs of the C_{11} NCS signal are shown in Supplementary Fig. 4. The amplitude of each waveform is normalized to the maximum of the waveform in (a). As seen from the decomposition, the signal features are mainly represented by $c_1(t)$ and $c_2(t)$, so only the first two IMFs are further processed by the following analysis.

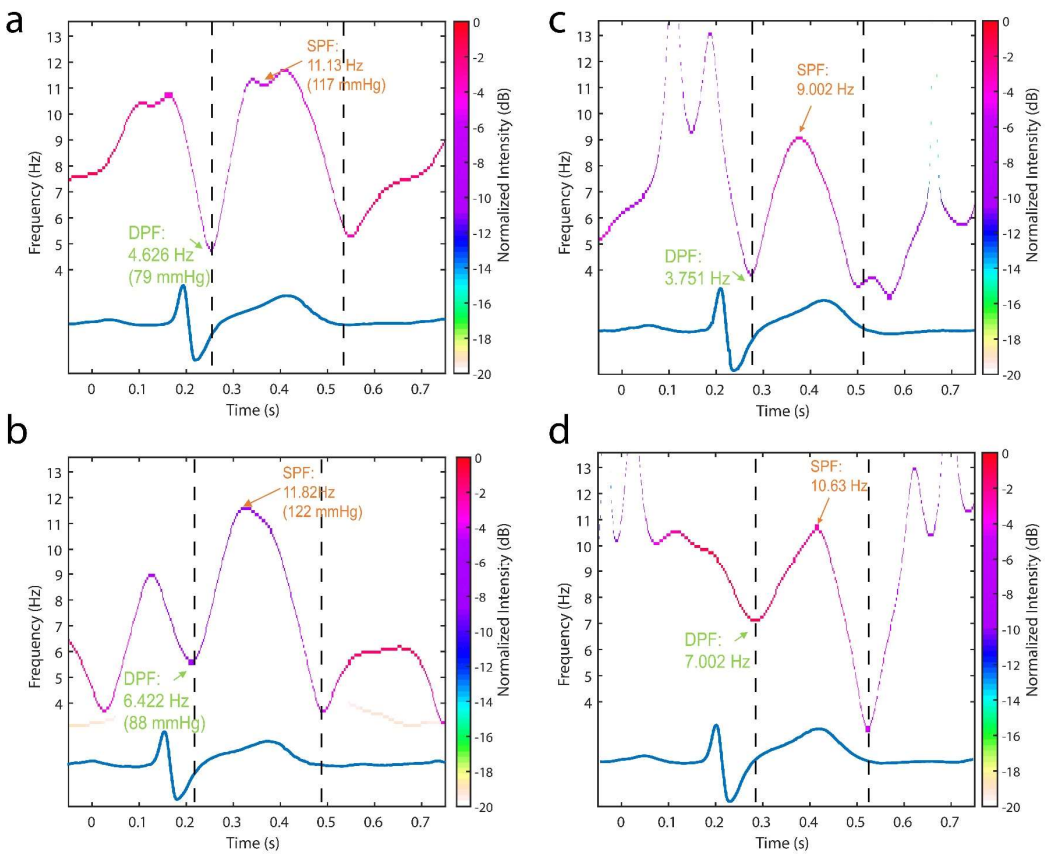

Supplementary Fig. 5. The HHT frequency-time BP analyses of the second person corresponding to Fig. 4. (a) C_{11} HHT when the person sat in the chair. The synchronized ECG signal (blue) indicates the timing and the ventricular ejection period is between the dash lines. (b) C_{11} HHT when the person took a standing posture. (c) C_{33} HHT when the person held breath after maximum exhalation, and (d) after maximum inhalation.

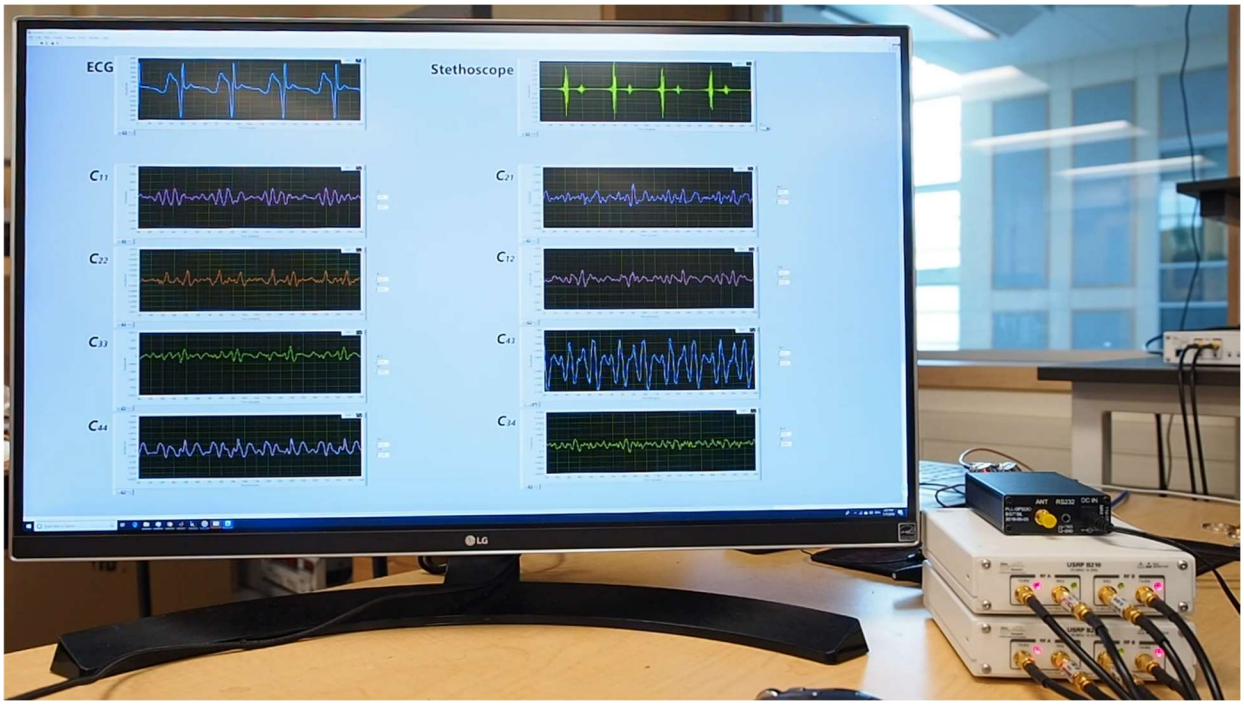

Supplementary Fig. 6. A sample display with eight coherent channels in MIMO NCS, as well as the synchronized ECG and stethoscope waveforms.

The waveforms of each channel are labeled on the screen as ECG, stethoscope, NCS backscattering channels of C_{11} to C_{44}, and cross-point channels of C_{21}, C_{12}, C_{43} and C_{34}. A real-time recording video is shown in Supplementary Movie 2.

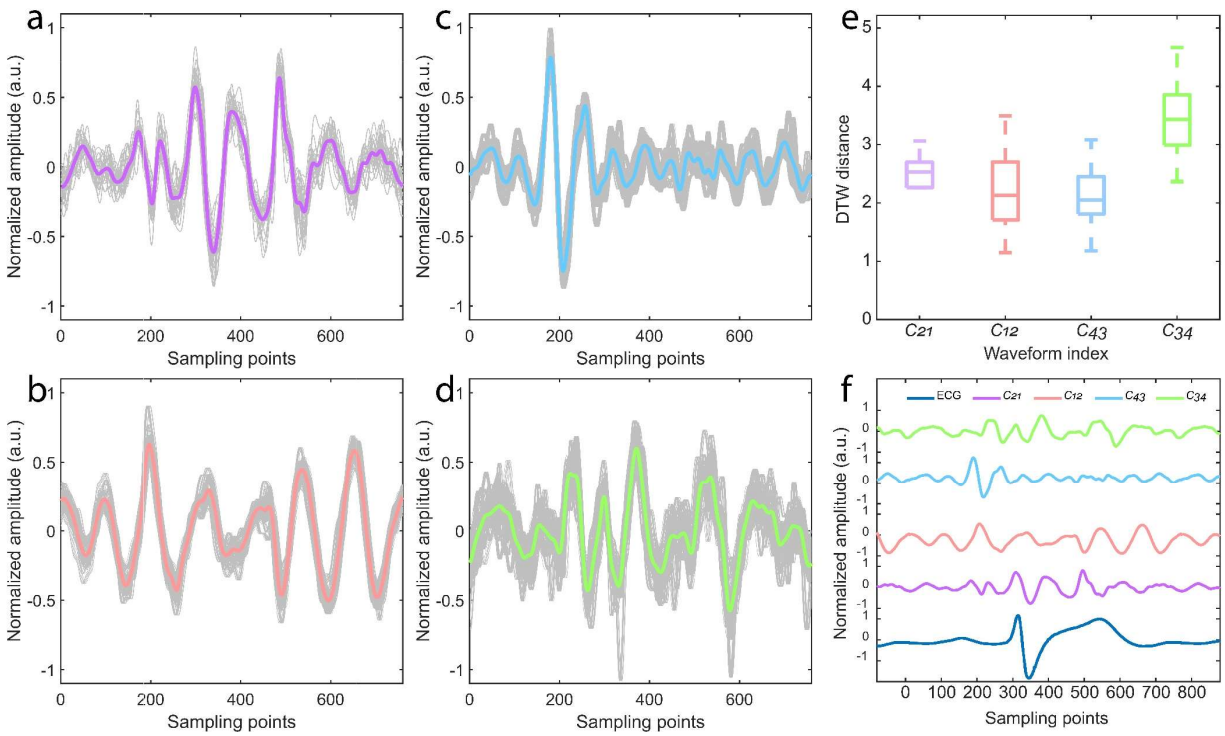

Supplementary Fig. 7. The DTW waveform analyses of 200 heartbeats observed from the same NCS cross-point setup on a second person: (a) C_{21}; (b) C_{12}; (c) C_{43}; (d) C_{34}. The purple, red, blue and green curves are the averaged waveforms to serve as the template. (e) The DTW distances against the corresponding template waveforms. (f) The C_{21} to C_{34} waveform templates in comparison with ECG.

In Supplementary Fig. 7, a second user was tested under the same NCS cross-point setup described in Fig. 6. The averaged segment length is 760 sampling points under the same sampling rate of 1 kSps. The timing features with significant signal strength in the templates are similar between the two users. Variation of waveforms in Fig. 6 and Supplementary Fig. 7 could be caused by the placement of the sensing antenna and the physiological differences between individuals. This requires further investigation in the future.

Captions of the Supplementary Movies:

Supplementary Movie 1: The audio sound playback from the stethoscope and NCS signals.

Supplementary Movie 2: Sample real-time recordings shown on a display.

Appendix B

(PDF downloaded from IEEE) P. Sharma, X. Hui and E. C. Kan, “An RF sensor for monitoring respiratory patterns”, *41st Annual Intl. Conf. IEEE Engineering in Medicine and Biology Society (EMBC'19)*, Berlin Germany, July 23 – 27, 2019.

. Limited circulation. For review only.

A Wearable RF Sensor for Monitoring Respiratory Patterns*

Pragya Sharma, Xiaonan Hui, Edwin C. Kan, *Member, IEEE*

***Abstract*—We present a non-invasive approach for continuous monitoring of respiration dynamics using a wearable radio-frequency (RF) sensor based on near-field coherent sensing. A continuous-wave RF signal at 1.8 GHz is generated by a software-defined radio, with both transmitter (Tx) and receiver (Rx) antennas placed close to the xiphoid process. The experimental prototype of the mobile sensor can modulate the internal organ motion in the near-field region of the Tx antenna and is then received by the nearby Rx antenna to be demodulated and sampled. Through peak detection, we have identified inhalation and exhalation peaks of each breath cycle to estimate the breath rate and the lung volume. The extracted respiratory parameters are compared with the conventional chest belts data for various simulated respiratory conditions including voluntary deep, fast-shallow and slow-shallow breathing. We also characterized simulated central sleep apneas, Cheyne-Stokes, Biot's, ataxic and coughing conditions. To accurately identify obstructive apnea, we presented a two-sensor approach that can capture paradoxical movement of thorax and abdomen. The on-line recognition of these respiratory patterns can be employed not only to continuously monitor patients with chronic respiratory disorders but also to provide real-time feedback for future therapeutic purposes.**

I. Introduction

Non-invasive respiration monitoring has received a lot of interest in recent years [1], which has led to many research works on a robust, accurate, comfortable and affordable sensor that can provide the two key respiratory parameters of breath rates (BR) and lung volume (LV). As respiratory failure is often difficult to predict, such sensor can be even more useful for long-term continuous on-line measurements on patients pre-diagnosed with respiratory disorders, where the risk of mortality can be effectively reduced [2]. With high prevalence of sleep-breathing disorders such as central sleep apnea (CSA) and obstructive sleep apnea (OSA) in patients with symptomatic chronic heart failure (CHF) [3], continuous overnight monitoring becomes mandatory. Acute or chronic opioid use has also been linked to severe respiratory disorders, starting from respiratory pauses, delays in expiration and decreased LV that can lead to eventual respiratory arrest and death [4].

While many mobile respiratory sensors for exercise and wellness monitoring aim to estimate BR only, additional information on LV provides richer information for respiratory health diagnostics. The approach to non-invasive respiratory analysis depends on the physiological parameters to be measured. Airflow sensors that estimate the volume of air expired over time can get accurate information on BR [5], but require mouthpieces or facemasks to collect the air for LV, which can not only be uncomfortable and conspicuous but may also interfere with the normal breathing process. The pulse oximetry can provide information about blood O_2 content, but has a slow response to apnea-like conditions and suffers from motion artifact [6]. Another physiological parameter affected by respiration is the change in thorax and abdomen circumferences, which are related to lung expansion and contraction [7]. Body belts worn at both thorax and abdomen can get accurate respiratory patterns to estimate BR and detect some abnormal breathing conditions, while LV can be derived only after gold-standard spirometer calibration, which requires an exhalation into a mouthpiece for one time before taking continuous measurements on the same person.

Apart from the above clinically accepted technologies, other sensors such as ballistocardiography sensor under mattress can also be used to extract respiratory information [8]. This however vastly limits the application to sleep and is prone to noise due to any other body movement. Often only BR can be estimated with significant signal processing, while no LV dynamics can be available. Another commercially available technology is based on non-contact Doppler radar detection by an external reference reader [9]. While cardiopulmonary signals can be derived [10], movement of the person under test as well as any other motion in the surrounding can affect the collected data. LV can be roughly estimated [11] but may vary drastically as the calibration depends on subject position, relative distance and orientation of person and antenna. Additionally, it is difficult to get information about the obstructed breathing condition, as the remote Doppler sensor only measures the surface motion of either thorax or abdomen, depending on the body location where the radar antenna is directed to.

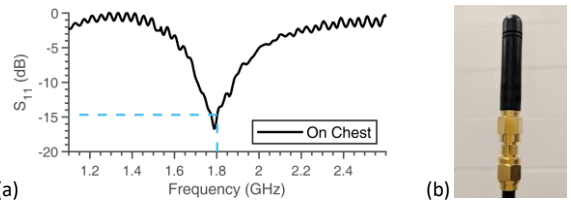

Figure 1. (a) Measured antenna S_{11} characteristics with chest placement showing $S_{11} = -15$ dB at 1.8 GHz. (b) The monopole whip antenna used for the NCS setup.

In this study, we employ a non-invasive method based on radio-frequency (RF) near-field coherent sensing (NCS) [12]

* Research supported by US Army Discovery Award through the CDMRP Program PR182496 and by US Department of Energy ARPA-E Project DE-AR0000946.

P. Sharma, X. Hui and E. C. Kan are with the School of Electrical and Computer Engineering, Cornell University, Ithaca, NY 14853 USA (e-mail: {ps847, xh273, eck5}@cornell.edu).

Manuscript 1864 submitted to 2019 41st Annual International Conference of the IEEE Engineering in Medicine and Biology Society (EMBC). Received February 20, 2019.

to measure the respiratory patterns in terms of both BR and LV, which can be applied to identifying various respiratory dynamics. NCS can record dielectric boundary movement of internal organs and body surfaces in the near-field region of the transmitter (Tx) antenna. Although NCS can be implemented by passive radio-frequency identification (RFID) tags to maximize the wearer comfort and minimize the tag cost [13], the present paper employs another approach with both Tx and receiver (Rx) antennas on the chest as a self-contained active mobile unit without need of an external reference reader, which is then feasible for both indoor and outdoor applications. The NCS measurement is less sensitive to wearer body movement and ambient motion which can be filtered out as the common-mode signal and is thus more feasible for continuous monitoring. Additionally, this setup can be adapted to two independent sensors to differentiate thorax and abdomen breathing patterns to identify OSA by its thoracoabdominal asynchrony. We can also recognize coughing by its dynamic signature in waveform energy, where BR and LV are not representative parameters.

II. Experimental Setup

A. Sensor Configuration

We have implemented the respiratory sensor prototype by commercial off-the-shelf (COTS) components. Ultra-high frequency (UHF) monopole antennas are used at both Tx and Rx. UHF is preferred as the signal power can be significantly coupled into the heart and lungs in the near-field. As the Rx signal consists of both the modulated and unmodulated parts, the relative antenna position and the body placement are optimized to obtain the clearest respiratory signal. With the antenna placed on the chest, the return loss S_{11} is shown in Fig. 1(a), and the antenna photo is shown in Fig. 1(b). The antennas are operated at 1.8 GHz, close to the minimum S_{11} point.

The RF front end is implemented by a National Instrument Ettus B210 software-defined radio (SDR), with LabVIEW for real-time data observation and recording. It is a quadrature implementation as shown in Fig. 2(a), which gives robust readout especially during the time when no breathing motion is present. The carrier frequency is set at 1.8 GHz, with a sinusoidal baseband set at 20 kHz for the sensor placed near thorax. The Tx power is at −15 dBm, which is well below the safety limits for human studies [14]. The use of baseband modulation allows multiple sensors to share the same radio by assigning different baseband tones at the same carrier frequency. SDR B210 supports a 2×2 multiple-input-multiple-output (MIMO) setup to implement two NCS sensors. The channel tone of 70 kHz is used for the other Tx – Rx placement at abdomen, so that abdomen and thorax movements can be individually evaluated in Section IV. The demodulated baseband is sampled at 10^6 samples per second (Sps) by the built-in analog-to-digital converter (ADC).

As our sensing approach modulates the near-field motion onto the RF carrier, the demodulated waveform can be a function of the antenna placement on the chest. A single sensor can be more conveniently deployed, where the Tx – Rx antenna pair is placed below the xiphoid process to effectively capture the respiratory motion by lungs, diaphragm and abdomen together, as shown in Fig. 2(b), with only faint signal from heartbeat. The sensor can work over layers of clothing without skin contact and does not need to be held tightly against the chest, greatly improving user comfort. This setup can correctly capture the BR and LV parameters with high accuracy for most breathing patterns and showed low sensitivity to location of the body placement. Tests with the sensor placed 5 cm above and below the xiphoid process showed that respiration can be clearly captured at all three locations, requiring only different calibration coefficients. We have additionally explored two-sensor placement to measure the abdomen and thorax movement separately, with one sensor placed high at the thorax, and the other at the abdomen. This allows our sensor to accurately monitor the scenario of out-of-phase abdomen and thorax motion in OSA [15] with paradoxical breathing.

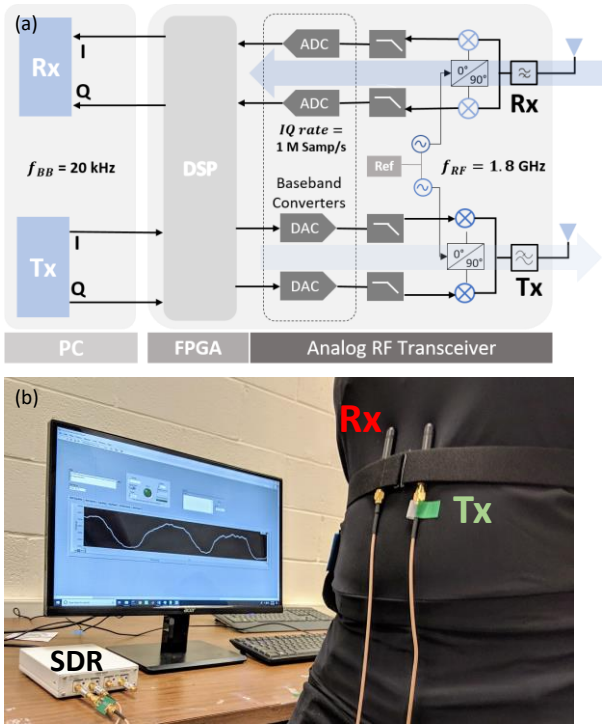

Figure 2. (a) SDR architecture showing one of the two Tx – Rx chains. Two Tx and two Rx share an LO. (b) Placement of Tx and Rx antennas below the xiphoid, together with the chest-belt Hexoskin for comparison. SDR and LabVIEW for signal demodulation and analysis are also illustrated.

B. Comparison with Chest-Belt Measurements

To calibrate our NCS measurements, we have used a Hexoskin smart shirt [16] that monitors respiration by respiratory inductance plethysmography (RIP) belts. Wires incorporated into fabric elastic tension bands are placed around the thorax and abdomen for RIP. During the respiration process, the lungs expand and contract, which is observed as a change in the self-inductance of the coils to derive the respiratory waveform at 128 Hz. BR and LV are then estimated at 1 Hz. The NCS measurements are originally sampled at 500 Hz, and the BR and LV are also calculated at 1 Hz for easy comparison. Fig. 3(a) shows an example of the NCS respiration waveform with the sensor placed below the xiphoid process, and the thorax and abdomen waveforms

Manuscript 1864 submitted to 2019 41st Annual International Conference of the IEEE Engineering in Medicine and Biology Society (EMBC). Received February 20, 2019.

retrieved from Hexoskin (Hx) during normal spontaneous breathing conditions. The corresponding BR from NCS, denoted as BR_{NCS}, and from Hexoskin as BR_{Hx} is shown in Fig. 3(b) in breaths per minute (BPM). LV under this condition is often denoted as tidal volume.

C. Data Collection

We validated the accuracy of NCS respiration waveforms and parameters with different voluntary breathing exercises, first by only one sensor near the xiphoid process. We simulated 1) normal, 2) deep, 3) slow-shallow and 4) fast-shallow breathing conditions. Synchronous Hexoskin respiration data were collected. Additionally, we collected data and performed BR and LV analyses on several simulated abnormal respiratory patterns including, 1) CSA, 2) Cheyne-Stokes, 3) Biot's, and 4) ataxic breathing [17].

We also performed data collection with two NCS sensors, one at abdomen and one at thorax, while performing isovolumetric abdomen movement. Repeated abdomen contraction and relaxation movements were executed with breath holding, i.e., neither inhalation nor exhalation. As the total LV is conserved, this leads to out-of-phase movement of thorax and abdomen, similar to breathing during airway collapse or paradoxical breathing when thorax moves out as abdomen pushes in. Finally, we explored the coughing recognition from extracted NCS waveforms.

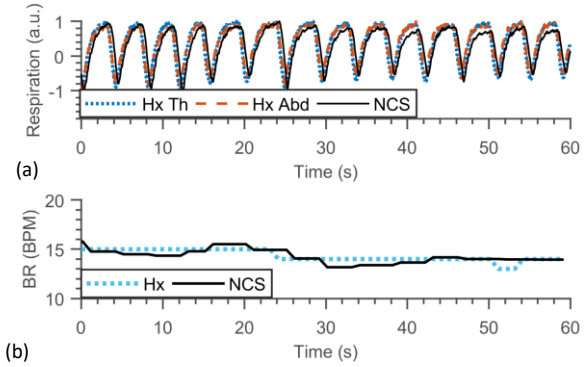

Figure 3. (a) Normalized respiratory waveforms from Hexoskin thorax (Hx Th) and abdomen (Hx Abd) body belts and NCS. (b) Nearly constant breath rates estimated from Hexoskin and NCS in the normal breathing range of 12 – 20 BPM.

III. Signal Analyses

A. The Signal Model

The near-field motion is modulated onto the received data and can be retrieved by signal processing of the demodulated baseband data. The Tx quadrature baseband is presently a simple sinusoidal tone given by

$$I_{Tx}(t) = A\cos(2\pi f_{BB}t)$$
$$Q_{Tx}(t) = A\sin(2\pi f_{BB}t). \quad (1)$$

Here f_{BB} is the baseband frequency and A is the amplitude. Multiplexing is possible by setting different baseband frequencies or code divisions for different channels. B210 supports two different channels that can be operated simultaneously. This digital baseband passes through the digital-to-analog converter (DAC) and is then mixed with the carrier frequency, f_{RF}. The Tx signal is modulated by the physical motion in the near-field region of the Tx antenna and the Rx signal is demodulated and sampled by the ADC to get the baseband quadrature, which needs to be bandpass-filtered around the channel tone f_{BB} to obtain data from different channels

$$I_{Rx}(t) = A(t)\cos(2\pi f_{BB}t + \theta(t))$$
$$Q_{Rx}(t) = A(t)\sin(2\pi f_{BB}t + \theta(t)). \quad (2)$$

From the quadrature baseband, the NCS signal is the modulated amplitude

$$NCS(t) = \sqrt{I_{Rx}(t)^2 + Q_{Rx}(t)^2}. \quad (3)$$

This is a strong function of the antenna characteristics caused by the near-field coupling to the internal organs. Respiration pattern can be readily extracted from this signal by a simple bandpass filtering to remove the DC level and any high frequency noise. The quadrature scheme will render more recognizable $I_{Rx}(t)$ and $Q_{Rx}(t)$ even when $NCS(t)$ is stationary when no breathing motion is present.

B. The Peak Detection Algorithm

Peak detection is performed to find maxima and minima in the respiration waveform to register the accurate end points of expiration and inspiration. The detected peak locations are used to estimate BR and LV. A modified version of automated multiscale-based peak detection (AMPD) [18] algorithm is used, due to its effectiveness against noisy quasi-periodic waveforms and its simplicity in terms of no free parameter selection. The limitations of AMPD include: 1) long processing time and large memory requirement for a long signal segment, and 2) highest frequency (f_{max}) should not be larger than 4 times the lowest frequency (f_{min}) in one signal segment. As we have large frequency ranges of 0.03 – 1 Hz in respiration waveforms, where sudden frequency jump is not expected over a small segment, signals were divided into windows with 50% overlap. The overlap length ($l_{overlap}$) was selected to include one cycle at a very low frequency, which is taken as 6 BPM for the breath. For this small window, it will satisfy the frequency range limit of [f_{min}, $4f_{min}$], while allowing the signal to have broad frequency range over long time duration. The processing speed, computation and memory requirements of algorithm are also improved at the same time.

C. Respiratory Parameters

The time between two successive peaks is taken as the cyclic interval of breath. BR is calculated by finding interval of complete breath cycles in the last 8 s, which gives good estimate of respiratory rhythms by capturing short-lasting changes in breathing conditions, such as pauses greater than 10 s in apnea conditions. Additionally, LV is an important parameter to be accurately measured, as it provides information on how much volume of air is transported into or out of the lungs in each respiratory cycle. Both parameters can provide better assessment of the pulmonary health condition.

Manuscript 1864 submitted to 2019 41st Annual International Conference of the IEEE Engineering in Medicine and Biology Society (EMBC). Received February 20, 2019.

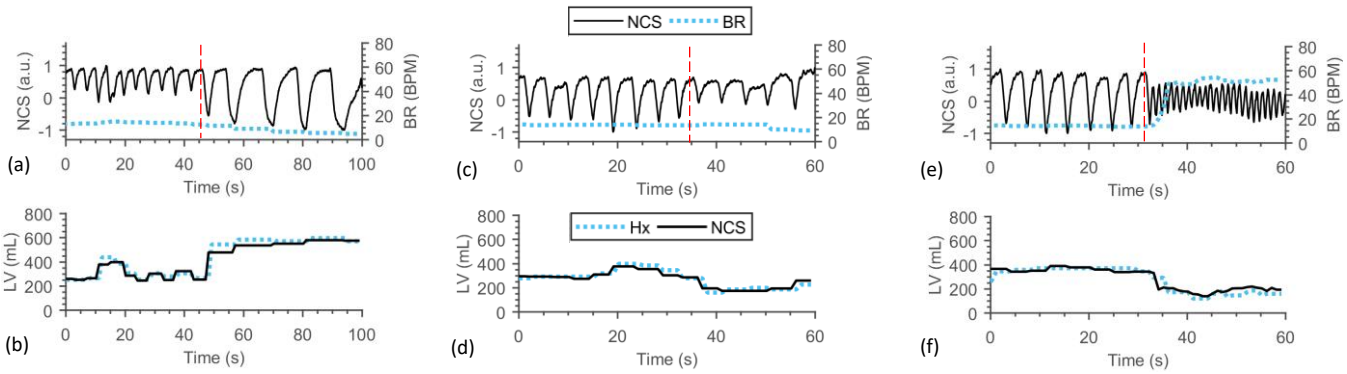

Figure 4. The top row shows normalized NCS respiration waveforms in solid black lines with transitions from normal to different breathing conditions, indicated by vertical dashed red lines. Estimated BR from NCS is also shown in BPM, as dotted blue lines. BR obtained from Hexoskin is very close in this set of experiments, and is hence not shown. The bottom row shows the corresponding LV estimate from Hexoskin (dotted blue lines) and NCS (solid black lines). (a) and (b) show transition from normal to deep breathing at t = 45 s. (c) and (d) show normal to slow-shallow breathing transition at t = 35 s, accompanied with decreased LV. (e) and (f) show transition to rapid shallow breathing at t = 32 s, marked with lower LV and higher BR.

We calibrated our NCS LV (LV_{NCS}) measurements by fitting it to Hexoskin LV estimate (LV_{Hx}) in the calibration phase for each person under test. LV_{NCS} is simply the difference between NCS waveform values at the peak points of inspiration and expiration for each breath cycle and is quadratically fitted $(a \times LV_{NCS}^2 + b \times LV_{NCS} + c)$ to LV_{Hx} during the calibration time.

IV. Results

A. Normal, Deep and Shallow Breathing

We performed data collection showing transitions among normal, deep and shallow breathing conditions. The normal BR for adults during rest is in the range of 12−20 BPM. The normal breathing pattern extracted from NCS and Hexoskin is shown in Fig. 3(a). All respiration waveforms are normalized. Fig. 4(a) shows transition between normal and deep breathing conditions. BR estimated from NCS is also shown, and is very close to that from Hexoskin, which is not shown for graphical clarity. The corresponding LV estimates by Hexoskin and NCS are shown in Fig. 4(b). Two shallow breathing conditions were also considered, one with normal or slow BR, and the other with high BR. Slow-shallow breathing leads to low LV estimates and is one of the possible indicators of respiratory depression induced by opioid abuse. Fig. 4(c) shows transition from normal to shallow breathing conditions with similar BR, marked by a sharp decrease in LV. On the other hand, the breathing pattern of rapid shallow breathing in Fig. 4(e) is marked with increased BR and reduction of LV in comparison with the normal breathing conditions. This pattern can be triggered by multiple scenarios, including anxiety attacks, asthma and chronic obstructive pulmonary disease (COPD). All transitions are marked with vertical dashed red lines.

B. Central Sleep Apnea (CSA)

CSA is a sleep disorder, marked by cessation of air flow for at least 10 s, lasting up to several minutes, without any muscle activity or cough reflex, as the autonomic nervous system stops giving signals for autonomous respiration. This breathing disorder is frequently observed among people suffering from chronic heart failure and brain diseases, among other reasons, as well as can be induced by opiate uses.

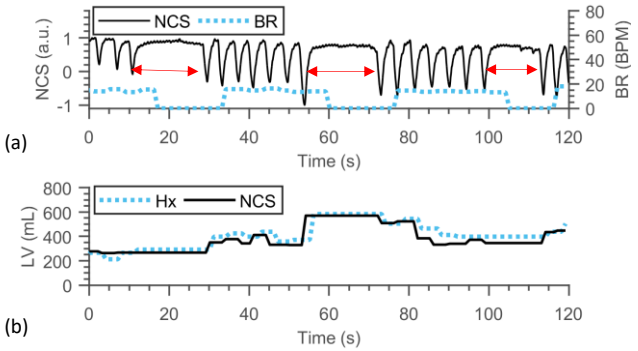

Figure 5. (a) NCS respiration waveforms with CSA, showing normal breathing with pauses between 12 – 28 s, 56 – 70 s and 102 – 112 s, indicated by the red arrows. Notice that although the NCS waveform indicates the breath pause timing instantaneously, BR drops to nearly zero only after a delay due the moving sampling window of 8 s. (b) LV estimates by calibrated NCS and Hexoskin.

Fig. 5(a) shows the respiratory pattern with sections of normal breathing with in-between voluntary breath holding marked by the red arrows, lasting around 10 – 15 s. Although the NCS waveform shows the instantaneous transition to a nearly constant value, BR drops to zero only after a delay, as it is calculated by counting the number of complete breath cycles in the last 8 s window. The seemingly delayed drop in BR is an artifact from the window size selection; large window will have larger delay appearance while small window may miss a slow cycle and report zero BR. NCS can output the accurate time registry for the end points of inhalation and exhalation and can thus be used for breathing cycle parameters other than BR. Nevertheless, the CSA pattern of interest here can still be derived from the present BR curve. The corresponding LV is shown in Fig. 5(b), which is only updated when a breath motion is observed. As there is a complete cessation of breathing, LV is not updated until normal breathing resumes and the next breath cycle is detected.

Manuscript 1864 submitted to 2019 41st Annual International Conference of the IEEE Engineering in Medicine and Biology Society (EMBC). Received February 20, 2019.

C. *Cheyne-Stokes Breathing*

This is a variant of CSA, with the periodic shallow breathing pattern alternating with deep over-breathing and apnea, which leads to a crescendo-decrescendo waveform accompanied with the apnea state. Cheyne-Stokes breathing is found in the same patient group as those patients suffering from CSA induced by heart failure, kidney failure and stroke. Fig. 6(a) shows that we can clearly capture the breath pauses, also indicated by the NCS waveform and BR. The shallow and deep over-breathing patterns can also be clearly observed from the rise and fall of LV_{NCS} in Fig. 6(b). In contrast, LV_{Hx} captures the increase in LV by deep over-breathing, but not the decrease during the shallow breathing period.

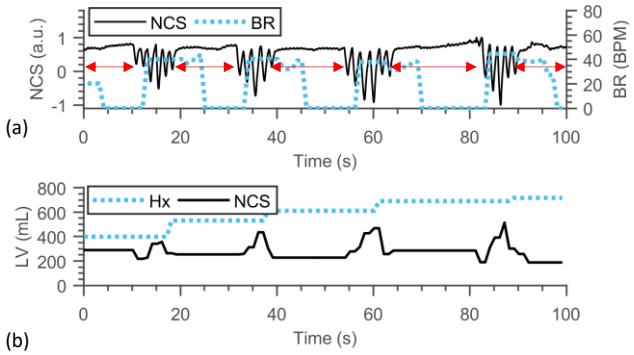

Figure 6. (a) The NCS respiration waveform and BR for the Cheyne-Stokes breathing pattern, separated by breath pauses marked with the red arrows. (b) The corresponding LV by Hexoskin and NCS, where Hexoskin cannot correctly capture the rise and fall pattern in LV.

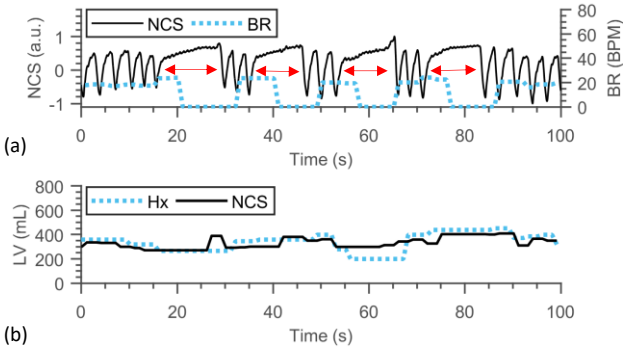

Figure 7. (a) The NCS respiration waveform showing Biot's breathing with periods of apnea indicated by the red arrows, followed by rapid regular breathing. (b) LV estimates from Hexoskin and NCS.

D. *Biot's Breathing*

This breathing pattern is characterized by periods of apnea followed by fast respiration cycles with regular magnitudes. Different from Cheyne-Stokes, it lacks the crescendo-decrescendo cycles, and is irregular with varying periods of apnea. This breathing pattern is a result of damages to the central pattern generator in medulla, possibly due to stroke, trauma or injury. It is also observable in the case of opioid intoxication, which may also result in CSA and Cheyne-Stokes. Fig. 7(a) shows sections of fast breathing with breath pauses, marked by an initial increase and then decrease in BR. The corresponding LV variation is shown in Fig. 7(b) where the constant LV period corresponds to apnea.

E. *Ataxic Breathing*

Ataxic breathing involves irregular breathing cycles, followed by irregular pauses and increasing apnea time. This pattern is observed when Biot's breathing deteriorates due to further damage to the brain center responsible for Biot's breathing. Fig. 8(a) shows experimentally performed breathing pattern. During this irregular rapid breathing, complete exhalation is not performed, resulting in lower LV estimates. Fig. 8(b) shows NCS capturing decrease of LV and then increase at the last irregular breathing due to complete exhalation. No change is observed during breath hold. Hexoskin missed the decrease in LV during rapid breathing.

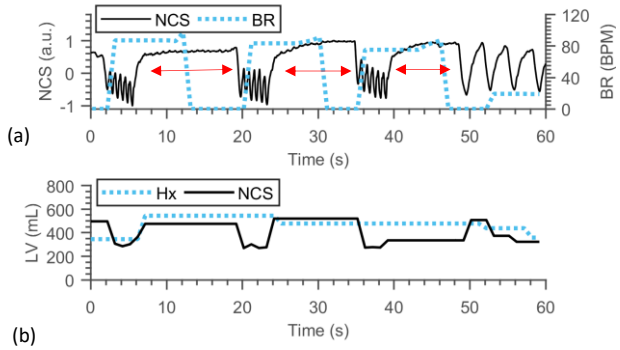

Figure 8. (a) The NCS waveform showing ataxic breathing with irregular rapid breaths followed by periods of apnea. (b) The correlated LV estimates from NCS and Hexoskin. NCS shows decrease in LV during the rapid irregular breathing.

F. *Isovolumetric Motion*

One of the major sleep apneas is OSA, caused by respiratory muscle weakness or airduct blockage. This apnea is characterized by asynchronous movement of the thorax and abdomen that can be observed as a time lag of the thoracoabdominal motion or complete out-of-phase motion of thorax and abdomen.

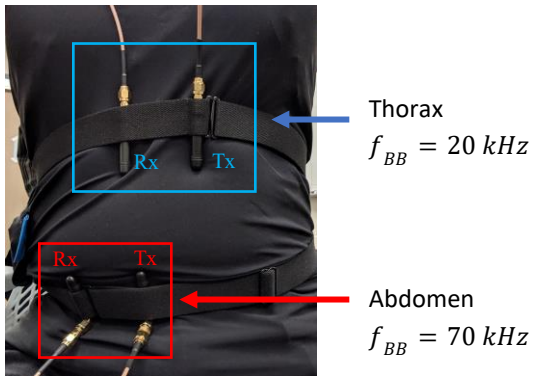

Figure 9. Setup showing two Tx – Rx antenna pairs to observe movement at thorax and abdomen. The person is wearing a Hexoskin smart shirt, and the sensors are placed close to the body belts at thorax and abdomen.

We performed isovolumetric abdomen movement by successively contracting and relaxing the abdomen muscles, without inhalation and exhalation. This resulted in a pure paradoxical breathing motion where thorax and abdomen are moving in the opposite direction. With only one sensor placed below the thorax, it gets coupled to diaphragm, lungs and some abdomen motion, and gives accurate LV estimations only when both abdomen and thorax are in sync. However,

Manuscript 1864 submitted to 2019 41st Annual International Conference of the IEEE Engineering in Medicine and Biology Society (EMBC). Received February 20, 2019.

when abdomen and thorax are moving asynchronously, this setup becomes sensitive to the sensor placement on the chest, with ambiguous results based on dominating thorax or abdomen movement. To separately observe both thorax and abdomen motion, we used B210 in the 2×2 MIMO mode with one pair of Tx – Rx on thorax, and the other pair on the abdomen, with different baseband modulation to separate coupling of both movements. Two NCS sensors are placed at thorax and abdomen in front of the body, resulting in coupling to the near-field thorax and abdomen movement respectively. Fig. 9 shows the setup with two sensors, thorax sensor is placed in line with the xiphoid process and abdomen sensor is placed lower, both in line with the RIP belts.

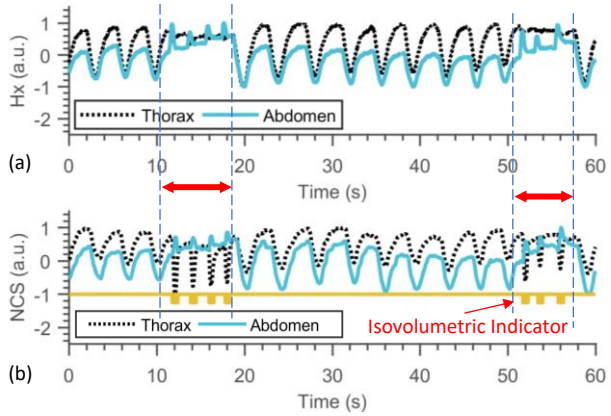

Figure 10. (a) Hexoskin thorax and abdomen waveforms with normal breathing and instances of isovolumetric abdomen contraction, marked by the red arrows. The breathing transitions are marked by the vertical dashed blue line. (b) Respiration waveforms from two NCS sensors showing asynchronous motion of thorax and abdomen during isovolumetric movement, similar to Hexoskin waveforms. Isovolumetric indicators as gold squares show instances of out-of-phase thorax and abdomen waveforms, detected from negative product of their slopes.

Fig. 10(a) shows the RIP body-belt data, showing regular breathing with intervals of paradoxical abdomen and thorax movement. This strong voluntary movement is clearly observable in the NCS data from thorax and abdomen sensors in Fig. 10(b). Hexoskin thorax belt does not clearly show opposite movement in all the cases, such as $t = 55$ s. A simple algorithm can detect time instances with isovolumetric breathing. As the slope of abdomen and thorax waveforms are opposite during isovolumetric inhalation and exhalation, we perform slope estimation at each sample point, using current and previous data points and calculate product of the two slope estimates at abdomen and thorax. The sign of product is negative during isovolumetric breathing, as indicated in Fig. 10(b) by gold squares. The extracted NCS waveform from multiple sensors can accurately capture the asynchronous thoracoabdominal movements when OSA is of high concerns.

G. *Coughing*

As the NCS sensor can capture the near-field motion at high sampling rate, we can easily capture signatures of other common breathing conditions such as coughing and sneezing. We performed some preliminary data collection to observe voluntary coughing patterns with one sensor below the xiphoid process. Fig. 11(a) shows the low-frequency (LF) NCS signal where regular breathing is mixed with irregular coughing signatures. Cough instances can be more clearly detected from filtered high-frequency (HF) component, as shown in Fig. 11(b), where NCS waveform is filtered between 15 – 50 Hz. A cough was predicted if the waveform energy increased above a certain threshold, empirically selected to be 100 times the energy of HF component during regular breathing. Results of this cough indicator are shown in Fig. 11(b) as well. Multiple sensors and sensor position can be optimized in the future to possibly recognize coughing signatures at different respiratory tracts of pharynx, larynx, trachea and bronchi.

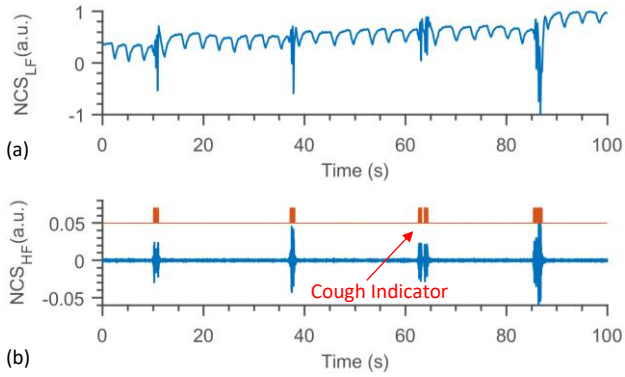

Figure 11. NCS waveform showing coughing instances at t = 20, 45, 68 and 85 s. (a) NCS LF component between 0.02 – 10 Hz, showing breathing and coughing movement. (b) Only HF component is shown with frequencies between 15 – 50 Hz, along with cough indicator based on detecting high energy instances.

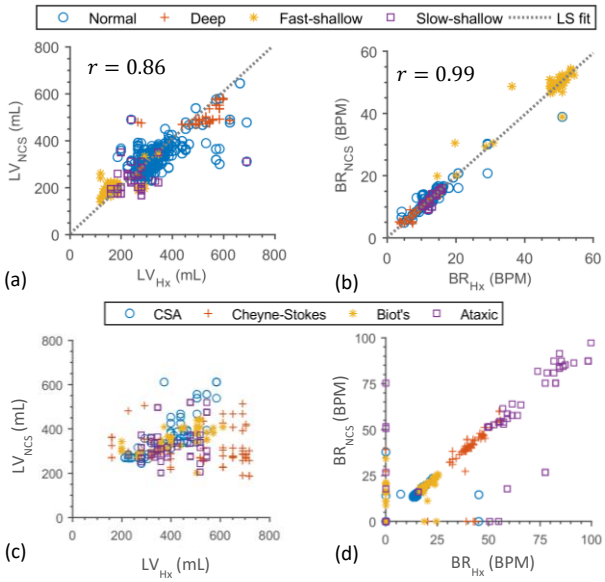

Figure 12. (a) Calibrated LV_{NCS} vs LV_{Hx} for normal, deep, fast-shallow and slow-shallow breathing conditions, showing the dotted least-squares fit line. Legend is shown at the top. (b) BR estimates, BR_{NCS} vs BR_{Hx} under the same breathing conditions. (c) and (d) show scatter plots, LV_{NCS} vs LV_{Hx} and BR_{NCS} vs BR_{Hx} respectively under various respiratory disorder conditions, only to illustrate low correlation between computed estimates from NCS and Hexoskin. Legend is shown at the top.

V. Benchmark

To benchmark the overall NCS results against Hexoskin, we performed linear regression and calculated the correlation between BR and LV estimated from Hexoskin and NCS waveforms, on two data sets of 10 mins each, including

normal, deep, slow-shallow and fast-shallow breathing. Result showed very high Pearson's correlation coefficient value for BR, $r(BR_{Hx}, BR_{NCS}) = 0.99$, and slightly lower for LV, $r(LV_{Hx}, LV_{NCS}) = 0.86$. Figs. 12(a) and 12(b) show the scatter plot of LV_{NCS} vs LV_{Hx} and BR_{NCS} vs BR_{Hx}, respectively, together with the regression line. Instances of different breathing conditions are also marked, where the outlier cases are mainly at the transition point of two breathing conditions.

For comparison, we have also shown NCS vs Hexoskin scatter plots under various respiratory disorders in Figs. 12(c) and 12(d). These scatter plots summarize earlier observations in Figs. 5 – 8, where NCS and Hexoskin LV estimates were poorly correlated as LV_{Hx} often missed sudden changes in breathing patterns. BR estimates are more correlated, with some outliers on the axes, again possibly due to differences at transition points to apnea or missed breath peaks.

VI. Conclusion and Future Works

The aim of the paper is to present an RF-based wearable sensor prototype that can estimate various respiratory patterns for wellness and disorder diagnostics. Because of the simple RF architecture, this system can be implemented as a small-sized active unit placed over the clothes without requiring any skin contact, and can then directly transmit sampled respiration waveform in established digital protocols. The small form factor can enable increased comfort and obscure placement over the conventional body belts and thus can be used for continuous respiration measurements over long term.

The NCS setup offers multiple advantages over existing contactless doppler radar measurements [9]: 1) Less sensitive to user and ambient motion; 2) The entire unit is on the chest without need of an external reader which is difficult to use in outdoor scenarios; 3) LV calibration is convenient without dependence on the user's location in the room or orientation with respect to the antenna; 4) Multiple units can separate thoracic and abdominal motion for more accurate LV estimates [7].

Automated respiratory disorder analysis based on cough sounds has been of interest in recent years [19], [20]. As NCS can directly capture lung and larynx movement due to coughing with very high sampling rates, it may offer higher reliability, especially in high-noise ambient, or when multiple people are present.

Future work will focus on improved system design for wearables, and improved signal processing techniques to capture real-time information related to respiration health. The current peak detection algorithm cannot be implemented in a real-time manner but only after a window duration, which needs to be improved. A detailed human study including age, sex and body mass index (BMI) would also be needed before clinical validation.

References

[1] M. Folke, L. Cernerud, M. Ekström, and B. Hök, "Critical review of non-invasive respiratory monitoring in medical care," *Med. Biol. Eng. Comput.*, vol. 41, no. 4, pp. 377–383, Jul. 2003.

[2] M. Á. Martínez-García *et al.*, "Continuous positive airway pressure treatment reduces mortality in patients with ischemic stroke and obstructive sleep apnea: A 5-year follow-up study," *Am. J. Respir. Crit. Care Med.*, vol. 180, no. 1, pp. 36–41, 2009.

[3] O. Oldenburg, B. Lamp, L. Faber, H. Teschler, D. Horstkotte, and V. Töpfer, "Sleep-disordered breathing in patients with symptomatic heart failure A contemporary study of prevalence in and characteristics of 700 patients," *Eur. J. Heart Fail.*, vol. 9, no. 3, pp. 251–257, 2007.

[4] D. Wang and H. Teichtahl, "Opioids, sleep architecture and sleep-disordered breathing," *Sleep Med. Rev.*, vol. 11, no. 1, pp. 35–46, 2007.

[5] F. Q. AL-Khalidi, R. Saatchi, D. Burke, H. Elphick, and S. Tan, "Respiration rate monitoring methods: A review," *Pediatr. Pulmonol.*, vol. 46, no. 6, pp. 523–529, 2011.

[6] N. Netzer, A. H. Eliasson, C. Netzer, and D. A. Kristo, "Overnight pulse oximetry for sleep-disordered breathing in adults: a review," *Chest*, vol. 120, no. 2, pp. 625–633, 2001.

[7] K. Konno and J. Mead, "Measurement of the separate volume changes of rib cage and abdomen during breathing," *J. Appl. Physiol.*, vol. 22, no. 3, pp. 407–422, 1967.

[8] "EMFIT sleep tracking & monitoring with heart-rate-variability." [Online]. Available: https://www.emfit.com/. [Accessed: 02-Feb-2019].

[9] C. Li, V. M. Lubecke, O. Boric-Lubecke, and J. Lin, "A review on recent advances in Doppler radar sensors for noncontact healthcare monitoring," *IEEE Trans. Microw. Theory Tech.*, vol. 61, no. 5, pp. 2046–2060, 2013.

[10] Y. S. Lee, P. N. Pathirana, C. L. Steinfort, and T. Caelli, "Monitoring and analysis of respiratory patterns using microwave doppler radar," *IEEE J. Transl. Eng. Heal. Med.*, vol. 2, pp. 1–12, 2014.

[11] W. Massagram, N. Hafner, V. Lubecke, and O. Boric-Lubecke, "Tidal volume measurement through non-contact Doppler radar with DC reconstruction," *IEEE Sens. J.*, vol. 13, no. 9, pp. 3397–3404, 2013.

[12] X. Hui and E. C. Kan, "Monitoring vital signs over multiplexed radio by near-field coherent sensing," *Nat. Electron.*, vol. 1, pp. 74–78, 2018.

[13] P. Sharma and E. C. Kan, "Sleep scoring with a UHF RFID tag by near field coherent sensing," in *IEEE MTT-S Int. Microw. Symp. Dig.*, 2018, pp. 1419–1422.

[14] "OSHA safety and health topics: Radiofrequency and microwave radiation standards." [Online]. Available: https://www.osha.gov/SLTC/radiofrequencyradiation/standards.html. [Accessed: 02-Feb-2019].

[15] W. T. McNicholas, "Diagnosis of obstructive sleep apnea in adults," *Proc. Am. Thorac. Soc.*, vol. 5, no. 2, pp. 154–160, 2008.

[16] "Hexoskin smart shirts - cardiac, respiratory, sleep & activity metrics." [Online]. Available: https://www.hexoskin.com/. [Accessed: 02-Feb-2019].

[17] G. Yuan, N. A. Drost, and R. A. McIvor, "Respiratory rate and breathing pattern," *McMaster Univ. Med. J.*, vol. 10, no. 1, pp. 23–25, 2013.

[18] F. Scholkmann, J. Boss, and M. Wolf, "An efficient algorithm for automatic peak detection in noisy periodic and quasi-periodic signals," *Algorithms*, vol. 5, no. 4, pp. 588–603, 2012.

[19] K. Kosasih, U. R. Abeyratne, and V. Swarnkar, "High frequency analysis of cough sounds in pediatric patients with respiratory diseases," in *Proc. IEEE Annu. Int. Conf. Eng. Med. Biol. Soc.*, 2012, pp. 5654–5657.

[20] J. Monge-Álvarez, C. Hoyos-Barceló, P. Lesso, and P. Casaseca-de-la-Higuera, "Robust detection of audio-cough events using local Hu moments," *IEEE J. Biomed. Heal. Informatics*, vol. 23, no. 1, pp. 184–196, 2019.

Manuscript 1864 submitted to 2019 41st Annual International Conference of the IEEE Engineering in Medicine and Biology Society (EMBC). Received February 20, 2019.

Appendix C

(PDF downloaded from Nature) P. Sharma, X. Hui, J. Zhou, T. B. Conroy and E. C. Kan, “Robust cardiopulmonary monitoring using wearable radio-frequency sensors”, *Nature Partner Journal (NPJ), Digital Medicine*, doi: 10.1038/s41746-020-0307-6, July 2020.

npj | Digital Medicine

www.nature.com/npjdigitalmed

ARTICLE OPEN

Check for updates

Wearable radio-frequency sensing of respiratory rate, respiratory volume, and heart rate

Pragya Sharma[1]✉, Xiaonan Hui[1], Jianlin Zhou[1], Thomas B. Conroy[1] and Edwin C. Kan[1]

Many health diagnostic systems demand noninvasive sensing of respiratory rate, respiratory volume, and heart rate with high user comfort. Previous methods often require multiple sensors, including skin-touch electrodes, tension belts, or nearby off-the-body readers, and hence are uncomfortable or inconvenient. This paper presents an over-clothing wearable radio-frequency sensor study, conducted on 20 healthy participants (14 females) performing voluntary breathing exercises in various postures. Two prototype sensors were placed on the participants, one close to the heart and the other below the xiphoid process to couple to the motion from heart, lungs and diaphragm, by the near-field coherent sensing principle. We can achieve a satisfactory correlation of our sensor with the reference devices for the three vital signs: heart rate ($r = 0.95$), respiratory rate ($r = 0.93$) and respiratory volume ($r = 0.84$). We also detected voluntary breath-hold periods with an accuracy of 96%. Further, the participants performed a breathing exercise by contracting abdomen inwards while holding breath, leading to paradoxical outward thorax motion under the isovolumetric condition, which was detected with an accuracy of 83%.

npj Digital Medicine _####################_ ; https://doi.org/10.1038/s41746-020-0307-6

INTRODUCTION

In addition to the effective treatment of diseases, modern medicine has been extended towards an overall healthier living with improved day-to-day quality of life[1,2] and integrated end-of-life care not restricted to clinical visits[3,4]. This requires novel solutions for noninvasive vital-sign sensing without skin contact that can be integrated effectively into various lifestyles over broad age-groups. Such a technique could potentially help patients of asthma, chronic obstructive pulmonary disease (COPD)[5], and sleep apnea by continuous monitoring of heartbeat and respiration.

In clinical practices, pulmonary function tests are generally assessed by spirometry[6] and physical examinations[7]. The latter might not require any specialized instrument but is limited by the experience of the physician and is not quantitative. Spirometry provides detailed parameters characterizing lung function but requires attentive participation of the patient with forced breathing maneuvers, and is thus not feasible for continuous long-term measurements, or patients suffering from asthma. Whole-body plethysmography[8] is used to measure absolute air volume in the lungs and breathing resistances without extensive voluntary exercises but still requires some patient cooperation. This poses a challenge for respiratory disorder detection in patients that are unable to follow the instructions due to weakness, coma, or other cognitive failures. Other alternatives for respiratory monitoring[9,10] require calibration for the volume estimate, including nasal probes[11] for airflow information, and strain or inductance belts at thorax and abdomen[9,12], which need to maintain reasonable tension in all breathing conditions to measure chest-wall motion. Local strain sensors[13] are more comfortable, but require tight skin contact to measure chest-wall motion. Gold-standard heartbeat monitoring uses electrocardiogram (ECG) with multiple adhesive skin-contact electrodes to monitor the electrical activity of the cardiac muscle. Pulse oximetry is a less invasive method of extracting the heartbeat, however, it requires a stable probe in direct contact with the skin[14–16]. Other noninvasive and non-skin-touch sensing technologies have been proposed, but also with their limitations. Thoracic surface and body vibrations due to heartbeat have been studied in detail using seismocardiography (SCG)[17–19] and ballistocardiography (BCG)[17,20–22], respectively, for signatures under different abnormalities. Both sensors measure either displacement, velocity, or acceleration originated from the heartbeat but observed at the body surface. Film-based displacement sensors may be affected by artifacts from structural vibrations in a moving wheelchair[23] or ambulance. Integrated solutions like smart shirts[24] with ECG, chest belts, and accelerometers can provide detailed cardiopulmonary characteristics, but have a large device form-factor, and are unsuitable for bedridden and geriatric patients where snug-fit clothing and skin-contact electrodes are impractical due to concerns of comfort and bed sores[25,26]. Ambient optical[27] and radio-frequency (RF) sensing[28] records surface motion from breathing and heartbeat with limited signal-to-noise ratio (SNR)[29,30], and requires the reader to be in the line of sight (LoS) to the torso[31,32]. Far-field RF has additional limitations on the maximum number of subjects that can be measured simultaneously[33]. Respiratory volume (RV) is even more difficult to retrieve, as it is affected by body posture and orientation variation[32,34] with respect to the antennas or cameras. Some noticeable work has been done using RF in the near-field region[35,36] that can couple to internal dielectric boundary change to clearly measure respiratory motion, but heartbeat can only be extracted during breath-hold.

Near-field coherent sensing (NCS)[37] is a noninvasive technique that works by transmitting a low-power continuous wave (CW) RF signal into the body with over-clothing antennas. The near-field coupling to the internal dielectric boundary motion results in a direct measurement of the heart, lung, and diaphragm motion, in contrast to surface motion sensors. Detailed high-frequency heartbeat characteristics associated with the S1 and S2 sounds can also be potentially extracted from over-clothing placement[38]. However, a detailed comparison with echocardiogram can help clarify this observation, while a further improvement from possible sensor fusion with SCG and phonocardiogram (PCG) needs to be

[1]School of Electrical and Computer Engineering, Cornell University, Ithaca, NY, USA. ✉email: ps847@cornell.edu

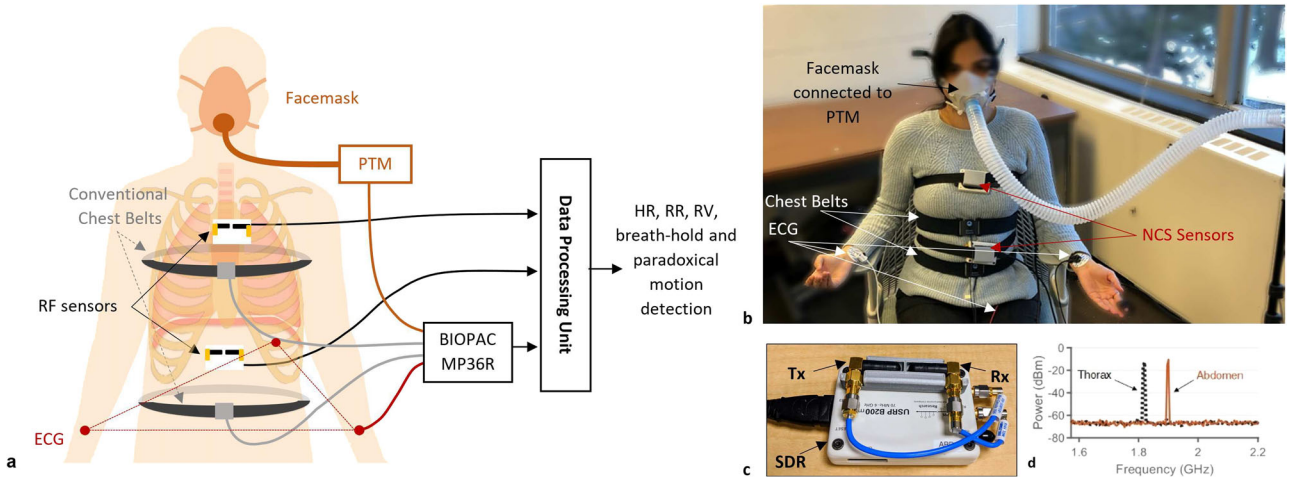

Fig. 1 The experimental system. a Schematics of NCS and BIOPAC sensors and data flow. **b** Experimental setup with the participant wearing NCS and BIOPAC sensors in the sitting posture. The photo was taken and published with the written informed consent of the subject. **c** The NCS sensor consisting of SDR as well as the Tx and Rx antennas in a 3D-printed package. **d** Spectrogram of thorax and abdomen NCS sensors at their respective carrier frequencies of 1.82 GHz (−12.84 dBm) and 1.9 GHz (−10.42 dBm).

investigated in future studies. The wearable RF sensor design has high ambient motion tolerance with the receiver placed close to the transmitter, making NCS less affected by environmental changes compared to direct far-field reflection[39], where ambient motion within the antenna radiation pattern can cause significant interference. Multiple sensors can be placed on the body to couple to both respiratory and heartbeat motion with frequency multiplexing and can be easily extended to monitor multiple people in the same room. Owing to its simple transceiver architecture, this sensor can be readily designed in a small, convenient form factor, as well as made wireless-capable at low cost.

In our earlier work, we have demonstrated preliminary NCS results where RV and respiratory rate (RR) can be estimated with high accuracy for one participant in sitting posture[40]. In this paper, we present a setup to accurately estimate the heart rate (HR) and respiratory effort, including RR and RV, over 20 participants with varying body mass index (BMI) and gender. Further, as RV is sensitive to body posture and breathing styles, we have presented analyses over various postures, as well as during conscious and spontaneous breathing exercises with a large breathing range of 0–45 breaths per minute (BPM) and a resting HR in the range of 50–90 beats per minute (BPM). A short calibration period by a gold-standard pneumotachometer (PTM) was performed for each subject and posture once, and the corresponding model was used on NCS and chest belts for further voluntary breathing exercises.

RESULTS

NCS sensor and test system architecture

The NCS sensing approach is based on the near-field coupling of ultra-high frequency (UHF) waves with the nearby dielectric boundary motion. The dielectric composition in the near-field region of an antenna will modulate its characteristics. For a single antenna, this change can be measured from the antenna reflection parameter S_{11}. For an antenna pair, this can be derived from the cross-coupling S_{21}. As the transmitter (Tx) and receiver (Rx) signal chains are better isolated in the S_{21} measurements with less self-interference and higher SNR, we opt to place an antenna pair as part of the NCS sensor to the region of interest, where the intended surface and internal boundary motion can be retrieved after baseband demodulation. Notice that UHF has reasonable penetration into dielectrics in the near-field, and thus the internal dielectric motion during breathing and heartbeat can be locally modulated onto the specific antenna pair. We have placed two NCS sensors on the chest, one below the xiphoid process close to the diaphragm, and another near the heart. These sensors measure the abdomen and thorax respiratory motion as well as the heartbeat, by effectively capturing the geometrical changes in these organs along with other associated muscles.

Figure 1a shows the NCS system architecture with sensor placement, data collection and processing flow. It also shows the reference sensors by BIOPAC (BIOPAC Systems, Inc., Goleta, CA), including ECG, chest belts and PTM connected to a facemask. A participant wearing all sensors in the sitting posture is shown in Fig. 1b. Two NCS sensors are held on the body with loosely placed belts. The abdomen sensor is placed slightly below the xiphoid process to be close to the diaphragm, and the thorax sensor close to the heart, so that it can couple both heartbeat and lung motion. These lightweight and small sensing units consist of RF Tx and Rx antennas connected to the software-defined radio (SDR) transceiver (Fig. 1c) to perform NCS measurements with a low RF power of less than −10 dBm (Fig. 1d), well under the safety limits set by occupational safety and health administration (OSHA)[41].

The acquired BIOPAC and NCS signals are processed to estimate RV, RR, and HR statistics. The normalized BIOPAC thorax and abdomen chest-belt signals are shown as reference in Fig. 2a. Figure 2b shows normalized unfiltered NCS data from thorax and abdomen sensors, with strong respiratory motion modulation. Heartbeat is also modulated clearly on the NCS thorax waveform and can be properly filtered to remove respiratory motion. Supplementary Fig. 1 shows the filtered heartbeat waveform from NCS and the HR extraction techniques under motion artifact.

RV calibration model

A calibration model is developed to estimate RV from NCS and chest belts in various postures and breathing conditions using airflow estimates from the pre-calibrated PTM connected to a facemask (Fig. 1b). While PTM is a kind of spirometer, we have referred to it as such to state explicitly that the airflow is estimated from the pressure change. The facemask design includes a separator between nose and mouth and is tightly strapped on to minimize any air leakage from the mouth. Participants are requested to inhale and exhale by mouth only, and they can feel rather uncomfortable during PTM measurements. Thus, PTM is removed from the participant except during the short initial calibration routine of 30 s, with 15 s of each normal and deep breathing. Instantaneous volume is computed by integrating the

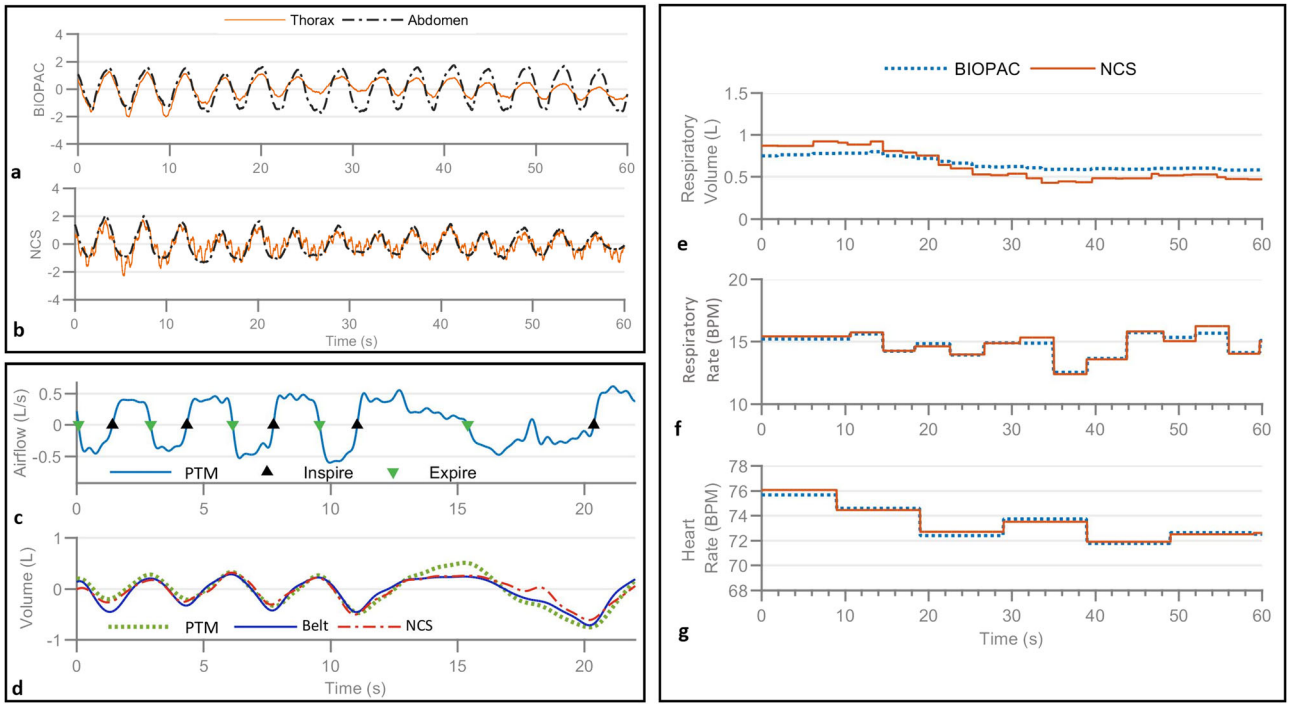

Fig. 2 Examples of the sensor outputs and estimated RV, RR, and HR. a, **b** The normalized BIOPAC chest-belt signals (**a**) and normalized unfiltered NCS signals (**b**) showing respiration waveforms during tidal (normal) breathing. The NCS thorax signal shows strong heartbeat motion as well. **c** The PTM airflow signal with detected inspiration and expiration start points. **d** The extracted instantaneous volume Vol_{PTM} (dotted green) from the airflow, and calibrated chest belts (blue) and NCS (dashed-dotted red) respiration volume waveforms. **e**–**g** The analysis of the data shown in **a** and **b**; **e** and **f** show RV and RR, respectively, from NCS and BIOPAC chest belts; **g** shows the HR from NCS and BIOPAC ECG.

airflow rate for each breath cycle to get Vol_{PTM}. Waveforms from both BIOPAC chest belts and filtered NCS respiration waveforms are then calibrated by the least-square fitting of linear relation:

$$a \cdot \mathrm{Resp}_{\mathrm{Th}} + b \cdot \mathrm{Resp}_{\mathrm{Abd}} + c = \mathrm{Vol}_{\mathrm{PTM}}, \quad (1)$$

where $Resp_{Th}$ and $Resp_{Abd}$ are thorax and abdomen respiratory waveforms, respectively. Figure 2c shows PTM airflow waveform during the calibration, with the corresponding Vol_{PTM} and calibrated NCS and chest-belt volumes in Fig. 2d. RV is defined as the volume of the air exchanged during each inhalation and exhalation and is calculated as the peak height of each breath cycle. Figure 2e shows estimated RV from chest belts and NCS data shown in Fig. 2a, b, which have similar trends but NCS has shown more minute variations. This is consistent with Fig. 2d around 18 s, where the small perturbation in airflow is captured by NCS but not chest belts.

For RV calibration, as the posture can affect the breathing pattern and lung capacity, separate calibration is necessary[12] for supine, lateral recumbent, and sitting postures for each participant. As the chest circumference has a significant variation across different postures, BIOPAC chest-belt tension requires re-adjustment to accurately measure respiration. The NCS sensor, on the other hand, only requires stable placement in the near-field region and does not require changes across different postures. Furthermore, during the sitting posture, we performed two more experiments with participants in relaxation and attention-task states without additional calibration. Frequent involuntary posture changes were observed during both states, either for comfort or in response to task failure or success. With these posture changes, tension-based BIOPAC belts inclined to move toward a stable, minimal-circumference position, i.e., lower for the thorax and upward for the abdomen belt, resulting in loss of tension and erroneous measurements. As the NCS belts and sensors were loosely placed, a posture change could cause the antennas to move closer or further away from the body, thus scaling the waveform amplitude. RV of BIOPAC and NCS during the known normal breathing sections were tested to apply a scaling correction. Detailed correction steps are discussed in the "Data Processing" section.

Overall statistics

With tests in multiple postures and under different breathing exercises, we have performed analyses of 100 experiments, with over 590 min of total recorded data for 20 participants. Figure 3 shows the results across all three postures, with different breathing styles. We can achieve a high correlation of NCS and BIOPAC for RV ($r_{RV} = 0.84$), RR ($r_{RR} = 0.93$), and HR ($r_{HR} = 0.95$), as shown in the scatter plots in Fig. 3a–c. We have employed the Bland-Altman ($B\&A$) plot to quantify the agreement between NCS and BIOPAC, both of which may have errors. This agreement is estimated by the mean (m) and standard deviation (σ) of the measurement differences. $B\&A$ plots can also identify possible outliers visually by a XY scatter plot, with the Y axis as the pairwise difference, and the X axis as the mean of the two measurements. The systematic bias is estimated as the mean difference m, and limits of agreement (LoA) within which 95% of the differences are expected to lie, are estimated as $\mathrm{LoA} = m \pm 1.96 \cdot \sigma$, assuming a normal distribution. Figure 3d–f show good agreement of both the sensors with low mean deviations ($m_{RV} = 9.6$ mL, $m_{RR} = 0.05$ BPM, $m_{HR} = -0.5$ BPM) and narrow LoA, as denoted by the dashed lines around the mean value. The results for each participant individually are shown in Supplementary Table 1.

Variation over breathing patterns

As breathing is a hybrid voluntary-autonomous process, we have collected data during both conscious and spontaneous states. During conscious state, participants performed guided normal,

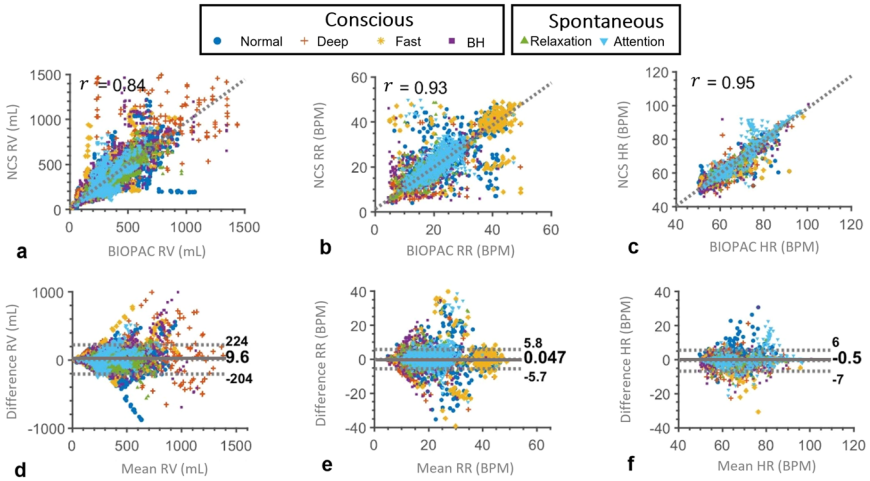

Fig. 3 Correlation and agreement between NCS and BIOPAC estimate of RV, RR, and HR over the entire data. The label shows a marker for each breathing style, including conscious normal, deep, fast and breath-hold (BH), as well as spontaneous breathing in relaxation and attention states. **a**–**c** Scatter plots of NCS vs. BIOPAC RV, RR, and HR, respectively, with denoted Pearson's correlation coefficient, *r*, showing a high correlation between the two sensors. **d**–**f** *B&A* plots of NCS and BIOPAC showing the bias *m* at the center (solid line) and the corresponding LoA (dotted lines) given by $m \pm 1.96 \cdot \sigma$.

Table 1. Correlation and *B&A* statistics.

Measurement		(a) Different breathing patterns						(b) Different postures with breathing protocol		
		Normal	Deep	Fast	Hold	Relaxation	Attention	Supine	Lateral recumbent	Sitting
RV (mL)	*r*	0.88	0.80	0.76	0.84	0.93	0.76	0.81	0.89	0.81
	m	0	60	18	33	−10	11	2	18	27
	σ	89	186	144	138	65	97	121	115	132
RR (BPM)	*r*	0.95	0.91	0.89	0.77	0.93	0.87	0.94	0.93	0.93
	m	0.05	0.02	−0.49	−0.13	0.11	0.19	−0.06	0.06	−0.08
	σ	2.48	2.58	6.66	4.09	1.72	2.48	2.84	3.60	3.52
HR (BPM)	*r*	0.95	0.93	0.90	0.96	0.98	0.95	0.96	0.93	0.94
	m	−0.69	−0.98	−1.70	−0.80	−0.23	0.04	−0.70	−0.62	−1.22
	σ	2.90	3.45	4.38	2.92	1.81	3.67	2.72	3.54	3.20

deep, fast breathing and breath-holds. For the spontaneous tests, no breathing instructions were provided and instead, participants were first asked to relax and then execute an attention-engaging task. As performing the task required the participants to be seated, spontaneous breathing tests were performed only in the sitting posture. Figure 3 showed the results over all the experiments with breathing styles denoted by different markers. As normal breathing is similar to spontaneous breathing, most of these points are overlapped. The fast breathing pattern is centered around the instructed 40 BPM in the RR plots. Deep breathing is indicated by low RR around 6 BPM, as well as high RV. These points are also spread out with a low correlation between NCS and chest belts, possibly due to data distortion from the large motion, resulting in nonlinear strain gauge response, as well as NCS sensor motion relative to the body. Breath-hold periods have low RR at the beginning of the hold period and may also be accompanied with deep breaths after the long holding period, thus are seen closer to the deep-breathing points in both RV and RR plots. Zero RR is not marked, but these periods are treated separately during the breath-hold detection stage. Supplementary Fig. 2 shows an example of one participant following the conscious breathing protocol in the supine posture, and the extracted RV, RR and HR over time with consistent observations. Table 1a compares the correlation and *B&A* statistics for different breathing patterns. The relaxation state with spontaneous breathing shows the highest correlation of NCS and BIOPAC sensors for RV and HR estimates, close to conscious normal breathing results. This could be due to the regular breathing pattern with few motion artifacts. In comparison, participants tended to move in response to stress during the attention test, leading to motion artifacts.

Variation over postures

Adjusting body postures can lead to RV variations, as respiratory mechanisms are affected by different resistance or compliance of the lung and chest-wall components. Thus, we performed tests with the guided breathing protocol in three postures: laying on a bed in supine and left lateral recumbent postures and sitting in a chair. The average reference RV, calculated over all 20 participants during the identical protocol of voluntary breathing exercises, is observed to be highest at 329 mL in the supine posture, followed by sitting and lateral recumbent at 317 and 263 mL, respectively. The RR has the opposite trend with average RR of 17.3, 19, and 19.5 BPM in supine, sitting, and lateral recumbent postures, respectively. The average HR is highest during sitting at 67.6 BPM, compared to 65.3 and 63.8 in supine and lateral recumbent postures, respectively. These results are summarized in Supplementary Table 2. The detailed statistics for each posture are shown in Table 1b. Good correlation is observed across all the postures,

Table 2. Detection of breath-hold (BH) and paradoxical abdomen-thorax (PAT) motion.

BH ($n = 80$)		NCS		PAT ($n = 58$)		NCS	
		Detected	Missed			Detected	Missed
BIOPAC	Detected	74	3	BIOPAC	Detected	42	9
	Missed	3	0		Missed	6	1

with supine showing the least bias (m) for RV and RR estimates with narrow LoA (small σ), possibly due to the stable posture. No other clear trend is observed, indicating that the estimates are more sensitive to breathing types and patterns than to the posture. Supplementary Fig. 3 shows the correlation and *B&A* plots for different postures, both with and without the simulated breathing exercises.

Breath-hold detection accuracy

Each participant was instructed to perform two breath-holds in both supine and lateral recumbent postures for a maximum duration of 20 s, simulating central sleep apnea (CSA), which is indicated by breath cessation for at least 10 s[42]. A simple detection algorithm was implemented based on the inspiration peak-to-peak interval. Overall, both NCS and BIOPAC performed well for breath-hold detection, as shown in Table 2, which shows both sensors detected 74 cases out of 80 annotated cases, with each missing 3 non-overlapping instances. The errors possibly originate from the participant's incompliance to the breath-hold protocol. Small torso motion is coupled differently to the two sensors, leading to incorrect peak detection during breath-hold. Supplementary Fig. 4 shows the NCS and BIOPAC respiratory waveforms with detected peaks during breath-holds for representative good and poor cases.

Paradoxical abdomen-thorax motion detection accuracy

To test the separate thorax and abdomen motion, the participants were asked to perform an isovolumetric abdomen exercise while holding breath. With no airflow, the inward abdomen contraction results in outward motion of the thorax, as the total lung volume is conserved[43], simulating paradoxical abdomen-thorax motion similar to obstructive sleep apnea (OSA) with complete closure of the airway. We used the slope-product of thorax and abdomen respiration waveforms to detect paradoxical motion in BIOPAC and NCS waveforms, as shown in Fig. 4, where three instances of isovolumetric maneuver are successfully detected by both the sensors. While some participants were able to successfully perform breath-hold and abdomen contraction, anomalous instances when paradoxical behavior was not observed can be attributed to the following possible reasons. (1) Placement sensitivity of sensors: the BIOPAC thorax belt placed near the xiphoid process may be coupled to the abdomen motion, and similarly the NCS sensor can be coupled to the accessory muscles. Cross-coupling between the two motions will reduce the paradoxical motion detectability. (2) Participants were unable to perform the isovolumetric exercise correctly during the intended period while following the breath-hold constraint. (3) The signal is lost due to sensor instability during the large chest circumference change resulting from the abdomen contraction. Overall, the algorithm was designed to be able to detect even slight paradoxical motion, resulting in the similar performance of both sensors as shown in Table 2. Both NCS and BIOPAC can detect 42 out of 58 instances, with fewer missed cases for BIOPAC (6) than for NCS (9). Supplementary Fig. 5a, b show two examples of poor detection for NCS and BIOPAC, respectively. While the algorithm performs well, as seen in these figures, it is more sensitive to baseline drift and other motion artifacts. Thus, sensor placement needs to be further investigated for robust paradoxical motion recognition.

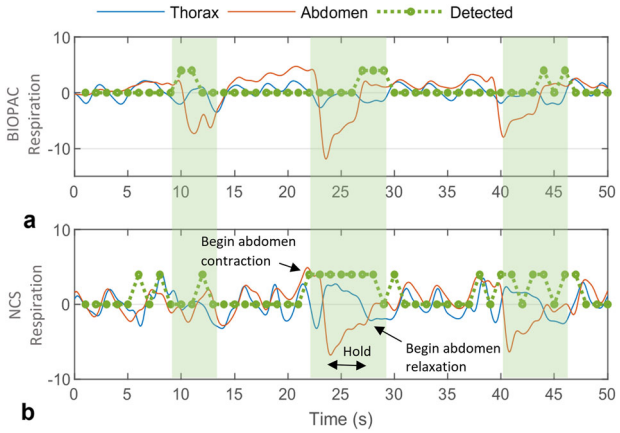

Fig. 4 An example of normalized thorax and abdomen respiration waveforms during the isovolumetric maneuver by one participant. a Normalized BIOPAC chest-belt waveforms and **b** Filtered NCS respiration waveforms. The intended paradoxical motion windows are marked by green-shaded areas and detected instances are shown by the positive value of dotted green lines. Timing of abdomen contraction, hold, and relaxation is denoted during the second cycle of the NCS waveform. Both BIOPAC and NCS can detect all three instances of paradoxical abdomen-thorax motion.

Motion interference with NCS

Our wearable NCS sensor setup has a high tolerance for ambient motion interference. As shown in Supplementary Fig. 6, there is no interference from a nearby walking person on the NCS data, due to the strong near-field coupling. Additional tests are performed with the motion of different body parts during breath-holds, as shown in Supplementary Figs. 7 and 8. There is no effect of hand motion on BIOPAC sensors, nor the NCS sensors unless it is very close to the antenna pair. ECG becomes noisy with the hand motion, likely due to electromyogram (EMG) interference. During arm motion, both BIOPAC thorax and abdomen belts show signal anomalies, while only the thorax NCS is affected. Additional studies are required to examine internal muscle motion interference resulting from near-field coupling, and separate the external arm motion coupling, as abdomen NCS still shows clear signal without any interference.

While external motion causes limited interference, large spurious torso motion results in motion artifacts. Respiratory measurements from BIOPAC chest belts can be interfered with belt displacement due to body movement, and an entire signal segment can be missed if the participant performs heavy or forced exhalation that leads to loss of tension. NCS waveforms are prone to motion artifact due to the current antenna pair packaging, which is loosely placed over the clothes with semi-isotropic radiation patterns. Free antenna movement relative to the body surface may result in signal artifacts, making NCS well-suited for static and quasi-static conditions, for example, when a person is typing, driving, or sleeping.

Table 3. Comparison with other noninvasive methods.

Paper	Sensor	Statistics			Experimental conditions
		Respiratory rate	Respiratory volume	Heart rate	
Massagram et al.[34]	Far-field doppler RF; 1 m LoS	–	Sitting: $r = 0.77$; $m = 39$ mL; $\sigma = 107$ mL Supine: $r = 0.72$; $m = 24$ mL; $\sigma = 129$ mL	–	• 8 healthy • spirometer
Nguyen et al.[32]	Directional far-field CW RF	–	Bed accuracy: 95.4% (error 58 mL)	–	• 6 healthy • spirometer
Adib et al.[33]	Far-field FMCW RF; 1–8 m LoS	Accuracy: 99.3% (error 0.09 BPM)	–	Accuracy: 98.5% (error 0.95 BPM)	• 14 healthy • chest-belt/ oximeter
Reyes et al.[27]	Smartphone camera	$r = 1.0$; RMSE = 0.4 BPM; $m = -0.02$ BPM; $\sigma = 0.42$ BPM	$r = 0.98$; RMSE = 182 mL; $\sigma = 185$ mL	–	• 15 healthy • spirometer
Brüllmann et al.[12]	RIP chest belts	–	Healthy: $m = 0$ mL; $\sigma = 55$ mL Patients: $m = 20$ mL; $\sigma = 100$ mL	–	• 5 healthy, 12 patients • flow meter
Chu et al.[13]	On-skin strain sensor	–	$r = 0.96$; $m = -77$ mL; $\sigma = 152$ mL	–	• 7 healthy • spirometer
NCS[37,40]	Wearable RF	$r = 0.93$; $m = 0.05$ BPM; $\sigma = 2.93$ BPM	$r = 0.84$; $m = 10$ mL; $\sigma = 109$ mL	$r = 0.95$; $m = -0.5$ BPM; $\sigma = 3.32$ BPM	• 20 healthy • PTM

A comparison of the proposed NCS method (across all positions and breathing styles) with existing technologies, focused on respiration. Gold-standard spirometer respiratory volume accuracy tolerance is ±3%[6]. Different performance metrics are used across papers, including percentage accuracy, root mean square error (RMSE), correlation coefficient (r), mean (m) and standard deviation (σ) of the differences of measured and reference data (*B&A* statistics). Experimental conditions show number of participants and the reference measurement device for each work. The last row shows the results of the presented work.
LoS line of sight, *FMCW* frequency modulated continuous wave, *RIP* respiratory inductance plethysmography.

As errors in either BIOPAC or NCS respiratory data will result in inconsistent RV and RR, which reduces the reported accuracy, data quality score is defined, where poor respiration data quality intervals are rejected. Similarly, poor heartbeat data is also discarded based on NCS data quality. Further quality estimation details are discussed in the "Data Processing" section.

DISCUSSION

Following the prescribed routines, the subjects performed breathing exercises with large RR variation, from breath-holds and slow deep-breathing around 6 BPM to panting around 40 BPM. Our sensor and algorithm can achieve high accuracy under these large variations, with no special clothing or environmental requirements, thus promoting the applicability in real-life conditions for continuous monitoring of healthy subjects. A brief comparison with other noninvasive techniques focused on respiration is presented in Table 3. Different statistics are reported, including percentage accuracy and root mean square error (RMSE), apart from the ones used in this paper, r, m, and σ. Our proposed NCS method provides a good estimation of both heart and respiratory motion characteristics with increased user comfort. The accuracy tolerance for a well-calibrated gold-standard spirometer is ±3%[6]. For example, a quiet breath of 0.4 L will be measured as 0.4 ± 0.012 L, and a deep breath of 2 L will be measured as 2.0 ± 0.060 L. Table 1a shows the σ for different breathing patterns, with low values in spontaneous normal breathing conditions, $\sigma_{Relax} = 0.065$ L, $\sigma_{Attention} = 0.097$ L, and $\sigma_{Normal} = 0.089$ L during the breathing protocol. While these values are higher than acceptable clinical values, they can be utilized for preliminary analysis where quantitative evaluation of respiratory efforts including both RR and RV along with HR is helpful, especially for geriatric patients with low cognitive function, where dyspnea information can only be currently determined from self-reporting or a caregiver's visual observation[44,45].

The limitations of the current setup include data distortion due to antenna motion relative to the body, sensor placement sensitivity and arduous calibration requirements. The former issue of antenna motion can be readily resolved by improved antenna packaging and garment integration of the antenna with conductive fibers[46]. While sensor placement requirements are less stringent for most routines, it becomes more important for accurate paradoxical abdomen-thorax motion monitoring, as NCS sensor coupling to diaphragm and lungs is observed to be position sensitive and needs to be carefully deployed. Our calibration protocol requires participants to breathe only through the mouth while wearing a facemask for a brief duration. This calibration is mainly to give an absolute scale in RV and can be omitted if the percentage volume change is sufficient.

Additionally, the NCS sensor with its small form-factor and simple transceiver architecture can be incorporated inconspicuously into the fabric with an improved wireless design and can be worn over multiple layers of clothing without requiring any direct skin contact. We have used frequency division for multiplexing two sensors, which can be easily extended to place more sensors at different locations on the body, as well as on multiple people simultaneously. The Tx signal can be further modulated with a unique pseudo-noise code known to the corresponding Rx. These design options in NCS provide higher signal isolation against ambient interferences and inter-sensor collision than implementations based on the direct far-field RF and optical sensors. The detailed respiratory and heartbeat characteristics also open other areas of applications, including cough monitoring, stress detection, and overall ambulatory healthcare monitoring.

METHODS

Hardware setup

The NCS sensor prototype is implemented by an Ettus universal software radio peripheral (USRP) B200mini[47] SDR, with monopole helical antennas

(Taoglas TG.19.0112), packaged in a three-dimensional-printed case, as shown in Fig. 1c. The relative antenna placement is designed to adjust the direct Tx-Rx coupling and enhance the sensitivity to the reflected signal from internal organs. Two SDR units are multiplexed by frequency, with the carrier frequencies of 1.82 and 1.90 GHz. This setup is a variation of the previous multiple-input multiple-output (MIMO) implementation[40] to improve sensor stability and participant comfort. The baseband tone is set at $f_{BB} = 51$ kHz, sampled at 2×10^6 samples per second (Sps), where the quadrature baseband signals $I(t)$ and $Q(t)$ are simple sinusoidal tones. The intended motion is modulated on the IQ amplitude (NCS_{amp}) and phase (NCS_{ph}), and can be extracted as,

$$NCS_{amp}(t) = \sqrt{I_{Rx}(t)^2 + Q_{Rx}(t)^2}, \quad (2)$$

$$NCS_{ph}(t) = \text{unwrap}\left(\tan^{-1}\left(\frac{Q_{Rx}(t)}{I_{Rx}(t)}\right) - 2\pi f_{BB} t + \theta_0\right), \quad (3)$$

where θ_0 is a constant phase offset including the initial phase and accumulation from the Tx-Rx path and cables. While both amplitude and phase contain the modulated motion, their coupling strength varies with the sensor placement, which provides further resistance to noises when both magnitude and phase are included for further analysis. Additional studies are needed to clearly understand the coupling tradeoffs. For this work, we opted to use the best reference-correlated signal during the calibration phase for both thorax and abdomen sensors. For respiration, chest-belt signals are taken as reference, and for heartbeat, bandpass filtered (0.9–1.8 Hz) ECG signal is taken as the reference. The final demodulated data is sent to the control computer by a universal serial bus. The Tx powers are −12.84 dBm and −10.42 dBm for the thorax and abdomen, respectively, as shown in Fig. 1d, significantly below the allowable OSHA radiation exposure limit[41].

Reference measurements are performed by BIOPAC sensors, including a 3-lead ECG SS2LB, two torso belts SS5LB and PTM SS11LB, placed as shown in Fig. 1a, b. The pre-calibrated PTM measures the airflow rate in L/s from the mouth using a facemask and is only placed on the subject for short calibration periods. For the remaining breathing exercises, reference respiration is only recorded by two belts placed at thorax and abdomen that measure the change in local tension. During the experiment, male participants wore the thorax belt at 2–3 cm below the armpits, while female participants wore the belt below the breasts, close to the xiphoid process and costal margin, considered as the dividing line between the rib cage and abdomen. This placement is selected for belt stability and user comfort. All sensors are connected to a 4-channel data acquisition unit BIOPAC MP36R[48].

Participants and protocol

The human study protocol was approved by the Cornell Institutional Review Board (IRB), and participants provided written informed consent to take part in the study. Twenty-five healthy participants with no known history of cardiopulmonary diseases were recruited and instructed to follow breathing routines to the best of their abilities, without over-exerting, in a sequence of three postures: supine, left lateral recumbent and sitting upright in a chair. The instructions were provided to the participants in real-time using LabVIEW in both audio and visual formats. The data collection was carried out in a standard laboratory room with drywalls and supporting metal frames, without any radiation-absorbent material. The environment consisted of standard furniture, including a bed, desks, and chairs, along with computers and various units of laboratory equipment. The participant attire was not controlled, and the NCS sensors were placed over their daily clothing, including shirts and loosely fitted hoodies made of different fabric materials. Five participants' data was rejected due to poor calibration data in any one of the three postures, which showed inconsistency due to either an inability to follow the mouth-only breath instruction or from the loose placement of the facemask that caused air leakage.

The 20 eligible participants included 14 females and 6 males with age from 18 to 34-year-old ($\mu = 22.9$, $\sigma = 3.3$), weight from 49.8 to 79.5 kg ($\mu = 62.2$, $\sigma = 9.3$) and height from 158 to 183 cm ($\mu = 167$, $\sigma = 6.8$). The body mass index (BMI) of the participants fell within the slightly underweight to slightly overweight range from 18.3 to 26.8 kg/m^2 ($\mu = 22.2$, $\sigma = 2.2$).

A fixed breathing protocol of ~6 min was executed in each posture after calibration, which included:

1. Normal breathing for 120 s.
2. Deep breathing for 60 s.
3. Fast breathing for 30 s.
4. Normal breathing for 30 s.
5. Breath-hold for maximum 20 s, followed by normal breathing for 20 s. Repeat once.

During normal or tidal breathing, no inhalation or exhalation instructions were provided, but the participants were asked not to take any deep breaths or long pauses. During deep breathing, real-time instructions were given to start inhaling and exhaling with fixed durations of 4 and 6 s, respectively, which gave a RR of 6 BPM. Similarly, instructions were given for fast breathing at a rate of 40 BPM, with equal time for inhalation and exhalation. These instructions were provided as a guideline, and participants were advised to perform normal breathing if they felt uncomfortable during any of the routines, resulting in some variations around the expected rates. The procedure was clearly explained to the participants, with short examples for practice, before recording the calibration and main routines.

For observing separate thorax and abdomen motion, the participants were asked to perform the isovolumetric exercise with the following steps during breath-hold: contract the abdomen inwards, maintain the position for 3 s, then relax abdomen back to normal. Three such maneuvers were performed, separated by normal breathing intervals of 10 s to simulate paradoxical abdomen-thorax motion as observed in OSA. As this motion is difficult to perform without extended practice, this exercise was only performed in the sitting posture, so that the participants could learn the motion, while looking at their real-time NCS waveforms.

With the participants continued to be seated in a chair, an additional series of exercises were performed to test the breathing patterns in the relaxation state and under the given attention-engaging task. The participants were asked to close their eyes and relax for 5 min. This relaxed period allowed free-breathing over time without any instructions, thus increasing the likelihood of non-voluntary tidal breathing. The next routine was designed using PsyToolkit[49,50] to render the participants under an attentive and cognitive task, where they watched and reacted to anomalous jumps of an on-screen rotating clock hand by pressing the space bar. Instantaneous feedback was given by flashing an on-screen indicator light of correct keypress, to ensure continuous attention. This routine was performed for 6.5 min and rendered non-voluntary breathing patterns under fast temporal variations due to induced stress. Both routines utilized the RV calibration from the previous sitting posture.

Data processing

The synchronization among NCS and BIOPAC sensors is achieved by system time stamps and improved by maximizing the correlation between respiration data from two measurement systems, resulting in synchronization on the order of hundreds of ms (<1 s). The data collected from both sensors is downsampled to 500 Sps before further analysis in MATLAB.

Peak detection. For peak detection, a moving average-crossing algorithm[51] is implemented, which is effective for signals with varying amplitude and frequency characteristics, such as the respiration signal here with the RR in the range of 0–45 BPM, without any manual tuning. A moving average is estimated at every point using a given window length, resulting in a moving average curve (MAC). This window length is selected to have approximately one respiratory cycle in each window and is constantly updated by taking Fourier transform over a fixed period to estimate the RR. The points where MAC crosses the original signal are labeled as intercepts and are classified as up or down intercepts for positive and negative slopes, respectively. Finally, a maximum is marked as the maximal point between two up-down intercepts and a minimum is also marked similarly. This algorithm is used in the estimation of all the three parameters: RV, RR and HR.

RV estimation. PTM measures the airflow rate, from which the beginning of each inhalation and exhalation points are identified by a simple zero-cross detection algorithm, based on the change of sign before and after the zero-crossing points, and the slope at these points. Integration is performed over each inhalation and exhalation cycle to get the instantaneous air volume, Vol_{PTM}, without aggregating a bias over time. Least-square fitting is performed for solving Eq. (1) by a trust-region algorithm with bounded constraints of $a,b > 0$. RV is estimated as the average volume exchanged in each respiratory cycle over a window of 15 s, with at least two peaks in the window to get a robust estimate.

Owing to sensor motion over time, mostly resulting from a posture change, the estimated RV may deviate from its original calibration. An additional

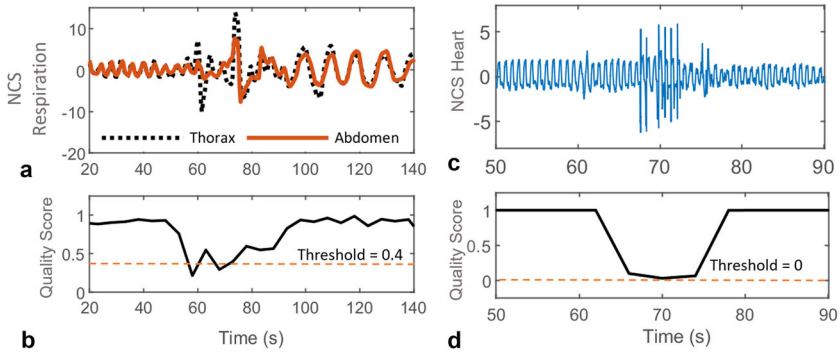

Fig. 5 The quality score for respiration and heartbeat waveforms with motion artifact instance between 60–80 s. A fixed, empirically selected threshold is used to reject poor data, given by a low quality score. **a** Normalized NCS thorax and abdomen respiration waveforms. **b** Respiration quality score in the range [0,1], showing poor quality with a score less than the threshold (0.4). **c** Normalized filtered NCS heartbeat waveform modulated on the thorax sensor, with most of the artifact filtered out. **d** Quality score normalized by tanh() in the range [−1, +1]. A low threshold of 0 is selected, as the second-harmonic method used for heart rate estimate provides even higher motion tolerance.

corrective step is performed if the estimated RV during normal breathing section of the breathing exercise routine $RV(Normal)_{Routine}$, deviates more than ±5% from the calibrated $RV(Normal)_{Calibration}$, derived from the first 15 s of calibration. The NCS and BIOPAC RV is multiplied with a corresponding scaling factor (SF) given as $RV(Normal)_{Calibration}/RV(Normal)_{Routine}$, assuming the normal breathing routine has nearly constant RV for the same person over time. To validate this correction, an additional RV calibration consistency study was conducted on one subject over three consecutive days in the sitting posture. The subject performed the calibration, immediately followed by the voluntary breathing exercise routine. Supplementary Table 3 shows the detailed results, with RV before scaling correction, and the required SF to improve the match when using day-1 calibration for all successive days. The $RV(Normal)_{Calibration}$ lies within a narrow range of 0.37–0.43 L, showing consistency in normal breathing volume for a healthy individual over time. Little scaling is required to correct RV when calibrated immediately before the routine, resulting in scaling factors close to 1 on day-1. Variations in sensor placement and coupling strength result in scaling factors other than 1 to correct the RV for the next two days. Supplementary Fig. 9a, b show instantaneous volume and RV estimated on day-2 using day-1 calibration, with NCS underestimating and BIOPAC overestimating the expected $RV(Normal)_{Calibration} = 0.37$ L, derived from day-1. The corrected scaled RV in Supplementary Fig. 9c shows improved agreement of NCS and BIOPAC to each other, as well as to the calibration value. As SF assumes accurate $RV(Normal)_{Calibration}$, some error may be introduced from inconsistencies in the calibration and correction process, including variation due to small calibration duration, difference in resistance when breathing through the mouth, and change in RV(Normal) over time. The correction assumes knowledge of normal breathing period, that can be potentially identified based on the normal RR and HR range of an individual.

We have also studied the influence of different simulated airway resistances on RV by introducing two resistances: (1) KN95 mask covering face and mouth while breathing normally through the nose, and (2) straw with a 4 mm inner diameter while only breathing through the mouth. The extracted instantaneous volume, RV and RR from chest belts and NCS are shown in Supplementary Fig. 10. RV calibration was performed before the entire routine. While breathing through mask does not show any noticeable change in RV and RR estimates, breathing through straw shows decreased RV towards the beginning with constant RR, followed by an increase in RV with decreased RR. This opposite RV and RR behavior indicate the increased respiratory effort required due to the resistance offered by the narrow straw. The consistency of RV between the NCS and BIOPAC suggests that the respective calibration remains reasonable within the tested range of varying simulated airway resistance.

RR estimation. The NCS signal is bandpass filtered with the cut-off frequencies of 0.05 and 0.8 Hz to derive the respiration waveforms from both the sensors. As the diaphragm and resulting abdomen motion is usually larger, the respiration waveform from the abdomen NCS sensor alone is used to estimate RR. This sensor also has a weaker heartbeat coupling, and thus filtering requirements are less stringent during fast breathing and breath-hold. Similarly, the BIOPAC abdomen belt is also used to estimate RR with the same algorithm. RR is calculated as the number of detected breath cycles over the maximum window of the past 15 s. For each window, the number of cycles is calculated as the number of inhalation peaks minus 1, and the total time is the interval between first and last inhalation peaks. If no complete cycle is detected during the entire window, the RR is marked as 0. Figure 2f shows calculated RR from NCS and BIOPAC during a normal breathing section, between 12–17 BPM. Supplementary Fig. 2d shows estimated RR over varying normal, deep and fast breathing and breath-holds, in the range of 0–45 BPM.

HR estimation. The heartbeat waveform is modulated strongly on the thorax sensor and can be separated from the respiration by proper filtering. However, during the fast breathing exercise, the RR can be around 40 BPM, close to the HR, resulting in filtering ambiguity. Therefore, we have used the second harmonic of the heartbeat waveform (Supplementary Fig. 1) to estimate the peak-to-peak heartbeat interval with reduced interferences from respiration and motion. The Fourier transform is used to first estimate the approximate HR, which guides the filtering to retrieve the second harmonic with a bandwidth of 0.8 Hz. The same peak detection method is then used to find peaks of the second-harmonic waveform. Instantaneous HR is estimated as an inverse of each heartbeat interval, taken as the sum of two neighboring peak-to-peak periods, as shown in Supplementary Fig. 1. This HR is averaged over a window of 10 s to suppress any outliers. The reference HR is estimated from the ECG waveform with bandpass filtering between 0.4 and 20 Hz, which removes any baseline drift and suppresses the low-frequency P and T waves. The sharp QRS complex peak is then detected with a simple slope-based peak detection algorithm. Figure 2g shows the average HR by both the sensors. Supplementary Fig. 2b shows the strong heartbeat modulated on the thorax NCS sensor while performing different breathing exercises, especially visible in the breath-hold periods, with the corresponding HR from both sensors in Supplementary Fig. 2e.

Breath-hold detection. This is based on estimating the time interval between two peaks at the end of inspiration, which consists of one exhalation and one inhalation duration. True detection is marked if a breath-hold period is larger than a fixed duration in the annotated breath-hold period, otherwise a missed detection is marked. To simulate CSA characterized by repeated interruptions in breathing during sleep[42], we used our breath-hold data collected in supine and lateral recumbent postures, with participants performing two consecutive breath-holds in each posture, separated by normal breathing periods. For consistency, the same algorithm is used to estimate the numbers of pauses from both BIOPAC abdomen belt and NCS.

Paradoxical abdomen-thorax motion detection. Isovolumetric exercises lead to opposite slopes of thorax and abdomen respiration waveforms during abdomen contraction and relaxation periods, denoted by a negative product of instantaneous slopes, which are scaled to [−1, 1] using a tanh() function before estimating the product, then moving-averaged over a window of 1 s and thresholded (<0) to give the detected instances. The ground-truth window is manually labeled, and a true detection is marked if it overlaps with the detected periods, otherwise, a missed detection is marked. As the slope sign is independent of waveform scaling, this detection does not require PTM calibration.

Data quality estimation. Different approaches are followed for respiration and heartbeat data quality estimation.

(1) Respiration data quality: As thorax and abdomen sensors are independently placed, motion artifacts may be present differently, leading to a poor correlation between the two measurements. Also, data from NCS and BIOPAC chest belts can show dissimilar artifacts, with both or only either one of them showing the artifact. Thus, correlations between thorax and abdomen chest belts, and NCS and chest belts for both thorax and abdomen are calculated with an epoch duration of 5 s. Final data quality is taken as an absolute of the product of all these correlations, with higher values indicating better quality, as shown in Fig. 5a, b. A fixed threshold is empirically selected, below which the RR and RV estimates are discarded.

(2) Heartbeat data quality: As the NCS heartbeat waveform is only extracted from the thorax sensor, a different artifact detection algorithm is used, similar to that presented in our previous work[52]. An outlier detection algorithm based on one-class support vector machine (OCSVM)[53] is implemented to detect artifacts in the filtered heartbeat waveform. To speed up signal processing, the motion detection algorithm is implemented on a window of 4 s. The algorithm is trained on the entire routine and a window is marked as an outlier if the tanh() normalized score is <0. Figure 5c, d show the filtered heartbeat waveform from the NCS thorax sensor and the corresponding score, respectively. For ECG waveforms, QRS complex peaks are less sensitive to noise, and thus no separate artifact detection is implemented. HR estimation is discarded if the window contained any poor-quality period.

Reporting summary

Further information on research design is available in the Nature Research Reporting Summary linked to this article.

DATA AVAILABILITY

The collected and analyzed data sets during the current study are available from the corresponding author upon request.

CODE AVAILABILITY

The LabVIEW code for data collection is available at https://github.com/EdwinKanLab/Respiration_Heart_Study_2019, and MATLAB codes for data processing are available from the corresponding author upon request.

Received: 28 February 2020; Accepted: 26 June 2020;

REFERENCES

1. Matheson, E. M., King, D. E. & Everett, C. J. Healthy lifestyle habits and mortality in overweight and obese individuals. *J. Am. Board Fam. Med.* **25**, 9–15 (2012).
2. Sanchis-Gomar, F. et al. Physical inactivity and low fitness deserve more attention to alter cancer risk and prognosis. *Cancer Prev. Res.* **8**, 105–110 (2015).
3. Detering, K. M., Hancock, A. D., Reade, M. C. & Silvester, W. The impact of advance care planning on end of life care in elderly patients: randomised controlled trial. *BMJ* **340**, c1345 (2010).
4. Mitchell, G. Rapidly increasing end-of-life care needs: a timely warning. *BMC Med.* **15**, 126 (2017).
5. Rubio, N. et al. Home monitoring of breathing rate in people with chronic obstructive pulmonary disease: observational study of feasibility, acceptability, and change after exacerbation. *Int. J. Chron. Obstruct. Pulmon. Dis.* **12**, 1221–1231 (2017).
6. Graham, B. L. et al. Standardization of spirometry 2019 update an official American Thoracic Society and European Respiratory Society technical statement. *Am. J. Respir. Crit. Care Med.* **200**, 70–88 (2019).
7. DePaso, W. J., Winterbauer, R. H., Lusk, J. A., Dreis, D. P. & Springmeyer, S. C. Chronic dyspnea unexplained by history, physical examination, chest roentgenogram, and spirometry: analysis of a seven-year experience. *Chest* **100**, 1293–1299 (1991).
8. Wanger, J. et al. Standardisation of the measurement of lung volumes. *Eur. Respir. J.* **26**, 511–522 (2005).
9. Farré, R., Montserrat, J. M. & Navajas, D. Noninvasive monitoring of respiratory mechanics during sleep. *Eur. Respir. J.* **24**, 1052–1060 (2004).
10. Massaroni, C. et al. Contact-based methods for measuring respiratory rate. *Sensors* **19**, 908 (2019).
11. Rofail, L. M., Wong, K. K. H., Unger, G., Marks, G. B. & Grunstein, R. R. Comparison between a single-channel nasal airflow device and oximetry for the diagnosis of obstructive sleep apnea. *Sleep* **33**, 1106–1114 (2010).
12. Brüllmann, G., Thurnheer, R. & Bloch, E. Respiratory monitoring by inductive plethysmography in unrestrained subjects using position sensor-adjusted calibration. *Respiration* **79**, 112–120 (2010).
13. Chu, M. et al. Respiration rate and volume measurements using wearable strain sensors. *NPJ Digit. Med.* **2**, 8 (2019).
14. Tremper, K. K. Pulse oximetry. *Chest* **95**, 713–715 (1989).
15. Biswas, D., Simoes-Capela, N., Van Hoof, C. & Van Helleputte, N. Heart rate estimation from wrist-worn photoplethysmography: a review. *IEEE Sens. J.* **19**, 6560–6570 (2019).
16. Zheng, Y. et al. Unobtrusive sensing and wearable devices for health informatics. *IEEE Trans. Biomed. Eng.* **61**, 1538–1554 (2014).
17. Inan, O. T. et al. Ballistocardiography and seismocardiography: a review of recent advances. *IEEE J. Biomed. Heal. Inform.* **19**, 1414–1427 (2015).
18. Taebi, A., Solar, B., Bomar, A., Sandler, R. & Mansy, H. Recent advances in seismocardiography. *Vibration* **2**, 64–86 (2019).
19. Xia, Z., Member, S., Shandhi, M. H. & Member, S. Non-contact sensing of seismocardiogram. *IEEE Sens. J.* **18**, 5956–5964 (2018).
20. Pinheiro, E., Postolache, O. & Girão, P. Theory and developments in an unobtrusive cardiovascular system representation: Ballistocardiography. *Open Biomed. Eng. J.* **4**, 201–216 (2010).
21. Kim, C. S. et al. Ballistocardiogram: Mechanism and potential for unobtrusive cardiovascular health monitoring. *Sci. Rep.* **6**, 1–6 (2016).
22. Sadek, I., Seet, E., Biswas, J., Abdulrazak, B. & Mokhtari, M. Nonintrusive vital signs monitoring for sleep apnea patients: a preliminary study. *IEEE Access* **6**, 2506–2514 (2018).
23. Pinheiro, E., Postolache, O. & Girão, P. Study on ballistocardiogram acquisition in a moving wheelchair with embedded sensors. *Metrol. Meas. Syst.* **19**, 739–750 (2012).
24. *Hexoskin Smart Shirts-cardiac, Respiratory, Sleep & Activity Metrics*, https://www.hexoskin.com/ (2020).
25. Bansal, C., Scott, R., Stewart, D. & Cockerell, C. J. Decubitus ulcers: a review of the literature. *Int. J. Dermatol.* **44**, 805–810 (2005).
26. Zeevi, T., Levy, A., Brauner, N. & Gefen, A. Effects of ambient conditions on the risk of pressure injuries in bedridden patients—multi-physics modelling of microclimate. *Int. Wound J.* **15**, 402–416 (2018).
27. Reyes, B. A. et al. Tidal volume and instantaneous respiration rate estimation using a volumetric surrogate signal acquired via a smartphone camera. *IEEE J. Biomed. Heal. Inform.* **21**, 764–777 (2017).
28. Li, C., Lubecke, V. M., Boric-Lubecke, O. & Lin, J. A review on recent advances in Doppler radar sensors for noncontact healthcare monitoring. *IEEE Trans. Microw. Theory Tech.* **61**, 2046–2060 (2013).
29. Naishadham, K. et al. Estimation of cardiopulmonary parameters from ultra wideband radar measurements using the state space method. *IEEE Trans. Biomed. Circuits Syst.* **10**, 1037–1046 (2016).
30. Droitcour, A. D., Boric-Lubecke, O. & Kovacs, G. T. A. Signal-to-Noise ratio in Doppler radar system for heart and respiratory rate measurements. *IEEE Trans. Microw. Theory Tech.* **57**, 2498–2507 (2009).
31. Zito, D. et al. SoC CMOS UWB pulse radar sensor for contactless respiratory rate monitoring. *IEEE Trans. Biomed. Circuits Syst.* **5**, 503–510 (2011).
32. Nguyen, P., Zhang, X., Halbower, A. & Vu, T. Continuous and fine-grained breathing volume monitoring from afar using wireless signals. In *IEEE INFOCOM 2016 - The 35th Annual IEEE International Conference on Computer Communications*, pp. 1–9 (IEEE, San Francisco, CA, 2016). https://doi.org/10.1109/INFOCOM.2016.7524402.
33. Adib, F., Mao, H., Kabelac, Z., Katabi, D. & Miller, R. C. Smart homes that monitor breathing and heart rate. *In Proceedings of the 33rd Annual ACM Conference on Human Factors in Computing Systems (CHI '15)*, pp 837–846 (Association for Computing Machinery, New York, NY, USA, 2015). https://doi.org/10.1145/2702123.2702200.
34. Massagram, W., Hafner, N., Lubecke, V. & Boric-Lubecke, O. Tidal volume measurement through non-contact Doppler radar with DC reconstruction. *IEEE Sens. J.* **13**, 3397–3404 (2013).
35. Pfanner, F., Allmendinger, T., Flohr, T. & Kachelrieß, M. Modelling and simulation of a respiratory motion monitor using a continuous wave Doppler radar in near field. *Proc. SPIE Med. Imag.* **8668**, 1–12 (2013).
36. Teichmann, D., Kuhn, A., Leonhardt, S. & Walter, M. The main shirt: a textile-integrated magnetic induction sensor array. *Sensors* **14**, 1039–1056 (2014).
37. Hui, X. & Kan, E. C. Monitoring vital signs over multiplexed radio by near-field coherent sensing. *Nat. Electron.* **1**, 74–78 (2018).
38. Hui, X., Sharma, P. & Kan, E. C. Microwave stethoscope for heart sound by near-field coherent sensing. In *EEE MTT-S International Microwave Symposium (IMS)*, pp. 365–368 (IEEE, Boston, MA, USA, 2019). https://doi.org/10.1109/MWSYM.2019.8700904.

39. Li, C., Cummings, J., Lam, J., Graves, E. & Wu, W. Radar remote monitoring of vital signs. *IEEE Microw. Mag.* **10**, 47–56 (2009).
40. Sharma, P., Hui, X. & Kan, E. C. A wearable RF sensor for monitoring respiratory patterns. In *41st Annual International Conference of the IEEE Engineering in Medicine and Biology Society (EMBC)*, pp. 1217–1223 (IEEE, Berlin, Germany, 2019). https://doi.org/10.1109/EMBC.2019.8857870.
41. Occupational Safety and Health Administration, United States Department of Labor. *OSHA safety and health topics: Radiofrequency and microwave radiation standards*, https://www.osha.gov/SLTC/radiofrequencyradiation/standards.html (2020).
42. Muza, R. T. Central sleep apnoea-a clinical review. *J. Thorac. Dis.* **7**, 930–937 (2015).
43. Konno, K. & Mead, J. Measurement of the separate volume changes of rib cage and abdomen during breathing. *J. Appl. Physiol.* **22**, 407–422 (1967).
44. Ambrosino, N. & Scano, G. Dyspnoea and its measurement. *Rev. Lit. Arts Am.* **1**, 100–107 (2004).
45. Campbell, M. L., Templin, T. & Walch, J. A respiratory distress observation scale for patients unable to self-report dyspnea. *J. Palliat. Med.* **13**, 285–290 (2010).
46. Gordon, P. H., Chen, R., Park, H. & Kan, E. C. Embroidered antenna characterization for passive UHF RFID tags. In *IEEE RFID Conf.*, https://arxiv.org/abs/1710.02237 (2016).
47. USRP B200mini. https://www.ettus.com/all-products/usrp-b200mini-board/ (2020).
48. *Data acquisition and analysis system with AcqKnowledge for MP36R* (BIOPAC Systems, Inc., 2020). https://www.biopac.com/product/mp36r-systems/.
49. Stoet, G. PsyToolkit: a software package for programming psychological experiments using Linux. *Behav. Res. Methods* **42**, 1096–1104 (2010).
50. Stoet, G. PsyToolkit: a novel web-based method for running online questionnaires and reaction-time experiments. *Teach. Psychol.* **44**, 24–31 (2017).
51. Lu, W. et al. A semi-automatic method for peak and valley detection in free-breathing respiratory waveforms. *Med. Phys.* **33**, 3634–3636 (2006).
52. Sharma, P. & Kan, E. C. Sleep scoring with a UHF RFID tag by near field coherent sensing. In *IEEE/MTT-S International Microwave Symposium - IMS*, pp. 1419–1422 (IEEE, Philadelphia, PA, 2018). https://doi.org/10.1109/MWSYM.2018.8439216.
53. Scholkopf, B., Williamson, R., Smola, A., Shawe-Taylor, J. & Platt, J. Support vector method for novelty detection. In *Proceedings of the 12th International Conference on Neural Information Processing Systems (NIPS'99)*. pp. 582–588 (MIT Press, Cambridge, MA, USA, 1999).

ACKNOWLEDGEMENTS

We wish to thank Dr. Ana Krieger of Weill Cornell Center for Sleep Medicine for consultation on respiratory characteristics in apnea and many other helpful suggestions. This project is supported by Department of Energy (DoE) of the United States under the Advanced Research Projects Agency—Energy (ARPA-E) DE-AR0000946, and by Department of Defense (DoD) of United States through Office of the Congressionally Directed Medical Research Programs (CDMRP) Discovery Award PR-182496.

AUTHOR CONTRIBUTIONS

P.S. executed the study design, data collection, analysis and interpretation, and paper preparation. X.H. and J.Z. contributed to the NCS sensor design and revision. T.B.C. was involved with data analyses. E.C.K. supervised the study design and interpretation, as well as overall project management. All authors read and approved the paper.

COMPETING INTERESTS

The authors declare no competing interests.

ADDITIONAL INFORMATION

Supplementary information is available for this paper at https://doi.org/10.1038/s41746-020-0307-6.

Correspondence and requests for materials should be addressed to P.S.

Reprints and permission information is available at http://www.nature.com/reprints

Publisher's note Springer Nature remains neutral with regard to jurisdictional claims in published maps and institutional affiliations.

Open Access This article is licensed under a Creative Commons Attribution 4.0 International License, which permits use, sharing, adaptation, distribution and reproduction in any medium or format, as long as you give appropriate credit to the original author(s) and the source, provide a link to the Creative Commons license, and indicate if changes were made. The images or other third party material in this article are included in the article's Creative Commons license, unless indicated otherwise in a credit line to the material. If material is not included in the article's Creative Commons license and your intended use is not permitted by statutory regulation or exceeds the permitted use, you will need to obtain permission directly from the copyright holder. To view a copy of this license, visit http://creativecommons.org/licenses/by/4.0/.

© The Author(s) 2020

Supplementary Information

Wearable Radio-Frequency Sensing of Respiratory Rate, Respiratory Volume, and Heart Rate

Pragya Sharma[1]*, Xiaonan Hui[1], Jianlin Zhou[1], Thomas B. Conroy[1] and Edwin C. Kan[1]

[1] School of Electrical and Computer Engineering, Cornell University, Ithaca, NY, USA
*e-mail: ps847@cornell.edu

Contents:

Supplementary Fig. 1. NCS heartbeat waveform and HR extraction 3

Supplementary Fig. 2. Examples of a 5-minute breathing protocol for one participant 4

Supplementary Fig. 3. Comparison of NCS and BIOPAC data 5

Supplementary Fig. 4. Breath-hold detection for two participants on instances of good and poor cases 6

Supplementary Fig. 5. Two representative cases for paradoxical abdomen-thorax motion detection 6

Supplementary Fig. 6. The effect of ambient motion on BIOPAC and NCS signals 7

Supplementary Fig. 7. The effect of hand motion on BIOPAC and NCS signals 7

Supplementary Fig. 8. The effect of arm motion on BIOPAC and NCS signals 8

Supplementary Fig. 9. Results of calibration consistency test 8

Supplementary Fig. 10. Studying the effect of simulated airway resistance variation 9

Supplementary Table 1. Correlation and B&A statistics for each participant 10

Supplementary Table 2. Average RV, RR and HR over 3 postures: supine, left lateral recumbent and sitting 10

Supplementary Table 3. RV calibration consistency test over 3 consecutive days 10

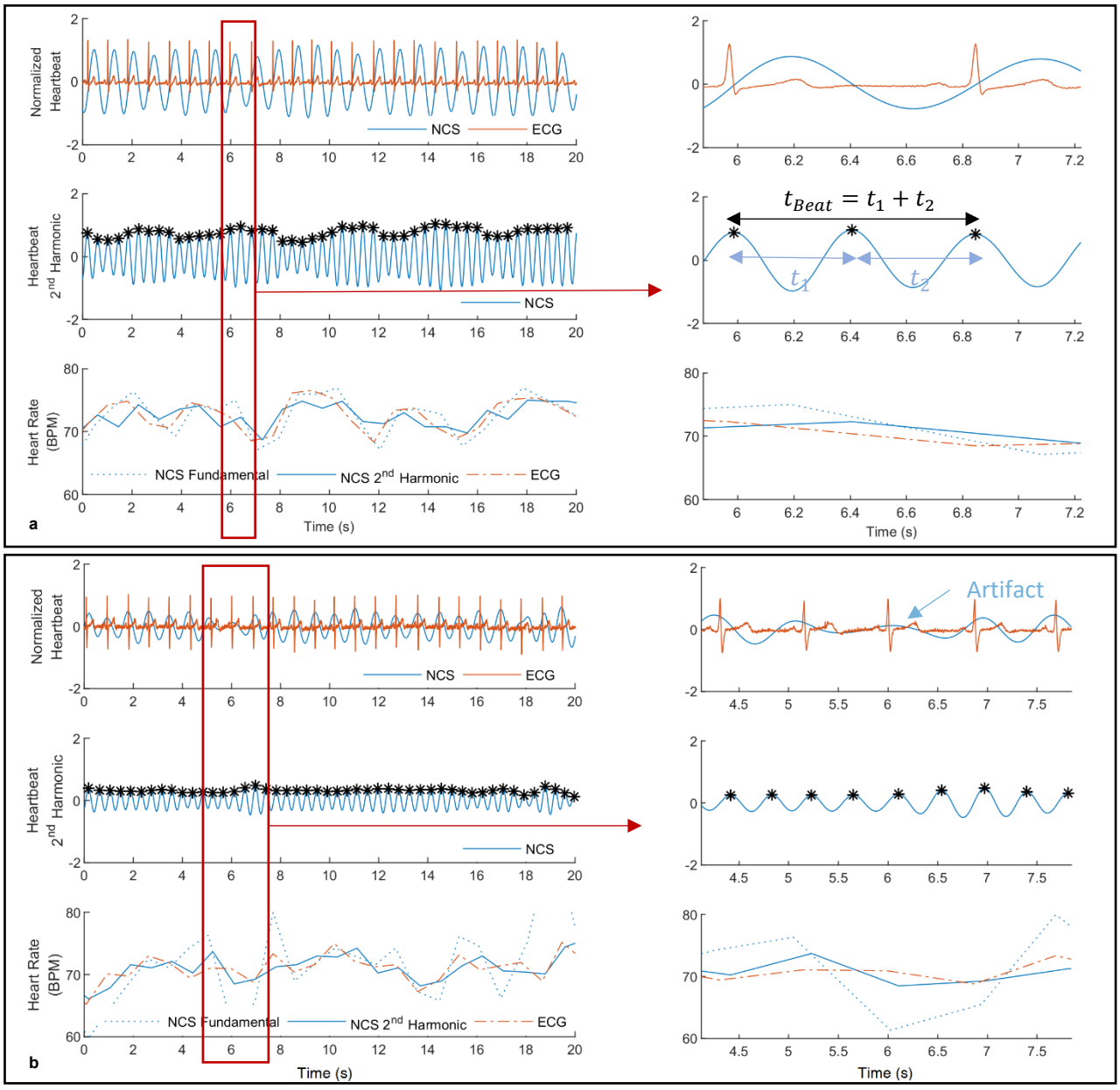

Supplementary Fig. 1. NCS heartbeat waveform and HR extraction. *Left:* Band-pass filtered NCS heartbeat waveforms and heart rate extraction from 2nd harmonic, showing instances without motion artifact (**a**) and with motion artifact (**b**). **a** Top figure shows ECG and filtered NCS heartbeat waveform from the thorax sensor. The middle figure shows 2nd harmonic of the NCS heartbeat waveform with detected peaks. The bottom figure shows the instantaneous heart rate, which is the inverse of each beat-to-beat interval, t_{Beat}, from fundamental NCS (dotted blue), harmonic NCS (solid blue) and ECG (dash-dotted orange). **b** The same heart rate extraction plots for another participant, showing periods of motion artifact at $t = 6$ s and 18 s, where the fundamental NCS heartbeat would have resulted in wrong heart rate estimation, but the 2nd harmonic is less affected. *Right:* Zoomed-in version of the left figures, showing t_{Beat} calculation from NCS 2nd harmonic as the sum of adjacent beat-to-beat intervals.

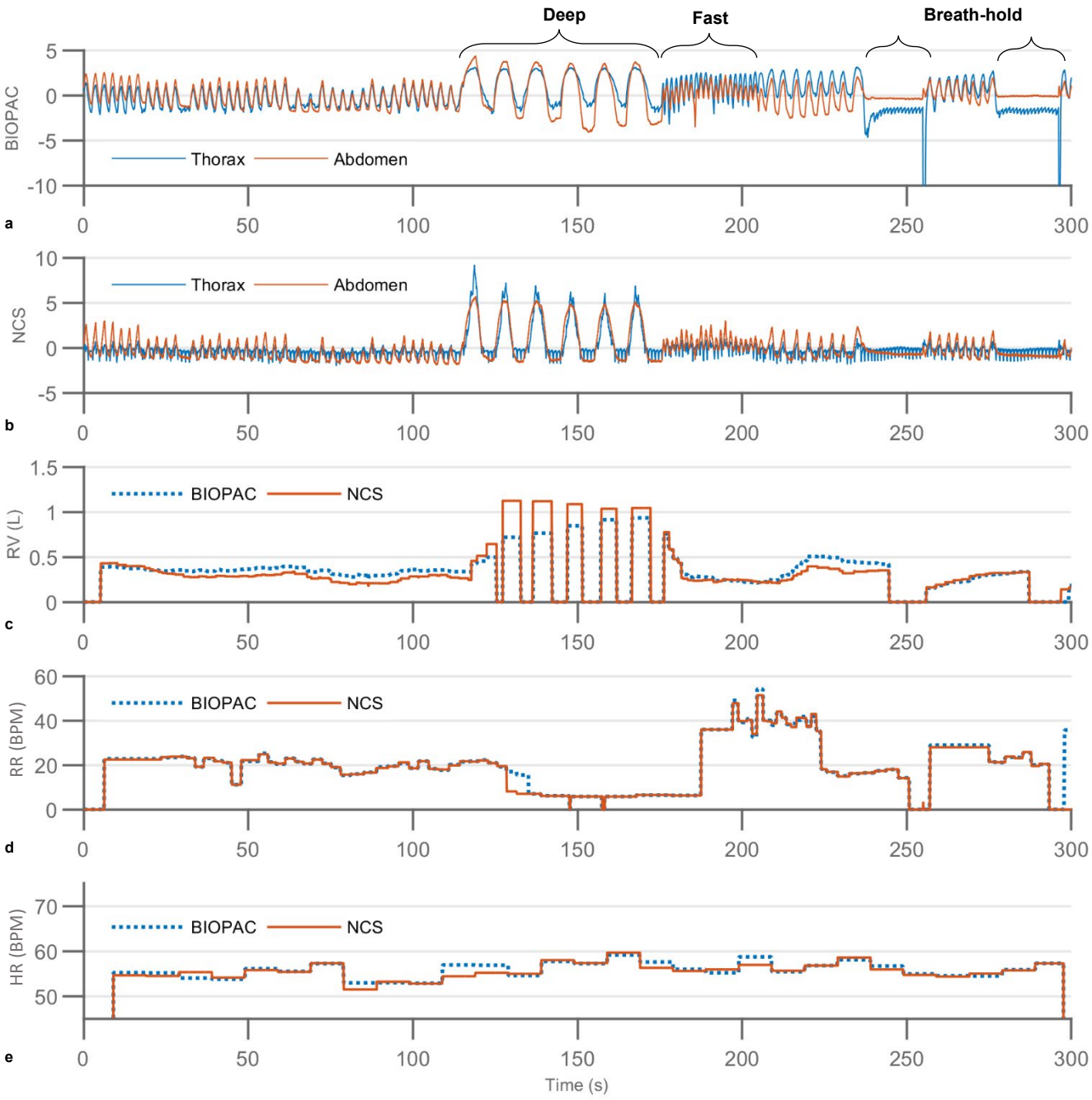

Supplementary Fig. 2. Examples of a 5-minute breathing protocol for one participant. The subject is in the supine posture while performing normal, deep, fast breathing and breath-hold. **a** Normalized BIOPAC chest-belt data at thorax and abdomen. During breath hold the thorax belt also shows a weak heartbeat motion. Different breathing periods are indicated here, with normal breathing in the unmarked sections. **b** Normalized NCS respiration data from thorax and abdomen sensors, as well as strong heartbeat on the thorax waveform. **c** RV during different breathing styles, based on the average volume exchanged in each inhalation and exhalation cycle over the past window containing at least two peaks, thus resulting in 0 estimates when the number of peaks is less than two (slow breathing). **d** RR estimation from NCS and BIOPAC clearly showing different breathing periods, with the normal RR around 20 BPM. **e** HR estimation from both sensors showing average resting HR in the range of 55 — 60 BPM.

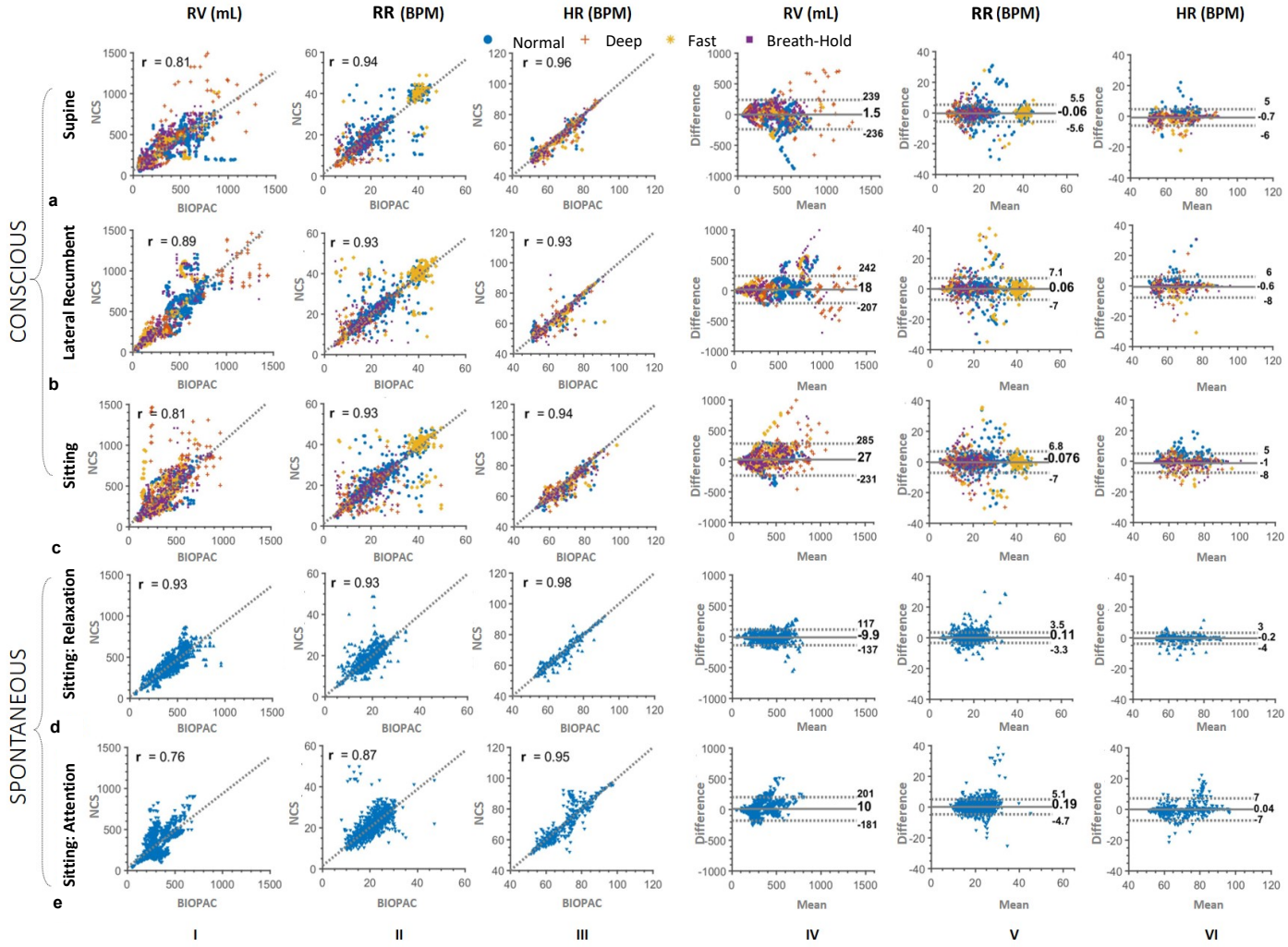

Supplementary Fig. 3. Comparison of NCS and BIOPAC data. Scatter (I – III) and $B\&A$ plots (IV – VI) between NCS and BIOPAC showing correlation coefficients (r), bias (m) and limits of agreement (LoA: $m \pm 1.96 \cdot \sigma$) for the RV, RR and HR across all routines. **a – c** The results across supine, lateral recumbent and sitting postures while following the breathing protocol of normal, deep, fast breathing and intermittent breath-hold. Different breathing protocol periods are indicated with a specific marker. **d, e** The spontaneous breathing protocol results in the relaxation and attention states with the participant sitting upright.

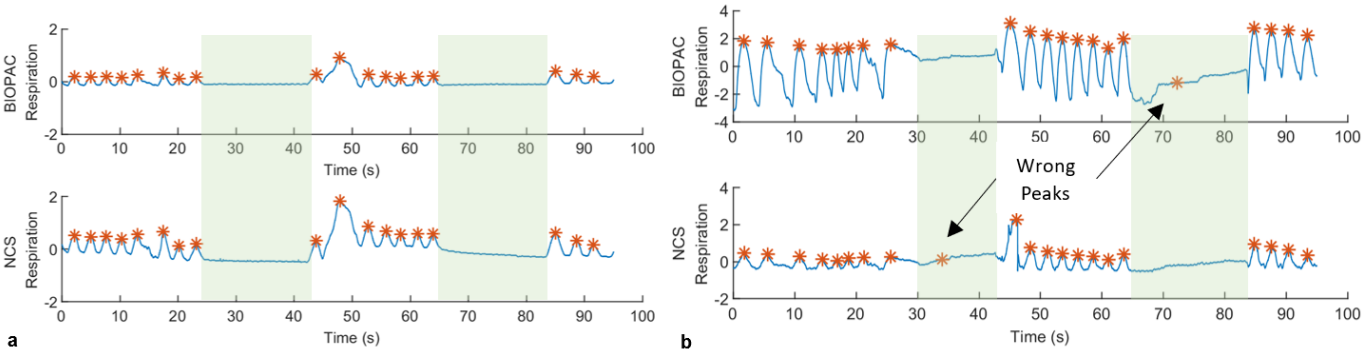

Supplementary Fig. 4. Breath-hold detection for two participants on instances of good and poor cases. Green shaded sections show manually annotated simulated apnea durations. The top and bottom figures show normalized BIOPAC and NCS abdomen respiration waveforms with detected peaks. The participant can perform the breath hold without any motion in **a**, leading to accurate detection. In **b**, wrong peaks are detected in both NCS and BIOPAC waveforms as shown, due to artifacts and peak detection limitations, as the participant is not able to maintain the breath hold without any motion. The motion coupling is different for the two sensors, as seen around $t = 68$ s, where BIOPAC shows some abdomen motion leading to wrong peak detection, but not NCS.

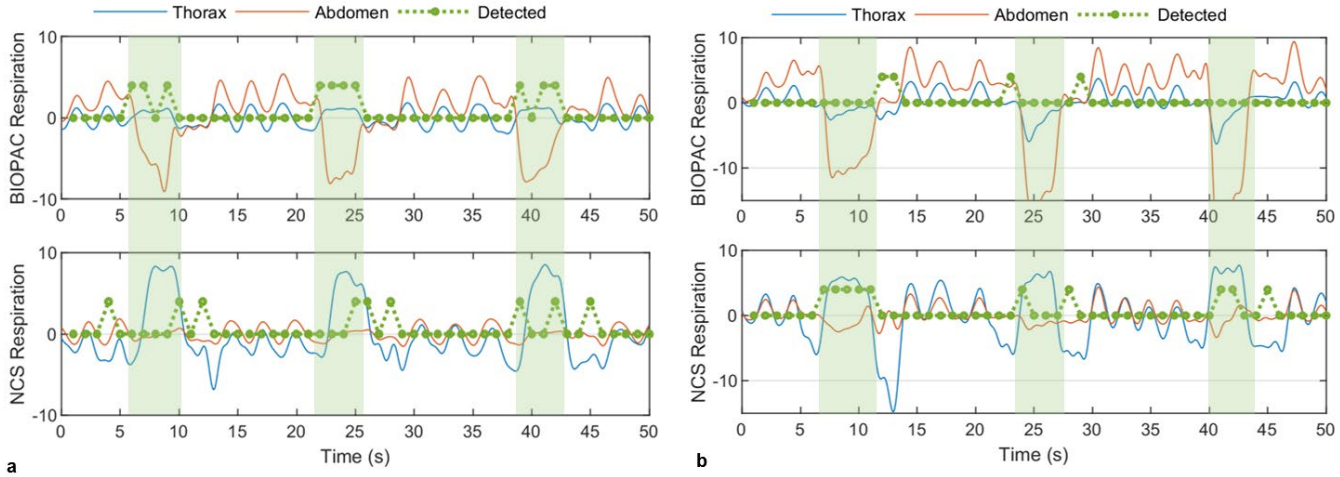

Supplementary Fig. 5. Two representative cases for paradoxical abdomen-thorax motion detection. Normalized respiratory waveforms from BIOPAC chest belts and filtered NCS are plotted in top and bottom figures, respectively. Intended instances are manually annotated by the green shaded areas. The detected periods are shown by the dotted green lines. True detection is marked if the annotated window overlaps with the observed instances. **a** The BIOPAC waveforms show clear paradoxical motion visually, as well as by the algorithm. NCS thorax and abdomen sensors do not show a complete paradoxical motion visually, but there are periods of opposite slope leading to detection of the second and third instances. Better abdomen sensor placement is required. **b** NCS waveforms show clear paradoxical motion visually, as well as by the algorithm. BIOPAC thorax belt do not show clear paradoxical motion in all three instances and requires better placement.

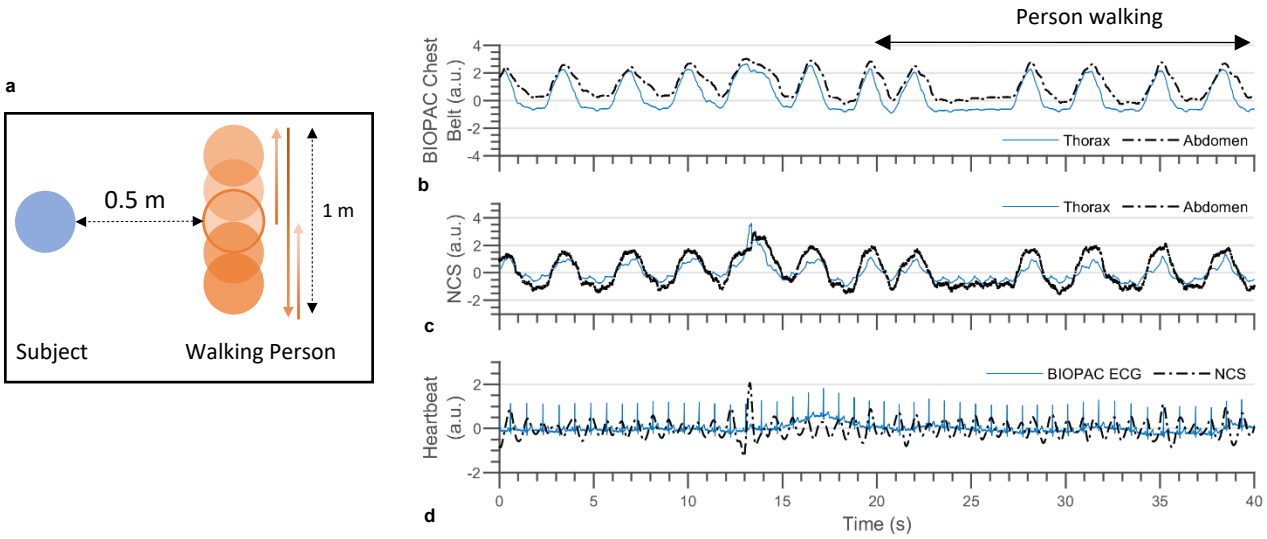

Supplementary Fig. 6. The effect of ambient motion on BIOPAC and NCS signals. Subject is seated at rest with a person standing nearby at a distance of 0.5 m. At $\boldsymbol{t = 20\ s}$, the person starts walking forward and backward at a speed of 0.73 m/s as shown in **a**. **b** Normalized BIOPAC chest belt waveforms showing clear respiratory signal with no motion interference. **c** Normalized NCS waveforms showing both respiration and clear heartbeat without any motion interference. **d** Clear heartbeat signal is observed from both ECG and NCS without any interference.

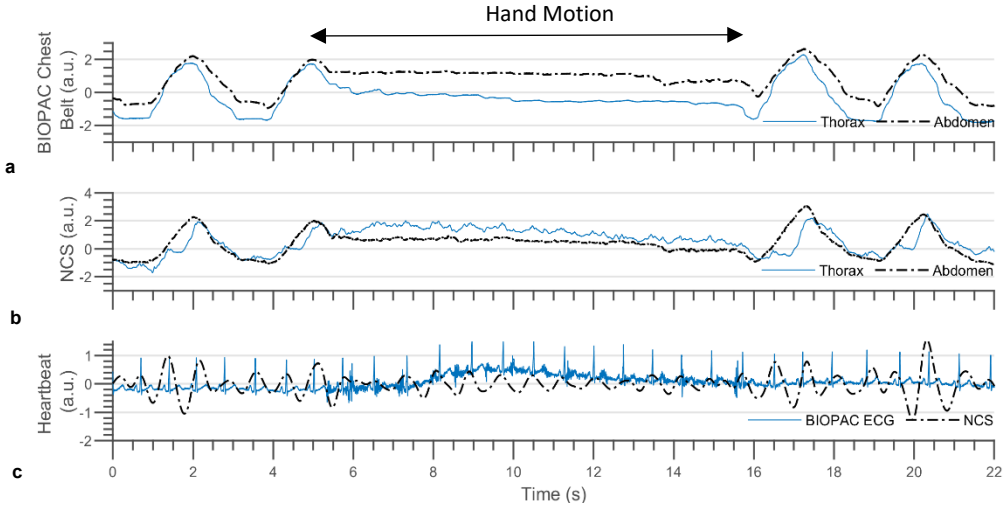

Supplementary Fig. 7. The effect of hand motion on BIOPAC and NCS signals. The subject is seated at rest with hands resting on thighs, performing normal breathing for the first 5 s. For the next 10 s, repeated instances of fist opening and closing are performed with the right hand, while holding breath. **a** Normalized BIOPAC chest-belt waveforms showing clear respiratory signals with no motion artifact. **b** Normalized NCS waveforms showing respiratory motion, with minimal motion artifact. **c** Heartbeat motion can be correctly extracted from NCS after further processing. Some interference is observed in the ECG waveform during the hand motion, but the R peaks can still be clearly seen.

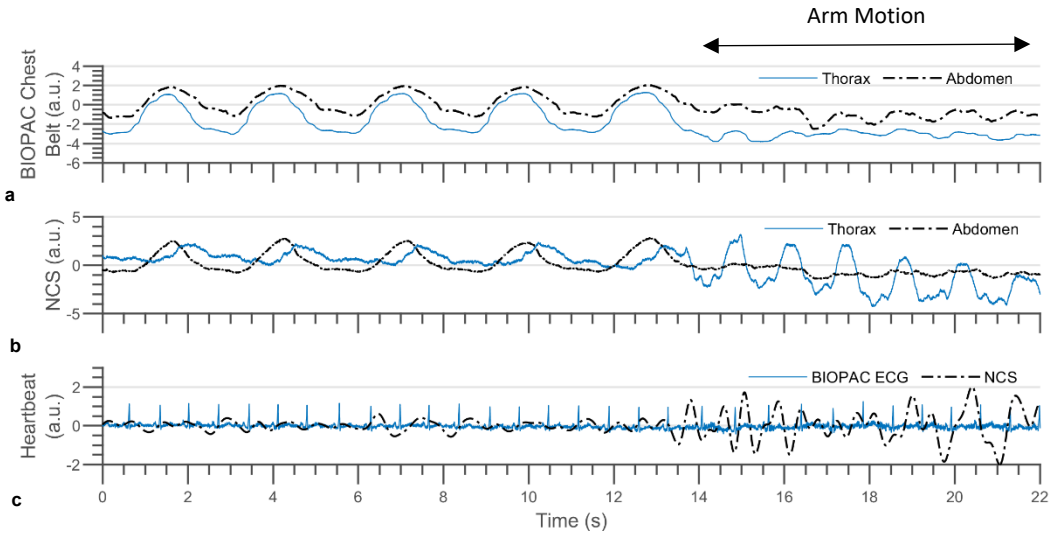

Supplementary Fig. 8. The effect of arm motion on BIOPAC and NCS signals. The subject is seated at rest with horizontal forearms in front of the body and upper arms in the vertical position. Forward arm swinging motion is performed starting at $\boldsymbol{t = 14\ s}$, with maximum angle of around $\mathbf{30}°$, while holding breath and keeping forearms horizontal. **a** Normalized BIOPAC chest-belt waveforms showing clear respiratory signals and some motion interference during the breath hold period with arm motion. **b** Normalized NCS waveforms showing respiratory motion without any interference to the abdomen sensor, but arm motion is captured in the thorax sensor. **c** The heartbeat signal from NCS is interfered due to the arm swing and HR can only be possibly extracted from the harmonic.

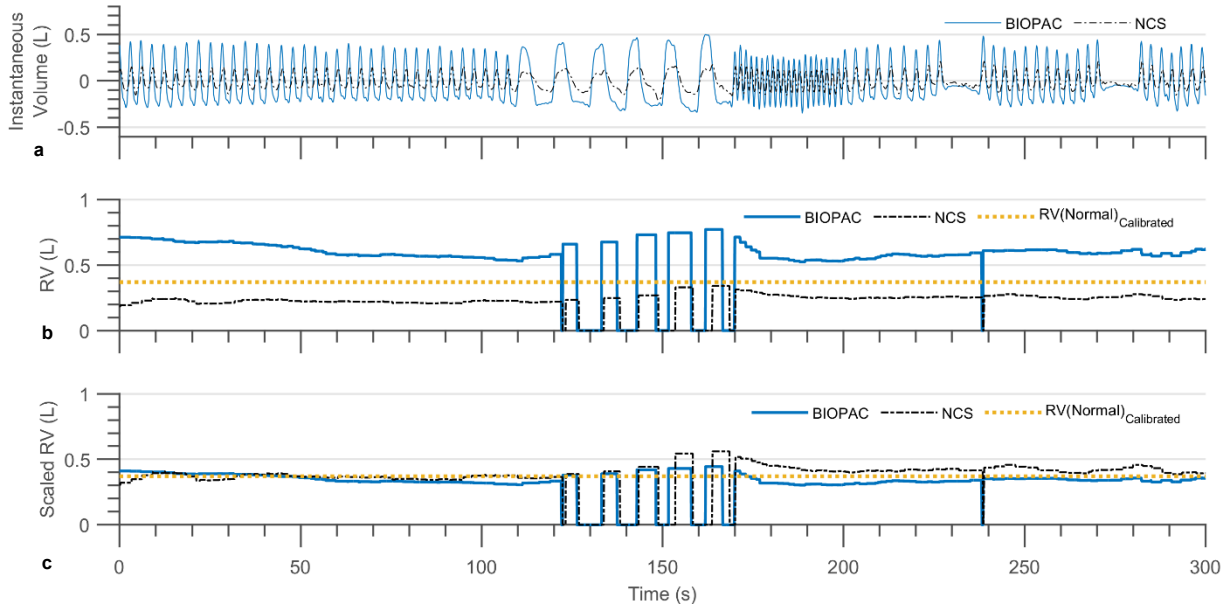

Supplementary Fig. 9. Results of calibration consistency test: using RV calibration from day-1 on day-2 data, both collected in sitting posture. Subject is performing voluntary breathing exercises in the routine. **a** Calibrated instantaneous volume from BIOPAC and NCS. **b** Estimated RV from the top plot with BIOPAC overestimating and NCS underestimating the expected $\mathrm{RV(Normal)}_{\mathrm{Calibration}} = 0.37$ L. **c** Scaled RV estimation that corrects the error based on a normal breathing section.

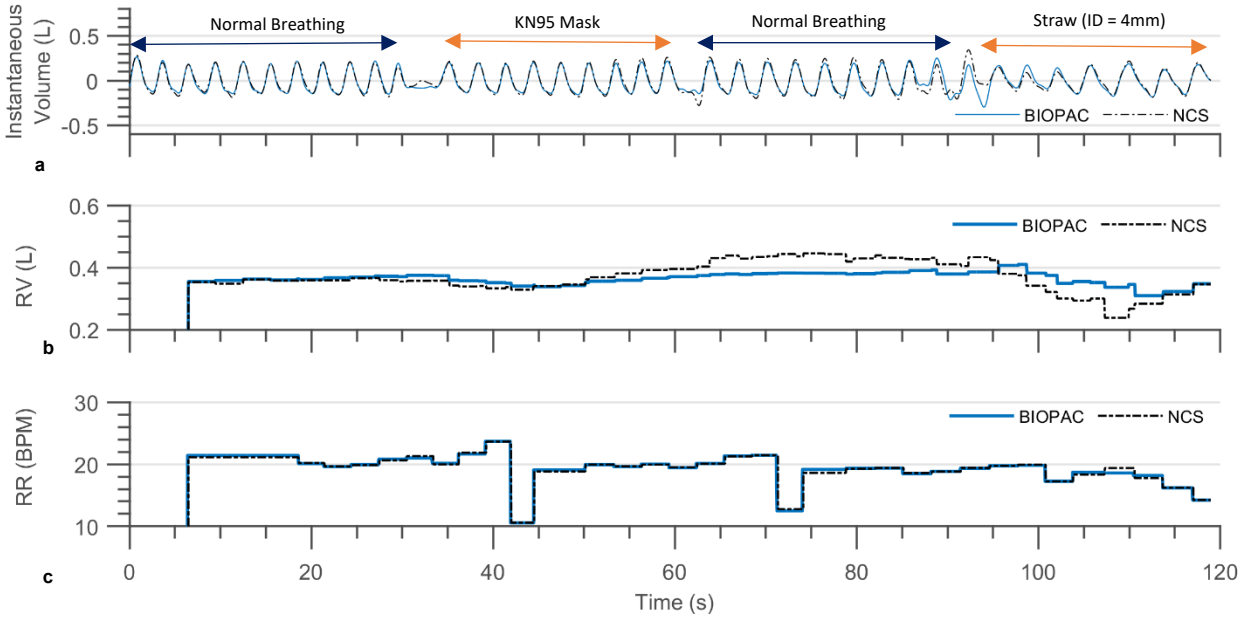

Supplementary Fig. 10. Studying the effect of simulated airway resistance variation. Subject is sitting upright while performing normal breathing. Two external resistances are introduced: 1) KN95 mask, while breathing normally through nose, and 2) straw with an inner diameter (ID) of 4 mm, only breathing through mouth. **a** & **b** plots show **c**alibrated instantaneous volume and derived RV estimates respectively, **c** shows corresponding RR. The response to mask is nearly not distinguishable from the normal breathing from both RV and RR estimates, slight dips around $t = 45$ s and 70 s are due to the breath holds during the transition periods. Breathing through straw shows decreased RV in the beginning, while maintaining same RR, the following increase in RV is associated with decreased RR, showing the increased respiratory effort required due to the resistance offered by the narrow straw. While both NCS and BIOPAC can capture these trends, NCS appears to be more sensitive to the RV changes.

Supplementary Table 1. Correlation and $\boldsymbol{B\&A}$ statistics for each participant

Measurement		Subjects																		
		1	2	3	4	5	6	8	9	10	11	12	13	14	15	16	17	18	19	20
RV (mL)	$\mathbf{r}$	0.6	0.85	0.68	0.73	0.71	0.80	0.45	0.80	0.20	0.84	0.97	0.90	0.76	0.71	0.86	0.72	0.92	0.43	0.82
	$\boldsymbol{m}$	40	4	210	12	-8	58	21	-57	88	-12	-29	-9	-41	14	21	-3	1	0	-46
	$\boldsymbol{\sigma}$	125	41	195	39	102	93	96	123	179	84	36	83	64	55	105	188	28	99	140
RR (BPM)	$\mathbf{r}$	0.85	0.91	0.87	0.92	0.90	1	0.93	0.90	0.97	0.91	0.91	0.91	0.97	0.78	0.82	0.91	0.90	1.00	0.93
	$\boldsymbol{m}$	-0.07	0.20	0.88	-0.27	0.17	-0.02	-0.27	0.01	-0.16	0.32	-0.46	-0.13	-0.20	0.39	0.53	0.50	0.27	0.01	-0.29
	$\boldsymbol{\sigma}$	3.08	2.50	5.38	2.86	2.64	0.68	2.45	3.36	2.09	2.80	3.85	2.49	1.99	4.26	4.84	2.63	2.87	0.45	3.43
HR (BPM)	$\mathbf{r}$	0.97	0.45	0.36	0.57	0.98	0.87	0.33	0.92	0.81	0.87	0.61	0.91	0.92	0.81	0.74	0.72	0.80	0.86	0.92
	$\boldsymbol{m}$	-0.20	-1.06	-3.96	-0.36	-0.20	-0.06	0.08	0.20	-0.41	-0.39	-0.90	-1.01	0.10	-0.13	-0.27	-1.06	-0.12	-0.33	-0.11
	$\boldsymbol{\sigma}$	1.26	4.42	6.08	2.92	1.19	2.20	7.44	1.13	2.15	2.40	2.43	2.79	2.10	2.31	1.83	2.58	1.00	1.63	1.42

Table showing Pearson's correlation coefficient (r), and mean bias (m) and standard deviation (σ) of the difference of NCS and BIOPAC estimates ($B\&A$ statistics) for each subject across all the postures and breathing styles. Subject 7 is not shown here, as at least half of the data is discarded due to poor quality, resulting in a small data set for any statistical analysis.

Supplementary Table 2. Average RV, RR and HR over 3 postures: supine, left lateral recumbent and sitting

Posture	RV (mL)	RR (BPM)	HR (BPM)
Supine	329 ± 200	17.3 ± 8.5	65.3 ± 9.9
Left Lateral Recumbent	263 ± 210	19.5 ± 9.5	63.8 ± 9.7
Sitting	317 ± 179	19 ± 9.7	67.6 ± 9.3

Table showing mean (m) $\pm$ standard deviation (σ) of the RV, RR and HR statistics over different postures. The data is collected over all 20 participants following the same voluntary breathing exercise routine of normal, deep, and fast breathing, as well as breath holds. Average RV is observed to be highest in the supine posture, followed by sitting and lateral recumbent, while RR has the opposite trend. HR is highest in the sitting posture, followed by supine and lateral recumbent postures. The standard deviation likely demonstrates variation introduced from different breathing exercises.

Supplementary Table 3. RV calibration consistency test over 3 consecutive days

1. Day $\boldsymbol{i}$	**2. $\mathbf{RV(Normal)_{Calibration}}$**	**3. $\mathbf{RV(Normal)_{Routine}}$** (Calibration: Day $\mathbf{1}$)	**4. Scaling Factor, $\boldsymbol{SF}$** (Calibration: Day **1**)
$\boldsymbol{i = 1}$	$\mathrm{RV}_{PTM} = 0.37\ L$	$\mathrm{RV}_{NCS} = 0.39\ L$, $\mathrm{RV}_{BIOPAC} = 0.35\ L$	$SF_{NCS} = 0.95, SF_{BIOPAC} = 1.06$
$\boldsymbol{i = 2}$	$\mathrm{RV}_{PTM} = 0.43\ L$	$\mathrm{RV}_{NCS} = 0.22\ L$, $\mathrm{RV}_{BIOPAC} = 0.65\ L$	$SF_{NCS} = 1.68, SF_{BIOPAC} = 0.57$
$\boldsymbol{i = 3}$	$\mathrm{RV}_{PTM} = 0.43\ L$	$\mathrm{RV}_{NCS} = 0.24\ L$, $\mathrm{RV}_{BIOPAC} = 0.60\ L$	$SF_{NCS} = 1.54, SF_{BIOPAC} = 0.62$

Table displaying the normal breathing RV calibration and scaling factor consistency over three days of testing on the same subject. Each day consisted of a calibration period immediately followed by a breathing routine, performed while sitting upright. **1.** The day of the measurements. **2.** The normal RV estimated from the PTM during the calibration routine. All three RV estimates are close to each other, within a range of 0.06 L. **3.** The normal breathing RV for NCS and BIOPAC during the breathing exercise routine, derived using calibration from day 1 for all three days. **4.** The calculated scaling factor to accurately map the routine's normal RV to normal RV of day 1 calibration. Little scaling is required to correct RV when calibrated immediately before the routine, resulting in scaling factors close to 1 on day-1. Variations in sensor placement and coupling strength result in scaling factors other than 1 to correct the normal RV on the next two days.

Appendix D

(PDF downloaded from IEEE) X. Hui, P. Sharma and E. C. Kan, “Microwave stethoscope for heart sound by near-field coherent sensing”, *International Microwave Symposium (IMS)*, Boston, MA, June 2 – 7, 2019.

Microwave Stethoscope for Heart Sound by Near-Field Coherent Sensing

***Abstract*—Heart sound at the S1 and S2 points in the cardiogram provides important diagnostic information for cardiovascular disorders. The century-old acoustic stethoscopes remain the main tool, but the signal quality deteriorates significantly over clothes and under noisy ambient. We demonstrate for the first time an UHF microwave technique to directly retrieve the heart sound through layers of clothing with improved user convenience and privacy. Adapted from the previous near-field coherent sensing technique, two system improvements on the frequency selection and balancing bridge design have enabled higher receiver gain to clearly retrieve the heart sound over layers of clothing. We performed dynamic time warping to compare the waveforms acquired from the acoustic and microwave methods, and present the effects of clothing and waveform signatures from individual users.**

***Index Terms*—harmonic backscattering; heart sound; impedance matching; radio frequency; vital-sign monitoring.**

I. Introduction

Auscultatory stethoscopes have been a standard diagnostic tool for cardiopulmonary functions for more than 200 years. Thanks to the high sensitivity and large dynamic range for acoustic signal processing by human or devices, detailed heart sound at the S1 and S2 points of the cardiogram can be retrieved [1]. However, because of the large acoustic impedance mismatching in various materials, especially for air gaps, the transducing diaphragm or bell of the stethoscope needs to be in tight skin touch for best signal quality. The sensation of the practice thus causes concerns for comfort and privacy, which discourages long-term daily monitoring. Other cardiovascular tools such as electrocardiogram (ECG) [2] and photo-plethysmography (PPG) [3] cannot detect the heart sound, although simultaneous measurements can provide clues of S1 and S2 timing. Methods based on radio frequency (RF) for heartbeats have been investigated for many years [4], but the signal quality is limited by strong respiration interference and low signal-to-noise ratio (SNR) from minute chest surface vibration. The system dynamic range is often poor due to strong self-jamming. Thus, most of these radar-based methods can only recover the fundamental heartbeat and its variation, not the heart sound. Through meticulous signal processing, some part of the heart sound can be detected [5], but the signal quality is worse than the conventional stethoscope.

The previous near-field coherent sensing (NCS) method [6] can provide improved signal quality and touchless operation, but further system improvements both on the coupling to the sound source and on the transceiver sensitivity and SNR are required to accurately retrieve the feeble heart sound. In this paper, we have adapted the passive harmonic RFID (radio-frequency identification) tag as the heartbeat sensor [6]. We first discuss the frequency strategy of antenna impedance matching to increase the energy coupling deep into the motion source that produces the heart sound. We then introduce an adaptive bridge circuit module to balance the NCS-modulated and non-modulated signals, which can significantly improve the sensing dynamic range. We then benchmark our experimental microwave NCS method against the conventional acoustic stethoscope (Thinklabs One) by waveform comparison through continuous wavelet transform (CWT) and dynamic time warping (DTW) on S1 and S2 sounds individually, and verify the operations over layers of clothing. Our convenient "microwave stethoscope" can potentially monitor the heart sound in the long term for diagnostic purposes regardless of the ambient noise level, or serve as a biometric parameter that is robust against replay and clone attacks [7].

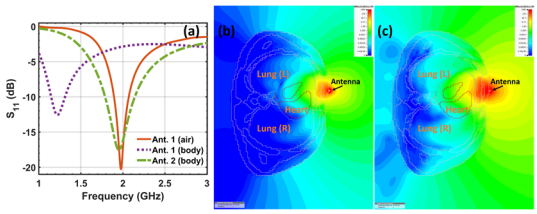

Fig. 1. The simulated NCS antenna detuning and body coupling. (a) S_{11} of an antenna designed to operate at 2 GHz in free air, and the corresponding detuning with chest placement; (b) EM power flow at 2 GHz of the NCS signal coupled into the human torso with poor impedance matching, and (c) with proper impedance matching.

II. Frequency Selection and Balance Bridge Design

The faint heart sound is embedded in the strong fundamental tone of the heartbeat, and possibly in the large respiration motion if the user does not hold the breath. All modules of signal transducing and processing need to be highly efficient and introduce least noises to retrieve heart sound. To strongly couple to the sound source deep in the heart tissues, microwave signals in the ultrahigh frequency (UHF) band (300 MHz – 3 GHz) are employed due to their reasonably small attenuation inside the human body, and can thus have effective signal transduction if the sensing antenna can be properly designed and placed. To study the antenna and frequency effects, we first construct a human torso electromagnetic (EM) simulation model in CST Microwave Studio [8]. The internal organ geometry and tissue property of the human torso are extracted from the Zubal Phantom [9]. Within the near-field region determined by the frequency, the sensing antenna can be placed close to the left pectoral major area, but over layers of clothing without skin touch. However, the proximity of the human tissue with high dielectric constant can detune the antenna, resulting in significant changes in the S parameters in both transmission towards the body and the antenna reflection. The radiation pattern would change as well.

In view of the system design, the antenna can be considered as the matching component between the RF impedance (often around 50 Ω) and the impedance of the joint region of the free space and the torso. For the CST simulation in Fig. 1(a), S_{11} of a 2-GHz dipole antenna is shown as the red solid line when the

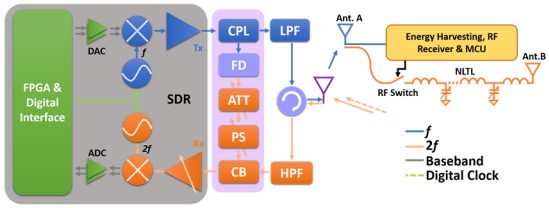

Fig. 2. The NCS experimental setup with a passive sensing RFID tag in the front pocket on the chest area. DAC: digital to analog converter; ADC: analog to digital converter; SDR: software defined radio; CPL: coupler; FD: frequency doubler; ATT: tunable attenuator; PS: phase shifter; CB: combiner; LPF: low-pass filter; HPF: high-pass filter; NLTL: non-linear transmission line.

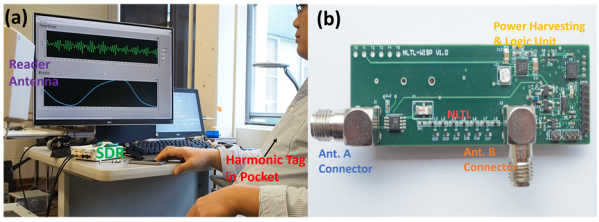

Fig. 3. (a) The NCS experimental setup with passive RFID tag in the front pocket on the chest area. (b) The harmonic tag in the pocket.

antenna operates in the free space. However, when that antenna is placed near the chest area, S_{11} will be shifted to the purple dotted line, which means the frequency near 2 GHz can no longer have good emission efficiency due to high reflection. To better couple into the heart sound source deep inside the torso volume, we can either shift the operation frequency to the band with low S_{11}, or redesign the antenna geometry to fit the original 2 GHz band. The green dashed line is the redesigned antenna matched with the torso placement. The reflection at 2 GHz is improved from –3 dB to –18 dB.

To further demonstrate the deep coupling to the internal organs, Figs. 1(b, c) show the power flow at 2 GHz with the chest antenna in Fig. 1(a). For the original antenna with poor impedance match (the purple dotted line), little RF energy is coupled to the heart, while the revised antenna (the green dashed line) can provide stronger coupling which also increases the total strength of the backscattered signal. Hence, with the same noise floor, both SNR and sensitivity will be improved.

Another aspect that can affect the heart sound quality is the signal dynamic range. There are two signal paths received by the reader: The signal modulated by the internal heartbeat and the non-modulated backscattering RF signal. Based on the NCS setup [4], the two parts are coherent and the internal motion can be derived from the demodulated amplitude, similar to the interferometer structure. However, the received signal strength (RSS) of the non-modulated signal is usually much larger than the modulated part due to the antenna directivity, coupling efficiency, reflection coefficient and energy loss caused by human tissue. Hence, the low noise amplifier (LNA) at the receiver (Rx) front end can be easily saturated by the non-modulated signal, i.e., the Rx gain can be added to the modulated signal is limited by the high level of the non-modulated signal. Even though the harmonic sensing RFID can provide high isolation between the transmitter (Tx) and Rx to boost the system SNR, the sensitivity limitation originated from the finite Rx dynamic range can be relieved if we can balance the NCS-modulated and non-modulated signals before LNA.

A balance bridge structure is thus inserted to adaptively compensate the amplitude and phase of the non-modulated signal. As shown in Fig. 2, the software defined radio (SDR) is configured as the harmonic RFID reader, so the local oscillator of the Rx is twice the frequency of the Tx and shares the same clock source. The Tx signal goes through the 10-dB coupler (CPL), and the major part of the energy is transmitted by the dual band antenna through the low-pass filter (LPF) and the circulator. The harmonic RFID tag is placed to the chest area to sense the heartbeat. The downlink wireless signal at the frequency f is received by antenna A of the tag [10]. Part of the energy is harvested and the other part is coupled to the nonlinear transmission line (NLTL) [11] to generate the harmonic signal as the sensing signal which is transmitted out by antenna B. In Fig. 2, the uplink signals are in the orange color, where the NCS-modulated RF signal is the dash arrow and the non-modulated signal is the solid arrow. The uplink signal received by the dual-frequency antenna goes through the circulator and the high-pass filter.

The smaller signal derived from the 10-dB coupler is doubled by the frequency doubler (FD), and then adaptively adjusted by the tunable attenuator (ATT) and phase shifter (PS) to tune the non-modulated signal, which is added to the received NCS-modulated signal by the combiner (CB). The combined signal then goes through the SDR Rx chain. The circuit modules from the CPL of the Tx side to the CB at the Rx side constitute the balance bridge, which will increase the Rx dynamic range by matching the NCS-modulated and non-modulating signals. The feedback control loop for ATT and PS is based on the received signal from SDR, where the Rx gain can be further boosted to amplify the NCS-modulated vital-sign signal to reveal the signal details for heart sound. In the present experimental design, at least another 10-dB gain at the Rx chain can be added. Based on the received signal, the balance bridge can also be used to compensate the interferences caused by the whole body motion and other sources with more sophisticated processing, such as the pilot tone signal injection in Tx to analyze the received signal and to manipulate ATT and PS [12].

III. Experimental Results

The NCS measurement setup is shown in Fig. 3. The harmonic tag is put into the front pocket on the chest area. The SDR by Ettus B210 is connected to the computer through its USB port, and the RF ports are connected to the balance bridge, circulator and then the dual-band reader antenna. The vital-sign signals are demodulated by the SDR and the host computer as shown on the screen.

We used a monopole antenna as the sensing antenna for NCS, whose S_{11} is shown in Fig. 4(a). The red solid line with the center frequency of 2.1 GHz represents operation in free space. For placement near the chest area, the antenna S_{11} response will shift to the green dashed line with the center frequency at

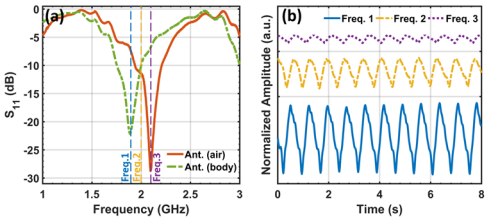

Fig. 4. The experimental results in various frequencies. (a) S_{11} of the NCS antenna when it is operated in air (the red solid curve), and placed on the chest (the green dashed curve). (b) The heartbeat signal waveforms demodulated from the chest tag in Fig. 3 with different sensing frequencies. The NCS signals from the blue solid curve (impedance matched condition), yellow dashed curve and the purple dotted curve correspond to Freq. 1, 2, and 3 in Fig. 4(a), respectively.

1.9GHz. The reflection around 2.1 GHz is now much higher. To achieve large energy coupling and high SNR in NCS, the downlink signal should be changed to 950 MHz so that the sensing antenna is well matched at 1.9 GHz. As shown in Fig. 4(b), the blue solid line is the heartbeat signal acquired by the uplink at 1.9 GHz (corresponding to Freq. 1 in Fig. 4(a)). The yellow dashed line with the uplink at 2.0 GHz (Freq. 2 in Fig. 4(a)) and the purple dotted line at 2.1 GHz (Freq. 3 in Fig. 4(a)) have much weaker NCS signals due to less energy coupling inside the torso. Notice that the RF radiation efficiencies at Freq. 2 and Freq. 3 are still reasonably high, estimated at 90% and 80% at S_{11} of −10dB and −7dB, respectively. Therefore, most of the degradation in the NCS signal can be attributed to the reduction in the tissue coupling. All measurements are conducted under the same setting and extraction procedure except the different frequencies.

With operation at the frequency with antenna impedance matching (950 MHz for downlink and 1.9 GHz for uplink), ATT and the PS in the balance bridge can be tuned to achieve higher Rx gain. The received heartbeat signal waveforms are shown in Fig. 5. The purple curve is the NCS heartbeat raw data. Because the NCS signal is related to the mechanical motion of the dielectric boundaries, the strong fundamental heartbeat signal is dominating. However, because with the improved system design, the weaker high-frequency signal can still be amplified and captured within the ADC resolution. The blue curve is the NCS heartbeat signal when a 6-58 Hz bandpass filter is applied. The repeatable details now reveal more heartbeat features. The pink curve represents the signal after a 16-58 Hz bandpass filter where the timing of S1 (yellow arrows) and S2 (green arrows) in the cardiogram can be clearly

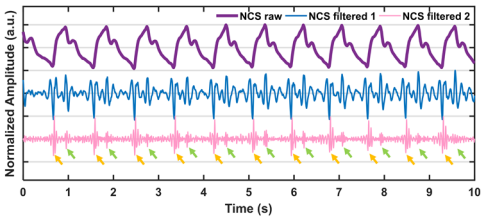

Fig. 5. The experimental extraction of the heartbeat waveforms from NCS. Bandpass filter 1 of 6 – 58 Hz shows high-frequency features without the fundamental heartbeat; Bandpass filter 2 of 16 – 58 Hz shows the S1 (yellow arrows) and S2 (green arrows) locations.

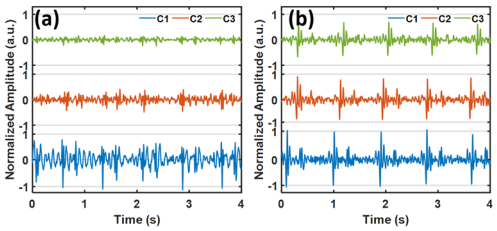

Fig. 6. The heart sound waveforms with layers of clothes. (a) The stethoscope recordings: C1 for direct skin contact; C2 for outside a shirt and a sweater; C3: for additional coat. Signals are severely degraded due to acoustic impedance mismatch. (b) The waveforms from NCS recordings: C1 for outside the shirt without direct skin contact. C2 and C3 are the same conditions as (a).

observed. We feed the filtered signal to a speaker, where S1 and S2 caused by the closure of the atrioventricular (AV) valves and semilunar (SL) valves respectively can be clearly audible. Audio file links will be provided after the double-blind review.

In Fig. 6, we illustrate the NCS advantage for operations over layers of clothing. Due to acoustic impedance mismatch and damping, the stethoscope recording deteriorates severely in Fig. 6(a) even when appropriate pressure was applied, while NCS maintains the waveform features with slight decrease in magnitude in Fig. 6(b) over shirt, sweater and coat.

IV. Heart Sound Analyses

For heart-sound recordings to be used for diagnostic and biometric purposes, we need to validate the signal consistency within one user at different time instances, and sufficient distance between two users. Sample waveforms from the acoustic stethoscope and the NCS system are shown in Fig. 7, which have the same AV and SL valve origins but different transducing paths. The transient waveforms in Figs. 7(a, b) can be potentially matched by spectral equalization, but such practice will be specific to each user and thus less useful. To compare our NCS heart sound to the acoustic stethoscope, we first show the continuous wavelet transform (CWT) analyses in Fig. 7(c, d), which illustrates the related heart-sound content

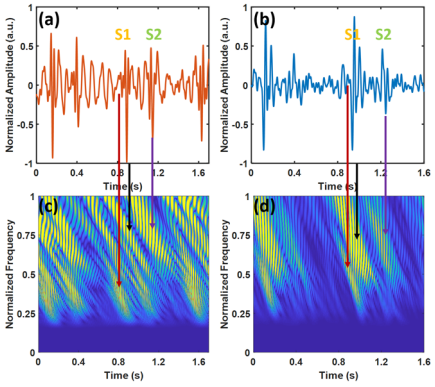

Fig. 7. Heart sound analyses from a single user. (a) The heart sound waveform recorded by the acoustic stethoscope. (b) The heart sound waveform processed from the NCS system. (c) The continuous wavelet transform (CWT) time-frequency analysis of (a). (d) CWT analysis of (b). The red, black and purple arrows indicate the similar time-frequency components of stethoscope and NCS heart sounds.

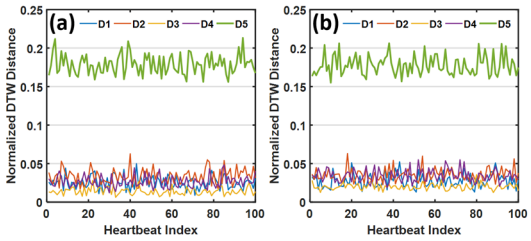

Fig. 8. Heart sound analyses from a single user. (a) The normalized DTW distance of S1 waveforms. D1: between the S1 waveform and that of the next heartbeat from stethoscope. D2: between two recordings from stethoscope. D3: between the S1 waveform and that of the next heartbeat from NCS. D4: between two waveforms from NCS. The distance is normalized to the distant value between the averaged NCS S1 waveform and the zero-amplitude signal. D5: between two waveforms from stethoscope and NCS. (b) Similar analyses as (a) but for S2 waveforms.

with similar time-frequency patterns. NCS has more distinctive features than stethoscope possibly due to the more concentrated coupling regions around the heart, and stethoscope can contain other sounds from the torso and the ambient even though the recording was done with breath withholding. We then opt for the dynamic time warping (DTW) method commonly used in voice recognition [13] for waveform comparisons. The D1 – D4 curves in Fig. 8(a) show the S1 signal self-consistency in both stethoscope and NCS by the comparison with the next heartbeat and between two instances of recordings. The DTW distance is normalized by the signal distance to the null vector. The D5 curve shows the DTW distance between the stethoscope and NCS. Despite of the different transducing paths, the normalized distance is still small around 0.18 as the two signals are correlated to the same sound source. The same trend can be observed for the S2 signal in Fig. 8(b).

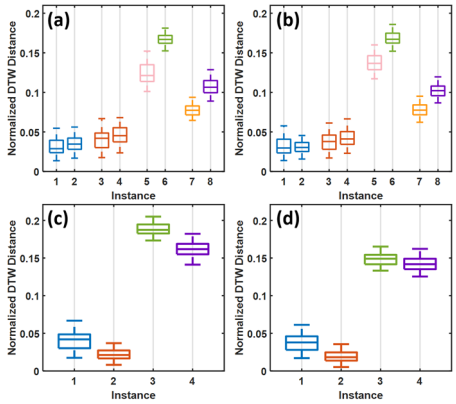

Fig. 9. Normalized DTW distance for heart sound to illustrate the effects from different users and NCS designs. (a) S1 analysis for one user. Instance 1: between the first array of S1 waveforms (Array 1) and their own averaged waveform from stethoscope. Instance 2: between the second array of S1 waveforms (Array 2) and the averaged waveform of Array 1 from stethoscope. Instances 3 and 4 are the comparable data sets from the NCS signals. Instance 5: between the stethoscope S1 waveforms and the NCS averaged S1 waveform. Instance 6: between the NCS S1 waveforms and the stethoscope averaged S1 waveform. Instance 7: between the NCS S1 waveforms at 2.0 GHz and the NCS averaged waveform template in Instance 3 at 1.9 GHz. Instance 8: between the NCS S1 waveforms at 2.1 GHz and the NCS averaged waveform template in Instance 3 at 1.9 GHz. (b) Similar analyses as (a) but for S2 waveforms of one user. (c) NCS S1 analyses for two users. Instance 1: between User 1 (male) waveforms and his own averaged template. Instance 2: between User 2 (female) and her own averaged template. Instance 3: between User 2 waveforms and the averaged template from User 1. Instance 4: between User 1 waveforms and the averaged template from User 2. (d) Similar analyses as (c) but for S2 waveforms.

In Fig. 9, we will use the normalized DTW distance to illustrate the effects from different users and NCS system designs. For one user, the signal self-consistency from stethoscope and NCS can be established from the very small distance in Instances 1 – 4 for S1 and S2 in Figs. 9(a) and (b), respectively. Instances 5 and 6 show the distance between stethoscope and NCS, which is similar to the analysis in Fig. 8. Instances 7 and 8 illustrate the signal degradation effect when the NCS antenna is not operated at the impedance-matching frequency, where larger distance would be observed for less signal consistency. Finally, in Figs. 9(c) and(d), two users with their own NCS signal self-consistency (Instances 1 and 2) have much larger distance (Instances 3 and 4) in both S1 and S2 waveforms.

V. Conclusion

In this paper, we improve the sensing antenna matching and the balance bridge design to improve the NCS sensitivity to retrieve heart sound. We compared the S1 and S2 sounds retrieved from NCS and stethoscope, and benchmarked the signal consistency within one user and sufficient difference between two users. We demonstrate that NCS has similar heart sound content to the conventional stethoscope, and offers operations over clothing and in noisy ambient.

References

[1] J. R. Kindig, *et al*, "Acoustical perfomance of the stethoscope: A comparative analysis," *Am. Heart J.*, vol. 104, pp. 269-275, 1982.

[2] P. Kligfield,*et al*, "Recommendations for the standardization and interpretation of the electrocardiogram," *Circulation*, vol. 115, no.10, pp. 1306-1324, Mar. 2007.

[3] J. Allen, "Photoplethysmography and its application in clinical physiological measurement," *Physiol. Meas.* vol. 28, 2007.

[4] C. Li, *et al*, "A review on recent progress of portable short-range noncontact microwave radar systems," *IEEE Trans. Microw. Theory Tech.*, vol. 65, pp. 1692-1706, 2017.

[5] C. Will, et al., "Radar-based heart sound detection," *Scientific Reports*, vol. 8:11551, DOI: 10.1038/s41598-018-29984-5, July 2018.

[6] X. Hui and E. C. Kan, "Monitoring vital signs over multiplexed radio by near-field coherent sensing," *Nature Electronics*, doi: 10.1038/s41928-017-0001-0, vol. 1, 2018.

[7] K. Phua, *et al*, "Heart sound as a biometric," *Pattern Recognition*, vol. 41, no. 3, pp. 906-919, 2008.

[8] CST Microwave Studio by Computer Simulation Technology [Online]. Available: http://www.cst.com

[9] I.G. Zubal, *et al*, "Computerized three-dimensional segmented human anatomy," *Med. Phys.*, vol. 21, pp. 299-302, 1994.

[10] Y. Ma, X. Hui and E.C. Kan, "Harmonic-WISP: A passive broadband harmonic RFID platform," *2016 IEEE MTT-S International*, 2016.

[11] F. Yu, K.G. Lyon and E. C. Kan, "A novel passive RFID transponder using harmonic generation of nonlinear transmission lines," *IEEE Trans. Microw. Theory Tech*., vol. 58, pp. 4121-4127, 2010.

[12] R. Neji, and J. Cioffi, "Pilot tone selection for channel estimation in a mobile OFDM system," *IEEE Transactions on Comsumer Electronics*, vol. 44, no. 3, pp.1122-1128, 1998.

[13] H. Sakoe and S. Chiba, "Dynamic programming algorithm optimization for spoken word recognition," *IEEE Trans. on Acoust., Speech, and Signal Process.* vol. 26, pp. 43-49, 1978.

Appendix E

(PDF preprint) X. Hui, T. B. Conroy and E. C. Kan, “Near-field coherent sensing with harmonic analysis and balance signal injection”, accepted in *IEEE Trans. MTT*.

Near-field Coherent Sensing of Vibration with Harmonic Analysis and Balance Signal Injection

Xiaonan Hui, *Student Member, IEEE*, Thomas B. Conroy, and Edwin C. Kan, *Senior Member, IEEE*

***Abstract*—The near-field coherent sensing (NCS) system can detect weak cyclic motion inside living bodies, such as human wrist pulses and the heartbeat of small animals. To couple significant energy to the motion source, a GHz RF carrier was employed, where the vibration amplitude is often much smaller than the wavelength. To optimize the signal quality, we presented a small-signal model with nonlinearity analysis by Jacobi-Anger expansion. The quiescent-point determination and signal composition were then discussed to guide the hardware and algorithm design. The model was validated by electromagnetic simulation in CST Studio and a simple robotic platform. A novel algorithm of adaptive control by signal injection can boost the signal magnitude and data converter utilization. The signal-to-quantization-noise ratio (SQNR) is improved by 35 dB and signal-to-noise ratio (SNR) by more than 10 dB. Sensing of vocal cord vibration was demonstrated as a potential application, where the harmonic radio frequency identification (RFID) system was chosen for its low noise floor to achieve high-fidelity recording of music scales and procedure words.**

***Index Terms*—Biomedical signal processing, microwave sensors, signal analysis.**

I. Introduction

Near-field coherent sensing (NCS) [1] employs radio frequency (RF) carriers to measure the cyclic motion inside the living body such as heartbeat dynamics [2], respiratory features [3], [4], artery pulses [1], [5], and blood pressures [1], [2] for human and animals [6]. Different from the far-field RF systems that detect the body surface motion by backscattering [7]–[9], NCS couples the electromagnetic (EM) energy inside the body by the near field. The proximity of the near-field coupling enables precise monitoring of local physiological movement, such as multi-point observation of different parts of the heartbeat [2]. The sampling rate can be very high to accommodate fast heart rates of hundreds of beats per minute [6], as well as the tissue vibration characteristics [2], [10], as shown in the recovery of heart sounds. The ultra-high-frequency (UHF) band (0.3 – 3 GHz) is the preferred carrier due to stronger energy coupling and less dispersion inside the body, but the motion amplitude of interest can then be much smaller than the wavelength. For performance optimization, we present the small-signal modulation model to guide the hardware and algorithm design in this paper.

This project is supported by the DoD CDMRP Discovery Award PR-182496, NIH R21 DA049566-01 and NSF 2033838. X. Hui, T. B. Conroy, and E. C. Kan are with Cornell University, Ithaca, NY 14853, USA. The corresponding author is X. Hui, E-mail: xh273@cornell.edu.

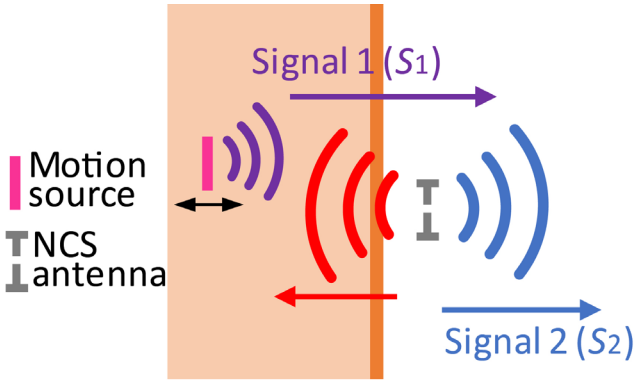

Fig. 1. The illustration of the near-field coherence sensing (NCS) principle.

Furthermore, we chose to monitor vocal cord vibration as an illustration of the NCS system design process. Non-audial glottal sensing is useful in many applications, such as covert recording [11], communication in extremely noisy ambient environments, and speech therapy. Camera recording of the throat surface is presently used for clinical diagnosis [12], [13], where a high frame rate is employed to obtain the vibration dynamics. However, the equipment cost and the required line-of-sight (LoS) alignment to the camera prohibit common usage and long-term monitoring. In addition, high-speed cameras often require strong illumination, and thus causes discomfort for users in practice. Electroacoustic transducer systems such as the stethoscope and microphone [14], [15] on the throat suffer from acoustic interference from mouth and other ambient sources. Ultrasound systems [16], [17] have also been used in clinical diagnostics; however, the transducer probe must remain in contact with the skin using gels to maintain proper acoustic impedance match. The bulky system size and high power consumption also restrict broad applications. The NCS method mixes the mechanical vibration signal with an RF carrier in the UHF band, where the resulting percentage bandwidth becomes much smaller than those in the ultrasound and stethoscope systems. Thus NCS can achieve stable sensing without an equalizer in view of the Bode-Fano limit [18] that governs the trade-off between the percentage bandwidth and impedance match.

Interactions between EM waves and different parts of the human body have been broadly investigated by various groups [7], [19]–[22]. The studied hardware systems include Doppler radar [23], [24], frequency modulated continuous wave

(FMCW) radar [25]–[27], UWB radar [28], [29] and RFID systems [1], [22]. Acquisition of throat vibration to evaluate speech and tones is one of the applications. Because of the small-magnitude and high-frequency features of the glottis vibration, usually millimeter wave and sub-Terahertz systems are preferred in order to realize high sensitivity [21], [30], [31]. Lower-frequency radar systems in the UHF band need to employ the Doppler mode to achieve sufficiently high sensitivity [9], [32]. The proposed method in this paper presents an alternative architecture, where the UHF sensing signal is applied to a harmonic RFID system with balance signal injection to implement the NCS principle. The passive harmonic tag can be readily integrated with clothes, necklace or pasted on the skin, and the wearable device can be miniaturized without the constraint of battery. Compared to radar-based systems, NCS utilizes the near-field coupling of the antenna to direct more energy into the human tissue and the vibration source underneath the skin, avoiding major reflection caused by the body surface. Signal modulation happens mostly at the vibration source inside the body, not at the skin surface which contains only attenuated and distorted characteristics of the internal vibration.

The main contribution of this paper over our previous NCS work [1], [6], [10] is the improved accuracy in capturing internal vibration over a large frequency range up to 400 Hz, where the vocal cord monitoring is demonstrated as the main application. Frequency much higher than 400 Hz is readily realizable, but not experimentally tested in this paper. In order to achieve satisfactory tonal performance, we analyze the harmonic components in the NCS signal to guide the system design, and introduce the balance signal injection to provide proper conditioning as well as to improve the bit depth of the output. We first described the NCS signal model in Sec. II, including the modulation nonlinearity, signal composition, and setup of the optimal quiescent point. In Sec. III, the signal model was validated first by a known vibration source with tunable magnitude, and then by electromagnetic simulation using CST Microwave Studio [33]. Sec. IV introduced the harmonic RFID system [1], [34] and the adaptive control based on signal injection to minimize waveform distortion and maximize the output quality of the data converter. In Sec. V, the vocal-cord recording by the harmonic RFID system was conducted and the measurements from music scales and procedure words were analyzed.

II. NCS Signal Model

The NCS operation can be described by a simplified model in Fig. 1. When the NCS sensing antenna (grey dipole) is placed close to the skin (orange layer) within the near-field region, a significant amount of the RF energy (red wave) will be coupled into the tissue (box). Another part of the tissue (pink block) with different permittivity from the surrounding tissue will reflect the impinging RF signal (red arrow) to form a backscattered signal (purple arrow). We will first assume a simple cyclic motion of the permittivity boundary, such as motion caused by heartbeats, arterial pulses, respiration or vocal cord vibration:

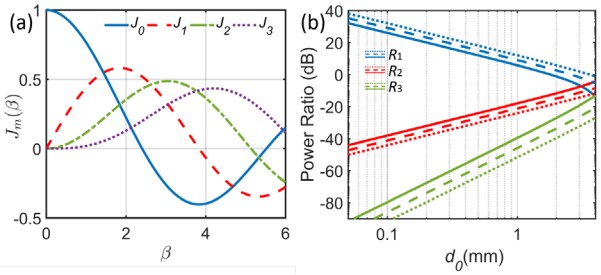

Fig. 2. (a) The Bessel function of the first kind from orders 0 to 3 as blue, red, green and purple curves, respectively. (b) The power ratios between the fundamental frequency and DC: $R_1 = (J_0)^2/(2J_1)^2$ (blue), fundamental frequency and 2nd harmonic: $R_2 = (J_2)^2/(J_1)^2$ (red), and fundamental frequency and 3rd harmonic: $R_3 = (J_3)^2/(J_1)^2$ (green). The solid lines are under the condition of ε_r = 43.6 and the carrier frequency of 1.8 GHz. Both the dashed and dotted lines have ε_r =21.2 but at the carrier frequency of 1.8 GHz and 900 MHz, respectively.

$$d(t) = d_0 \sin(\Omega t) \tag{1}$$

where $d(t)$ describes the motion of interest, d_0 is the vibration magnitude, and Ω is the single-tone vibration frequency. The phase of the backscattered signal will be modulated as

$$S_1 = A_1 e^{j[\omega_c t + \beta \sin(\Omega t)]} = A_1 e^{j\beta \sin(\Omega t)} e^{j\omega_c t} \tag{2}$$

where A_1 is the amplitude of the backscattered signal, ω_c is the frequency of the RF carrier, and β is the modulation coefficient. The modulation coefficient β is related to the mechanical vibration amplitude d_0 and the RF wavelength in the surrounding tissue λ_r, and can be simplified as

$$\beta = 4\pi \frac{d_0}{\lambda_r} \,. \tag{3}$$

On the other hand, part of the RF signal is not modulated (blue wave) and directly transmitted to the receiver (Rx) antenna. The received signal S_2 (blue arrow) can be written as

$$S_2 = A_2 e^{j(\omega_c t + \phi_0)} = A_2 e^{j\phi_0} e^{j\omega_c t} \tag{4}$$

where A_2 is the signal amplitude and ϕ_0 is the phase offset. At the coherent receiver, S_2 will be down converted to the baseband, and only the direct-current (DC) component in Eq. (4) will remain. However, S_1 is more complicated and contains the vibration signal on phase modulation. S_1 can be decomposed by the Jacobi-Anger expansion [35], [36], which is commonly used in frequency or phase modulation analyses:

$$S_1 = A_1[J_0(\beta) + 2j^m \sum_{m=1}^{\infty} J_m(\beta)\cos(m\Omega t)]e^{j\omega_c t} \,. \tag{5}$$

$J_m(\bullet)$ is the Bessel function of the first kind of order m,

$$J_m(x) = \sum_{n=0}^{\infty} \frac{(-1)^n}{n!\Gamma(m+n+1)} \left(\frac{x}{2}\right)^{2n+m} \tag{6}$$

where $\Gamma(\bullet)$ denotes the gamma function. $J_m(\beta)$ is plotted in Fig. 2(a) for m = 0 to 3. The received signal is the combination of S_1 and S_2:

$$S_r = S_1 + S_2 = S_{baseband} e^{j\omega_c t} \tag{7}$$

where the demodulated baseband signal $S_{baseband}$ is

$$S_{baseband} = A_1 J_0(\beta) + 2j^m A_1 \sum_{m=1}^{\infty} J_m(\beta)\cos(m\Omega t) + A_2 e^{j\phi_0} \,. \tag{8}$$

From Eq. (8) we can extract the signal components from different frequencies in the base band as

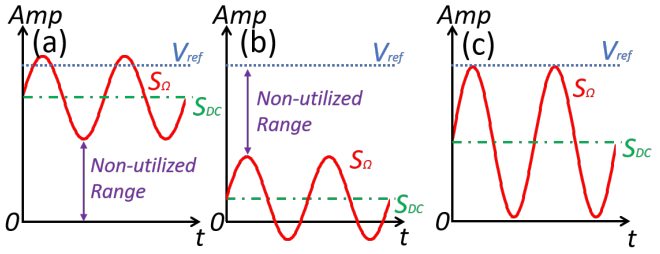

Fig. 3. The AC signal and DC bias in different conditions. (a) γ<1, (b) γ>1, (c) γ=1 and when both S_{DCbias} and S_{Ω_PP}/2 are equal to V_{ref}/2 after tuning the Rx gain.

$$\begin{cases} S_{DC} = A_1 J_0(\beta) + A_2 e^{j\phi_0} \\ S_\Omega = 2jA_1 J_1(\beta)\cos(\Omega t) \\ S_{2\Omega} = -2A_1 J_2(\beta)\cos(2\Omega t) \\ S_{3\Omega} = -2jA_1 J_3(\beta)\cos(3\Omega t) \end{cases} \quad (9)$$

where S_{DC} is the DC component, and S_Ω, $S_{2\Omega}$ and $S_{3\Omega}$ are the fundamental, 2nd harmonic and 3rd harmonic components, respectively. The sign of each term and the imaginary unit j can be interpreted as the constant phase delay in the quadrature sampling scheme. From Fig. 2(a) we can see that, when approaches 0, resulting from small d_0 or large λ_r, the dominant component is DC. As d_0 increases, the fundamental oscillation component is much stronger than the harmonics within the small-signal level when $\beta << 1$. Here we focus on β, rather than d_0, because of the wavelength dependence that makes β a more representative factor. However, when β increases larger than 1, the harmonics from nonlinearity will become more significant, such as the zero-crossing point of J_1 around β = 4 in Fig. 2(a) where the fundamental oscillation is minimized and harmonics are relatively high. Ideally, as observed from S_Ω, the internal motion will only modulate the amplitude of the demodulated signal, and the phase is not modulated as described in the NCS principle [1]. We should note that the harmonics here are not the mechanical harmonic signals caused by the nonlinearity of the organ tissue, but by the result from sensor modulation. In order to obtain a good modulation linearity, the vibration amplitude d_0 should be kept small comparing to λ_r/π in the surrounding tissue. According to Eq. (3), when the RF signal is at 1.8 GHz and the surrounding muscle permittivity (ε_r) is 43.6, β/d_0 can be calculated as 0.496 mm^{-1}. The power ratios (solid lines) along with the vibration amplitude are calculated as shown in Fig. 2(b). $R_2 = (J_2)^2/(J_1)^2$ represents the 2nd-order nonlinearity, while $R_3 = (J_3)^2/(J_1)^2$ is the 3rd-order nonlinearity. Based on this calculation, the sensing system will have a high linearity of −24 dB 2nd harmonic power ratio and −52 dB 3rd harmonic power ratio when the vibration amplitude is d_0 = 0.5 mm (β = 0.48 and d_0/λ_r = 0.08), as in the solid line. However, when d_0 = 2.5 mm (β = 2.4, d_0/λ_r = 0.4), R_2 and R_3 will degenerate to −9.5 dB and −23 dB. $R_1 = (J_0)^2/(2J_1)^2$ is the ratio between the fundamental signal and the DC by-product. At the small-signal region with $d_0 \cong$ 0.5 mm, the ratio is 12 dB, which implies the AC component is strongly biased by DC.

When the surrounding tissue permittivity is reduced, the nonlinearity will also be reduced, as shown by the dashed lines in Fig. 2(b) where the permittivity is 21.2 which is close to that of the lungs. When we additionally reduce the sensing frequency to 900 MHz with permittivity of 21.2, R_2 and R_3, as shown by the dotted lines in Fig. 2(b), will be −16 dB and −35 dB, respectively, at d_0 = 2.5 mm. However, the DC component will also increase in these scenarios, which can cause saturation. The two factors of nonlinearity and DC biasing need to be mitigated together for performance optimization.

A_1 and A_2 are related to the details of the application configurations, including the sensing antenna design, tissue condition, and Rx antenna position. These factors can be difficult to control exactly. For example, when $A_2 >> A_1$, the low-noise amplifier (LNA) in the RF front-end can be saturated by the non-modulated part before the modulated signal can be properly amplified and sampled. As a result, it will reduce the resolution of the digitized signal because of the limited dynamic range of the analog-to-digital convertor (ADC). A typical unipolar data converter relates the analog signal $S_{baseband}$ to the digital bits (b_1, ..., b_N) by [37]:

$$S_{baseband} = V_{ref} \frac{b_1 \times 2^0 + b_2 \times 2^1 + \cdots + b_N \times 2^{N-1}}{2^N - 1} \quad (10)$$

where N is the number of bits in the digital signal and V_{ref} is the reference voltage often externally provided by a bandgap reference circuit. If S_{DC} is minimized, the negative part of S_Ω may not be properly sampled, causing signal distortion by truncation.

The common technique of using a high-pass filter to remove the DC part before differential ADC cannot be applied here. Vital signs can have temporal characteristics down to 0.03 Hz, for example when tracking deep breathing and breath hold [3], [4], [38]. An analog decoupling capacitor would need to be prohibitively large to provide such low corner frequency. Furthermore, to avoid ambiguity in DC drift, a digitally-formed chopping signal or an intermediate frequency above 10 kHz is desirable in the baseband. Safe removal of the DC bias before ADC will require a notch filter with the quality factor exceeding 10^4. Therefore, we will need to consider the DC part explicitly before feeding the amplitude-modulated signal to ADC.

We propose to inject a controllable coherent signal to Rx. The injecting bias signal S_{bias} is introduced as

$$S_{bias} = A_b e^{j(\omega_c t + \phi_b)} = A_b e^{j\phi_b} e^{j\omega_c t} \quad (11)$$

where A_b is the amplitude and ϕ_b is the baseband phase offset of S_{bias}, both of which are controllable. The received signal can then be presented as the sum of Eqs. (7) and (11) as

$$S_{rb} = S_1 + S_2 + S_b = (S_{baseband} + A_b e^{j\phi_b}) e^{j\omega_c t} \quad . \quad (12)$$

The DC component in Eq. (9) can be rewritten as

$$S_{DCbias} = A_1 J_0(\beta) + A_2 e^{j\phi_0} + A_b e^{j\phi_b} \, , \quad (13)$$

and the rest of the signal components in Eq. (9) remain the same. We define γ as the signal bias indicator

$$\gamma = \frac{S_{\Omega_PP}}{2|S_{DCbias}|} = \frac{2A_1 J_1(\beta)}{|A_1 J_0(\beta) + A_2 e^{j\phi_0} + A_b e^{j\phi_b}|} \quad (14)$$

where S_{Ω_PP} is the peak-to-peak value of the fundamental oscillation signal. In order to achieve optimal signal bias, we can control the amplitude A_b and phase ϕ_b of the bias signal.

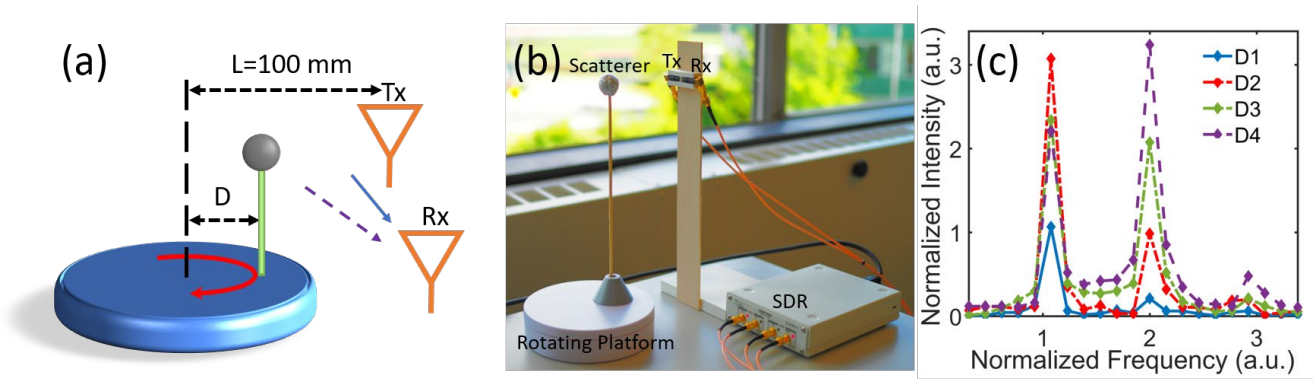

Fig. 4. The mechanical platform for the small signal verification. (a) The system schematic. (b) The photo of the experimental setup. (c) The power spectra of the experimental data with different oscillation magnitudes.

When $\gamma < 1$, as shown in Fig. 3(a), the DC amplitude is greater than the magnitude of the fundamental frequency. This over-biased condition caused by the DC amplitude term results in an under-utilization of the ADC range, and possibly truncation caused by ADC saturation where the signal swing is over the upper bound of ADC denoted by V_{ref}. On the other hand, when $\gamma > 1$ in Fig. 3(b), the target signal in under-biased biased, causing inefficient use of the ADC range as well as signal distortion due to the swing under the lower bound of ADC. When $\gamma = 1$, this undesired signal truncation and distortion can be avoided. Furthermore, when both $|S_{DCbias}|$ and $S_{\Omega-PP}/2$ are approximately equal to half of V_{ref}, as shown in Fig. 3(c), the ADC range will be fully utilized and the best signal resolution can be achieved. When $S_{baseband}$ is properly biased without any saturation or truncation, the ADC utilizing ratio η can be defined as

$$\eta = \frac{S_{\Omega-PP}}{V_{ref}}, (0 < \eta < 1) \quad . \tag{15}$$

Similarly, the ADC bit depth can be defined as

$$Q = \log_2(\eta) + N \quad . \tag{16}$$

In order to make the system robust for large dynamic range, Q should be reasonably smaller than N to reserve for the varying vibration magnitude. The signal-to-quantization noise ratio ($SQNR$) introduced at ADC can be estimated as [39]:

$$SQNR = 6.02Q + 1.76\text{dB} \quad . \tag{17}$$

Proper DC bias and amplification of S_Ω will render $SQNR$ to be larger than the intended system signal-to-noise ratio (SNR) to avoid system degradation due to ADC. Even higher $SQNR$ will have a diminishing return in performance at the expense of circuit overheads, as the sensor output will be limited by the overall SNR. Therefore, an acceptable target of $Q = Q_0$ can be set as

$$Q_0 \geq \frac{SNR - 1.76}{6.02} \quad . \tag{18}$$

In Eqs. (1) and (2), the amplitude d_0 and frequency Ω of the mechanical vibration are introduced to the NCS signal model. When the mechanical vibration is approximated by a string oscillation model [40], [41], the relationship of d_0 and Ω can be presented as

$$E = \frac{1}{2}\mu\lambda_m\Omega^2 d_0^2 \tag{19}$$

where E is the energy of the mechanical oscillation, μ is the mass per unit length, λ_m is the corresponding wavelength. When the tissue vibration has a constant length of l, the energy E_l on this part can be presented as

$$E_l = \frac{E}{\lambda_m} l = \frac{1}{2}\mu\Omega^2 d_0^2 l = \frac{1}{2} M\Omega^2 d_0^2 \tag{20}$$

where $M = \mu l$ is the vibration mass. Eq. (20) indicates that when the vibration energy is constant, d_0 is inversely proportional to Ω. This will be another guideline to tune η, as the system often needs to capture a broad range of the mechanical vibration in different d_0 and Ω.

III. Model Validation

A. Robotic Platform with Known Vibration

A mechanical platform is built to verify the signal model. As shown in Fig. 4(a), the scatterer (grey ball) is mounted on a turntable (blue plate) rotating clockwise. The transmitter (Tx) antenna is deployed 100 mm away from the rotating axis, and the scatterer rotating radius D is used to emulate different vibration magnitudes. The photo of the experimental setup is shown in Fig. 4(b), where the scatterer ball is wrapped by the aluminum foil and mounted on a wooden stick. The software define radio (SDR, Ettus USRP B210) is configured as the transceiver operating at 1.8 GHz. Fig. 4(c) is the power spectra calculated from the experimental data with different oscillation magnitudes. The curves D1 to D4 (blue solid, red dotted, green dash-dotted, and purple dash) are the results from D of 10, 20, 30, and 40 mm, respectively. The frequency is normalized to the rotating speed, which is 10 RPM, and the fundamental frequency, 2nd and 3rd harmonics are shown at the markers of 1, 2 and 3. Each calculated frequency point is denoted as the diamond mark on the curve. The power intensity is normalized to the fundamental frequency peak of D1 and its profile is limited by the fast-Fourier transform (FFT) sampling points.

TABLE I. Comparison of 2nd- and 3rd-order Nonlinearity from Measurements and the Small-signal Model

Magnitude D (mm)	10	20	30	40
R_2 by measurements (dB)	–9.02	–5.32	–0.52	1.66
R_2 by the small-signal model (dB)	–10.27	–7.13	–2.17	2.35
R_3 by measurements (dB)	–28.42	–17.97	–11.41	–7.63
R_3 by the small-signal model (dB)	–27.46	–19.56	–10.43	–5.28

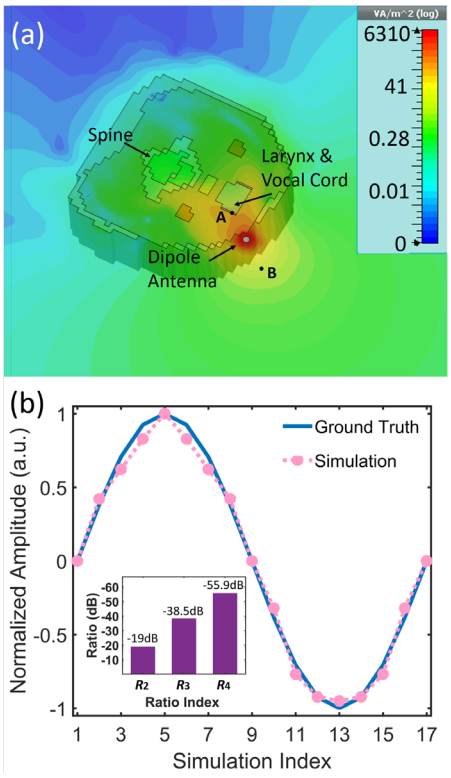

Fig. 5. The CST simulation of the larynx and vocal cord structure. (a) The cross section of the neck area, where the color contour shows the power flow. The power flow at Point A is 235.7 W/m^2, and Point B is 8.6 W/m^2. (b) The demodulated vocal cord vibration signal extracted from the far-field (pink) in comparison with the ground truth (blue). The insert shows the ratios of fundamental oscillation to the 2nd harmonic (R_2), 3rd harmonic (R_3), and 4th harmonic (R_4) from the simulation results.

The nonlinearity factors R_2 and R_3 by measurements are compared with those by Eq. (9) of the small-signal model, and are summarized in Table I, where the match is more than reasonable considering the simplification made in Fig. 1. As D increases, the nonlinearity becomes more obvious, and the total signal power is also stronger.

B. *Electromagnetic simulation*

We will now verify the feasibility of the analytical small-signal formulation by CST Microwave Studio [33] on the throat microphone model. As shown in Fig. 5(a), the neck part with larynx and vocal cord is composed by the computerized tomography (CT) data and the bio-material library in CST. A dipole antenna is deployed and driven by the discrete port with the default 1 W input at 1.8 GHz and 50-Ω impedance. The color contours show the significant RF power flow of the neck cross section, especially considering the symmetric radiation pattern of the dipole antenna in free space. Within the near-field region of the antenna, the electromagnetic field can be regarded as a time-varying static field, which helps more energy couple into the human tissue with a higher dielectric constant [42]. To illustrate this enhanced coupling, two points are added equidistant and symmetric to the dipole antenna are monitored as Points A and B, which are in the human tissue near the vocal cord and outside the body, respectively. The power flow at Points A and B are 235.7 W/m^2 and 8.6 W/m^2, as recorded from the simulation when the antenna is fed by a 30-dBm source of 50-Ω impedance. The significantly higher power flow at Point A indicates that more energy is directed to the sensing area in the human tissue, which is resulted from the NCS principle. The dimension of the vocal cord is modified to emulate the motion of the permittivity boundary, following the ground-truth sinusoidal curve (blue) in Fig. 5(b) by 17 simulation points. The far-field (2 meters away from the dipole antenna) electric filed is recorded as the received signal for each simulation condition. We set the received signal from simulation index 1 as the non-modulated signal, and then normalize the received signal as the pink dots in Fig. 5(b). From the simulation results we can see that the interpreted pink curve matches the ground truth with reasonable distortion which is used to extract the harmonic components. The nonlinear factors of R_2, R_3, and R_4 from the simulation results are compared to Eq. (9) and summarized in Table II. Notice that the simulation is a quasi-static setup and

TABLE II. COMPARISON OF NONLINEARITY FROM SMALL-SIGNAL MODEL AND CST SIMULATION

	R_2 (2nd/1st)	R_3 (3rd/1st)	R_4 (4th/1st)
CST simulation (dB)	–19.0	–38.5	–55.9
Small-signal model (dB)	–18.2	–42.3	–59.1

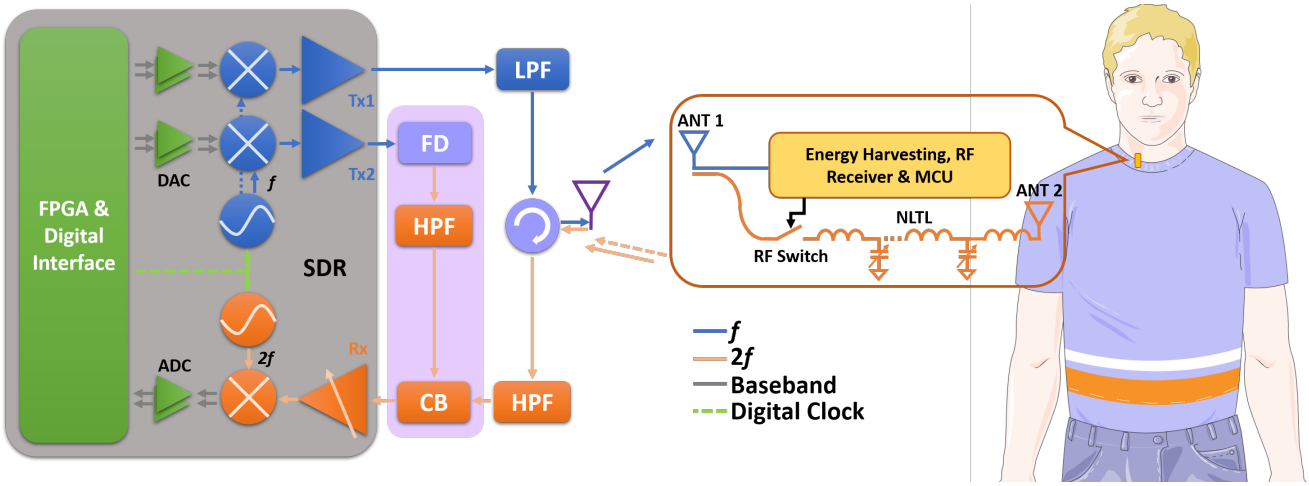

Fig. 6. The schematic of the NCS vocal cord sensor based on the harmonic RFID system.

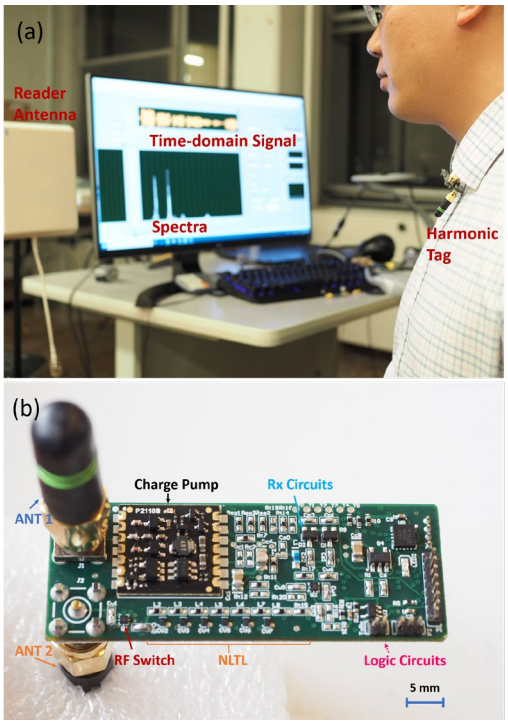

Fig. 7. (a) The photo of the NCS vocal-cord sensor. A harmonic tag is attached on the collar and the reader antenna is about 1.5 meters away. The demodulated time-domain signal and spectra are shown on the screen. (b) The photo of the harmonic tag deployed in the experiment.

the dynamic Doppler effect is not accounted for.

IV. Experimental System for Vocal Cord Sensing

A. The Passive Harmonic RFID System

We used the vocal-cord vibration as the vital-sign source to demonstrate the small-signal analysis and the associated signal adaptation. The harmonic RFID system [1], [34] was chosen to illustrate the NCS vocal-cord sensing. Fig. 6 shows the system schematic and an experiment photo is shown in Fig. 7(a). A passive harmonic tag by a printed circuit board (PCB), as shown in Fig. 7(b), was deployed on the collar close to the larynx. The schematic of the harmonic tag is in the insertion of Fig. 6. The harmonic reader was configured by the same SDR in Sec. III. The downlink signal was generated from Tx1 at 900 MHz and 30 dBm, which went through a circulator, fed to a dual-band antenna through a low-pass filter (LPF), and was finally received by antenna 1 (ANT 1) of the harmonic tag. Part of the energy was harvested by the RF-to-DC converter to power up the tag digital circuits, and another part of the energy was coupled to the nonlinear transition line (NLTL) to generate the 2nd harmonic signal at 1.8 GHz to be emitted from Antenna 2 (ANT 2) for NCS sensing. The RF switch before the NLTL was to modulate the tag ID on the uplink signal with on-off keying (OOK) for tag multiplexing. As described previously in Fig. 6, two parts of the NCS signals, i.e., the vital-sign modulated signal and non-modulated signal (orange arrows with the dashed and solid lines), were received by the harmonic reader. According to Eq. (11), another Tx (Tx2) of the SDR was configured to generate S_{bias} at 900 MHz, and up-converted by a frequency doubler (FD), which was then filtered by a high-pass filter (HPF) and injected into the received NCS signal in the combiner (CB) to be received by the SDR Rx for further demodulation and processing. As shown in Fig. 7(a), the dual-band reader antenna was approximately 1.5 meters away from the harmonic tag. The received vocal-cord signals are shown on the computer screen. The bias signal S_{bias} from Tx2 were controlled by adjusting the phase ϕ_{Tx2b} and amplitude A_{Tx2b} of the corresponding I/Q signals generated by the digital-to-analog convertor (DAC), so that the amplitude and the phase of the injected signal can be tuned accordingly. Both ADC and DAC were set to 1 MSps (10^6 samples per second) and the frequency of the I/Q signals was set as 110 kHz. The magnitude of the digitized signal was extracted as the raw NCS signal and then down sampled to 40 kSps (10^3 samples per second) for the vocal-cord vibration signal analysis.

In the system configuration as shown in Fig. 6, the RFID reader is similar to the DC-coupled CW radar transceiver [23], [43], but with a synchronized harmonic Rx. Due to the frequency isolation between reader Tx and Rx, the Rx noise floor can be readily lower with a simpler hardware design, using LPF and HPF at Tx and Rx, respectively, to achieve better Rx sensitivity and SNR. The harmonic RFID tag makes the sensing to be local by near-field coupling, so that the sensing spatial resolution does not rely on the reader Tx and Rx antenna directivities, but mainly by the near-field proximity of the sensing signal from the harmonic tag. Because the harmonic reader in this work shares similarities with DC-coupled CW radar, the DC cancelation methods [24], [43], [44] applied in these radar systems could be adapted in the NCS system. In this work, we instead opt to use a separate Tx2 to provide the balance signal S_{bias} for DC adjustment, mostly to allow for future system extensibility. For example, to extend the system to simultaneous multi-tag sensing with the tag CDMA protocol [45], S_{bias} in the reader needs to follow the tag CDMA as well in order to balance the signal bit-by-bit from each tag according to the CDMA code table. Simultaneous multi-point sensing is one of the major differences between the far-field radar system and the proposed NCS system [2], in which case the balance signal injection from Tx2 is necessary. In addition, S_{bias} can further provide more flexibility and faster response time for future noise cancelling algorithms to compensate external interferences [5], [20], [46], which is important to mitigate motion interferences.

The link budget between the reader and the harmonic sensing tag can be estimated by Frii's law,

$$P_r = P_t + G_t + G_r + 20\log(\frac{\lambda}{4\pi L}) \quad (21)$$

where P_t and P_r are the reader Tx and tag Rx power, G_t and G_r the reader Tx and tag Rx antenna gain, λ the wavelength, and L the distance between Tx and Rx. We estimate the link budget under the condition of P_t = 30 dBm, G_t = 8 dB, G_r = 3dB, and λ = 0.3 m for the downlink and 0.15 m for the uplink of harmonic backscattering. When L = 3 m, the tag Rx power will be 0 dBm. The nonlinear transmission line (NLTL) has a 2nd-harmonic conversion loss of 15 dB, which renders the tag Tx as well as the NCS detecting signal at −15 dBm. We estimated the total

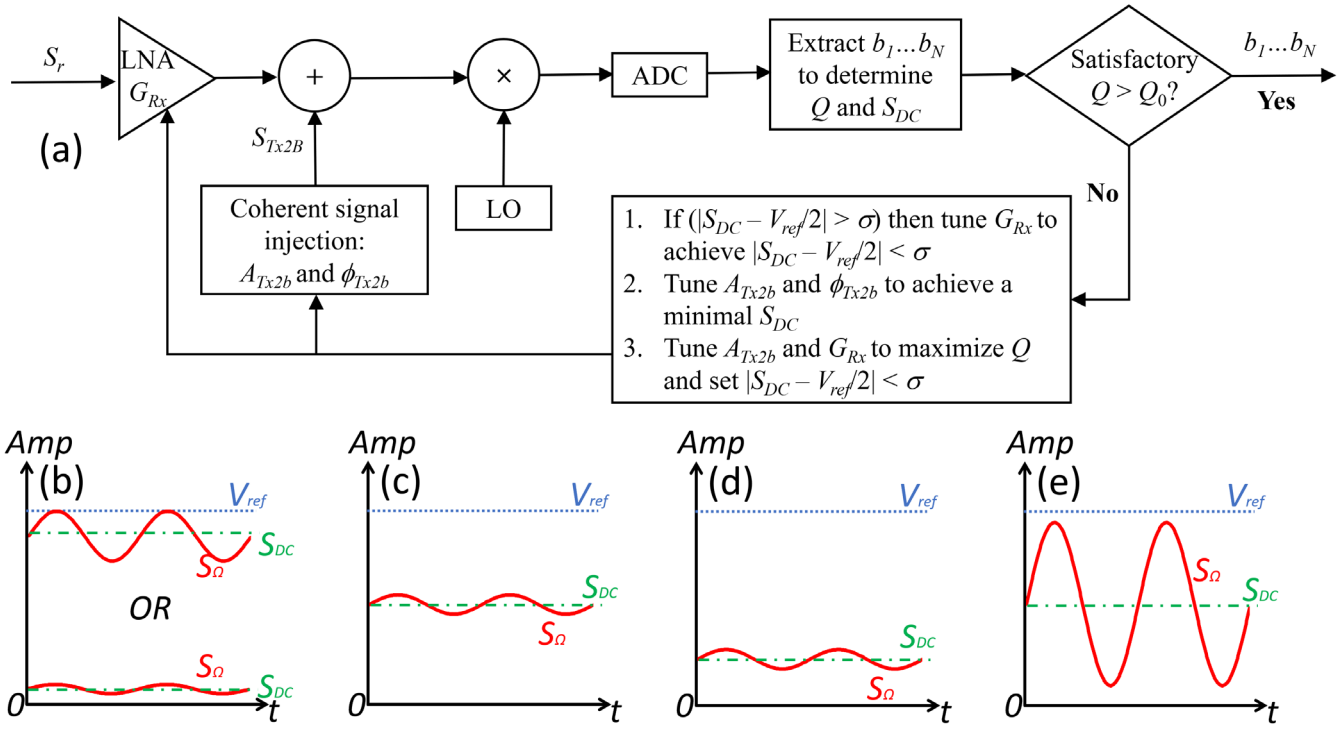

Fig. 8. The signal flow to maximize Q without DC decoupling before ADC. (a) The signal diagram with the digital feedback control. (b) Two possible scenarios of the incoming signal are shown with improper S_{DC} and NCS S_Ω, where S_{DC} is tuned approximately to $V_{ref}/2$ by G_{Rx} in (c), followed by Tx2 injection with tunable ϕ_{Tx2b} and A_{Tx2b} to compensate the non-modulated part, which is manifested in a significantly reduced S_{DC} in (d). Finally, A_{Tx2b} and G_{Rx} were adjusted simultaneously until a sufficiently large $Q > Q_0$ is reached in (e). Q_0 and voltage tolerance σ are preset parameters. LNA stands for low-noise amplifier; LO for local oscillator.

body coupling loss at 26 dB from the simulation results shown in Fig. 5. Then based on Frii's equation of the uplink, the reader Rx power will be −78 dBm. With a noise floor of −110 dBm, which can be readily achieved in the harmonic RFID system due to the downlink-uplink isolation and narrow bandwidth, the resulting reader Rx SNR is 32 dB. When L is shorter, the signal strength and SNR will be higher. This simplified link budget analysis has not considered potential sources of strong RF interferences. Additionally, at the maximum operating range, the tag Rx power and the reader Rx SNR can be further degraded in realistic scenarios. On the other hand, the system performance can be improved by reducing the reader Rx noise floor, increasing tag harmonic generation efficiency, and more sophisticated signal modulation methods.

The harmonic RFID system has several advantages to realize wireless NCS for vocal-cord sensing. The passive design by PCB emulates the commercial RFID paper tag [47] with integrated circuits (IC), so the size can be eventually reduced significantly and integration with garment does not have the concern of battery maintenance and recharging. The 2nd harmonic backscatter as the uplink signal will not be polluted by the downlink signal from the strong reflection by the body. If Tx and Rx were to operate at the same band, the strong reflection can easily saturate and jam Rx. With the harmonic backscatter design, the large spectral separation isolates the downlink and uplink well, and the weak backscattered NCS signal will not be overwhelmed by the phase noise skirt from the high-power Tx. Hence the sensitivity and SNR can be much higher than the conventional RFID system [48], [49].

B. The Signal Adaptive Control Method

To optimize the operational point before ADC without resorting to DC decoupling, the amplitude A_{Tx2B} and phase ϕ_{Tx2B} of the Tx2 baseband signal can be controlled, as well as the gain G_{Rx} of Rx low-noise amplifier (LNA). Closed-loop feedbacks are implemented to update these parameters as shown in Fig. 8. The signal flow is shown in Fig. 8 (a). In the booting process, A_{Tx2B} is set to zero and the algorithm will first analyze $S_{baseband}$. For example, two possible sets of digitally sampled S_{DC} and S_Ω are shown in Fig. 8(b), where the signal strength is either too strong or weak, and the gain of Rx G_{Rx} will be tuned until to the proper S_{DC} level is reach with a tolerance σ of $V_{ref}/2$, as shown in Fig. 8(c). Both modulated and non-modulated levels are controlled by G_{Rx}, which is the reason why the system cannot achieve the optimal operational point by tuning G_{Rx} alone. When S_{DC} is biased at the middle of the ADC range, A_{Tx2B} and ϕ_{Tx2B} will be tuned next. The signal from Tx2 is coherent with the received signal, as both are derived from the same clock reference. The control software adjusts both A_{Tx2B} and ϕ_{Tx2B} while monitoring S_{DC} to reach a minimum level as shown in Fig. 8(d). Then G_{Rx} and A_{Tx2B} are boosted together in steps while monitoring the signal level to set S_{DC} back $V_{ref}/2$ with proper $Q > Q_0$, as shown in Fig. 8(e).

V. Vocal-Cord Experiments

To verify our theory and system capability, we performed vocal-cord sensing by egophony. The system in Figs. 6 and 7(a) was first operated without Tx2 injection. In order to adjust the signal level, only the Tx1 power and G_{Rx} were adjusted to tune

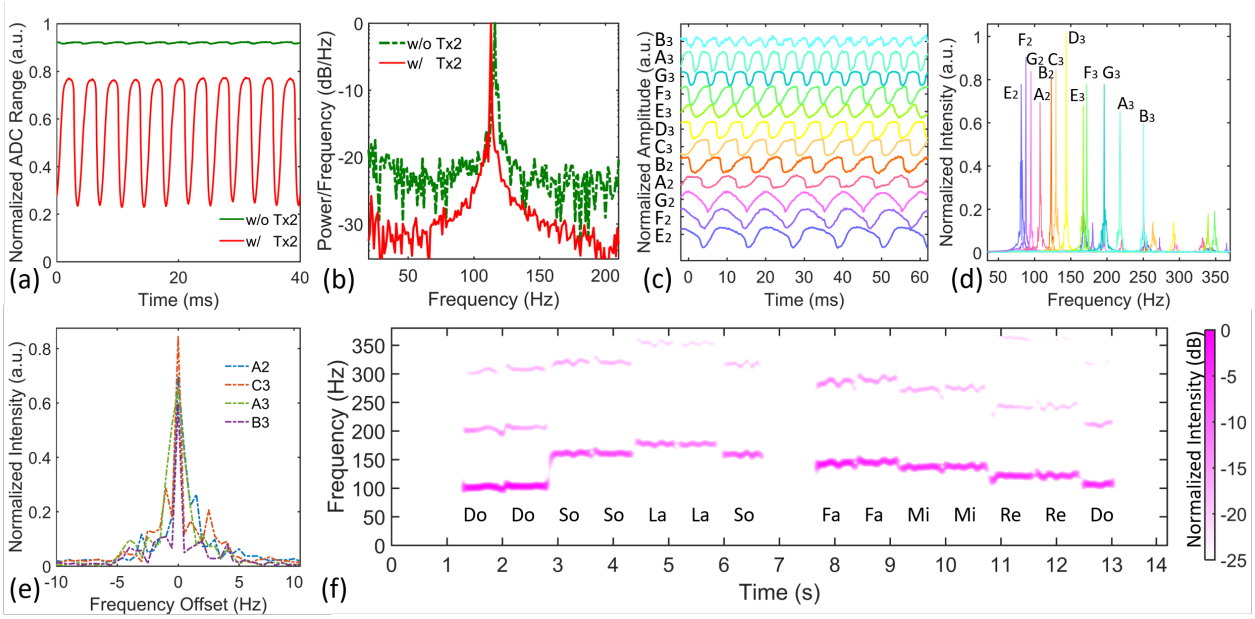

Fig. 9. The experimental data of the recorded vocal-cord vibration calibrated with musical notes. (a) The NCS signal without Tx2 injection (green) and with nearly optimal Tx2 injection (red). (b) The power spectral density of the curves in (a). (c) The time-domain NCS signal from pitch E_2 to B_3. (d) The spectra of the signals in (c). (e) The zoomed-in spectral skirts of pitch A2 (blue), C3 (red), A3 (green) and B3 (purple). (f) The frequency-time analysis of the dynamic recording of "Twinkle, Twinkle, Little Star".

the signal to the best possible level. The person hummed a constant pitch at 110 Hz (musical note A_2) with a reference from an electronic keyboard. As shown by the green curve in Fig. 9(a), which was sampled by ADC and normalized to the full range, the signal without Tx2 signal injection was dominated by S_{DC} and the vibration was barely noticeable. The ADC utilization ratio η is at 0.0091 for the NCS signal, which corresponded to Q = 5.2 bits within the 12-bit ADC. The low ADC utilization ratio not only reduced the signal resolution with loss of waveform details, but also the ADC quantization noise and clock jitter noise were more significant to decrease the overall SNR. The corresponding power spectral density is shown in Fig. 9(b), where SNR was estimated to be 20 dB. At this operational point, if the signal were further amplified by increasing the Tx1 power or G_{Rx}, η and Q could increase only negligibly, with the risk S_{DC} saturating ADC with strong signal distortion. The measurement was conducted again with the feedback control in Fig. 8, and the recorded signal was shown as the red curve in Fig. 9(a). With Tx2 injection and properly tuned Tx1 power and G_{Rx}, the intended signal was biased properly and the ADC range was significantly more utilized where η = 0.54 and Q = 11.1 bits within the 12-bit ADC. The power spectral density was also shown in Fig. 9(b), where SNR was around 30 dB with 10 dB improvement from the previous scenario. When Tx2 injection is applied, Tx1 gain can be increased not only to generate stronger NCS signals, but also to relieve the concerns of LNA saturation. Evaluated from the retrieved Q values in Fig. 9(a), the NCS signal magnitude and ADC utilization ratios have been improved by 59 times, or equivalently 35 dB in SQNR. And SNR is improved by 10 dB from the power spectral density analysis.

Following the test, the person followed the keyboard in GarageBand [50] to hum the notes from E_2 to B_3. The time-domain signals and spectra are shown in Figs. 9(c) and (d), respectively. From the time-domain signals we can clearly see that the waveforms are not the monotone sinusoidal shape due to the harmonics caused by both the vocal cord vibration characteristics and sensor nonlinearity. Most of the harmonics likely come from the tone of the person under test, as the low level of the vibration amplitude and the low equivalent permittivity around the vocal cord can hardly generate such strong harmonics. Considering the tissue permittivity and operating frequency, the NCS 2nd- and 3rd-order nonlinearity can be estimated between the solid and dashed lines in Fig. 2(b) with β approximately at 0.62. The time-domain signals also have the trend of showing lower amplitudes for the higher pitch,

TABLE III. THE FREQUENCY MEASUREMENTS FROM THE SPETRA PEAKS IN EGOPHONY

Pitch	E_2	F_2	G_2	A_2	B_2	C_3	D_3	E_3	F_3	G_3	A_3	B_3
Freq. (Hz)	82.41	87.31	98.00	110.00	123.47	130.81	146.83	164.81	174.61	196.00	220.00	246.94
Meas. (Hz)	81.5	88.0	95.0	107.5	123.0	129.5	143.5	167.5	172.0	196.0	218.0	249.5
Error (Hz)	−0.91	0.69	−3.00	−2.5	−0.47	−1.31	−3.33	2.69	−2.61	0	−2.00	2.56
Error SD (Hz)	1.95											
SNR (dB)	36.2	36.8	36.5	35.7	36.3	36.5	37.3	35.6	36.2	36.2	35.4	35.0

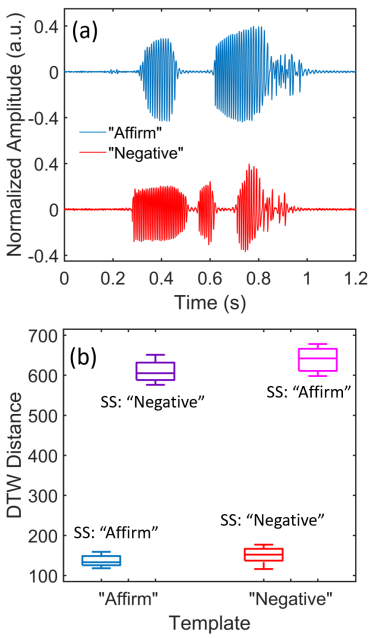

Fig. 10. The vocal cord detection for the procedure words "Affirm" and "Negative". (a) The representative time domain signals of "Affirm" (blue) and "Negative" (red). (b) The box-whisker plots of the DTW distances for the signal recognition.

which is caused by the effect explained in Eq. (20), as well as the vocal cord vibration range of the person under test. The spectra of each time-domain signal are shown in Fig. 9(d). The pitch names are denoted next to the corresponding peaks. The frequency values of each pitch, the measurements from the spectra, and the resulting errors are listed in Table III. The standard deviation (SD) of the frequency error is 1.95 Hz, which includes system errors, measurement inaccuracy, and possibly off-tune by the person. Based on the spectra, SNRs are calculated and listed in Table III. The highest SNR is achieved at the peak of D_3 which is 37.3 dB, and lowest is at B_3 which is still reasonable at 35 dB. The signal skirts can be clearly observed from each peak, which is caused by the pitch drifting or volume changing during the recorded data. The signal skirts of pitch A_2 (blue), C_3 (red), A_3 (green) and B_3 (purple) are shown in Fig. 9(e). The harmonics introduced by modulation nonlinearity should be below the noise floor according to the calculation in Fig. 2(b), with both R_2 and R_3 below –40 dB. The system was then tested with a continuous tune, when the person hummed the first four measures of "Twinkle, Twinkle, Little Star" in A-flat major (Do=A♭, 103.8 Hz). The NCS signal was recorded and then analyzed by the short-time Fourier transform (STFT) as shown in the frequency-time spectra of Fig. 9(f). The recovered audio is included in the Supplementary Video 1.

Because the vocal-cord NCS signal is from the permittivity boundary vibration within the near-field range of the sensing antenna, the system is immune to the ambient noise, which can be applied to the throat microphone in a noisy environment. The sensor can be configured to recognize the procedure words [51] in radio transmission as well. Two commonly used words "Affirm" and "Negative" were tested. The representative time-domain waveforms of the two words were shown in Fig. 10(a). The blue curve was the NCS signal of "Affirm" and the red one was "Negative". When the data were recorded, the background was constantly playing a loud rock music around 110 dB, but the signal is hardly affected. Then each word was recorded for 50 times to verify voice recognition. The waveforms in Fig. 10(a) were selected as the templates for each word. The recordings of "Affirm" and "Negative" were segmented and fed to the standard dynamic time warping (DTW) algorithm [52]. In Fig. 10(b), the blue and purple box-whisker plots were calculated from the DTW distances with the "Affirm" template, comparing with "Affirm" and "Negative" signal sequences (SS), respectively. The red and pink ones were from the "Negative" template, comparing with SS of "Negative" and "Affirm". The DTW results showed that the two words can be distinguished clearly by the NCS throat microphone.

VI. Discussion and Conclusion

We focused our analyses on the signal level, rather than the detailed electromagnetic level, to reach a tangible analytical small-signal model. Separation of the signals as modulated and non-modulated parts is sufficient to guide the quiescent point setup with Tx2 injection. NCS modulates only the local mechanical vibration in the near-field proximity of the sensing antenna, which not only mitigates the motion interference, but also improves the spatial resolution in the multi-tag scenario with multiple sensing points covering an area of interest [2], [53]. The NCS system demonstrated in this work can tolerate mild body movement, such as when the position of the tag is changed by the body surface movement. The feeble motion may only cause simultaneous phase changes in S1 and S2, therefore the demodulated NCS signal represented by the magnitude of the combined S1 and S2 will not be much affected. Additionally, body motion information can be evaluated from the phase change of S1 and S2 in the quadrature receiver. However, when the random body movement is strong, the NCS signal can be seriously interfered, particularly in a channel with heavy multi-path interferences. Fortunately, because the vocal cord vibration usually has much higher frequencies than the body movement and its harmonics, digital filtering to attenuate body motion interference can be more effective for vocal cord vibration retrieval than when the target vital signs have lower frequency features. According to the application of interest, the hardware for NCS can be adapted with different configurations and system sizes [1], [2], [6], [38].

In this paper, the small-signal model in the NCS system was presented, and injected balance signal compensation was utilized to optimize the signal quality. We then verified the analytical formulation by a robotic platform and electromagnetic simulation with known vibration magnitudes. The vocal-cord vibration sensing presented in this paper is a promising strategy to implement the throat microphone. By using the feedback control with signal quality verification, the ADC utilization ratio of the NCS signal can be improved by 59 times, or equivalently 35 dB in SQNR, and the system SNR by 10 dB. The continuous-tone experiments for the music-scale recording and procedure-word recognition were demonstrated as the potential applications.

REFERENCES

[1] X. Hui and E. C. Kan, "Monitoring vital signs over multiplexed radio by near-field coherent sensing," *Nat. Electron.,* vol. 1, no. 1, pp. 74, Jan. 2018.

[2] X. Hui, T. B. Conroy and E. C. Kan, "Multi-point near-field RF sensing of blood pressures and heartbeat dynamics," *IEEE Access*, vol. 8, pp. 89935–89945, May 2020.

[3] P. Sharma, X. Hui and E. C. Kan, "A wearable RF sensor for monitoring respiratory patterns," in *41st Annual International Conference of the IEEE Engineering in Medicine and Biology Society (EMBC)*, Berlin, Germany, July 2019.

[4] P. Sharma, X. Hui, J. Zhou, T. B. Conroy and E. C. Kan, "Robust cardiopulmonary monitoring using wearable radio-frequency sensors," *Nature Partner Journal (NPJ), Digital Medicine*, doi: 10.1038/s41746-020-0307-6, Aug. 2020.

[5] X. Hui and E. C. Kan "Seat integration of RF vital-sign monitoring," in *Proc. 2019 IEEE Int. Microw. Bio. Conf. (IMBioC),* Mar. 2019.

[6] X. Hui and E. C. Kan, "No-touch measurements of vital signs in small conscious animals," *Sci. Adv.,* vol. 5, no. 2, art. eaau0169, Feb. 2019.

[7] C. Li, V. M. Lubecke, O. Boric-Lubecke and J. Lin, "A review on recent advances in Doppler radar sensors for noncontact healthcare monitoring," *IEEE Trans. Microw. Theory Techn.* vol. 61, no. 5, pp. 2046–2060, Apr. 2013.

[8] C. Li *et al.,* "A review on recent progress of portable short-range noncontact microwave radar systems," *IEEE Trans. Microw. Theory Tech.*, vol. 65, no. 5, pp. 1692–1706, Jan. 2017.

[9] C. S. Lin, S. Chang, C. Chang and C. C. Lin, "Microwave human vocal vibration signal detection based on Doppler radar technology," *IEEE Trans. Microw. Theory Techn.* vol. 58, no. 8, pp. 2299–2306, Aug. 2010.

[10] X. Hui, P. Sharma and E. C. Kan, "Microwave stethoscope for heart sound by near-field coherent sensing," in *Proc. Microw. Symp. (IMS), 2019 IEEE MTT-S Int.*, Boston, MA, USA, June 2019.

[11] *Covert recording*, retrieved June 20, 2020. [Online]. Available: https://en.wikipedia.org/wiki/The_Thing_(listening_device)

[12] J. G. Švec, and H. K. Schutte, "Videokymography: high-speed line scanning of vocal fold vibration," *J. Voice*, vol. 10, no. 2, pp. 201–205, Jan. 1996.

[13] M. Hirano, Y. Yoshida, H. Matsushita and T. Nakashima, "An apparatus for ultra-high-speed cinematography of the vocal cords," *Annals of Otology, Rhinology & Laryngology*, vol. 83, no. 1, pp. 12–18, Jan. 1974.

[14] P. Lieberman, "Some acoustic measures of the fundamental periodicity of normal and pathologic larynges," *J. Acoustical Society of America*, vol. 35, no. 3, pp. 344–353 Mar. 1963.

[15] T. Miyoshi, "Electroacoustic converter film, flexible display, vocal cord microphone, and musical instrument sensor," U.S. Patent 9761784B2, Sep. 12, 2017.

[16] S. L. Hamlet and J. M. Reid, "Transmission of ultrasound through the larynx as a means of determining vocal-fold activity," *IEEE Transactions on Biomedical Engineering*, vol. 1, pp. 34–37, Jan. 1972.

[17] E. M. Friedman, "Role of ultrasound in the assessment of vocal cord function in infants and children," *Annals of Otology, Rhinology & Laryngology*, vol. 106, no. 3, pp. 199–209, Mar. 1997.

[18] R. M. Fano, "Theoretical limitations on the broadband matching of arbitrary impedances", *J. Franklin Inst.*, vol. 249, pp. 57–83, Jan. 1950.

[19] D. Vasisht *et al.,* "In-body backscatter communication and localization" in *Proc. 2018 Conference of the ACM Special Interest Group on Data Communication*, pp. 132–146, Aug. 2018.

[20] C. Li and J. Lin, "Random body movement cancellation in Doppler radar vital sign detection," *IEEE Transactions on Microwave Theory and Techniques*, vol. 56, no. 12, pp. 3143–3152, Dec. 2008.

[21] D. Rodriguez and C. Li, "Sensitivity and distortion analysis of a 125-GHz interferometry radar for submicrometer motion sensing applications," *IEEE Trans. Microw. Theory Techn.*, vol. 67, no. 12, pp. 5384–5395, Dec. 2019.

[22] A. Singh and V. M. Lubecke, "Respiratory monitoring and clutter rejection using a CW Doppler radar with passive RF tags," *IEEE Sensors J.*, vol. 12, no. 3, pp. 558–565, Mar. 2012.

[23] A. Rahman, V. Lubecke, E. Yavari, X. Gao and O. Boric-Lubecke, "High dynamic range DC coupled CW Doppler radar for accurate respiration characterization and identification", *Proc. 89th ARFTG Microw. Meas. Conf. (ARFTG)*, pp. 1–4, Jun. 2017.

[24] H.-C. Kuo *et al.*, "A fully integrated 60-GHz CMOS direct-conversion Doppler radar RF sensor with clutter canceller for single-antenna noncontact human vital-signs detection," *IEEE Trans. Microw. Theory Techn.*, vol. 64, no. 4, pp. 1018–1028, Apr. 2016.

[25] G. Wang, C. Gu, T. Inoue and C. Li, "A hybrid FMCW-interferometry radar for indoor precise positioning and versatile life activity monitoring," *IEEE Trans. Microw. Theory Techn.*, vol. 62, no. 11, pp. 2812–2822, Sep. 2016.

[26] J. Yan *et al.,* "Phase-based human target 2-D identification with a mobile FMCW radar platform," *IEEE Trans. Microw. Theory Techn.*, vol. 67, no. 12, pp. 5348–5359, Dec. 2019.

[27] C. Li, J. Wang, D. Rodriguez, A. Mishra, Z. Peng and Y. Li, "Portable Doppler/FSK/FMCW Radar Systems for Life Activity Sensing and Human Localization," in *2019 14th International Conference on Advanced Technologies, Systems and Services in Telecommunications*, Nis, Serbia, pp. 83-93, Oct. 2019.

[28] Y. H. Shin and J. Seo, "Towards contactless silent speech recognition based on detection of active and visible articulators using IR-UWB radar," *Sensors*, vol. 16, pp. 1812, Nov. 2016.

[29] P. Birkholz *et al.*, "Non-invasive silent phoneme recognition using microwave signals," *IEEE/ACM Transactions on Audio, Speech, and Language Processing*, vol. 26, pp. 2404–2411, 2018.

[30] S. Li *et al.*, "A 94-GHz millimeter-wave sensor for speech signal acquisition," *Sensors*, vol. 13, no. 11, pp. 14248–14260, 2013.

[31] M. Geiger, D. Schlotthauer and C. Waldschmidt, "Improved throat vibration sensing with a flexible 160-GHz Radar through harmonic generation," in *Proc. Microw. Symp. (IMS), 2018 IEEE MTT-S Int.*, Philadelphia, PA, USA, June 2018.

[32] C. Chang, C. Lin, S. Chang, C. Lin, Z. Jiang and S. Yu, "Glottal Doppler radar system and its applications to communication and speaker recognition," in *41st Euro. Microw. Conf.,* Manchester, UK, Oct. 2011.

[33] *CST Studio Suite*, retrieved June 20, 2020. [Online]. Available: https://www.3ds.com/products-services/simulia/products/cst-studio-suite/

[34] Y. Ma, X. Hui and E. C. Kan, "3D real-time indoor localization via broadband nonlinear backscatter in passive devices with centimeter precision," in *ACM Mobicom*, Oct. 2016, pp. 216–229.

[35] M. Abramowitz, and I. A. Stegun, *Handbook of Mathematical Functions with Formulas, Graphs, and Mathematical Tables*, US Government Printing Office, Dec. 1972.

[36] D. Colton and T. Kress, *Inverse Acoustic and Electromagnetic Scattering Theory*, Springer Nature, Nov. 2019.

[37] B. P. Lathi, *Modern Digital and Analog Communication Systems*, 3ed, Oxford University Press, Inc., 1998.

[38] J. Zhou, P. Sharma, X. Hui and E. C. Kan, "Wireless wearable RF sensor for long-term vital-sign monitoring on chelonians," *IEEE J. Electromagnetics, RF and Microwaves in Medicine and Biology,* doi: 10.1109/JERM.2020.2998761, 2020

[39] *Taking the mystery out of the infamous formula, "SNR = 6.02N + 1.76dB," and why you should care*, retrieved June 20, 2020. [Online]. Available: https://www.analog.com/media/en/training-seminars/tutorials/MT-001.pdf

[40] K. F. Ggraff, *Wave Motion in Elastic Solids*, Courier Corporation, Apr. 2012.

[41] R. L. Miller, "Nature of the vocal cord wave," *J. Acoustical Society of America*, vol. 31, no. 6, pp. 667–677, June 1959.

[42] V. P. Yakubov, V. P. Belichenko, S. E. Shipilov, A. S. Mironchev, A. V. Klokov and A. S. Zapansnoy, "The new near-field approach for microwave tomography of absorbing media," *J. App. Phys.*, vol. 126, no. 10, art. 105101, Sep. 2019.

[43] D. Tang, J. Wang, W. Hu, Z. Peng, Y. Chiang and C. Li, "A DC-coupled high dynamic range biomedical radar sensor with fast-settling analog DC offset cancelation," *IEEE Transactions on Instrumentation and Measurement*, vol. 68, no. 5, pp. 1441–1450, May 2019.

[44] P.-H. Wu, J.-K. Jau, C.-J. Li, T.-S. Horng and P. Hsu, "Phase- and self-injection-locked radar for detecting vital signs with efficient elimination of DC offsets and null points," *IEEE Trans. Microw. Theory Techn.*, vol. 61, no. 1, pp. 685–695, Jan. 2013.

[45] X. Hui, Y. Ma and E. C. Kan, "Code division multiple access in centimeter accuracy harmonic RFID locating system," *IEEE J. Radio Freq. Identif.,* vol. 1, no. 1, pp. 51–58, Aug. 2017.

[46] C. N. Hansen*, Understanding Active Noise Cancellation*, CRC Press, May 2002.

[47] *Alien Technology*, retrieved June 2020. [Online]. Available: https://www.alientechnology.com/products/tags/

[48] X. Hui and E. C. Kan, "Radio ranging with ultrahigh resolution using a harmonic radio-frequency identification system," *Nat. Electron.*, vol. 2, no. 3, pp. 125, Mar. 2019.
[49] Y. Ma and E. C. Kan, "Accurate indoor ranging by broadband harmonic generation in passive NLTL backscatter tags," *IEEE Trans. Microw. Theory Techn.*, vol. 62, no. 5, pp. 1249–1261, May 2014.
[50] *GarageBand*, retrieved June 20, 2020. [Online]. Available: https://apps.apple.com/us/app/garageband/id408709785
[51] *Procedure words*, retrieved June 20, 2020. [Online]. Available: https://en.wikipedia.org/wiki/Procedure_word
[52] H. Sakoe and S. Chiba, "Dynamic programming algorithm optimization for spoken word recognition," *IEEE Trans. Acoust. Speech Signal Process,* vol. 26, no. 1, pp. 43–49, Feb. 1978.
[53] X. Hui and E. C. Kan, "Collaborative reader code division multiple access in the harmonic RFID system," *IEEE J. Radio Freq. Identif.,* vol. 2, no. 2, pp. 86–92, July 2018.

Xiaonan Hui received the B.S. degree from Northeastern University, China in 2012, and the M.S. degree from Zhejiang University, China in 2015, all in electrical engineering. He is currently pursuing the Ph.D. degree in electrical and computer engineering at Cornell University, Ithaca, NY, USA.

Thomas Conroy received the B.S. degree from Clarkson University, Potsdam, New York in 2019 in electrical engineering. He is currently pursuing the Ph.D. degree in electrical and computer engineering at Cornell University, Ithaca, NY, USA.

Edwin C. Kan received the B.S. degree from National Taiwan University in 1984, and the M.S. and Ph.D. degrees from University of Illinois, Urbana-Champaign in 1988 and 1992, respectively, all in electrical engineering. He has served in the Air Force, Taiwan, R. O. China as a second lieutenant from 1984 – 1986. In January 1992, he joined Dawn Technologies as a Principal CAD Engineer. He was then with Stanford University as a Research Associate from 1994 to 1997. In 1997, he joined the School of Electrical and Computer Engineering, Cornell University, Ithaca, NY as an assistant professor, where he is now a professor. His research interests include RF biosensors, RFID, RF sensors for smart buildings, CMOS technology, Flash memory, molecular sensors, and technology computer-aided design (TCAD).

Appendix F

(PDF downloaded from IEEE) X. Hui and E. C. Kan, “Seat integration of RF vital-sign monitoring”, *International Microwave Biomedical Conf. (IMBioC)*, Nanjing, China, May 6 – 8, 2019.

Seat Integration of RF Vital-Sign Monitoring

Xiaonan Hui and Edwin C. Kan
School of Electrical and Computer Engineering
Cornell University, Ithaca, NY, USA
{xh273, eck5}@cornell.edu

***Abstract*—Monitoring of the vital signs including heartbeat, respiration and blood pressure for long duration is critical for driver alertness, smart home, E-health and Internet of Things (IoT), especially when the user takes a seat as in the cases of seniors, patients, and car drivers. The sensing system should be integrated into the seat cushion and "invisible" to the users to provide continuous, comfortable and convenient monitoring. However, current vital-sign sensing technologies often require skin-touch electrodes or external readers with clear line-of-sight, and are hence difficult to be deployed into the chair setup. Piezoelectric, accelerometer and ultrasound sensors can suffer from mechanical damping in soft cushion and limited sensitivity. The radar-based system provides non-contact measurements based on signal reflection from body surfaces, but high areal resolution to accommodate multiple observation points on one user often incurs significant system cost. In this work, an active near-field coherent sensing (NCS) system is integrated into generic seat structures to assess the heartbeat, respiration and blood pressure of the occupant. With the improved balancing bridge design, the weak cardiopulmonary signals from the back and the femoral pulse from the thigh area can be accurately detected for the pulse transit time and the derived blood pressure. Variation of sensing positions due to different postures and body sizes is investigate for robust placement considerations.**

I. Introduction

Vital-sign monitoring for long duration is a critical technology for E-Health, assisted living, driver alertness, wearables, and Internet of Things (IoT). Personal devices nowadays can provide heartbeat information through electrocardiogram (ECG) and photo-plethysmography (PPG) with direct skin contact [1,2], but the extra device carried by the user makes it not an "invisible" technique and hence less convenient and comfortable. In the present days, people spend enormous amount of time in some forms of sitting during work, leisure, driving and talking. Thus the extra wearable devices can be avoided if the sensing system can be integrated into the structures of sofas, driver seats, and lounge chairs. It is difficult to integrate ECG and PPG into the seat cushion, even considering capacitive ECG [3]. The piezoelectric and accelerometer-based methods [4,5] have been commercialized in smart beds, but still suffer from poor signal quality and problematic mechanical propagation due to the soft cushion materials in common chairs. The radio frequency (RF) methods [6] based on the signal reflection of the user body require an off-body reader with the antenna in the far fields.

This project is supported by Department of Energy (DoE) of United States under the Advanced Research Projects Agency – Energy (ARPA-E) project numbers: DE-AR0000528 and DE-AR0000946, as well as Cornell Technology Acceleration and Maturation (CTAM) Fund.

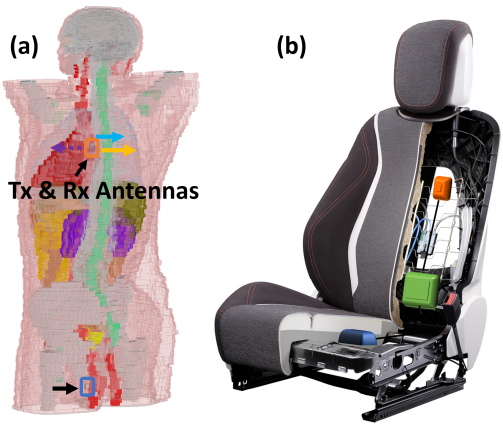

Fig. 1. Vital-sign monitoring by active near-field coherent sensing. (a) Deployment of the sensing antennas close to the heart from the back and the thigh artery from the bottom. (b) The conceptual illustration for integration with seat cushion.

Multi-point detection of a single occupant such as the heartbeat and femoral pulse involves narrow beamforming and remains challenging due to limited sensitivity and spatial resolution.

In this paper we introduce an active near-field coherent sensing (NCS) system [7] to monitor the vital signs of the seat occupant with multiple sensing points. The sensor can be integrated into the cushion and hence "invisible" to the user. The sensing antennas are placed close to the mechanical motion source of the targeted vital signs. As shown in Fig. 1(a), the back sensing antenna in the orange box is placed to the lower part of the left rhomboid major area in the electromagnetic torso model (left-back 45º view), and another antenna in the blue box is placed close to the upper thigh area for the femoral pulse. Fig. 1(b) shows a possible schematic for the NCS system integrated into the seat and back cushions. The orange block indicates the heart sensing module and the blue block the femoral pulse sensing module, which are connected to the central console (the green block) providing power, synchronization and signal processing. The seat NCS system can catch the heartbeat, respiration, pulse as well as the pulse transit time [8,9] to estimate the blood pressure.

II. System Design and Experiment Results

As shown in Fig. 1(a), when the antenna transmits the sensing signal, a significant part of the RF energy will couple into the human body (the purple arrow) in the near-field region, where the motion of the dielectric boundaries will change both the radiation into the free space and the reflection back to the transmitter (Tx) [7]. For the seat setup, far-field sensing is

inconvenient as an external reader off the chair is required, not to mention the noisy RF ambient in the case of car cabins. We can opt to use the NCS antenna reflection, which is however difficult to implement here as well. The NCS signals from the back and thigh are weaker than those from the chest and wrist due to deeper positions of the heart and artery. When the commercial antenna designed for free-space operations is deployed on the human body, the antenna will be detuned, resulting in a large antenna reflection to the receiver (Rx) low-noise amplifier (LNA). The weak NCS signal can be easily saturated out due to the limited precision of the analog-to-digital converter (ADC) in the baseband processing. Furthermore, a circulator with high Tx-to-Rx isolation is often bulky, lack of which will have further Rx saturation by self-interference to cause the loss of the NCS signal.

To reduce the overall system size and enable fast software-defined radio (SDR) prototyping, we design a new self-contained NCS system with a pair of small commercial antennas, where the motion of the dielectric boundary inside the body will modify the near-field coupling between the two antennas. The non-modulated coupling of the Tx-to-Rx signal in Fig. 2 including the signal at *f* in the blue arrow and the signal at *2f* in the orange arrow in all possible paths will need to be adaptively reduced by the balancing bridge to maximize the NCS sensitivity. The Rx antenna can be deployed closed to the Tx antenna for a small system size, as long as a significant portion of the RF energy from the Tx antenna will be in the desirable region inside the human body. The non-modulated signals should not saturate Rx due to LNA linearity and ADC dynamic range so that their magnitude and phase can be reasonably measured. The Rx signal model here is similar to the interferometer principle. When the amplitudes of the modulated and the non-modulated reference signals are on the same level, the system can achieve the best modulation efficiency and dynamic range in the demodulated signal magnitude after the Rx gain.

In Fig. 2, an SDR by Ettus X310 is configured as the 2nd harmonic transceiver, which is to reduce the self-interference and to improve the NCS signal-to-noise ratio (SNR) [10,11]. The Tx and Rx frequency synthesizers share the same clock source, so the transceiver is coherent and can demodulate both

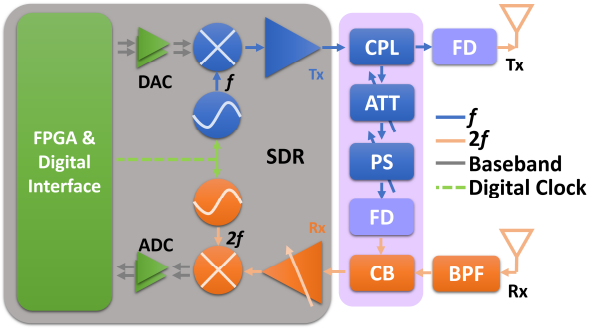

Fig. 2. The block diagram of a single-channel active NCS system with the balancing bridge to maximize the vital-sign sensitivity.

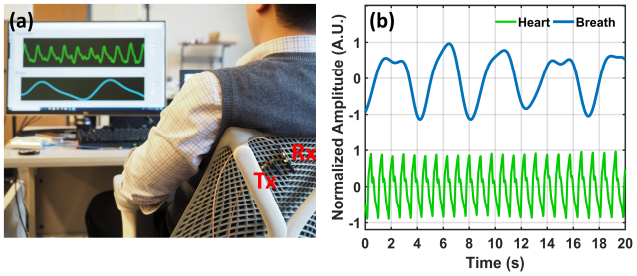

Fig. 3. Experimental setup on a seated user with NCS measurements. (a) Photo with the visible sensing antenna mounted on the outside back of the chair. (b) Measured respiration in blue and heartbeat in green.

the amplitude and phase information of the Rx signal. The Tx signal is transmitted from the Tx port at the frequency around 475 MHz. A major part of the RF energy is going through the coupler (CPL) to the frequency doubler (FD) and then to the Tx antenna where the sensing signal is coupled to the human body at the harmonic frequency in the 950 MHz band. The signal chain from CPL to the combiner (CB) is the balancing bridge which matches the received modulated and non-modulated signals to achieve high modulation efficiency and dynamic range. The coupled signal from CPL goes through the tunable attenuator (ATT) and tunable phase shifter (PS), which is then converted to the 2nd harmonic signal by the other FD. The balancing signal is then combined with the received NCS-modulated signal from the Rx antenna, feeding into the Rx port of the SDR. Based on the received signal, ATT and PS can be feedback-controlled to improve signal quality. The digital signals are processed in the computer with LabVIEW. The equivalent sampling rate of the vital signs is 500 Sps.

The sensing of heartbeat and respiration from the seatback Tx-Rx antennas is shown in Fig. 3(a). The computer screen shows the heartbeat (green) and the respiration (blue) waveforms. There is no need for direct skin contact. The sensing antennas are attached behind the seatback structure, and the person under test can wear daily clothes. In Fig. 3(b), the blue curve shows the respiration waveform after a bandpass filter from 0.1 Hz to 0.9 Hz. The green curve is the cardio waveform after a bandpass filter from 0.8 Hz to 50 Hz. Because the NCS signal measures the mechanical motion, the NCS heartbeat signal mostly reflects the fundamental beating. The balancing bridge not only can match the non-modulated

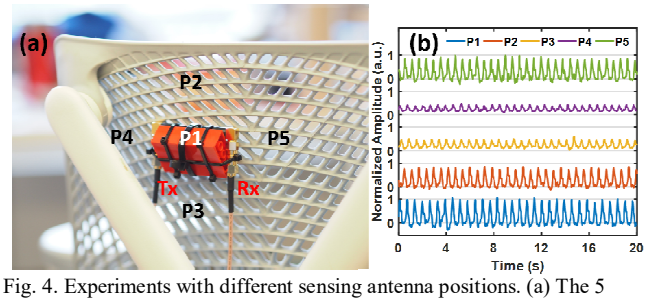

Fig. 4. Experiments with different sensing antenna positions. (a) The 5 positions of the sensing antenna. (b) The heartbeat signals of each position.

and modulated signals for high signal quality, but also can compensate for the interference from body motion. We also investigated the antenna placement variation for the heartbeat signal to estimate the posture and body size effects. At 5 positions (P1 to P5) in Fig. 4(a), the extracted heartbeat waveforms are shown in Fig. 4(b). The system setting was controlled to give the same measurement configurations, and the waveforms were normalized to the maximum amplitude of the signal from P1. When the sensing antenna pair was at P1, P2 and P5, the signal strength were at the similar level. At P3 and P4, the far offset to the heart position made the signal much weaker with reduced SNR.

Although the NCS system can apply code division multiple access (CDMA) on multiple tags to realize the synchronized multiple point monitoring [12], in this work, we adopted a parallel SDR system to detect the femoral pulse as the distal point. In the Ettus X310 SDR, we opted to use dual RF daughter boards (UBX 160-MHz) that were RF and baseband synchronized. Other SDR platforms such as Ettus B210 are also capable of providing two pairs of transceivers. The synchronized baseband can enable the reader CDMA protocol [13] for multiple readers sharing the same reading zone with minimal interference.

The femoral pulse can be used for two purposes: First, it provides another estimate of the heartrate even when the occupant does not lean back and the signal from the seat back is lost. Second, the pulse transit time (PTT) from the heart to the peripheral artery can be measured to estimate the blood pressure [8]. Because the NCS signal is dominated by the fundamental motion component in comparison with its harmonics, to achieve higher PTT accuracy, the signals are equalized to amplify the high-frequency components to pick out the sharp peaks [14]. As shown in Fig. 5(a), the sharp peaks of the equalized heartbeat (pink) and femoral pulse (light blue) waveforms were detected to calculate PTT. After calibration [9], the systolic (blue) and diastolic (orange) blood pressures were derived in Fig. 5(b), where the dash curves represented their moving averages for every 12 heartbeats. The green markers were the results measured from the OMRON BP760N arm-cuff blood pressure monitor, where the arm remained steady at the heart level. At the beginning, both systolic and diastolic pressures were slightly high around 131 mmHg and 90 mmHg, because the occupant under test just took the seat. The pressures dropped to 125 mmHg and 85 mmHg after quiet sitting. Compared to the cuff-based method, the current PTT method can estimate the blood pressures from each heartbeat and does not need extra wearing gadgets. However, individual user calibration and two-point monitoring are presently required.

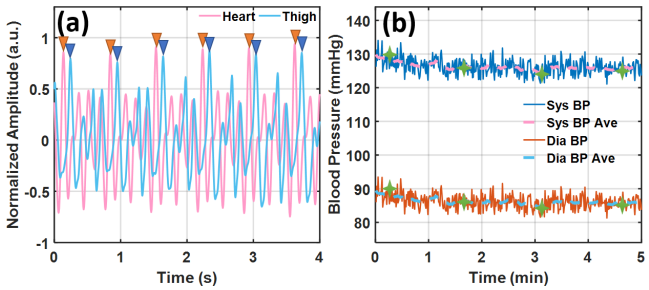

Fig. 5. The PTT-based blood pressure estimates. (a) The synchronized heartbeat and femoral pulse signals after the equalization. The markers indicate the peak for PTT calculation. (b) The calibrated PTT based blood pressure. The green markers are the results from a cuff-based commercial blood pressure monitor.

III. Conclusions

In this work, we demonstrated the NCS system integrated into the seat structure to monitor the vital signs of heartbeats, respiration, femoral pulses, and PTT-based blood pressures. The system is entirely embedded and invisible to the user. The new balancing bridge design at the RF transceiver front end can significantly improve the signal quality. Variations of sensor placement to account for different body sizes and postures are briefly investigated.

References

[1] P. Kligfield *et al*, "Recommendations for the standardization and interpretation of the electrocardiogram," *Circulation*, vol. 115, no.10, pp. 1306-1324, Mar. 2007.

[2] J. Allen, "Photoplethysmography and its application in clinical physiological measurement," *Physiol. Meas.* vol. 28, 2007.

[3] T. J. Sullivan, S. R. Deiss and G. Cauwenberghs, "Low-noise, non-contact EEG/ECG sensor," *2007 IEEE Biomedical Circuits and Systems Conference*, 2007.

[4] N. Bu, N. Ueno and O. Fukuda, "Monitoring of respiration and heartbeat during sleep using a flexible piezoelectric film sensor and empirical mode decomposition," *2007 29th Annual International Conference of the IEEE Engineering in Medicine and Biology Society*, 2007.

[5] T. Reinvuo *et al*, "Measurement of respiratory rate with high-resolution accelerometer and EMFit pressure sensor," *2006 IEEE Sensor Applications Symposium*, 2006.

[6] F. Adib, H. Mao, Z. Kabelac, D. Katabi and R.C. Miller, "Smart homes that monitor breathing and heart rates," *ACM CHI Conference on Human Factors in Computing Systems*, 2015.

[7] X. Hui and E. C. Kan, "Monitoring vital signs over multiplexed radio by near-field coherent sensing," *Nature Electronics*, doi: 10.1038/s41928-017-0001-0, vol. 1, Jan. 2018.

[8] L. A. Geddes *et al*, "Pulse transit time as an indicator of arterial blood pressure," *Psychophysiology*, vol. 18, pp. 71-74, 1981.

[9] R. Mukkamala *et al*, "Toward ubiquitous blood pressure monitoring via pulse transit time: theory and practice," *IEEE Transactions on Biomedical Engineering*, vol. 62, pp. 1879-1901, 2015.

[10] X. Hui and E. C. Kan, "No-touch measurements of vital signs in small conscious animals," *Sci. Adv.*, 2019 (under review).

[11] X. Hui and E. C. Kan, "Ultra-high-resolution radio ranging with the harmonic RFID system," *Nat. Elect.*, 2019 (under review).

[12] X. Hui, Y. Ma, and E. C. Kan, "Code division multiple access in centimeter accuracy harmonic RFID locating system," *IEEE Journal of RFID*, vol. 1 pp. 51-58, 2017.

[13] X. Hui and E. C. Kan, "Collaborative reader code division multiple access in the harmonic RFID system," *IEEE Journal of RFID*, vol. 2 pp. 86-92, 2018.

[14] X. Hui and E. C. Kan, "Accurate extraction of heartbeat intervals with near-field coherent sensing," *2018 IEEE International Conference on Communications (ICC)*, 2018.

Appendix G

(PDF preprint) Z. Zhang, P. Sharma, J. Zhou, X. Hui and E. C. Kan, “Furniture-integrated respiration sensors by notched transmission lines”, accepted in *IEEE Sensor J*., 2020.

Furniture-Integrated Respiration Sensors by Notched Transmission Lines

Zijing Zhang, Pragya Sharma, Jianlin Zhou, Xiaonan Hui and Edwin C. Kan, *Senior Member, IEEE*

***Abstract*— Non-invasive respiration sensors integrated into furniture can be invisible to the user and greatly enhance comfort and convenience to facilitate many applications. Current sensors often require user cooperation or fitting, which discourages frequent usage. We present a new respiration sensor integrated into a bed or a chair by modifying a radio-frequency (RF) coaxial cable structure with a designed notch. The lung motion is coupled to the electromagnetic leakage at the notch through near-field coherent sensing (NCS). The sensors, covered with fabrics and positioned under the abdomen and thorax, can capture the respiratory waveforms and derive the breath rate. The heart rate can also be evaluated in the same setup with proper filtering. The sensor design can tolerate large position variation to accommodate user uncertainties. Various voluntary exercises of normal, deep, fast, held and blocked breathing were measured under different postures of supine, recumbent and sitting by the carrier frequency range between 900MHz and 2.4GHz. The breath rate from 10 participants compare well with the synchronous commercial chest-belt sensors in all breathing routines.**

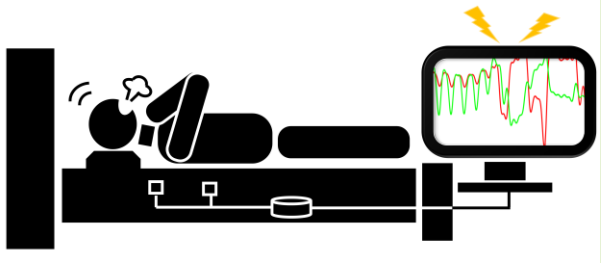

***Index Terms*— Microwave sensors; respiration sensors; apnea detection.**

I. INTRODUCTION

Monitoring respiration dynamics has many applications [1], including in wellness evaluation and diagnosis of respiratory disorders such as asthma [2], coughing, dyspnea, and chronic obstructive pulmonary diseases (COPD) [3]. It is also valuable for prognostic assessment of prevalent sleep disorders including central sleep apnea (CSA) and obstructive sleep apnea (OSA) [4]. Irregular breathing patterns can be an early indicator of cardiac arrest [5] and acute myocardial infarction [6]. Besides clinical applications, respiration monitoring can also be a useful gauge of cognitive load [7], emotional stress, and physical efforts during sports and exercises [8].

This work is supported by Department of Defense of United States through Office of the Congressionally Directed Medical Research Programs (CDMRP) Discovery Award PR-182496, and by National Institute of Health (NIH) DA049566-01A1. Z. Zhang, P. Sharma, J. Zhou, X. Hui and E. C. Kan are with School of Electrical and Computer Engineering, Cornell University, Ithaca, NY 14853, USA. E-mails: zz587@cornell.edu, ps847@cornell.edu, jz899@cornell.edu, xh273@cornell.edu, eck5@cornell.edu.

Current methods to monitor respiration efforts include spirometry [9], nasal airflow probe [10], capnography [11], strain gauges [12], respiratory inductance plethysmography (RIP) [13], pulse oximetry [14], skin strain sensors [15], optical and far-field RF sensing [16][17], and ballistocardiogram (BCG) [18]. Spirometry measures the volume and speed of inhaled and exhaled air by the lung, but requires attentive user participation. Nasal airflow probes utilize mouthpieces or facemasks, which are cumbersome and disruptive to the normal breathing patterns. Capnography needs similar conspicuous mouth or nasal cannula. Strain gauges and RIP by chest belts can measure the chest and abdominal wall movement during respiration, but the belt tension is required to capture the full breathing cycle which causes discomfort. The skin strain sensor involves tight skin contact which is also uncomfortable. Pulse oximetry monitors the oxygen saturation (SpO2) and offers mixed observation of respiration and circulation. Optical and RF sensing methods require the user to be stationary and the reader to be in a direct line-of-sight (LoS) to the front torso. BCG-based sensors often assume the user body weight as the quiescent point of operation, and can only be installed under the

XXXX-XXXX © XXXX IEEE. Personal use is permitted, but republication/redistribution requires IEEE permission.

See http://www.ieee.org/publications_standards/publications/rights/index.html for more information.

bed but not to the chair. Posture variation and movement on bed are problematic as well.

Transmission-line sensors have been used in biological and chemical sensing as well as health monitoring. A splitter-combiner structure can measure minute dielectric property changes in the near-field region [19]. A coplanar waveguide loaded with symmetric resonators can measure angular motion [20] and dielectric properties [21]. A resonator coupled to a transmission line was used to estimate glucose concentration [22]. The sensing modality is typically the variation of the resonance frequency, phase, and/or quality factor. The transmission-line structure is highly sensitive to small motion and composition changes, and hence has been rarely applied to the large motion of respiration. The highest sensitivity may not be favorable here, as tolerance to user variation and the capture of the full waveforms are also important in practical applications.

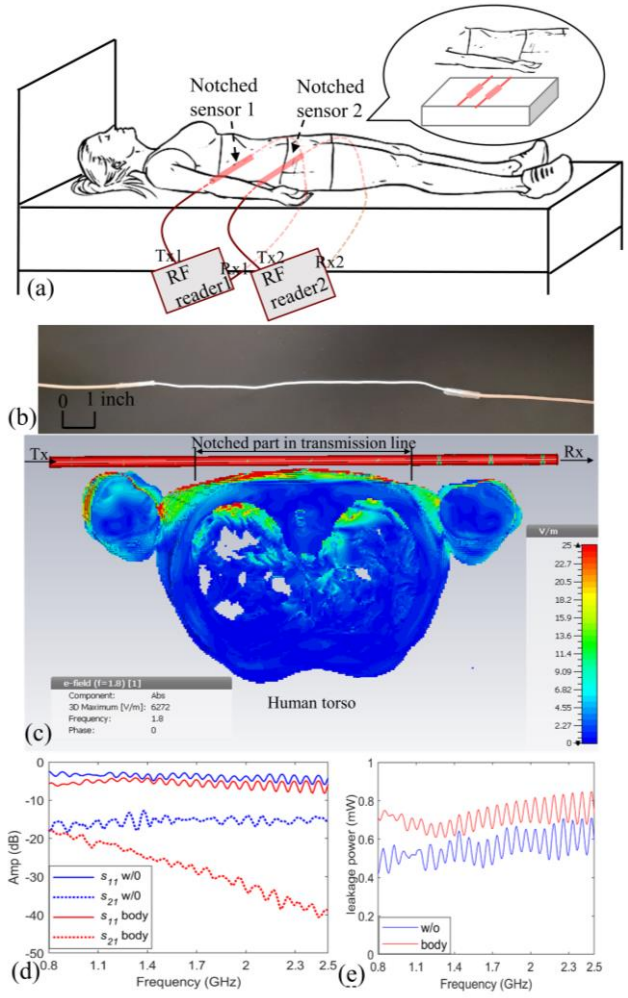

Fig. 1. Notched-cable respiration sensor setup: (a) System schematic with bed integration; (b) A photo of the notched cable; (c) Cross section of the CST simulation of a human torso with the NCS frequency at 0.9GHz; (d) Measured S_{11} and S_{21} results in 0.8 – 2.5 GHz after de-embedding. (e) Estimated leakage power from the notched sensor with 1mW input.

The notched transmission-line sensor proposed in this paper is adapted from the previous antenna-based near-field coherent sensing (NCS) [23], as shown in Fig. 1. In the near-field region, the dielectric boundary movement by internal organs and body parts will couple to the leaked electromagnetic (EM) energy from the notched part of the transmission line, and hence affect the signals at the transmitting (S_{11}) and receiving (S_{21}) ends. To connect to the sensing notch with high ambient isolation, we opt to use a miniature coaxial RF cable, as shown in Fig. 1(b), which is more feasible than the coplanar or slotline waveguides. The metal shield of the middle part is removed to allow the EM energy coupled into the nearby user body. Simulation by CST Microwave Studio [24] with the notched sensor on the human torso is shown in Fig. 1(c). The simplified torso model only includes the sweatshirt, skin, muscle, body fat, bones and lungs to save computational time. RF signals were emitted from the transmitter (Tx) and propagated down the transmission line. The EM leakage from the notched structure was coupled into the human body, and finally received by the receiver (Rx). We can clearly observe that the electric field was strongly coupled into the layers of skin, fat, muscle, and lungs. More details of the simulation setup are shown in supplementary Fig. 1.

The notch length L = 9 in is designed to accommodate the position uncertainties for different users on beds and chairs. As shown in Fig. 2, the notched cable was sewn on the bedsheet for the bed setup, while it was fixed at the back of the chair for the chair setup. Intermediate layers of thin fabric, plastic protector and foam can be added for comfort and aesthetic with little influence on performance. In comparison with either far-field [17] or near-field [25][26] effects of the sensing antenna structure, the present design can operate in a much broader bandwidth with a given hardware as indicated by the measured S_{21} in Fig. 1(d) and by the simulated S_{21} in Supplementary Fig. 1. As no RF radiation is intended and the Rx power can be anywhere between –5 dB to –50dB lower than the Tx power, the Bode-Fano limit on percentage bandwidth and impedance match [27] and spectral regulation are much more relaxed. Also, in contrast to wearable NCS sensors [23][25][26], the user may not need to tend to the sensor at all, which greatly reduces the comfort and conspicuousness concerns. We further demonstrated the capability of accurate respiration monitoring under various postures, including supine, recumbent and sitting. Different respiratory routines including voluntary deep, fast and tidal breathing, as well as breath holding and airway blockage exercises, can be identified accurately. Our sensor can also retrieve the heart rate in one setup, although the cardio waveform is clearest during breath holding with reduced interference by the large respiratory motion. We benchmarked our sensor against the chest-belt respiration measurements with high consistency. The validity of our system has been confirmed on 10 healthy adults.

II. Experimental Setup and Signal Processing

A. Notched sensor configuration

To demonstrate the broadband operability, continuous-wave (CW) signals between 0.8 and 2.5 GHz were tested by the

network analyzer (Keysight E5063A) in the bed setup. The EM energy emitted from Port 1 will partially leak out from the notch and couple to the surface and internal body motion of breathing and heartbeats, which will change the signal at Port 2 as represented by the scattering parameter S_{21}. Some of the traveling wave will be reflected back to Tx, and can be potentially evaluated as S_{11} or standing-wave ratios, as shown in Fig. 1(d) when the human body was lying on the bed (red line) and when the bed is empty (blue line). The RF carrier power is set at 0 dBm, and the leakage power from the notched structure can be estimated by $(1 - |S_{21}|^2 - |S_{11}|^2)\times$1mW after de-embedding the cable loss, as shown in Fig. 1(e).

Two sets of the notched-cable sensors underneath the thorax and abdomen regions can capture the separate motion during breathing. Multiplexing by frequency or chip codes is optional, as the cross coupling of the thorax and abdomen sensors is weak due to small far-field radiation. Two software-defined radios (SDR) by National Instrument Ettus B200mini were connected to two notched cables and then interfaced with the host computer through USB (Universal Serial Bus). Alternatively, one SDR by the two ports of Ettus B210 can be employed. When the participant is lying on the bed or sitting on the chair, the centers of the sensor notches have a horizontal distance d to the mediastinum, and the vertical distances h_1 and h_2 to the umbilicus for the thorax and abdomen sensors, as shown in Fig. 2(a). Figs. 2(b)(c) are the photos for the bed- and chair-integrated setups. In realistic deployment, we can also sew the sensor beneath the bed sheet and protective layers to facilitate routine changes, disinfection, and aesthetic design. For verification, we benchmarked the NCS results with the BIOPAC tension-belt sensors (BIOPAC Systems, Goleta, CA). Two torso belts, SS5LB and PTM SS11LB, were placed at thorax and abdomen, with the vertical positions right above the NCS sensors. A photo is shown in Fig. 2(d). The torso belts can measure the change in local tension due to the geometrical change during respiration. BIOPAC data are down-sampled to 500Hz. The synchronization between NCS and BIOPAC is achieved by buffering the NCS and BIOPAC data at approximately the same time within a few milliseconds.

In the SDR Tx signal chain, the digital baseband goes through the digital-to-analog converter (DAC) and is then mixed with the carrier frequency f_{RF}. The RF signal from the notched structure is coupled into internal body motion in the near-filed, received by Rx, and then demodulated and sampled by the analog-to-digital converter (ADC) to retrieve the baseband. Together with a baseband tone f_{BB} in the quadrature scheme, the NCS vital-sign signal is represented by the amplitude modulation on the quadrature signal as

$$NCS(t) = \sqrt{I_{Rx}(t)^2 + Q_{Rx}(t)^2} \quad (1)$$

$$I_{Rx}(t) = A(t)\cos(2\pi f_{BB}t + \theta_0) \quad (2)$$

$$Q_{Rx}(t) = A(t)\sin(2\pi f_{BB}t + \theta_0) \quad (3)$$

where θ_0 is the phase offset accumulated from the Tx-Rx signal chains. The baseband frequency is set at f_{BB} = 51 kHz for B200mini. When B210 is used for both channels, the two basebands are set at f_{BB1} =355 kHz and f_{BB2} = 440 kHz. f_{RF} is selected to be at one of 900MHz, 1.8GHz and 2.4GHz. As the respiration waveform is a low-frequency analog signal, we chose the superheterodyne scheme of converting the frequency twice by f_{BB} and f_{RF} to minimize the effects of the Flicker noise in f_{RF} local oscillators (LO) and to implement subcarrier multiplexing from f_{BB1} and f_{BB2} when needed. We have varied a few f_{BB} in supplementary Fig. 2 to substantiate our choices. The data converter has a sampling frequency of 1M samples per second (Sps) to enable the digital baseband processing, which is performed by the host computer. The demodulated respiration waveform is further down-sampled to 500 Sps, the same as the BIOPAC data. The allowable broad choice of f_{RF} is not only a unique feature over the antenna-based NCS approach, but can also facilitate system tuning after furniture integration so that f_{RF} can yield strong coupling to the user body with higher ambient tolerance.

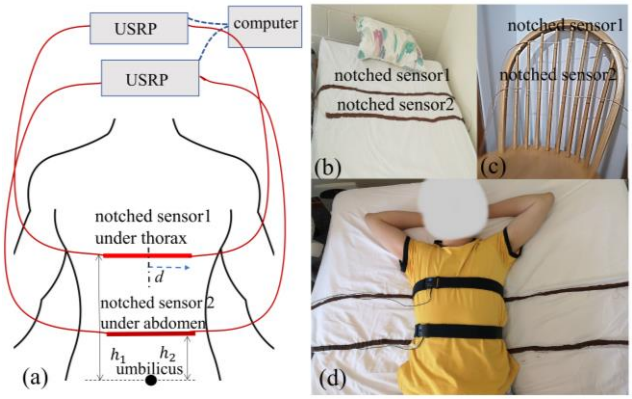

Fig. 2. Experimental setup of the notched sensors: (a) Sensor position variation with respect to the user body; (b) Bed integrated and (c) chair integrated setup; (d) A photo with the participant lying on the bed-integrated sensor and wearing commercial torso belts for benchmark.

B. Breath rate (BR) estimation

For estimation of the breath rate (BR), the waveform was first bandpass-filtered from 0.05Hz to 1Hz to remove the DC drift and high-frequency noises by post-processing in MATLAB. For peak detection to identify the inhalation and exhalation periods, we utilized the moving average-crossing algorithm [28], which is suitable to process broad range of varying frequencies, as we expect BR ranging from nearly 5 breaths per minute (BPM) to 40 BPM. A moving-average curve is first calculated at each time point in a given window length, which is around one respiration cycle and will be constantly updated. The points when the moving average curve crosses the original signal are marked as up-crossing points for positive slopes in the original signal or down-crossing points for negative. Local maximum is labelled as the maximal point between two up-down crossing points, and local minimum as the minimal point between two down-up crossing points. BR is finally calculated by counting the number of detected breathing cycles over a window size of 15s. One breathing cycle includes

an inhalation peak (maximum) and the trailing exhalation (minimum) peak. The number of cycles is calculated as the number of inhalation peaks minus 1, and the total period is between the two adjacent inhalation peaks.

C. Signal quality and bit depth

The signal quality can be assessed by the acquired bit depth of the respiratory waveform, which represents the signal resolution and provides insights into the amount of RF energy coupled inside the internal organ. In this paper, we define the bit depth of the signal quality Q as,

$$Q = \log_2 \frac{NCS_{pp}}{NCS_{DC}} + N - 1 \quad (4)$$

where NCS_{pp} is the peak-to-peak value in the quadrature-demodulated amplitude, NCS_{DC} is the DC amplitude at the local point, and N is the number of bits in ADC. NCS_{pp} can be retrieved by the peak detection algorithm, and NCS_{DC} can be obtained by the DC signal amplitude before filtering. Q has the meaning of the number of significant bits in the NCS signal. As the respiration waveform is cyclic around an equilibrium point, the larger the signal strength, the more bit depth can be retrieved by ADC, and hence the higher the signal resolution and the less quantization noises.

Signal-to-noise ratio (SNR) is another important parameter to evaluate the hardware system setup. We estimate SNR during the normal breathing period when BR is roughly constant. The fundamental breathing frequency can be determined from the largest nonzero spectral component. The 3-dB bandwidth of the breathing frequency includes all adjacent frequency components that decrease monotonically away from the maximum. The noise level is estimated by using the total power outside the 3-dB regions of the fundamental breathing frequency, its harmonics and the DC component.

Signal quality and SNR under different postures, breathing patterns, positions and frequencies can give guidance to the hardware design and signal processing to accommodate inevitable user variations in realistic applications. Larger signal quality often indicates higher SNR from the NCS signal strength, but in a less controlled ambient, SNR still offers additional useful information on ambient noises.

D. Isovolumetric breathing detection during airway blockage

One of the most common apneas is the obstructive sleep apnea (OSA). OSA often occurs when the throat muscles intermittently relax and block the airway during sleep. As the lung volume will remain nearly constant during OSA, the thorax and abdomen move asynchronously to generate a paradoxical motion. During our experiments, this symptom was simulated by the isovolumetric breathing exercise. By blocking the airway voluntarily with a nose pinch, abdomen contraction was performed with paradoxical expansion of the thorax and vice versa. To detect this paradoxical movement, we can use the slope-product of thorax and abdomen waveforms, which will be negative during the occurrence of isovolumetric breathing [29]. We use the tanh() function to rescale the slope-product to [-1,1] with a moving average over a 3s window [29].

III. Experimental Results

A. Benchmark with BIOPAC tension belts

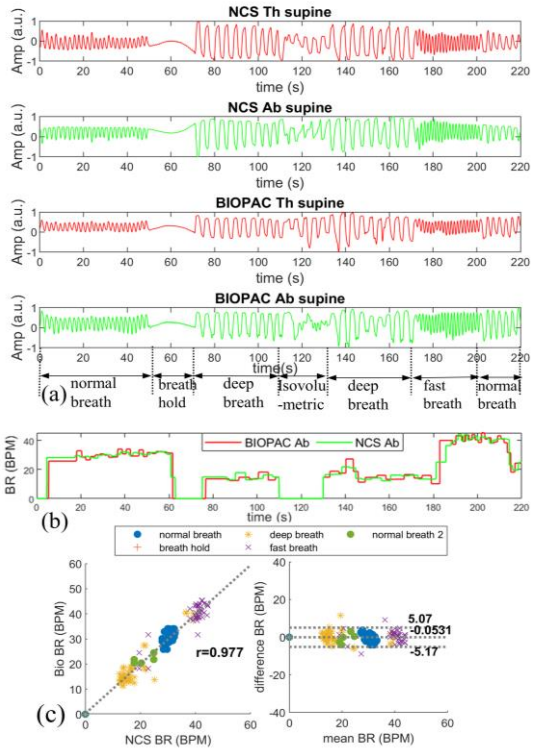

Fig. 3. Respiration monitoring in the supine posture with f_{RF} = 900MHz: (a) NCS and BIOPAC amplitude waveforms in thorax and abdomen during the whole breathing protocol. (b) Th breath rate (BR) calculated from NCS (green) and BIOPAC (red). (c) Correlation and agreement between NCS and BIOPAC BR data. Left: The scatter plot with denoted Pearson's correlation coefficient. Right: The Bland-Altman plot showing the mean difference m at the center dotted line and the corresponding limits of agreement (LoA) at the upper and lower dotted lines given by $m \pm 1.96\sigma$.

The NCS notched-cable sensor was benchmarked against the reference BIOPAC tension-belt sensors. Notice that both sensors can have errors in respiration monitoring, but due to the different signal transduction, the errors from the two methods should be reasonably uncorrelated. Vertical positions of the sensors are recorded by the distance to the umbilicus with h_{1NCS} = 8.5 in, h_{2NCS} = 2.5 in, $h_{1BIOPAC}$ = 9 in, and $h_{2BIOPAC}$ = 3.5 in. The breathing protocol in each posture has a length of 220 s, including 0 – 50 s: normal tidal breathing; 50 – 70 s: breath hold; 70 – 110 s: deep breathing; 110 – 130 s: isovolumetric exercise; 130 – 170 s deep breathing; 170 – 200 s: fast breathing; 200 – 220 s: normal breathing.

Fig. 3(a) shows the normalized NCS and BIOPAC amplitude waveforms in thorax and abdomen with the supine position on bed during the whole protocol. Both NCS and BIOPAC data can distinguish different breathing patterns clearly and show a good agreement. Fig. 3(b) shows BR calculated from NCS and BIOPAC abdomen amplitude, as the geometrical change from

diaphragm and abdomen is higher than that of thorax during respiration. When the negative slope product was detected during the isovolumetric exercise, BR was truncated to 0. BR estimation matched well with the breathing patterns, but a delay in time was observed due to the chosen 15-s epoch for BR calculation. Fig. 3(c) shows the correlation between NCS and BIOPAC. The BR data was preprocessed by getting rid of the outliers that were three standard deviations further away from the mean. The outliers only occurred at the beginning or ending of a specific breathing pattern due to the instability of a transition. These outliers were not included for correlation calculation. High correlation with a Pearson coefficient r = 0.977 is achieved. As the two sensors have uncorrelated errors, correlation is one of the possible indicators for inter-sensor consistency and overall BR accuracy. The Bland-Altman plot on the right presents the agreement by the mean (m) and limits of agreement (LoA). The X axis is the average of the two data, and the Y axis is the difference. The mean difference is m = −0.306 BPM, as shown in the middle dotted line. LoA within which 95% of the differences is estimated by $m \pm 1.96\sigma$, assuming a normal distribution. Low m and narrow LoA indicate that the errors in NCS and BIOPAC are uncorrelated and small. In Fig. 3, f_{RF} is set at 900MHz. Results with f_{RF} at 1.8GHz and 2.4GHz are shown in supplementary Fig. 3.

B. Posture variation

The NCS notched-cable sensor can be applied to different postures, including supine and recumbent on bed, and sitting on chair, which can be readily adapted for sleep study, driver seat and waiting-room chairs. In Fig. 4, we demonstrated the results from the recumbent and sitting postures. The breathing protocol was the same as in Fig. 3.

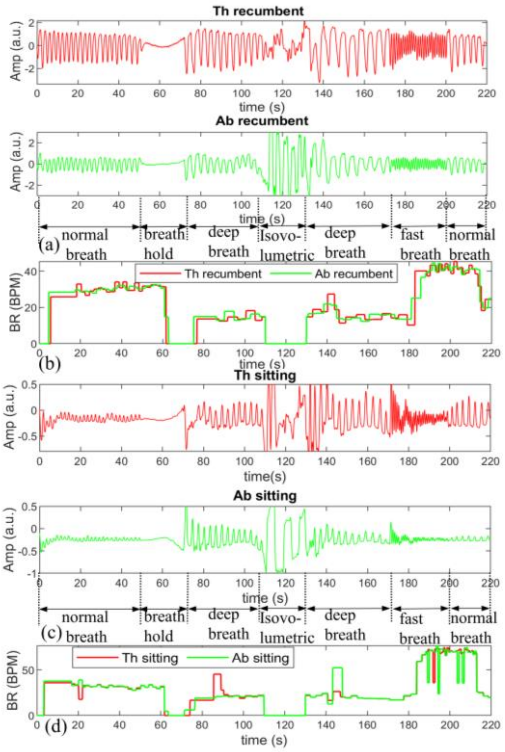

Fig. 4. Respiration monitoring in the recumbent and sitting postures: (a) Respiration waveforms from thorax and abdomen NCS sensors in the recumbent posture on bed with f_{RF} = 2.4GHz. (b) BR estimated from (a). (c) Respiration waveforms from thorax and abdomen NCS sensors in the sitting posture on chair with f_{RF} = 1.8GHz. (d) BR estimated from (c).

Waveforms were based on the normalized NCS amplitude after bandpass filtering of 0.05 − 1 Hz. For the recumbent posture in Figs. 4 (a)(b), h_1 = 8.5inches, h_2 = 2.5inches, and f_{RF} = 2.4GHz. For the sitting posture in Figs. 4 (c)(d), h_1 = 9.5inches, h_2 = 2inches, and f_{RF} = 1.8GHz. BR during the 20-s isovolumetric exercise was also truncated to zero once the negative slope product was detected. Data quality from the recumbent posture is sufficient for BR estimation, but slightly worse than that in the supine posture, which is likely due to less interaction area with the RF signal. As can be observed in the first 50-s normal breathing with reduced magnitude, the sitting posture suffered more noises and showed less clear breathing pattern. This may be due to possible slouching, which will seriously affect the abdomen waveforms. However, various breathing patterns can still be identified in Figs. 4 (a)(c), including tidal breathing, breath hold, deep breathing, and fast breathing. BR in Figs. 4 (b)(d) shows a good match between the thorax and abdomen sensors. Test results from other f_{RF} are shown in supplementary Fig. 4.

C. Position variation

One of the requirements for furniture-integrated sensors different from the wearable ones is the large placement tolerance to accommodate user variation in size and position. We tested the sensor performance when a horizontal shift d was introduced in the supine posture, which can commonly happen in realistic conditions. We confirmed that our notched cable system can tolerate up to d = 8 in, which should be sufficient in consideration of user uncertainties. The participants in our test have an average waist width around 12 in. To speed up the study, the breathing protocol was shortened to 160s, including 0 – 50 s: normal breathing; 50 – 70 s: breath hold; 70 – 110 s: fast breathing; 110 – 160 s: deep breathing. f_{RF} was set to 2.4GHz. Fig. 5(a) shows the normalized NCS waveforms after filtering with the horizontal shift of d = 0, 4, 8 in from the abdomen sensor. Different respiration patterns can still be clearly identified and the transition remained evident. Fig. 5(b) shows BR estimated from the respiration waveforms, where normal BR is around 20 BPM, fast BR around 35 BPM, and deep BR around 10 BPM. For d = 8 in, BR around the breath hold period is not as accurate as d = 0 and 4 in due to the reduced signal quality. Position variation results from other f_{RF} are shown in supplementary Fig. 5. We also tested the vertical position variation of h_1 = 1, 2.5, 4 in for abdomen sensor with the same protocol. Results are shown in supplementary Fig. 6.

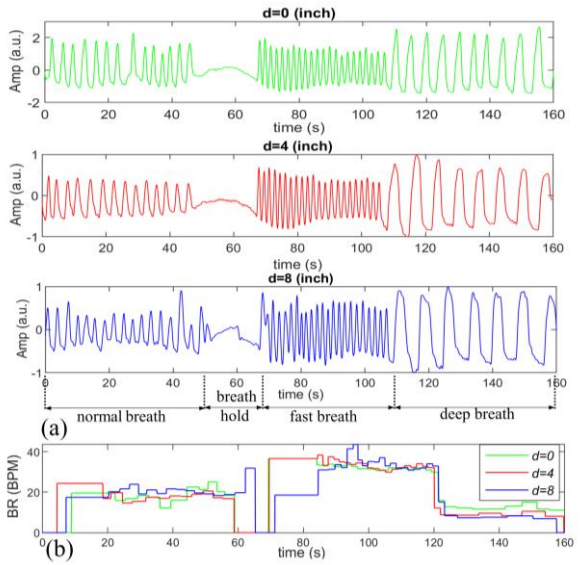

Fig. 5. (a) Respiration waveforms with horizontal shift of d = 0, 4, 8 inches for the abdomen sensor in the supine posture on bed. (b) BR estimated from the respiration waveforms for d = 0 (green); d = 4 in (red); d = 8 in (blue).

D. Isovolumetric exercises

The isovolumetric exercise was represented by paradoxical motion between thorax and abdomen. The 270-s breathing protocol was customized to increase the total period of isovolumetric motion including 0 − 40 s: normal breathing; 40 – 60 s: breath hold; 60 – 80 s normal breathing. Four isovolumetric exercises was then performed roughly during 80 – 100 s; 120 – 140 s; 160 – 180 s; 200 – 220 s, with normal breathing in between and afterwards.

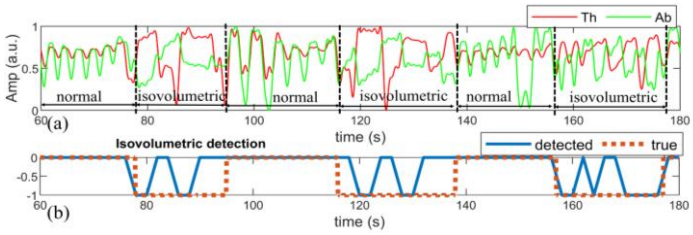

Fig. 6. Isovolumetric detection: (a) Respiration waveforms from thorax (red line) and abdomen (green line) sensors during three isovolumetric breathing exercises. (b) Detection by the slope-product method: The blue solid line by the NCS sensor and the orange dotted line from protocol annotation, where –1 indicates detection.

Fig. 6(a) shows an example of the waveforms from thorax and abdomen NCS signals during three isovolumetric cycles. f_{RF} was set to 900 MHz. As the waveforms indicate, in normal breathing periods, the thorax and abdomen moved synchronously; in the isovolumetric periods, the two motions were paradoxical to each other. The slope-product method was implemented in Fig. 6(b), where −1 indicates positive detection of isovolumetric motion and 0 indicates no occurrence. The annotated instruction to perform the isovolumetric exercise is shown as the orange dotted line and the NCS detection result as the blue solid line.

Isovolumetric exercises can be missed or falsely detected by NCS or BIOPAC. False statistics against the user instruction are summarized for 10 volunteers in Table I. NCS could detect a large portion of airway blockage successfully and performed slightly better than BIOPAC. Possible reasons for erroneous detection include: 1) The notched sensors couple into the motion of associated muscles whose movement during airway blockage can be complex instead of merely paradoxical; 2) Some participants had difficulty performing the isovolumetric exercise during airway blockage, or had introduced body motion artifacts during their attempts; 3) The thorax sensor was too low in position and had coupled in part of the abdomen motion as well.

TABLE I. CONFUSION MATRICES OF ISOVOLUMETRIC BREATHING DETECTION DURING AIRWAY BLOCKAGE BY NCS AND BIOPAC.

NCS			
Total number of epochs in 10 participants: 180		Detection	
		Positive	Negative
Airway blockage instruction	Positive	16	4
	Negative	10	150
accuracy		0.92	
sensitivity		0.8	
BIOPAC			
Total number of epochs in 10 participants: 180		Detection	
		Positive	Negative
Airway blockage instruction	Positive	11	9
	Negative	11	149
accuracy		0.89	
sensitivity		0.65	

E. Heart rate (HR) detection

With the same setup, the thorax NCS sensor can also retrieve the heart rate (HR) with reasonable accuracy. The test protocol was further simplified to normal breathing of 15 s and breath hold of 15 s, the latter of which had clearer heartbeat signals due to the lack of respiration interferences. The signal was first filtered by a bandpass filter between 0.1 − 5 Hz to remove the DC component and high-frequency noise. Fig. 7(a) shows the NCS waveform during normal breathing in time (left) and frequency (right) domains. Fig. 7(b) shows the breath-hold counterpart. The waveform has a typical characteristic of a main peak and a small recoil. HR can be observed as the fundamental, second and third harmonics in the spectrum. BR at 0.266 Hz and its harmonics can also be observed in Fig. 7(a). f_{RF} was set to 1.8 GHz, but HRcan be retrieved at other f_{RF} as well, which is shown in Supplementary Fig. 7.

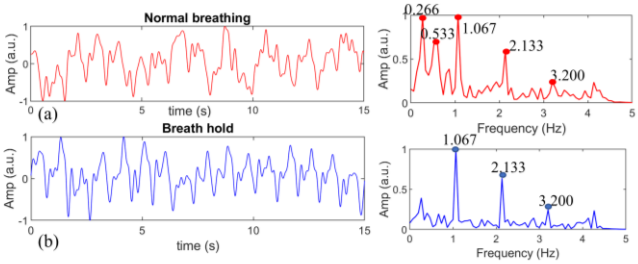

Fig .7. (a) Left: The heartbeat time-domain waveforms from the thorax sensor during normal breathing. Right: The corresponding spectrum with three HR peaks and two BR peaks indicated by the annotation above. (b) Left: The heartbeat waveforms during breath hold. Right: The corresponding spectrum with three peaks.

F. Signal quality and SNR

We have calculated the signal quality Q for different scenarios in Fig. 8. The means and standard deviations of Q in Fig. 8 are shown in Supplementary Table II. First, the breathing patterns over time can cause variation in Q. For the same setup, the deep breathing usually has the highest Q, and the breath hold the lowest. The position variation of d = 0, 4, 8 in is shown in Fig. 8(a) with f_{RF} = 2.4 GHz. When d becomes larger, most often Q decreases. We compare the thorax and abdomen sensors in Fig. 8(b) when they operated together in the supine position with f_{RF} = 2.4 GHz. Abdomen often has larger motion from the diaphragm and associated muscles, and overall larger Q. Using measurements in Fig. 8(c), we compared Q in the supine, recumbent, and sitting postures from the abdomen sensor with f_{RF} = 1.8GHz. The supine signal has larger Q than those by recumbent and sitting due to higher coupling strength between the RF signal and the body. Finally, for frequency variation in Fig. 8(d) at f_{RF} = 0.9, 1.8, and 2.4GHz, we used the abdomen sensor in the supine position for illustration. Q has a more complex relation with respect to f_{RF}, although 1.8 GHz usually performed the best. All frequencies can be employed to retrieve respiration waveforms, but different Tx and Rx gains need to be chosen in our adaptive-gain implementation in SDR.

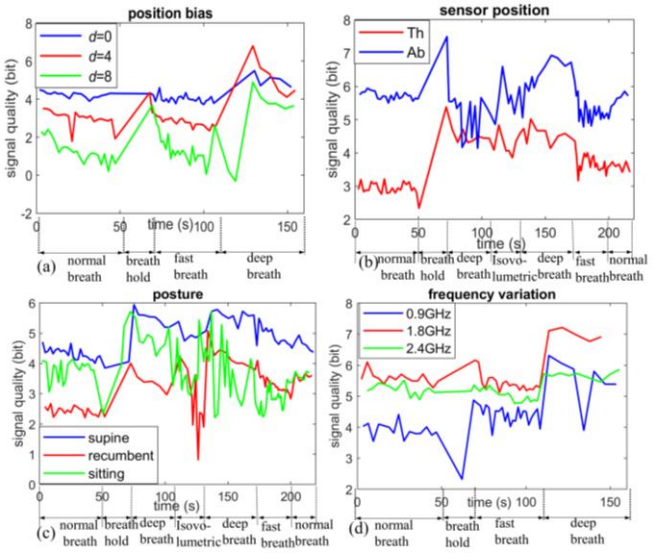

Fig. 8. Signal quality for (a) Position variation: d = 0 (green), 4 ins (red), and 8 ins (blue); (b) Sensor placement: thorax (blue) and abdomen (red); (c) Postures: sitting (red), supine (green), and recumbent (blue); (d) Carrier frequency: f_{RF} = 0.9 GHz (blue), 1.8 GHz (red), and 2.4 GHz (green).

The corresponding SNRs calculated in different conditions in Fig. 8 are shown in Table II. SNR is calculated during the normal breathing period of 0 – 50s when BR is roughly constant. The comparison of SNR under different conditions show similar trends to Q in our controlled ambient without additional interferences.

TABLE II. SNR CALCULATED IN DIFFERENT CONDITIONS

(a) Position bias	SNR (dB)	**(b) Sensor placement**	SNR (dB)
d = 0	16.2	Supine thorax	10.7
d = 4 in	6.60	Supine abdomen	14.3
d = 8 in	5.92		
(c) Posture	SNR (dB)	**(d) Frequency**	SNR (dB)
Supine	19.3	0.9GHz	8.41
Recumbent	14.6	1.8GHz	12.2
Sitting	8.05	2.4GHz	9.69

G. Comparison with antenna-based NCS sensors

We also compared the performance of the notched NCS sensor and the wearable antenna-based NCS sensor [26]. The wearable sensor consists of ultra-high frequency (UHF) monopole antennas used at both Tx and Rx. Two wearable sensors were separately attached to the thorax and abdomen in the front torso in the similar location of the BIOPAC chest belts. Two notched sensors were integrated to the chair setup in the back. One SDR by B210 was connected to two notched sensors and another B210 was connected to two wearable sensors. f_{RF} was set at 1.8GHz. The breathing protocol was the same as in Fig. 5. In Fig. 9(a), we demonstrated the waveforms of the wearable sensor (red) and the notched sensor (green) both at the abdomen position. In Figs. 9(b)(c), the corresponding BR and Q were extracted. BR from the two sensors are well matched, but the wearable sensors have a higher Q indicating better coupling strength than the notched sensor. This is reasonable because the wearable sensors were more closely attached to the body in the front torso. Also, the wearable sensors are monopole antennas with intentional radiation into the body, but the notched sensors depend only on near-field leakage by the evanescent mode.

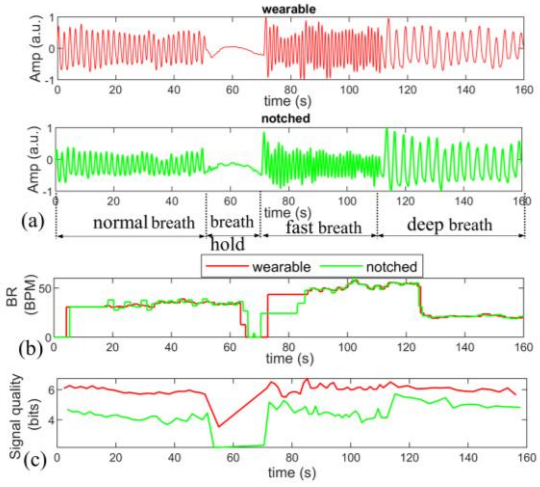

Fig. 9. (a) Waveforms of the wearable sensor (red) and the notched sensor (green) both at the abdomen position. (b)(c) The corresponding estimated BR and Q.

H. Two-tone measurements

We also confirmed the two-tone measurement capability in the notched sensor, which can enhance reliability by frequency

diversity. Different f_{RF} will have different body penetration depth, as indicated in the CST simulation of Supplementary Fig. 1(b). In comparison with the antenna-based NCS systems, dual-band antennas are more complicated to design, especially in the consideration of body antenna detuning. For the notched sensor, two f_{RF} can be applied simultaneously to one sensor, and one or two f_{RF} can be applied to two collocated cables with reasonable spatial isolation. In Fig. 10, two-tone Strategy 1 has a frequency multiplexing setup by two SDRs feeding into the same RF cable at the same time. Broadband 3dB splitters are utilized to combine two RF signals into one notched sensor and then splitting back to the Rx of the respective carrier. Two-tone Strategy 2 has two closely collocated notched cables. Two SDRs with different frequencies separately fed into two notched sensors. At the same position, we have two sensors by two f_{RF} with minimal interference to each other.

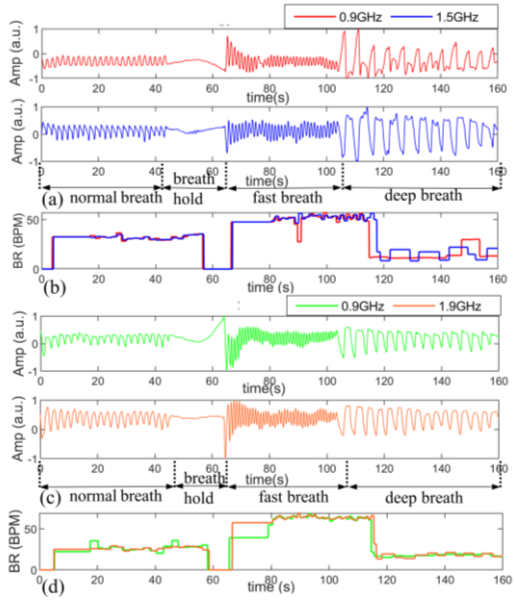

Fig. 10. (a) Two-tone Strategy 1: Respiration waveforms for 0.9 GHz (upper) and 1.5 GHz (lower); (b) The corresponding BR estimation. (c) Two-tone Strategy 2: Respiration waveforms for 0.9 GHz (upper) and 1.9 GHz (lower); (d) the corresponding BR estimation.

The 160-s protocol was the same as Fig. 4 for position variation testing in the supine posture with the abdomen sensor. In Figs. 10(a)(b), Strategy 1 of frequency multiplexing has f_{RF} at 0.9 GHz and 1.5 GHz. In Figs. 10(c)(d), Strategy 2 of the collocated sensor cables has f_{RF} at 0.9 GHz and 1.9 GHz. BR extracted from different f_{RF} is consistent for both strategies. Notice that the two-tone measurements can be employed for signal quality check or for coupling into different body depth. Optimal choices of multiple f_{RF} in different scenarios will need further study.

I. Validation on multiple participants

Finally, we have validated our system on 10 different participants. The routine was the same as that in Fig. 3 with the notched sensors on bed and commercial torso-belt sensors on the user body. The retrieved BR from 10 participants compare well with the synchronous chest-belt sensors in all breathing routines. The correlation and agreement plots between NCS and BIOPAC BR data of all 10 people are shown in Fig. 11. The correlation and B&A statistics of individual participants are shown in Table III. The isovolumetric exercise detection statistics of each participant were recorded in Supplementary Table II. Also, the body characteristics of each participant are recorded in Supplementary Table IV. For most cases, the correlation is relatively high, m is low and LoA is narrow. Only a small number of cases have a relatively lower correlation. Our present sample size is too small to draw reliable conclusion on the effects from body characteristics. However, it remains safe to say that the NCS system can accurately detect BR on different people, demonstrating high consistency with commercial torso-belt sensors.

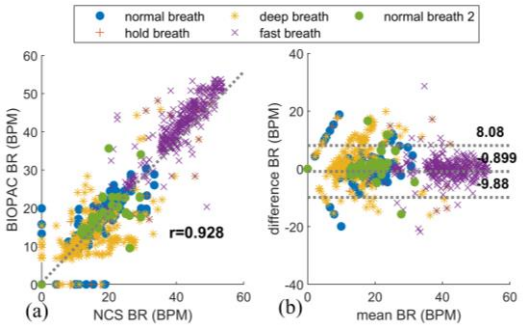

Fig.11. Correlation and agreement between NCS and BIOPAC BR data from 10 participants. (a): The scatter plot with denoted Pearson's correlation coefficient. (b): The Bland-Altman plot.

TABLE III. CORRELATION AND B&A STATISTICS FOR EACH PARTICIPANT

Case No.	r	m (RPM)	σ (RPM)
1	0.927	–1.65	4.50
2	0.987	0.586	2.24
3	0.951	–0.465	4.36
4	0.999	–0.0103	0.288
5	0.978	–0.210	2.12
6	0.805	–4.81	7.13
7	0.883	0.552	5.37
8	0.954	–0.631	4.22
9	0.955	0.131	3.27
10	0.913	–1.24	5.62

IV. CONCLUSION

In this paper, a new notched-cable sensor based on NCS for respiration monitoring was demonstrated. The sensor was integrated to a bed and a chair under layers of fabrics, and is hence highly comfortable, stable, accurate, and cost-effective. In comparison with the wearable sensors attached to the body, our system is invisible to the user with the least concerns of comfort and conspicuousness. Confirmed by experiments, our system has the following advantages: 1) Tolerance of large position variation to accommodate user uncertainty; 2) Posture applicability including supine and recumbent on bed, as well as sitting on chair; 3) Availability of HR estimation in one setup; 4) Identification of multiple breathing patterns including deep, fast, tidal, held and blocked breathing; 5) Broad bandwidth of operations to facilitate multiplexing and signal quality improvement in different scenarios.

There are still remaining issues for future work. The accuracy of paradoxical motion detection during isovolumetric exercise should be further improved. Also, larger variation on people size, body figure and breathing habits should be included in broader user study to further establish heuristic improvement from known body characteristics.

REFERENCES

[1] C. Massaroni, A. Nicolo, D. Lo Presti, M. Sacchetti, S. Silvestri and E. Schena, "Contact-based methods for measuring respiratory rate," *Sensors*, vol. 19, no. 4, Feb. 2019, art. 908, doi: 10.3390/s19040908.

[2] D. Oletic and V. Bilas, "Energy-efficient respiratory sounds sensing for personal mobile asthma monitoring," *IEEE Sens. J.*, vol. 16, no. 23, pp. 8295-8303, Dec. 2016, doi: 10.1109/jsen.2016.2585039.

[3] D. Naranjo-Hernández, A. Talaminos-Barroso, J. Reina-Tosina, L.M. Roa, G. Barbarov-Rostan, P. Cejudo-Ramos, E. Márquez-Martín and F. Ortega-Ruiz, "Smart vest for respiratory rate monitoring of COPD patients based on non-contact capacitive sensing," *Sensors*, vol. 18, no. 7, Jul. 2018, art. 2144, doi: 10.3390/s18072144.

[4] O. Oldenburg, B. Lamp, L. Faber, H. Teschler, D. Horstkotte and V. Topfer, "Sleep-disordered breathing in patients with symptomatic heart failure: a contemporary study of prevalence in and characteristics of 700 patients," *Eur. J. Heart. Fail.*, vol. 9, no. 3, pp. 251-257, Mar. 2007, doi: 10.1016/j.ejheart.2006.08.003.

[5] M. A. Cretikos, R. Bellomo, K. Hillman, J. Chen, S. Finfer and A. Flabouris, "Respiratory rate: The neglected vital sign," *Med. J. Austral.*, vol. 188, no. 11, pp. 657-659, Jun. 2008.

[6] P. Barthel, R. Wensel, A. Bauer, A. Müller, P. Wolf, K. Ulm, K.M. Huster, D.P. Francis, M. Malik and G. Schmidt, "Respiratory rate predicts outcome after acute myocardial infarction: A prospective cohort study," *Eur. Heart. J.*, vol. 34, no. 22, pp. 1644-1650, Jun. 2013, doi: 10.1093/eurheartj/ehs420.

[7] M. Grassmann, E. Vlemincx, A. von Leupoldt, J. M. Mittelstadt and O. Van den Bergh, "Respiratory changes in response to cognitive load: A systematic review," *Neural. Plast.*, vol. 2016, 2016, Art. no. 8146809, doi: 10.1155/2016/8146809.

[8] A. Nicolo, C. Massaroni and L. Passfield, "Respiratory frequency during exercise: The neglected physiological measure," *Front. Physiol.*, vol. 8, Dec. 2017, Art. no. 922, doi: 10.3389/fphys.2017.00922.

[9] W. J. DePaso, R. H. Winterbauer, J. A. Lusk, D. F. Dreis and S. C. Springmeyer, "Chronic dyspnea unexplained by history, physical examination, chest roentgenogram, and spirometry. Analysis of a seven-year experience," *Chest*, vol. 100, no. 5, pp. 1293-1299, Nov. 1991, doi: 10.1378/chest.100.5.1293.

[10] F. Q. Al-Khalidi, R. Saatchi, D. Burke, H. Elphick and S. Tan, "Respiration rate monitoring methods: A review," *Pediatr. Pulmonol.*, vol. 46, no. 6, pp. 523-529, Jun. 2011, doi: 10.1002/ppul.21416.

[11] A. Abid, "Model-based estimation of respiratory parameters from capnography, with application to diagnosing obstructive lung disease". *IEEE. Trans. Biomed. Eng*., vol. 64, no. 12, pp. 2957–2967, May. 2017.

[12] S. Gong, W. Schwalb, Y. Wang, Y. Chen, Y. Tang, J. Si, B. Shirinzadeh, and W. Cheng, "A wearable and highly sensitive pressure sensor with ultrathin gold nanowires," *Nat. Commun.*, vol. 5, Feb. 2014, Art. no. 3132, doi: 10.1038/ncomms4132.

[13] S. Stick, E. Ellis, P. LeSouëf and P. Sly, "Validation of respiratory inductance plethysmography (“Respitrace”®) for the measurement of tidal breathing parameters in newborns," *Pediatr. Pulmonol.*, vol. 14, no. 3, pp. 187-191, Nov. 1992.

[14] N. Netzer, A. H. Eliasson, C. Netzer and D. A. Kristo, “Overnight pulse oximetry for sleep-disordered breathing in adults: A review,” *Chest*, vol.120, no. 2, pp. 625–633, Aug. 2001.

[15] E. Nemati, M. J. Deen, and T. Mondal, "A wireless wearable ECG sensor for long-term applications," *IEEE Commun. Mag.*, vol. 50, no. 1, pp. 36-43, Jan. 2012.

[16] B. A. Reyes, N. Reljin, Y. Kong, Y. Nam and K. H. Chon, "Tidal volume and instantaneous respiration rate estimation using a volumetric surrogate signal acquired via a smartphone camera," *IEEE J. Biomed. Health Inform.*, vol. 21, no. 3, pp. 764-777, May 2017, doi: 10.1109/JBHI.2016.2532876.

[17] C. Li, V. M. Lubecke, O. Boric-Lubecke and J. Lin, "A review on recent advances in doppler radar sensors for noncontact healthcare monitoring," *IEEE Trans. Microw. Theory Tech.*, vol. 61, no. 5, pp. 2046-2060, Apr. 2013, doi: 10.1109/tmtt.2013.2256924.

[18] K. S. Park, S. H. Hwang, H. N. Yoon and W. K. Lee, "Ballistocardiography for nonintrusive sleep structure estimation," in *Conf. Proc. 36th IEEE Eng. Med. Biol. Soc.*, Aug. 2014, pp. 5184-5187.

[19] C. Song and P. Wang, “A radio frequency device for measurement of minute dielectric property changes in microfluidic channels”, *Appl. Physc. Lett.*, vol. 94, no. 2, Jan. 2009, Art. no. 023901.

[20] J. Naqui and F. Martin, "Transmission lines loaded with bisymmetric resonators and their application to angular displacement and velocity sensors," *IEEE Trans. Microw. Theory Tech.*, vol. 61, no. 12, pp. 4700-4713, Oct. 2013, doi: 10.1109/tmtt.2013.2285356.

[21] A. Ebrahimi, J. Scott and K. Ghorbani, “Differential sensors using microstrip lines loaded with two split-ring resonators”, *IEEE Sens. J.*, vol. 18, no. 14, pp. 5786-5793, May 2018, doi: 10.1109/jsen.2018.2840691.

[22] S. Harnsoongnoen and A. Wanthong, “Coplanar waveguide transmission line loaded with electric-LC resonator for determination of glucose concentration sensing”, *IEEE Sens. J.*, vol. 17, no. 6, pp. 1635-1640, Jan. 2017, doi: 10.1109/jsen.2017.2652121.

[23] X. Hui and E. C. Kan, "Monitoring vital signs over multiplexed radio by near-field coherent sensing," *Nat. Electron.*, vol. 1, no. 1, pp. 74-78, Jan. 2018, doi: 10.1038/s41928-017-0001-0.

[24] CST Microwave Studio, Computer Simulation Technology, (2020) [Online]. Available: http://www.cst.com

[25] P. Sharma and E. C. Kan, "Sleep scoring with a UHF RFID tag by near field coherent sensing," in *2018 IEEE/MTT-S International Microwave Symposium (IMS)*, Philadelphia, PA, June 10 – 15, 2018, pp. 1419-1422.

[26] P. Sharma, X. Hui and E. C. Kan, "A wearable RF sensor for monitoring respiratory patterns," in *41st Annual International Conference of the IEEE Engineering in Medicine and Biology Society (EMBC)*, Berlin, Germany, July 23 – 27, 2019: IEEE, pp. 1217-1223.

[27] R. M. Fano, "Theoretical limitations on the broadband matching of arbitrary impedance, " *J. Franklin Institution*, vol. 249, no. 1, pp. 57–83, Jan. 1950.

[28] W. Lu, M.M. Nystrom, P.J. Parikh, D.R. Fooshee, J.P. Hubenschmidt, J.D. Bradley and D.A. Low, "A semi-automatic method for peak and valley detection in free-breathing respiratory waveforms," *Med. Phys.*, vol. 33, no. 10, pp. 3634-3636, Oct. 2006, doi: 10.1118/1.2348764.

[29] P. Sharma, X. Hui, J. Zhou, T. B. Conroy and E. C. Kan, “Robust cardiopulmonary monitoring using wearable radio-frequency sensors”, *NPJ Digit. Med.*, vol. 3, doi: 10.1038/s41746-020-0307-6, July 2020.

Zijing Zhang received a B.Eng. degree in optoelectronic engineering from Huazhong, University of Science and Technology (HUST), Wuhan, China, in 2019. She is currently pursuing the Ph.D. degree in Electrical Engineering at Cornell University, Ithaca, NY, USA.

Pragya Sharma received a B.Tech. degree in electrical engineering from the Indian Institute of Technology (IIT), Kharagpur, India, in 2015. She is currently pursuing the Ph.D. degree in Electrical Engineering at Cornell University, Ithaca, NY, USA.

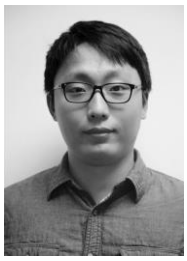

Jianlin Zhou received the B.S. degree in electronics and information engineering from Nanjing University of Science and Technology, Nanjing, China in 2013, and the M.S. degree in electrical and computer engineering from Northeastern University, Boston, MA in 2016. He has previously worked as a research support associate on ingestible electronics design for drug delivery and bio-sensing in Robert Langer Lab at Massachusetts Institute of Technology from 2016 to 2018. He is currently pursuing the Ph.D. degree in electrical and computer engineering at Cornell University, Ithaca, NY, USA.

Xiaonan Hui received the B.S. degree from Northeastern University, China in 2012, and the M.S. degree from Zhejiang University, China in 2015, all in electrical engineering. He is currently pursuing the Ph.D. degree in electrical and computer engineering at Cornell University, Ithaca, NY, USA.

Edwin C. Kan received the B.S. degree from National Taiwan University in 1984, and the M.S. and Ph.D. degrees from University of Illinois, Urbana-Champaign in 1988 and 1992, respectively, all in electrical engineering. He has served in the Air Force, Taiwan, R. O. China as a second lieutenant from 1984 – 1986. In January 1992, he joined Dawn Technologies as a Principal CAD Engineer. He was then with Stanford University as a Research Associate from 1994 to 1997. In 1997, he joined the School of Electrical and Computer Engineering, Cornell University, Ithaca, NY as an assistant professor, where he is now a professor.

Furniture-Integrated Respiration Sensors by Notched Transmission Lines

Zijing Zhang, Pragya Sharma, Jianlin Zhou, Xiaonan Hui and Edwin C. Kan, Senior Member, IEEE

XXXX-XXXX © XXXX IEEE. Personal use is permitted, but republication/redistribution requires IEEE permission.

See http://www.ieee.org/publications_standards/publications/rights/index.html for more information.

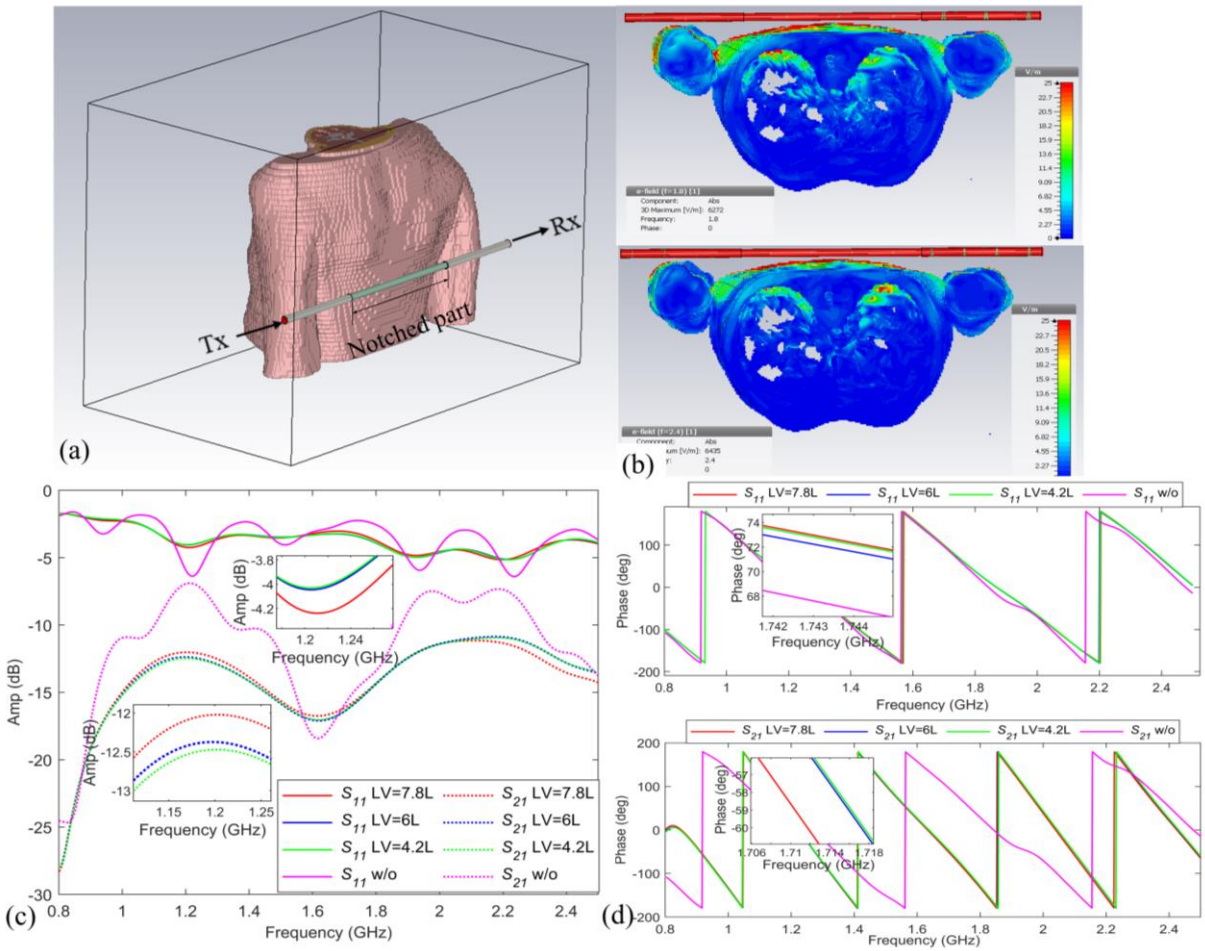

Supplementary Fig. 1. CST simulation model of a notched transmission line on a part of a human torso: (a) Geometrical setup. (b) The E-field distribution in the torso cross section 1 in above the xiphoid process at 1.8 GHz (upper) and 2.4 GHz (lower).(c) S_{11} (solid) and S_{21} (dotted) amplitudes in the frequency range of [0.8, 2.5] GHz with different lung volume (LV). The red lines are at the nominal maximal inhalation with LV = 7.8 L; The blue lines are at equilibrium with LV = 6 L; The green lines are at the nominal maximal exhalation with LV = 4.2 L; The purple lines are the notched transmission line in free space. (d) The corresponding phases of S_{11} (upper) and S_{21} (lower).

Supplementary Fig. 1 shows the CST Microwave Studio simulation model corresponding to Fig. 1(c) in the main article. A segment of the transmission line is notched in the middle part without the outer metal shield. EM energy is leaked out from the Tx port and received by the Rx port. The upper part of the human torso is simplified with only lungs, muscle, bones, body fat, skin and sweatshirt in Supplementary Fig. 1(a), following the CST human library [1]. The notched transmission line is closely placed beside the back of the human torso with a small airgap at the height of 1 in above the xiphoid process. Energy leaks from the notched part and couples into the human body which affects the reflection and transmission in the notched line. Supplementary Figs. 1(b) shows the electric-field magnitude and the torso cross section at 1.8 GHz (upper) and 2.4 GHz (lower). Supplementary Fig. 1(c) shows the amplitude of S_{11} and S_{21} in the frequency range of [0.8, 2.4] GHz and Fig. 1(d) shows the phases of S_{11} (upper) and S_{21} (lower). The lung volume (LV) at equilibrium is assumed to be 6 L as the average lung capacity of an adult male. To represent the breathing motion, LV is set at 7.8 L for maximum inhalation and 4.3 L at maximum exhalation. As LV changes, S_{11} and S_{21} change accordingly. For the given setup, S_{21} will be more sensitive in terms of percentage change. At different carrier frequencies, the coupling depths are slightly different. We also simulated the individual notched transmission line in the free space for comparison.

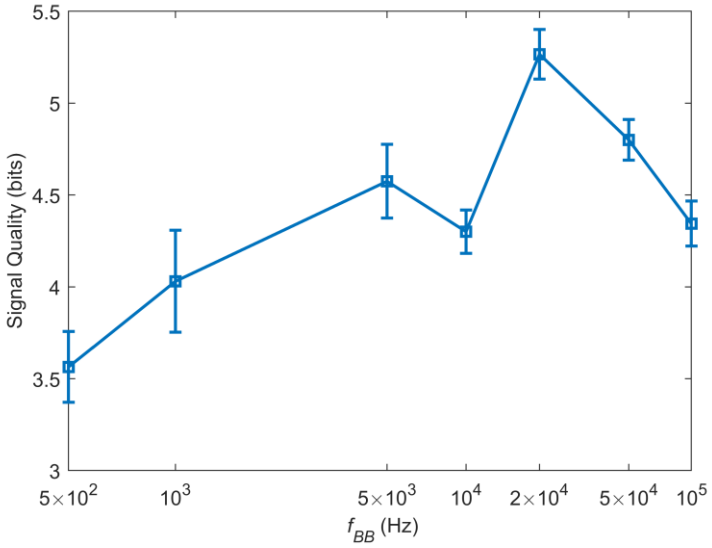

Supplementary Fig. 2. The relation between the signal quality and baseband frequency f_{BB} during 90s of normal breathing. At each f_{BB}, the middle square and the error bar represent the mean and standard deviation from all collected breath cycles.

Supplementary Fig. 2 shows the signal quality versus the baseband frequencies fBB. The breathing exercise was the tidal breathing for 90 s to minimize the variation from human factors. The result was from the abdomen sensor at the supine posture using B200mini at fRF = 0.9 GHz. At each fBB, the signal quality was evaluated by approximately 42 samples. The signal quality is degraded for very low fBB as dominated by the 1/f noise of the fRF local oscillator, or for very high fBB as dominated by the ADC jitter [2].

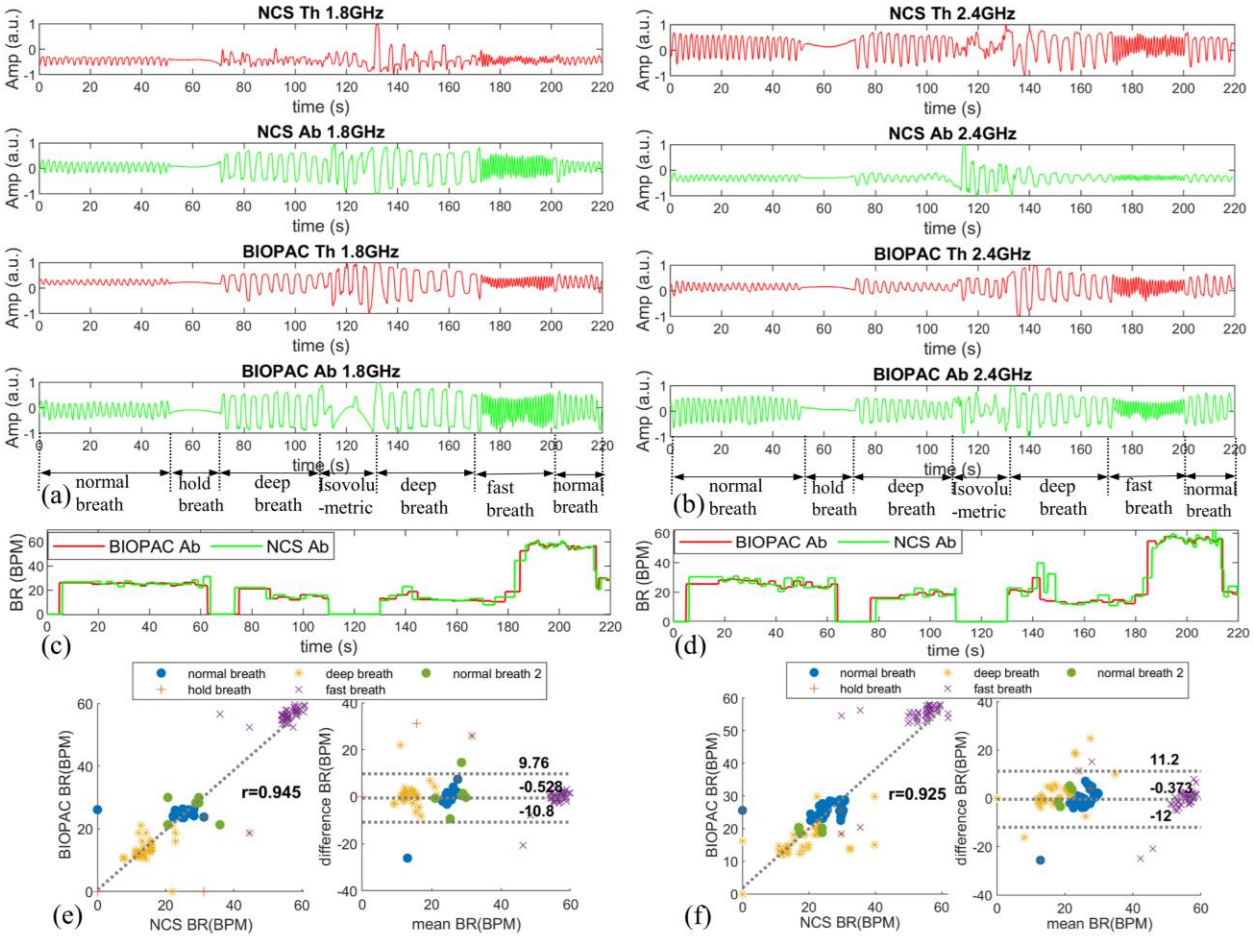

Supplementary Fig. 3. Thorax and abdomen NCS and BIOPAC sensor benchmark in the supine position on bed. (a) Amplitude waveforms at f_{RF} =1.8GHz and (b) at f_{RF} =2.4GHz. Texts below the figures indicate the specific breathing patterns. (c) Breath rate (BR) calculated from NCS (green) and BIOPAC (red) at f_{RF} =1.8GHz and (d) at f_{RF} =2.4GHz. BR of the isovolumetric exercise during 110s - 130s is set to zero. (e) The B&A plots at f_{RF} =1.8GHz and (f) at f_{RF} =2.4GHz. The scatter plots are shown with the Pearson's correlation coefficient. The agreement plots show the mean difference m at the center dotted line and the corresponding limits of agreement (LoA) at the upper and lower dotted lines given by $m \pm 1.96\sigma$.

Supplementary Figs. 3 shows the NCS and BIOPAC comparison with the supine position on bed when NCS uses different fRF from Fig. 3 in the main text. The normalized NCS and BIOPAC amplitude waveforms are shown at (a) fRF =1.8GHz and (b) fRF =2.4GHz. At both frequencies, NCS and BIOPAC data can distinguish different breathing patterns and show a good agreement to each other. BR calculated from NCS and BIOPAC abdomen amplitudes are shown at (c) fRF =1.8GHz and (d) fRF =2.4GHz. BR of the isovolumetric exercise period was truncated to 0. At 1.8GHz, BR is estimated around 27 BPM during normal breath, 15 BPM during deep breath, and 55 BPM during fast breath. The result from 2.4GHz is similar to 1.8GHz. BR estimation matches the breathing patterns, but a delay in time is observed, because our BR calculation is based on the data in the previous epoch. The B&A plots between NCS and BIOPAC are shown at (e) fRF =1.8GHz and (f) fRF =2.4GHz. High correlations of r =0.945 and r = 0.925 had been achieved under both fRF. From the B&A plot, the mean difference is m = –0.528 BPM for 1.8GHz and –0.373 BPM for 2.4GHz, as shown in the middle dotted line. Low m and narrow LoA indicate that the errors in NCS and BIOPAC are uncorrelated and small.

Results from Supplementary Fig. 3 along with Fig. 3 in main text give further confirmation of the feasibility of our notched sensor system operated in the broad bandwidth. The sensor can capture the breath waveforms clearly to derive BR accurately under different breathing patterns. The system can operate well at fRF =0.9, 1.8 and 2.4GHz,

and the correlation between our system and BIOPAC system is high.

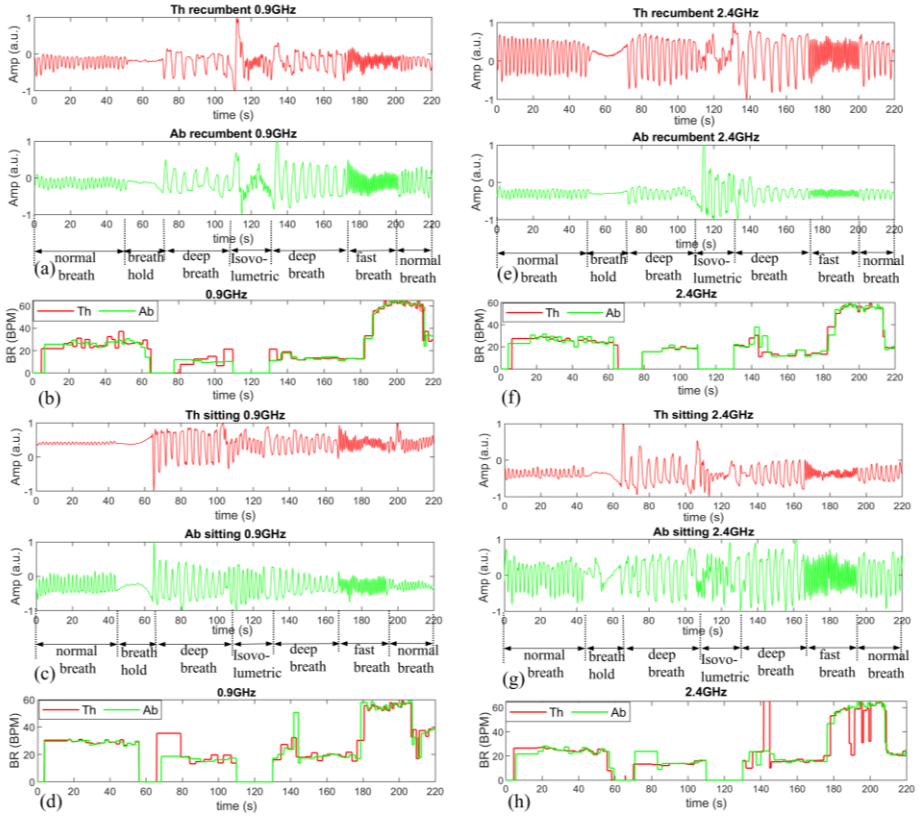

Supplementary Fig. 4. (a)(e) Respiration waveforms from thorax and abdomen NCS sensors at (a) f_{RF} =0.9GHz and (b) f_{RF} =2.4GHz in the recumbent posture on bed. Texts below the figures indicate the specific breathing patterns. (c)(d) BR estimated from the waveforms in (a)(b). BR of the isovolumetric exercise during 110-130s is set to zero. Respiration waveforms from thorax and abdomen NCS sensors in the sitting posture on chair at (e) f_{RF} =0.9 GHz and (f) f_{RF} =2.4 GHz. (g)(h) BR estimated from the waveforms in (e)(f).

Supplementary Fig. 4 shows respiration waveforms from thorax and abdomen NCS sensors and BR estimations in the recumbent posture on bed and sitting posture on chair at fRF =0.9 and 2.4 GHz. Thorax and abdomen sensors correlate with each other well. For the recumbent posture, BR is estimated around 25 BPM during normal breath, 13 BPM during deep breath, and 60 BPM during fast breath for 0.9 GHz. The BR estimated from 2.4 GHz is similar to 0.9 GHz. For the sitting posture, BR is estimated around 28 BPM during normal breath, 16 BPM during deep breath, and 55 BPM during fast breath for 0.9 GHz. BR estimated from 2.4 GHz corresponds well with those by 0.9 GHz.

Results from Supplementary Fig. 4 along with Fig. 4 in main text give further confirmation that our system can operate in supine and recumbent postures on bed, and the sitting posture on chair. Different respiration patterns can be distinguished clearly and BR can be accurately measured. The system can operate well in these postures at a broad range of fRF, including 0.9, 1.8 and 2.4 GHz.

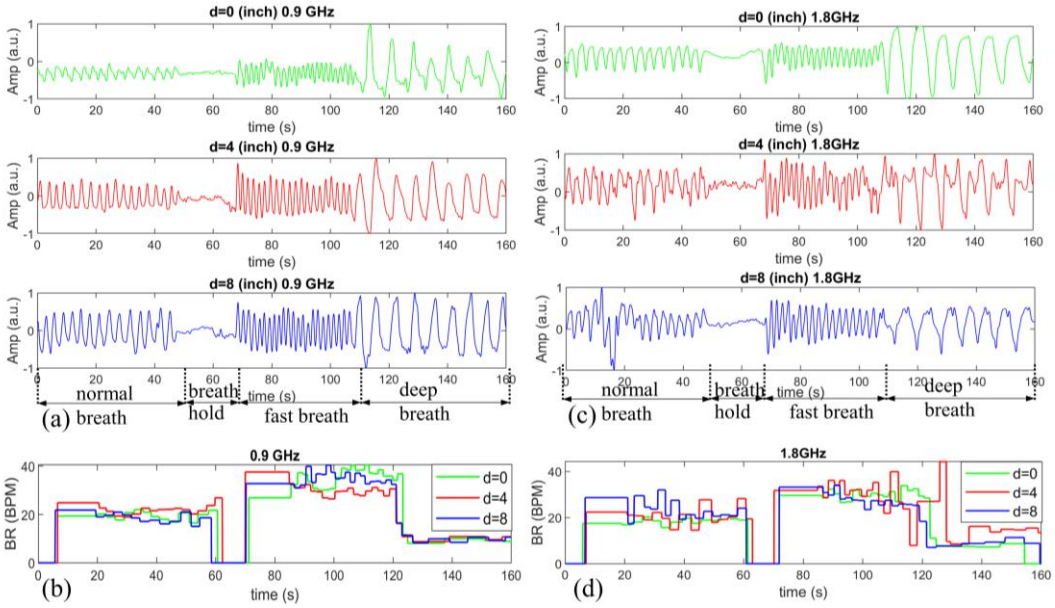

Supplementary Fig. 5. NCS recording under horizontal position variation. Respiration waveforms at (a) f_{RF} =0.9GHz and (b) f_{RF} =1.8GHz with horizontal shift of d = 0, 4, 8 in for the abdomen sensor in the supine posture on bed. Texts below the figures indicate the specific breathing patterns. BR estimated from the respiration waveforms at (c) f_{RF} =0.9 GHz and (d) f_{RF} =1.8 GHz for d = 0 (green); d = 4 in (red); d = 8 in (blue).

Supplementary Fig. 5 demonstrates respiration waveforms and BR estimated from the abdomen sensor with different horizontal shifts of d = 0, 4, and 8 in at fRF = 0.9 GHz and 1.8 GHz. For both frequencies, as the position shift increases, different respiration patterns can still be identified and the transition in between was evident. In spite of some small fluctuations, estimated BR are still similar under different horizontal shifts, which is around 23 BPM during normal breath, 10 BPM during deep breath, and 33 BPM during fast breath for 1.8 GHz. BR estimated from 0.9 GHz corresponds well with those by 1.8 GHz.

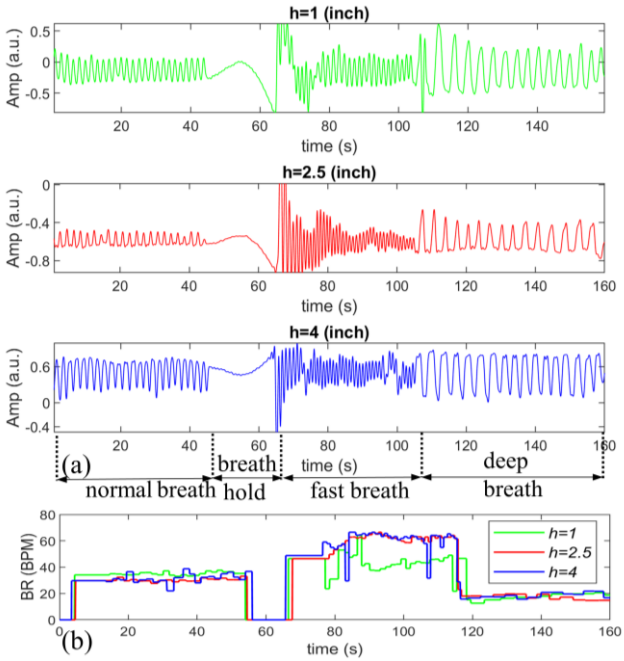

Supplementary Fig. 6. NCS recording under vertical position variation. (a) Respiration waveforms with vertical position of h = 1, 2.5, 4 in for the abdomen sensor in the supine posture on bed. Texts below the figures indicate the specific breathing patterns. (b) BR estimated from the respiration waveforms for h = 1 (green); h = 2.5 in (red); h = 4 in (blue).

Supplementary Fig. 6 demonstrates (a) respiration waveforms and BR estimated from the abdomen sensor (b) with different vertical position shift of h1 = 1, 2.5, 4 in (with respect to the umbilicus). The breathing protocol was the same as Supplementary Fig. 5. As a representative example, we only show the results at fRF =0.9GHz. Under different vertical position shifts, different breathing patterns can still be distinguished clearly. The smallest distance to the umbilicus, h1 = 1 in, is furthest to the lung and diaphragm, and thus has worse data quality compared with h1 = 2.5 and 4 in.

Results from Supplementary Figs. 5 and 6 along with Fig. 5 in the main text confirm that our notched sensor can operate under various horizontal and vertical shifts to accommodate practical user uncertainties.

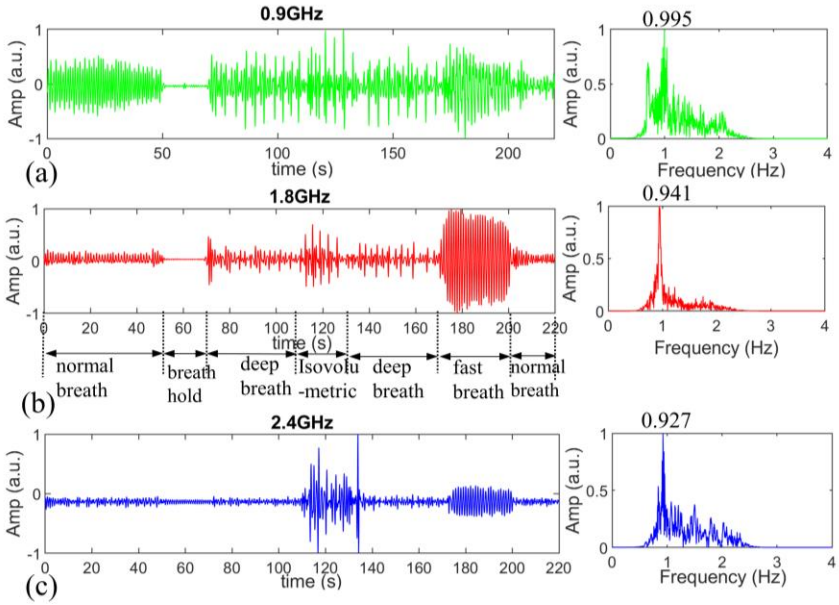

Supplementary Fig. 7. Left: Heartbeat waveforms from the thorax sensor after [0.8, 2] BPM bandpass filtering during the whole breathing protocol. Right: The corresponding frequency spectrum with HR peak indicated by the annotation above. (a) f_{RF} = 0.9 GHz; (b) f_{RF} =1.8GHz; (c) f_{RF} =2.4GHz.

Apart from the HR estimation during 15s as shown in Fig. 7 of the main text, we also extracted HR during the entire 220s breathing protocol. In order to reduce the respiration interference, the NCS signal was first filtered by a bandpass filter of [0.8, 2] BPM. Supplementary Fig. 7 demonstrates the waveforms from the thorax sensor and the corresponding frequency spectra at fRF = 0.9, 1.8 and 2.4 GHz. The HR peak was around 55-60 BPM. Second and third harmonics of HR were not clearly detected, because different breathing patterns and long protocol bring more interference.

SUPPLEMENTARY TABLE I. MEAN AND STANDARD DEVIATION OF SIGNAL QUALITY IN DIFFERENT CONDITIONS

(a) Position bias	m	σ	m_{normal}	σ_{normal}	**(b) Sensor placement**	m	σ	m_{normal}	σ_{normal}
d = 0	4.20	0.343	4.24	0.142	Supine thorax	3.70	0.670	2.96	0.144
d = 4 in	3.18	0.869	3.00	0.429	Supine abdomen	5.58	0.571	5.72	0.118
d = 8 in	1.60	1.117	1.27	0.581					
(c) Posture	m	σ	m_{normal}	σ_{normal}	**(d) Frequency**	m	σ	m_{normal}	σ_{normal}
Supine	4.83	0.522	4.32	0.180	0.9 GHz	4.38	0.710	3.91	0.225
Recumbent	3.12	0.700	4.32	0.132	1.8 GHz	5.68	0.558	5.58	0.187
Sitting	3.65	0.818	3.80	0.310	2.4 GHz	5.23	0.299	5.21	0.179

Supplementary Table I presents the means and standard deviations of the signal quality results in Fig. 8 of the main text. The means and standard deviations were calculated during the entire breathing protocol and during only the beginning period of normal breathing.

SUPPLEMENTARY TABLE II. ISOVOLUMETRIC EXERCISE DETECTION ACCURACY OF 10 PARTICIPANTS.

	NCS				BIOPAC			
Case No.	TP	TN	FP	FN	TP	TN	FP	FN
1	2	15	1	0	2	14	2	0
2	2	16	1	0	1	15	1	1
3	2	14	0	2	2	16	0	0
4	2	16	0	0	1	16	1	0
5	2	14	0	2	1	15	1	1
6	2	14	0	2	1	14	1	2
7	2	15	0	1	2	14	0	2
8	2	15	0	1	1	15	1	1
9	0	15	2	1	0	15	2	1
10	1	16	1	0	0	15	2	1

Supplementary Table II presents the statistics of isovolumetric exercise detection on each participant. The data contained 180s of the whole breathing protocol (20-200s) including an isovolumetric exercise of 20s. The epoch was chosen to be 10s here. The left table demonstrates the data from NCS sensor, and the right table demonstrates the data from BIOPAC sensor for benchmark.

SUPPLEMENTARY TABLE III. PERSONAL TRAIT OF 10 PARTICIPANTS.

Case No.	Height (cm)	Weight (kg)	Age	Gender	BMI
1	170	72	57	male	24.8
2	178	70	22	male	22.1
3	170	65	21	male	22.5
4	180	83	31	male	25.6
5	183	75	29	male	22.4
6	167	60	26	female	21.5
7	180	78	29	male	24.0
8	172	68	45	female	23.0
9	180	73	23	male	22.5
10	165	51	22	female	18.7

REFERENCES

[1] CST Voxel family, [Online]. Available:http://www.mweda.com/cst/cst2013/mergedProjects/CST_EM_STUDIO/common_tools/bio_models.html

[2] X. Hui and E. C. Kan, "Radio ranging with ultrahigh resolution using a harmonic radio-frequency identification system." *Nature Electron.*, vol. 2, no. 3, pp. 125-131, Mar. 2019.

Appendix H

(PDF manuscript under preparation) P. Sharma, Z. Zhang, X. Hui and E. C. Kan, “Attention monitoring using non-invasive vital-sign features”, manuscript under preparation.

ATTENTION MONITORING USING NON-INVASIVE VITAL SIGN FEATURES

1. Introduction

The provision of individually tailored sensory response systems have been of increasing importance in the recent years. Apart from sensing the surrounding context, it involves understanding the physical and physiological responses of the people. Using emotion recognition has been an important part of human-machine interaction system by teaching a robot to give appropriate facial and speech responses. Smart buildings can be enabled to adjust lighting according to the emotional state and keep track of mental health, including depression and anxiety monitoring and alert family when required. With increasing work-from-home jobs, forced by the COVID-19 pandemic, such systems are even more important to monitor work fatigue. Keeping track of fatigue or the opposite, attention, is even more important for people working in critical conditions like soldiers in action, heavy machine operators, air traffic controllers and drivers. With accurate knowledge of the attention state, actions in form of visual or sound stimuli can be provided if person is slipping into drowsiness or a less attentive state.

The capability of intelligent machine response requires understanding of human emotional and cognitive reactions. There has been a debate starting from the early philosophers if reason and emotion are two opposite or related concepts, with recent research demonstrating high level of interdependence [1]. When people perceive a vast amount of information, a subset processing is prioritized and extraneous irrelevant information filtered out, to access the conscious awareness, which can be termed as attention [2]. Thus, attention is a basic function that controls focus, vigilance, and response simultaneously [3]. It can be classified as two types: exogenous attention is sensory driven, involuntary response, while endogenous attention is a voluntary process, with conscious expectation of events [4]. There is another state called *emotional attention*, which is involuntary similar to exogenous attention, but has been suggested to rely on special neural circuitry involving amygdala [5]. Presently, the psychological and neuroscientific research has extensively modeled emotion and its impact on attention and decision making. Brain studies to differentiate the amygdala response to emotion and attention have suggested faster response to emotion over attention [6], [7], however, the overall results remain inconclusive [8]. In summary, emotional and attention states are highly intertwined, and the attention study can benefit from the vast research in emotion monitoring domain to understand various physiological reactions.

In this work, we have focused primarily on attention versus relaxation classification. The attention under study is endogenous, in response to certain events that user interacts with during a specific task. The relaxation has been loosely defined as a state similar to drowsiness or fatigue but covers a broader aspect of user inattentiveness including the meditative state. This is an important factor, as user needs to be attentive even though no harmful activity has been perceived for a long period, such as in driving or guarding. A study on 25 healthy participants sitting on the chair was performed while wearing NCS RF sensors on the thorax and abdomen with routines involving neutral, relaxation, and attention states while sitting in a chair. [9] included data from these routines, which validated the sensor performance for respiratory effort and heart rate monitoring. The next section presents related works in the area of attention detection and emotion monitoring. Sec. 3 presents a classification algorithm, including feature selection. The detailed

data collection routine during attention is presented in Sec. 4. Sec. 5 presents the detailed results using NCS and the reference sensors. Finally, conclusion and future work are presented.

2. Background and Related Work

Long-term attentive tasks may result in mental fatigue [8] and require constant attention monitoring. Developing a safety attention monitoring setup ideally requires complete occupant centric knowledge, i.e.:

1) Sensing the surroundings.
2) Sensing user's actions.
3) Sensing user's physiological responses like brain activity, heart and respiratory patterns, and motor expression including face, voice, and body.

The detailed sensing of user environment is very difficult and also not suitable in most real-life applications. Autonomous or assisted driving are steps in this direction but require a lot of research efforts that are difficult in all possible attention demanding scenarios. Even with this sensing, increased drowsiness can result in user inability to take an immediate action. Also, user action or response monitoring [10], [11] to record attention periodically can get very tiring and distracting by its own action. Thus, monitoring of physiological responses and motor expressions are often the most suitable techniques for many cases.

Existing attention monitoring techniques mostly detect fatigue as an alternative. While fatigue can be both physical and mental, only the latter has been included here. This technique

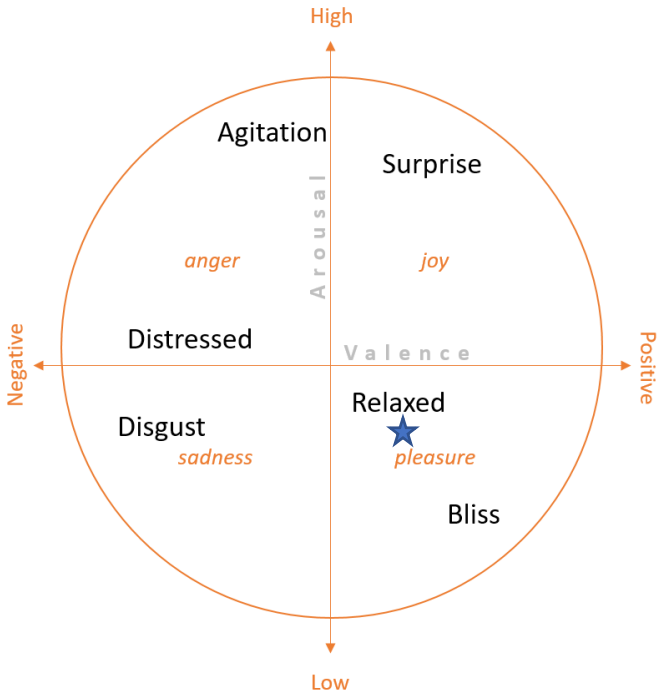

Figure 1 A two-dimensional arousal/valence model

only focuses on cases arising out of tiredness or boredom leading to sleepiness. Cases where user is relaxed and not expecting any events to occur are not counted, which can be extremely dangerous, for example, in sudden combat attacks. Thus, a broader comparison of attention versus relaxation needs to be performed. This can be enabled by interlink of attention and emotion. Emotions can be classified in different ways, where each feeling is an independent emotion of *joy, anger, sadness*, etc. [12] or they can be clustered in a smaller multidimensional space [13], [14], usually spanned by *valence* and *arousal* in addition to others. Valence is classified as positive or happy emotions versus negative or sad emotions. Arousal refers to the activation level and ranges from low to high and is easier to differentiate than valence [14]. Fig. 1 shows the 2D arousal and valence model. Since relaxed state is near the neutral valence and arousal states in the 2D model and attention may be accompanied with high agitation (high arousal – neutral valence) and distress (neutral arousal – negative valence), they are separable with this 2D model. In the following literature review, we will present the two areas of fatigue monitoring and emotion monitoring, due to connection of attention detection to both areas.

Fatigue monitoring: Previous research on attentiveness and fatigue detection comprises mainly of motor expression monitoring, including eye and mouth. The focus is mainly on fatigue detection, i.e., sleepiness which is characterized by change (increase or decrease) in blink rate and yawn, which may be an indicator of the arousal level [15]. As this approach requires facial expression monitoring, sensors in ambient are required. Thus, the system is often tailored to a specific setup like driving. PERCLOS (percentage of eye closure) has been widely used as an alertness measure but eye-only fatigue detection performance is inferior to EEG [16]. Computer-vision based eye detection systems and algorithms have been proposed [17]–[19], which may suffer from illumination conditions. Ji et al [20], [21] performed real-time driver fatigue prediction using near infra-red (IR) video cameras for eyelid, gaze, head movement and facial expression tracking with a probabilistic model. The best accuracy can be achieved with physiological parameter sensing which may be inconvenient for driving with wearable sensors [20], [21]. Other alternatives include piezoelectric sensors placed on the skin of eyelid for fatigue monitoring [22]. Electrooculogram (EOG) sensors have been used [23] to detect driver drowsiness.

Fatigue detection has also been performed by physiological measurements like changes in heart rate, brain activity, and thermoregulation, the last of which gives the best performance for monitoring physical fatigue in construction workers [24]. EEG has been extensively used for mental fatigue detection [25]–[29] with response time in 10s of seconds [29]. Skin conductance has also been used for mental workload [30].

Emotion monitoring: There has been a vast amount of research done in the area of emotion recognition from physiological signals [31]–[33]. The accuracy varies based on the recorded signals, sensing technology, emotion model and classification algorithms. The real-life implementation heavily depends on the required comfort level of the sensor and accuracy tradeoff, for example, pulse oximetry (SpO_2) sensing from the wristwatch may achieve limited accuracy with high comfort.

Facial expression, speech and other motor features have been extensively used for emotion recognition with improved results for multimodal approaches [34], [35]. A bimodal system used facial and acoustic information [34] to classify four emotions using k-nearest neighbor (kNN). A

hidden Markov model (HMM) with maximum likelihood classifier was used for automatic segmentation and recognition from a continuous video into a sequence of emotions in [36], with very low recognition rate for an unseen participant as display of emotions vary with ethnicity and gender. Deep learning based approaches have also been used in the recent years [37], [38], including transfer learning [39] for emotion detection. The performance of these methods relies on expressiveness of the user, accurate baseline estimates or a large training data across different races, illumination and background audio noises.

Galvanic skin response (GSR) or skin conductance (SC), blood volume pulse (BVP) and skin temperature (ST) from hands, and pupil diameter (PD) with an eye gaze tracking instrument were employed to monitor stress [40]. SVM classifier resulted in a high cross-validation (CV) accuracy with PD as the most important feature. The existing literature has difficulty in detecting intensity of emotion with only GSR and electromyography (EMG) [41], even with a relaxation baseline. Arousal versus valence classification has been performed using GSR and photoplethysmogram (PPG) [42] with leave-one-out subject accuracy of 70%, compared to 87% for a single-user model. While these parameters are important, they are associated with specific emotions. GSR and PD have been associated with arousal [43], [44]. EMG measurement of neck muscles could be indicator of stress, and it is a single dimensional valence measure [31]. Stress or anxiety may result in colder ST at the fingers. Thus, multiple sensors with different placements are required, all with direct skin contact, and are thus uncomfortable.

Another important category of work focuses particularly on heartbeat signals to measure heart rate variability (HRV) [45], [46]. Electrocardiogram (ECG) has been widely used for heartbeat based emotion recognition [47], [48]. A model based on empirical mode decomposition (EMD) with Hilbert-Huang transform (HHT) was used to derive features based on instantaneous frequency for arousal/valence study in [47]. As ECG requires skin contact, PPG has been seen as a desirable alternative, particularly with watch and fitness tracker integration [49], [50]. However, baseline drift, motion artifacts and signal quality need to be taken into account. As ECG has been established as a biometric tool [51], showing varying features across users, it should be used carefully for consistent emotion recognition across different subjects. Additionally, the emotion state has also been linked to correlation of respiration and heartbeat in [14], indicating correlation between different physiological channels. Only respiration signal has been used with high accuracy in [52], [53] by a deep learning approach.

Noninvasive wireless RF sensing has also been used for emotion detection [54]–[56]. The traditional far-field sensing mostly measures respiratory signals only, which can be 10 times stronger than the heartbeat [54]. The heartbeat features were stated to be indirectly extracted from respiration in [54], achieving a high average leave-one-subject CV accuracy of 94.4% for stress detection. Raw RF data was used in [55] to train a convolutional neural network (CNN) followed by a long short-term memory (LSTM) deep learning architecture. This achieved 67 – 87% accuracies to classify 4 different emotions with user-independent learning. HRV was extracted with signal processing tools [56] with an FMCW radar, resulting in a 70 – 75% accuracy for a person-independent 4-emotion classification, using the valence/arousal model. This work required a baseline neutral state corresponding to the specific day and person for feature calibration. These wireless sensing techniques are restricted to indoor setups, supporting only a limited number of users in the room.

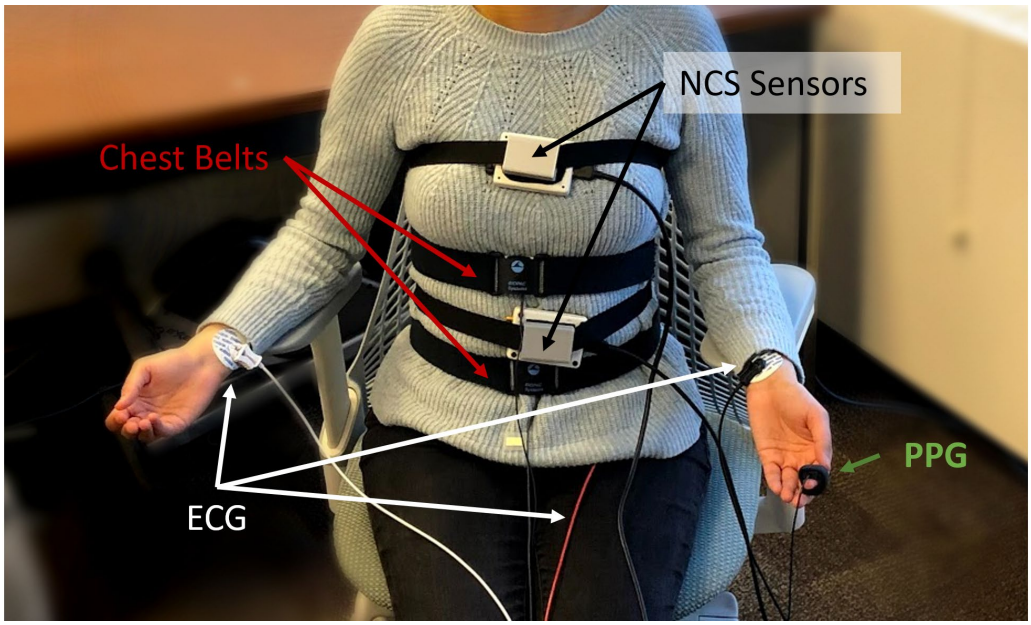

Figure 2 Setup for attention monitoring.

This work uses robust NCS wireless sensing, that can be placed over-the-clothes to record heartbeat and respiratory sensing. This allows us to monitor multiple people simultaneously without any interference from ambient motion, unlike existing approaches. With near-field coupling, we can get a noticeably clear heartbeat signal, in addition to the respiration for feature extraction. We have established relationship between emotion and attention and adopted similar tools as emotion recognition for a broader attention/relaxation classification, allowing applicability to different applications. Further, with passive and active setups, NCS has high comfort levels in comparison with other approaches requiring direct skin contact.

3. Experimental Setup

This experimental study was conducted approved by Cornell IRB and performed with participants informed written consent. The data collection was performed on 25 healthy subjects including 15 female subjects. The age range is 18 – 34 yrs., with BMI in the range 17.6 – 27 kg/m^2.

3.1 Vital Sign Sensors

Two NCS sensors were placed at thorax and abdomen along with reference BIOPAC chest belts and ECG. No facemask calibration was required, and an additional finger PPG was placed as shown in Fig. 2. In this chapter, three routines in the sitting posture are considered:

R1 Breathing exercise routine (Initial 120 s only): Perform normal breathing without any deep breaths or breath holds.
R2 Relaxation routine (5 minutes): Close eyes, relax, and spontaneous breathing with no additional instructions.
R3 Attention routine (6.5 minutes): Play a vigilance-testing game with spontaneous breathing.

The attention monitoring setup uses heartbeat and respiration signals from NCS and compares with the reference devices (ECG, chest belts and PPG). The information contained in these signals is discussed below.

Heartbeat: The gold standard sensor for heartbeat monitoring is ECG. The main features are heart rate, interbeat interval (IBI) and heart rate variability (HRV) [57] which can be measured in several different ways. HRV is the variation in IBI or RR interval (interval between two RR peaks in ECG) and reflects the effect of many physiological factors modulating normal heart rhythm.

Anatomically, the medulla located in the brainstem contains cell bodies for two main divisions of the autonomic nervous system (ANS), termed as sympathetic (SNS) and parasympathetic (PNS). Autonomic outflow from medulla is divided into sympathetic and parasympathetic (vagal) branches, that modulate the activity of heart and blood vessels. These modulations are reflected on the HRV and is thus used extensively to monitor ANS functions. As the ANS, together with the hypothalamus gives response to emotional cues, the HRV is related to emotional responses [57].

The two branches, SNS and PNS, exhibit distinct functions. The fibers of SNS are present throughout the atria, particularly concentrated in the sino-atrial (SA) node and ventricles, and when stimulate the cardiac muscles to increase the heart rate (HR) when activated. This stimulation occurs in response to stress and emotion intensity, and prepares the body for vigorous activity. PNS decreases the cardiac workload, primarily resulting from trauma and allergic reactions. The separate contributions from sympathetic and parasympathetic autonomic activity modulate the RR intervals of the QRS complex. The sympathetic activity exhibits a slow course of action, with effects observed 5 s after stimulation, returning to baseline after 20 – 30 s, and is thus associated with low frequency (LF) in range 0.04 – 0.15 Hz of modulation frequencies of HR. Parasympathetic activity response appears rapidly, response time of 400 ms and returns to baseline after 1s, associated with high frequency (HF) in range 0.15 – 0.4 Hz of modulation frequencies of HR [46].

The HRV feature based emotion detection has been explored in great details in recent years, with time-domain (e.g. SDNN, RMSSD), frequency domain (LF, HF, 2D LF-HF) and non-linear (entropy and Poincare plot features) [57]–[59] analysis. However, care must be taken in signal processing, as even slight inaccuracy in IBI estimation can result in a huge variation. Thus, various standardized data processing tools have been established for the ECG data. As PPG data does not have a sharp peak and may have a small peak immediately following the main peak (dicrotic notch), rigorous signal processing needs to be performed. For NCS heartbeat signal, 2^{nd} harmonic based peak detection has been shown to perform better in [9].

Respiration: Respiration is normally an unconscious, automatic and involuntary process, controlled by medulla and pons. Conscious factors can override the autonomous process for a limited period, for example, while speaking, smelling or breath hold. With the complexity of respiration system, and in general favorability of heartbeat monitoring, the observations such as respiratory sinus arrhythmia [60] and rate variation relationship lack complete understanding [61]. In general, respiration is modulated by various emotional reactions including stress, anger, and relaxation. For instance, a decrease in respiratory rate (RR) is observed in the relaxed state.

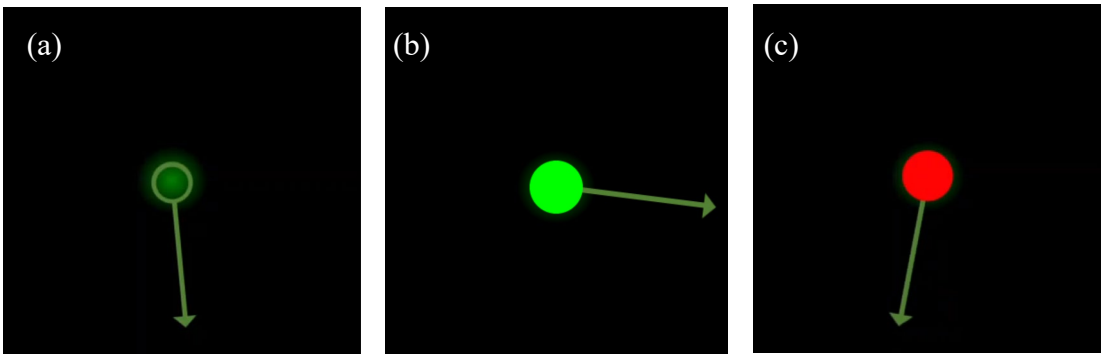

Figure 3 Attention test showing a clock hand. (a) Normal clock rotation. (b) Correctly detected jump. (b) Incorrect spacebar press or missed jump.

Tension, sudden fear or happy surprise may result in a breath hold, resulting in decreased RR, with increased variability. Deep and fast breathing can be anger or happiness. Further, while respiration is affected by emotions, voluntary respiration breathing techniques have been suggested to influence emotions and heartbeat [62]. Dyspnea or difficulty in breathing has been related to excitement or fatigue.

3.2 Attention Routine

A vigilance based game, based on traditional Mackworth clock test [63] was developed to engage the participant's attention. This routine was designed in PsyToolkit [64], [65], where a graphical interface displayed rotating clock hand as shown in Fig. 3. Intermittently, the clock hand jumped more than normal, and the participant was expected to press the spacebar. The speed, normal rotation angle and jump step were adjusted to keep the level easy. If participant pressed the spacebar correctly, the middle bulb glowed green. If jump was missed, or spacebar was wrongly pressed, it would glow red. These two instances are shown in Figs 3 (b) and (c), respectively.

The attention routine of 6.5 min includes:

1. 30 s instructions as shown in Fig. 4,
2. 30 s trial round,
3. 10 s wait,
4. 5 min test round.

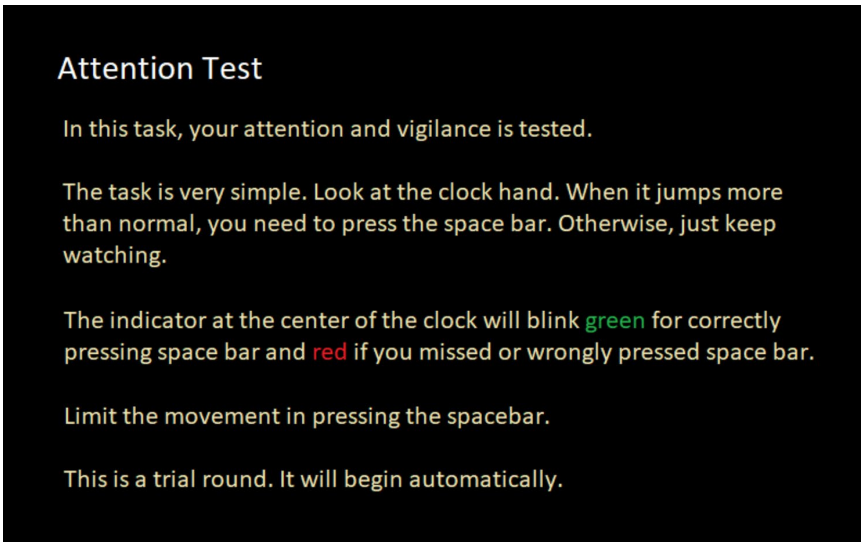

Figure 4 Instructions displayed at the beginning of the attention routine.

The normal clock hand rotation is 3.6°, and the abnormal jump is 5.4°. On each turn, a random number between 1 to 10 is generated, and abnormal jump occurs if number is 10. Thus, the probability for a uniform number generator is 0.1. A maximum reaction time of 1,000 ms is allowed. Following the test, it returns information about the game including: 1) time in ms from

1	2	3	4	5	6	7	8	9	
32351	1000	3	126	10	0	0	1	trial	★ Missed jump
32892	500	1	162	4	0	1	0	trial	★ Incorrect press
34437	1000	3	198	6	0	0	0	trial	
35483	1000	3	234	5	0	0	0	trial	
36530	1000	3	270	3	0	0	0	trial	
37577	1000	3	306	7	0	0	0	trial	
38622	1000	3	342	6	0	0	0	trial	
39671	1000	3	378	1	0	0	0	trial	
40714	1000	3	414	8	0	0	0	trial	
41759	1000	3	450	4	0	0	0	trial	
42806	1000	3	486	9	0	0	0	trial	
43853	1000	3	522	6	0	0	0	trial	
44896	1000	3	558	7	0	0	0	trial	
45942	1000	3	594	6	0	0	0	trial	
46596	611	1	684	10	1	0	0	trial	★ Correct detection
48037	1000	3	720	5	0	0	0	trial	

Figure 5 The test generated dataset giving timing and reaction information, with column numbers shown on the top.

start of the experiment corresponding to each rotation, 2) reaction time, 3) status (if a key was pressed), 4) current position of the clock hand in tenth of degrees, 5) generated random number, 6) value '1' if jump occurred and correctly detected, 7) value '1' for incorrect press, 8) value '1' if jump occurred and missed, and 9) 'trial' or 'test'. Fig. 5 shows the data arranged in columns, with three instances showing correctly detected jump, incorrect press and missed jump are indicated.

4. Algorithm

A feature-based machine learning (ML) classification algorithm approach has been used for attention and relaxation classification. The entire signal processing has been implemented in MATLAB.

4.1 Feature Extraction and Selection

The analysis is done at two different time scales. One uses the entire window of data collection for the routine, ranging from (2 min – 6.5 min) and another is ultra-short window of 90 s with 10 s slide. Features are generated as various statistical measures estimated on the parameters extracted from waveforms:

1. Heartbeat: IBI
2. Respiration: Inter-respiratory interval (IRI), uncalibrated tidal volume (TV) or peak height, inspiratory interval (t_{II}), expiratory interval (t_{EI}), t_{EI}/t_{II}.
   Statistical analysis: mean, variance, approximate entropy (ApEn), successive differences at first order (SD1) and second order (SD2).
   Frequency domain: LF, HF

A subsection of these features is used for classification, to reduce noise and improve classification. The features are ranked using minimum redundancy maximum relevance (MRMR) algorithm [66], using ground truth information of corresponding classes ($y = \{Relaxed, Attentive\}$). If a feature i, is differential for different classes, it should have large mutual information, $I(y, i)$. The mutual information is related to the joint probabilistic distribution of two variables (features) i & j, given as $I(i, j)$, and gives the level of similarity between the variables. The idea of minimum redundancy is to select the variables that are mutually maximally dissimilar. The two mutual information based criteria needs to be simultaneously optimized to generate results. The first feature is the one with highest $I(y, i)$, then rest are determined incrementally by optimization using a heuristic algorithm.

4.2 Classification Algorithm

Different classification algorithms have been implemented including support vector machines (SVM), kNN, trees, and their ensembles. The reported results are considered with the best accuracy. For longer window features, ensemble subspace discriminant achieves best results. For ultra-short feature analysis, kNN works best. A 5-fold cross validation (CV) has been implemented for model training, and performance analysis has been done on an unseen holdout set. The results show high accuracy for both subject-dependent and independent results.

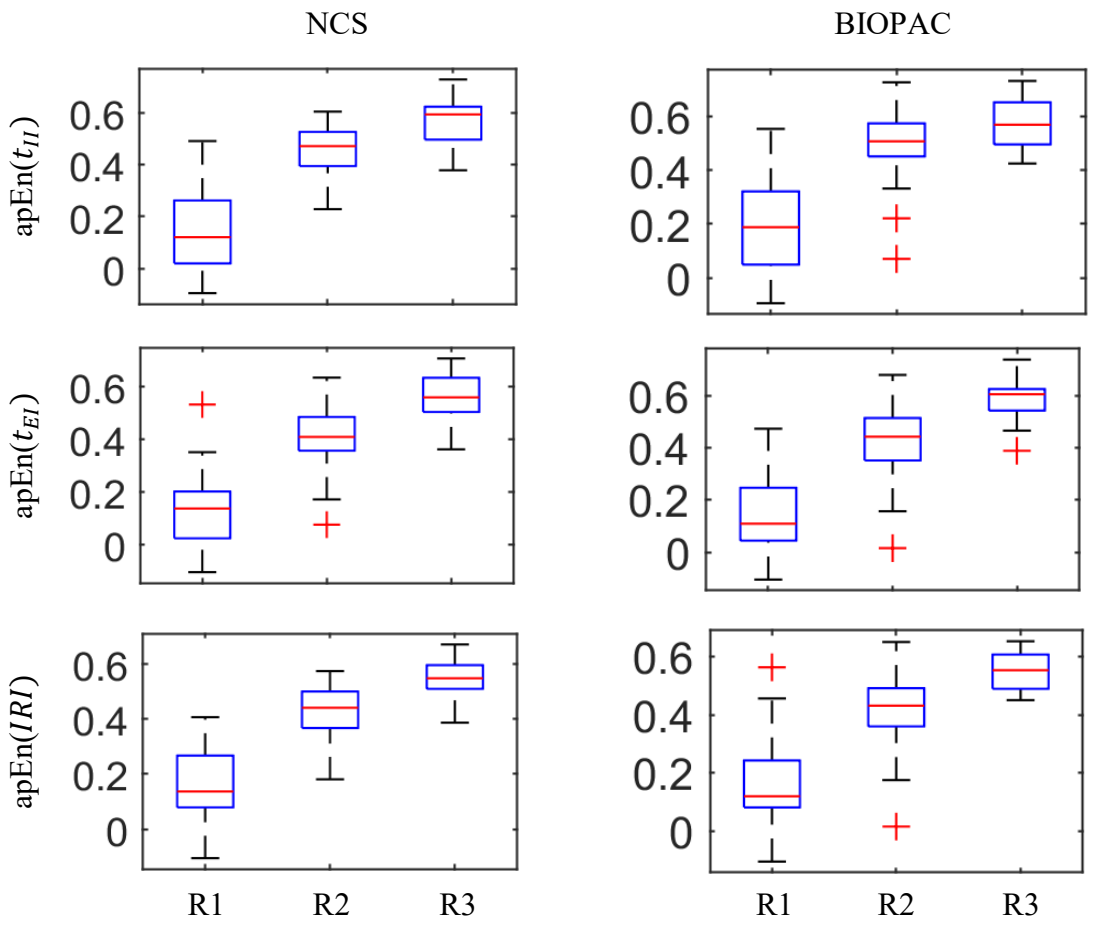

Figure 6 Approximate entropy (ApEn) feature values across different classes on the entire dataset for both NCS and BIOPAC. Large window sizes have been used.

Table 1 Features derived from respiration

$\text{mean}(t_{II})$	$\text{mean}(t_{EI})$	$\text{mean}(IRI)$	$\text{mean}(BR)$
$\text{mean}(TV)$	$\text{mean}(t_{EI}/t_{II})$	$\text{mean}(SD1_{II})$	$\text{mean}(SD1_{EI})$
$\text{mean}(SD1_{IRI})$	$\text{mean}(SD1_{TV})$	$\text{mean}(SD2_{II})$	$\text{mean}(SD2_{EI})$
$\text{mean}(SD2_{IRI})$	$\text{mean}(SD2_{TV})$	$\text{std}(t_{II})$	$\text{std}(t_{EI})$
$\text{std}(IRI)$	$\text{std}(BR)$	$\text{std}(TV)$	$\text{std}(t_{EI}/t_{II})$
$\text{std}(SD1_{II})$	$\text{std}(SD1_{EI})$	$\text{std}(SD1_{IRI})$	$\text{std}(SD1_{TV})$
$\text{std}(SD2_{II})$	$\text{std}(SD2_{EI})$	$\text{std}(SD2_{IRI})$	$\text{std}(SD2_{TV})$
$\frac{\text{mean}(SD1_{II})}{\text{std}(t_{II})}$	$\frac{\text{mean}(SD1_{EI})}{\text{std}(t_{EI})}$	$\frac{\text{mean}(SD1_{IRI})}{\text{std}(IRI)}$	$\frac{\text{mean}(SD1_{TV})}{\text{std}(t_{TV})}$
$\frac{\text{mean}(SD2_{II})}{\text{std}(t_{II})}$	$\frac{\text{mean}(SD2_{EI})}{\text{std}(t_{EI})}$	$\frac{\text{mean}(SD2_{IRI})}{\text{std}(IRI)}$	$\frac{\text{mean}(SD2_{TV})}{\text{std}(t_{TV})}$
$ApEn(t_{II})$	$ApEn(t_{EI})$	$ApEn(IRI)$	$ApEn(TV)$
$LF(t_{II})$	$LF(t_{EI})$	$LF(IRI)$	$HF(t_{II})$
$HF(t_{EI})$	$HF(IRI)$		

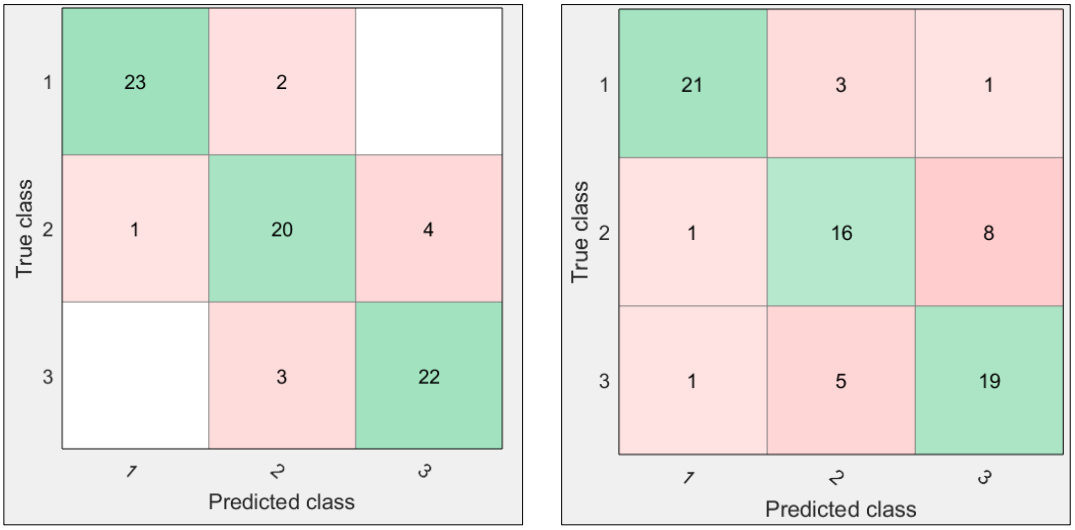

(b) NCS (a) BIOPAC

Figure 7 5-fold CV performance on the entire dataset using long-window respiratory features, for (a) NCS and (b) BIOPAC. The three classes are R1, R2 and R3.

5. Results

5.1 Feature Comparison and Subject-Dependent Results

In order to find out information within respiration, we first restrict the analysis to the respiratory features. With a larger window size, only a subset (11) of all the features are used, with the approximate entry being the maximally contributing feature. The approximate entropy

estimated on $t_{EI}, t_{II},$ and IRI are shown in Fig. 6, derived from both NCS respiratory waveforms and BIOPAC chest belt waveform at the abdomen. Fig. 7 shows the confusion matrix of average 5-fold CV performance on the entire NCS data, showing 86.7% accuracy for R1, R2 and R3 comparison. The corresponding BIOPAC performance is 74.7% accuracy.

For ultra-short windows, all 46 features are derived as shown in Table 1, and good results are seen when only top 10 features selected from the MRMR algorithm are used. Fig. 8 shows the feature importance versus the rank plot with top 6 features being: $\text{mean}(SD1_{II})$, $\text{mean}\left(\frac{t_{EI}}{t_{II}}\right)$, $\text{mean}(SD2_{IRI})/\text{std}(IRI)$, $\text{mean}(TV)$, $\text{mean}(SD2_{TV})/\text{std}(TV)$, $apEn(t_{EI})$. Here, $SD1_{t_{II}}$ is written as $SD1_{II}$ for simplification.

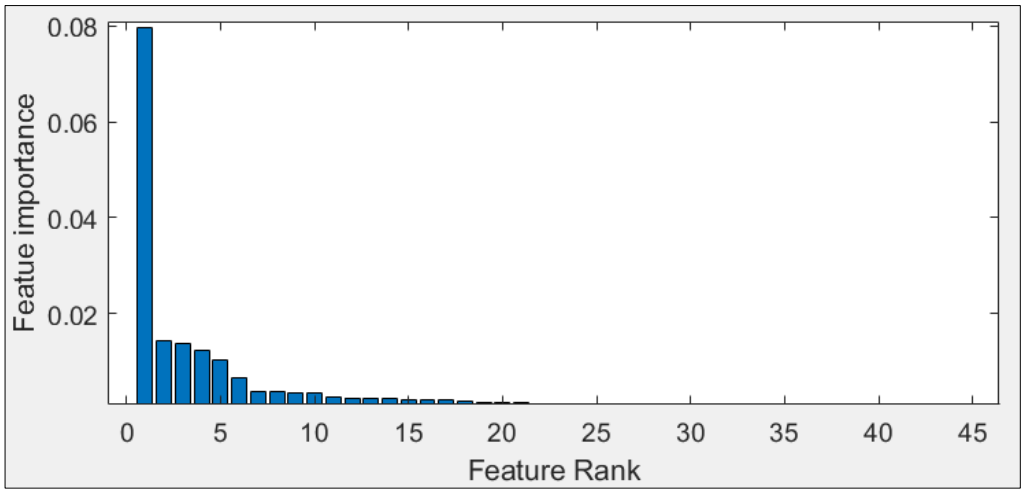

Figure 8 MRMR feature ranking results for ultra-short length features. Only top 6 ~ 10 have a high importance.

Fig. 9 shows the 5-fold CV accuracy performance with NCS and BIOPAC data, resulting in an accuracy of 98.6% and 97%, respectively. Fig. 10 shows the NCS performance with only top 10 features on training data and 25% randomly selected holdout data.

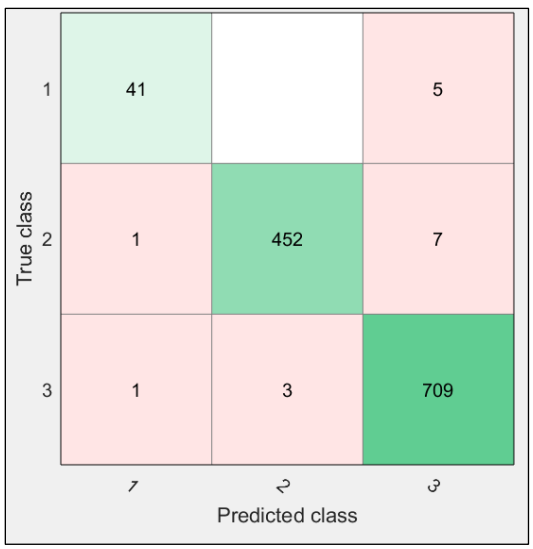

(a) NCS

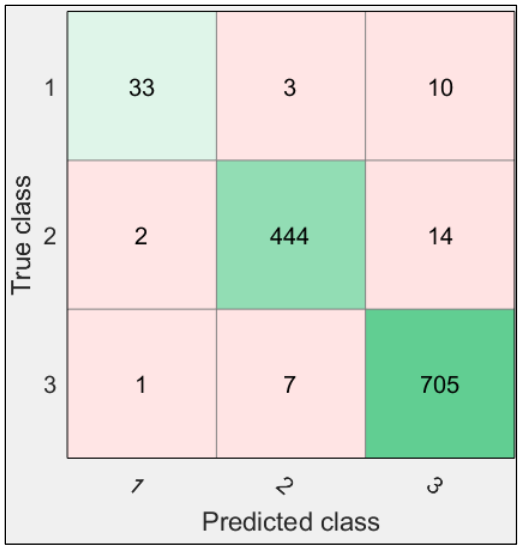

(b) BIOPAC

Figure 9 5-fold CV performance on the entire dataset using ultra-short respiratory features, for (a) NCS and (b) BIOPAC.

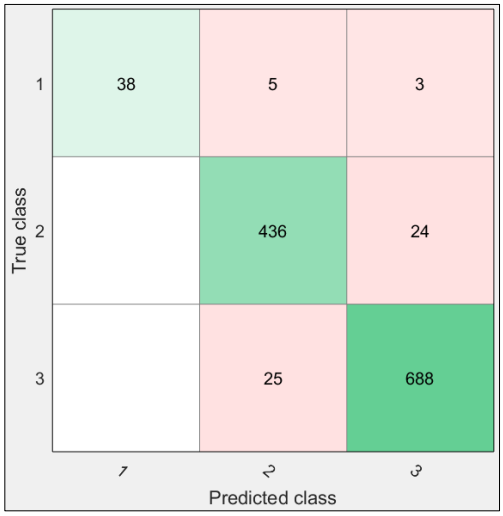

(a) NCS 5-fold CV

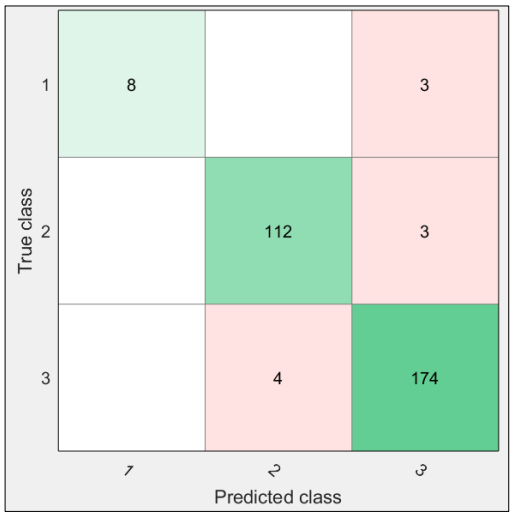

(b) NCS 25% holdout data

Figure 10 Using top-10 features for training (a) and testing (b) on the NCS derived respiration features.

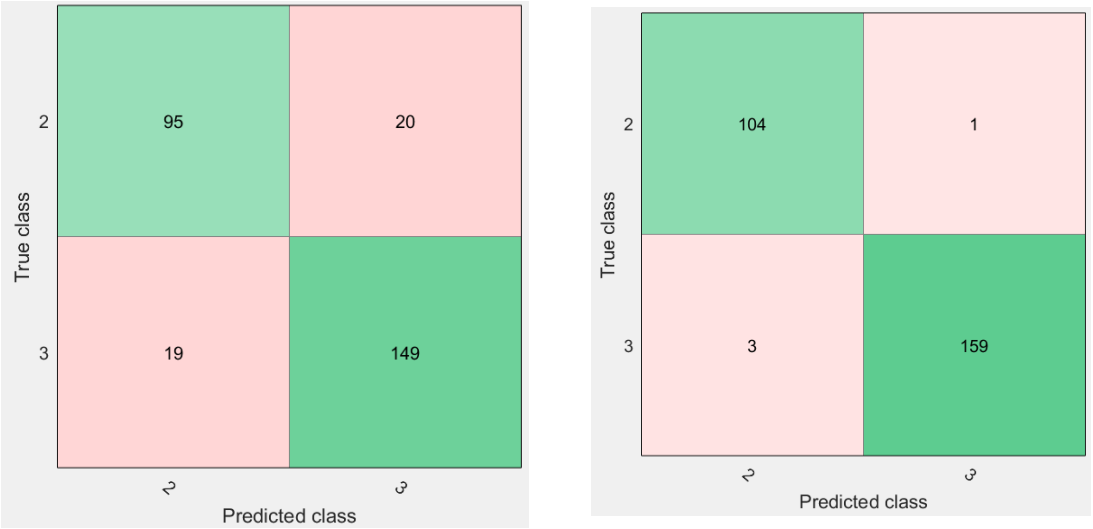

(a) NCS HRV (b) NCS Respiration

Figure 11 25% Holdout test dataset performance for R2 and R3 (relaxation and attention) classification using ultra-short features from (a) NCS HRV and (b) NCS Respiration data.

In the next step, HRV features are also estimated considering only two classes R2 and R3. This provided similar training performance, but slightly poorer performance on the holdout set than the respiration features, as shown in Fig. 11.

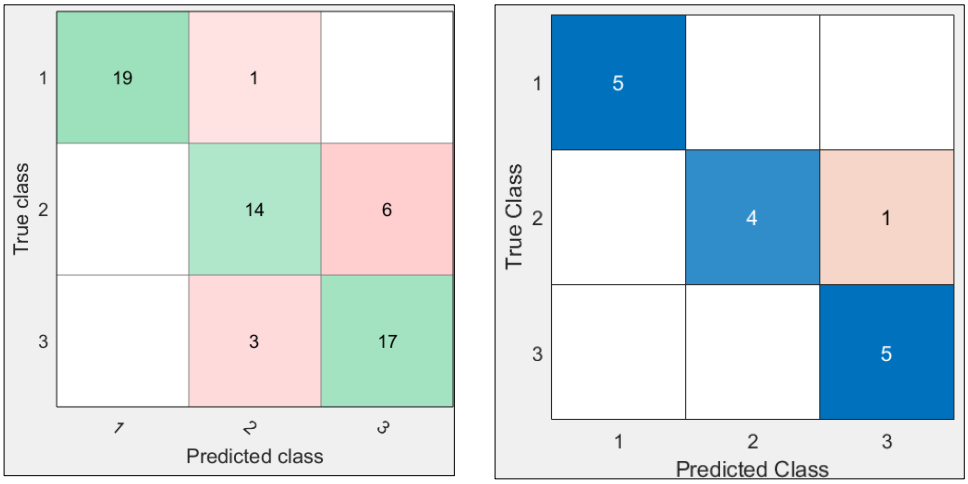

(a) NCS CV training performance (b) Testing on unseen participants

Figure 12 Subject-independent train-test results on the NCS data with longer features, showing very high accuracy.

5.2 Subject-Independent Results

Subject independent tests were performed with both the feature lengths. 20 participants were used for training and remaining for testing. In this case, results are still good for longer feature

lengths as shown in Fig. 12. However, for ultra-short features, performance degrades to 50% test accuracy which is better than by chance (33%) but still poor as shown in Fig. 13. This performance needs to be further investigated.

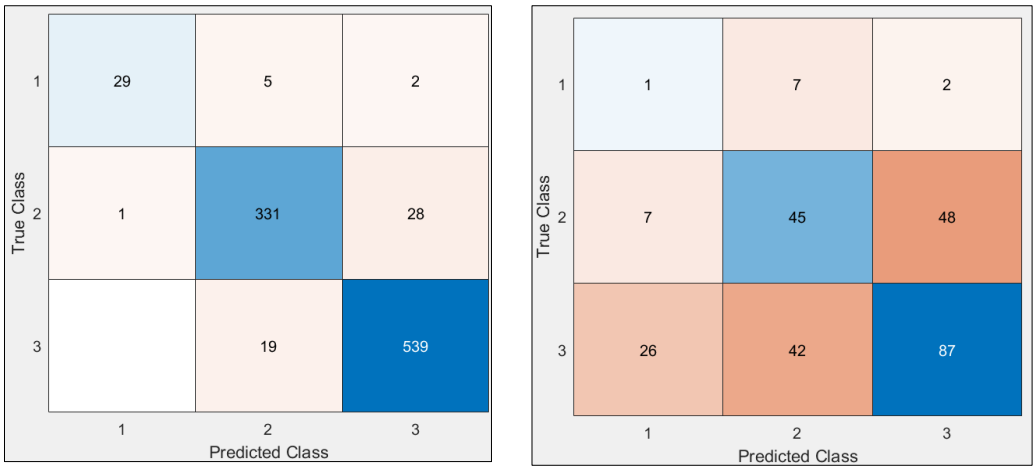

(a) NCS CV training performance (b) Testing on unseen participants

Figure 13 Subject-independent train-test results on the NCS data with ultra-short features.

5.3 Effect of Respiratory Pattern on Relaxation

While R1 is not part of relaxation/attention test, the participants are asked to perform normal breathing (with no deep breaths or breath holds) for 2 min. Further normal breathing does not require excess voluntary attention and is not stress inducing. This controlled breathing pattern is similar to relaxation state and tests are performed to verify this intuition. Fig. 14 (a) shows the CV accuracy of 80% when only R2 and R3 data from 20 participants is used for training the classifier. Then, R1 of all the participants and remaining 5 subjects was used as the holdout test set. Fig.14 (b) shows the results, when all 25 cases, for seen and unseen participants are classified as R2, thus validating the hypothesis.

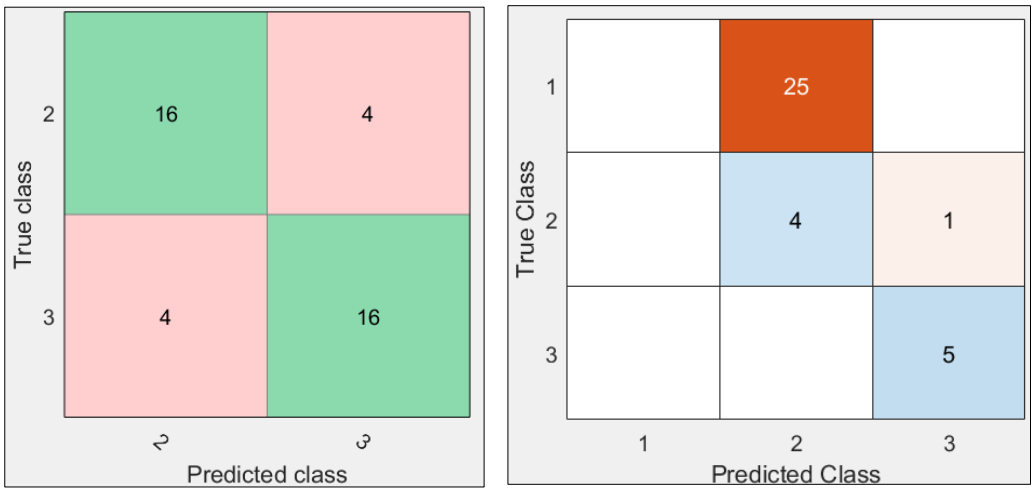

(a) NCS CV training performance

(b) Testing on unseen participants and R1 data

Figure 14 Validating normal breathing routine (R1) classification as relaxation routine (R2) when only two classes are considered.

6. Discussion

The ability to recognize attention and relaxation states is a major part of the emotion detection, which can enhance safety measures in place for critical conditions and help reduce the overall stress level. This thesis has presented a general discussion of what is "attention" and its psychological perspective, as well as neuroscientific research linking emotion and attention. This has allowed us to generalize attention or vigilance, and relaxation and study them with respect to a two-dimensional model, without limiting to stress or fatigue detection that are mostly treated as one-dimensional.

Further, the novel NCS sensor technology has been used to monitor both respiratory and heartbeat patterns. NCS presents a unique advantage that the sensor can operate in a passive mode with only Tx antenna on the chest [67], thereby making the setup more comfortable for certain environments like driving, while still giving strong heartbeat and respiratory signals. Other furniture integrated version can also be adopted with some tradeoff in relative sensor position and heartbeat sensing accuracy. Our results show significant accuracy with only respiration signals as well. While the presented HRV estimation algorithm performs really well for some cases, with sensor placement variation, performance can degrade for some cases, resulting in lower accuracy than expected. The addition of noninvasive pulse oximetry can also be done in future to possibly improve the overall estimate.

The feature window length and system response time to identify attention needs to be considered. The limitation of using respiratory features include 1) learning slow or fast breathing requires larger time window compared to HRV change, and 2) sudden inhalation or exhalation is a one-time event on a very small time scale. The feature identification on the respiration data can be further improved to incorporate these variations. Traditionally, HRV features have been widely investigated for long-term (24 h) and short-term (> 5 min), and the reliability of ultra-short HRV

(< 5 min) is not completely validated [68], but have been increasingly used for faster responses [69], [70]. The statistical features are also impacted by the window length and may be highly biased with shorter lengths. ApEn has shown to be unreliable for excerpts of <3 min [71]. These could be the possible reasons for poorer performance on the shorter interval of 90 s compared to the entire window lengths. Another possible reason is mislabeling and misclassification of transition periods. When estimated on the larger window, it results in averaging out the transition period information. However, shorter windows might be incorrectly labeled at the transition period from relaxation to attention, leading to poor learning, as well as poor test results on these instances. This needs to be further studied and routines can be made longer for future studies to drop such transition periods.

The results presented in this work have been collected on 22 subjects and extensive validation has been performed on unseen test data, unseen routines, as well as entirely unseen participants. With smaller window sizes, this works well if baseline information is collected for each subject. Picard et al [72] considered this phenomenon in detail, with one person selecting their own images to induce different emotions daily over multiple weeks. This showed more variation in day-to-day versus each emotion on the same day, showing huge baseline variation. Thus, future studies are required to consider daily variation in attention and relaxation classification.

The above baseline phenomenon needs to be compared with the human perception during the experimental data collection. This can only be estimated by user's own self report. In this work, participants were asked to fill a survey indicating their relaxation and stress levels on a scale, as well as giving brief descriptions. The term stress was used instead of attention, as attention is more abstract for users. During the relaxation routine, most people responded to feeling relaxed or sleepy. Mixed responses were derived during the attention routine. Some subjects got increasingly frustrated as they received negative feedbacks, while some were calmer as they were good at the exercise. The game level was easy so that participants could quickly learn it, however, for future studies, games should become adaptively complex to demand continuous attention of skilled players and reduce mislabeling. For presented results, as the survey feedback is not explicit, user data was not included to update labels. Another way to indicate real attention levels could be the response time from the game which is shown to be related to attention and fatigue [73]. Li et al [74] used another concept of group-based individual response specificity (IRS) for user-independent emotion recognition. In psychophysiology, IRS keeps individual's response consistency for different stimulus. Thus, for every new user, IRS levels are estimated and associated with the closest cluster of people, before emotion labeling. The best performance is achieved when population is classified in 10 clusters, however, tested only for 30 subjects. Thus, more subjects are needed to study the expected number of clusters and resulting performance improvement.

Overall, we have presented a novel sensor setup for the purpose of user-independent attention – relaxation classification using respiratory and heartbeat features, resulting in a good accuracy for real-life implementation. While there has been a lot of research in the area of emotion recognition, results must always be looked at carefully to understand consideration of participant and baseline variations in the study. Our approach shows good results for unseen participants with sufficient window sizes. With unique advantage of choices between passive and active NCS

setups, the presented monitoring setup is suitable for a wide range of applications, from soldiers, to drivers and pilots, and even hospitals to detect accurate attention, vigilance or stress versus relaxation states.

References

[1] T. Brosch, K. R. Scherer, D. M. Grandjean, and D. Sander, "The impact of emotion on perception, attention, memory, and decision-making," *Swiss Med. Wkly.*, vol. 143, p. w13786, 2013.

[2] J. Driver, "A selective review of selective attention research from the past century," *Br. J. Psychol.*, vol. 92, no. 1, pp. 53–78, 2001.

[3] M. M. Sohlberg and C. A. Mateer, *Introduction to Cognitive Rehabilitation: Theory and Practice*. Guilford Press, 1989.

[4] T. Brosch, G. Pourtois, D. Sander, and P. Vuilleumier, "Additive effects of emotional, endogenous, and exogenous attention: behavioral and electrophysiological evidence," *Neuropsychologia*, vol. 49, no. 7, pp. 1779–1787, 2011.

[5] P. Vuilleumier, "How brains beware: neural mechanisms of emotional attention," *Trends Cogn. Sci.*, vol. 9, no. 12, pp. 585–594, 2005.

[6] Q. Luo, T. Holroyd, C. Majestic, X. Cheng, J. Schechter, and R. J. Blair, "Emotional automaticity is a matter of timing," *J. Neurosci.*, vol. 30, no. 17, pp. 5825–5829, 2010.

[7] G. Pourtois, L. Spinelli, M. Seeck, and P. Vuilleumier, "Temporal precedence of emotion over attention modulations in the lateral amygdala: Intracranial ERP evidence from a patient with temporal lobe epilepsy," *Cogn. Affect. Behav. Neurosci.*, vol. 10, no. 1, pp. 83–93, 2010.

[8] L. Pessoa, "Emotion and attention effects: Is it all a matter of timing? Not yet," *Front. Hum. Neurosci.*, vol. 4, p. 172, 2010.

[9] P. Sharma, X. Hui, J. Zhou, T. B. Conroy, and E. C. Kan, "Wearable radio-frequency sensing of respiratory rate, respiratory volume, and heart rate," *npj Digit. Med.*, vol. 3, no. 1, p. 98, 2020.

[10] M. Basner and J. Rubinstein, "Fitness for duty: A 3 minute version of the Psychomotor Vigilance Test predicts fatigue related declines in luggage screening performance," *J. Occup. Environ. Med. Coll. Occup. Environ. Med.*, vol. 53, no. 10, p. 1146, 2011.

[11] J. Geiger-Brown, V. E. Rogers, A. M. Trinkoff, R. L. Kane, R. B. Bausell, and S. M. Scharf, "Sleep, sleepiness, fatigue, and performance of 12-hour-shift nurses," *Chronobiol. Int.*, vol. 29, no. 2, pp. 211–219, 2012.

[12] P. Ekman and W. V Friesen, "Constants across cultures in the face and emotion," *J. Pers. Soc. Psychol.*, vol. 17, no. 2, p. 124, 1971.

[13] W. M. Wundt, *Principles of physiological psychology*, vol. 1. Sonnenschein, 1904.

[14] J. Kim and E. Andre, "Emotion recognition based on physiological changes in music listening," *IEEE Trans. Pattern Anal. Mach. Intell.*, vol. 30, no. 12, pp. 2067–2083, 2008.

[15] L. K. McIntire, R. A. McKinley, C. Goodyear, and J. P. McIntire, "Detection of vigilance performance using eye blinks.," *Appl. Ergon.*, vol. 45, no. 2, pp. 354–362, Mar. 2014.

[16] U. Trutschel, B. Sirois, D. Sommer, M. Golz, and D. Edwards, "PERCLOS: An alertness measure of the past," University of Iowa, 2011.

[17] B. Mandal, L. Li, G. S. Wang, and J. Lin, "Towards detection of bus driver fatigue based on robust visual analysis of eye state," *IEEE Trans. Intell. Transp. Syst.*, vol. 18, no. 3, pp.

545–557, 2016.
[18] W. Yimyam and M. Ketcham, “Eye region detection in fatigue monitoring for the military using AdaBoost algorithm,” in *International Symposium on Natural Language Processing*, 2016, pp. 151–161.
[19] Y.-W. Chen and K. Kubo, “A robust eye detection and tracking technique using gabor filters,” in *Third International Conference on Intelligent Information Hiding and Multimedia Signal Processing (IIH-MSP 2007)*, 2007, vol. 1, pp. 109–112.
[20] Q. Ji, Z. Zhu, and P. Lan, “Real time non-intrusive monitoring and prediction of driver fatigue,” *IEEE Trans. Veh. Technol.*, vol. 53, no. 4, pp. 1052–1068, 2004.
[21] Q. Ji, P. Lan, and C. Looney, “A probabilistic framework for modeling and real-time monitoring human fatigue,” *IEEE Trans. Syst. Man, Cybern. Part A Syst. Humans*, vol. 36, no. 5, pp. 862–875, 2006.
[22] C. Lü, S. Wu, B. Lu, Y. Zhang, Y. Du, and X. Feng, “Ultrathin flexible piezoelectric sensors for monitoring eye fatigue,” *J. Micromechanics Microengineering*, vol. 28, no. 2, p. 25010, Jan. 2018.
[23] T. C. Chieh, M. M. Mustafa, A. Hussain, S. F. Hendi, and B. Y. Majlis, “Development of vehicle driver drowsiness detection system using electrooculogram (EOG),” in *International Conference on Computers, Communications, & Signal Processing with Special Track on Biomedical Engineering*, 2005, pp. 165–168.
[24] A. Aryal, A. Ghahramani, and B. Becerik-Gerber, “Monitoring fatigue in construction workers using physiological measurements,” *Autom. Constr.*, vol. 82, pp. 154–165, 2017.
[25] K. Q. Shen, X. P. Li, C. J. Ong, S. Y. Shao, and E. P. V. Wilder-Smith, “EEG-based mental fatigue measurement using multi-class support vector machines with confidence estimate,” *Clin. Neurophysiol.*, vol. 119, no. 7, pp. 1524–1533, 2008.
[26] K.-Q. Shen, C.-J. Ong, X.-P. Li, Z. Hui, and E. P. V Wilder-Smith, “A feature selection method for multilevel mental fatigue EEG classification,” *IEEE Trans. Biomed. Eng.*, vol. 54, no. 7, pp. 1231–1237, 2007.
[27] G. Borghini *et al.*, “Assessment of mental fatigue during car driving by using high resolution EEG activity and neurophysiologic indices,” in *IEEE Engineering in Medicine and Biology Society*, 2012, pp. 6442–6445.
[28] X. Zhou *et al.*, “Vigilance detection method for high-speed rail using wireless wearable EEG collection technology based on low-rank matrix decomposition,” *IET Intell. Transp. Syst.*, vol. 12, no. 8, pp. 819–825, 2018.
[29] L. J. Trejo, K. Kubitz, R. Rosipal, R. L. Kochavi, and L. D. Montgomery, “EEG-based estimation and classification of mental fatigue,” *Psychology*, vol. 6, no. 05, p. 572, 2015.
[30] Y. Shimomura, T. Yoda, K. Sugiura, A. Horiguchi, K. Iwanaga, and T. Katsuura, “Use of frequency domain analysis of skin conductance for evaluation of mental workload,” *J. Physiol. Anthropol.*, vol. 27, no. 4, pp. 173–177, 2008.
[31] M. Egger, M. Ley, and S. Hanke, “Emotion Recognition from Physiological Signal Analysis: A Review,” *Electron. Notes Theor. Comput. Sci.*, vol. 343, pp. 35–55, 2019.
[32] A. Dzedzickis, A. Kaklauskas, and V. Bucinskas, “Human emotion recognition: Review of sensors and methods,” *Sensors*, vol. 20, no. 3, 2020.
[33] L. Shu *et al.*, “A review of emotion recognition using physiological signals,” *Sensors*, vol. 18, no. 7, p. 2074, 2018.
[34] C. Busso *et al.*, “Analysis of emotion recognition using facial expressions, speech and multimodal information,” in *6th International Conference on Multimodal Interfaces*, 2004,

pp. 205–211.
[35] G. Castellano, L. Kessous, and G. Caridakis, “Emotion recognition through multiple modalities: face, body gesture, speech,” in *Affect and Emotion in Human-Computer Interaction: From Theory to Applications*, C. Peter and R. Beale, Eds. Berlin, Heidelberg: Springer Berlin Heidelberg, 2008, pp. 92–103.
[36] I. Cohen, A. Garg, and T. S. Huang, “Emotion recognition from facial expressions using multilevel HMM,” *Neural Inf. Process. Syst.*, vol. 2, 2000.
[37] B. Schuller, G. Rigoll, and M. Lang, “Speech emotion recognition combining acoustic features and linguistic information in a hybrid support vector machine-belief network architecture,” in *IEEE International Conference on Acoustics, Speech, and Signal Processing*, 2004, vol. 1, pp. I–577.
[38] L. Chen, W. Su, Y. Feng, M. Wu, J. She, and K. Hirota, “Two-layer fuzzy multiple random forest for speech emotion recognition in human-robot interaction,” *Inf. Sci. (Ny).*, vol. 509, pp. 150–163, 2020.
[39] D. Cevher, S. Zepf, and R. Klinger, “Towards multimodal emotion recognition in German speech events in cars using transfer learning,” *arXiv Prepr. arXiv1909.02764*, 2019.
[40] J. Zhai and A. Barreto, “Stress detection in computer users based on digital signal processing of noninvasive physiological variables,” in *IEEE Engineering in Medicine and Biology*, 2006, pp. 1355–1358.
[41] A. Nakasone, H. Prendinger, and M. Ishizuka, “Emotion recognition from electromyography and skin conductance,” in *International workshop on biosignal interpretation*, 2005, pp. 219–222.
[42] G. Udovičić, J. Derek, M. Russo, and M. Sikora, “Wearable emotion recognition system based on GSR and PPG signals,” in *International Workshop on Multimedia for Personal Health and Health Care*, 2017, pp. 53–59.
[43] M. M. Bradley, L. Miccoli, M. A. Escrig, and P. J. Lang, “The pupil as a measure of emotional arousal and autonomic activation,” *Psychophysiology*, vol. 45, no. 4, pp. 602–607, 2008.
[44] E. Gatti, E. Calzolari, E. Maggioni, and M. Obrist, “Emotional ratings and skin conductance response to visual, auditory and haptic stimuli,” *Sci. Data*, vol. 5, no. 1, p. 180120, 2018.
[45] J. Zhu, L. Ji, and C. Liu, “Heart rate variability monitoring for emotion and disorders of emotion,” *Physiol. Meas.*, vol. 40, no. 6, p. 64004, Jul. 2019.
[46] H. G. Kim, E. J. Cheon, D. S. Bai, Y. H. Lee, and B. H. Koo, “Stress and heart rate variability: A meta-analysis and review of the literature,” *Psychiatry Investig.*, vol. 15, no. 3, pp. 235–245, 2018.
[47] F. Agrafioti, D. Hatzinakos, and A. K. Anderson, “ECG pattern analysis for emotion detection,” *IEEE Trans. Affect. Comput.*, vol. 3, no. 1, pp. 102–115, 2012.
[48] E.-. Jang, B.-. Park, S.-. Kim, Y. Eum, and J.-. Sohn, “Identification of the optimal emotion recognition algorithm using physiological signals,” in *International Conference on Engineering and Industries (ICEI)*, 2011, pp. 1–6.
[49] R. Harper and J. Southern, “End-to-end prediction of emotion from heartbeat data collected by a consumer fitness tracker,” in *International Conference on Affective Computing and Intelligent Interaction (ACII)*, 2019, pp. 1–7.
[50] T. Bhowmik, J. Dey, and V. N. Tiwari, “A novel method for accurate estimation of HRV from smartwatch PPG signals,” in *IEEE Engineering in Medicine and Biology Society (EMBC)*, 2017, pp. 109–112.

[51] M. O. Diab, A. Seif, M. Sabbah, M. El-Abed, and N. Aloulou, "A review on ECG-based biometric authentication systems," in *Hidden Biometrics: When Biometric Security Meets Biomedical Engineering*, Singapore: Springer, 2020, pp. 17–44.
[52] Q. Zhang, X. Chen, Q. Zhan, T. Yang, and S. Xia, "Respiration-based emotion recognition with deep learning," *Comput. Ind.*, vol. 92–93, pp. 84–90, 2017.
[53] S. Oh, J. Y. Lee, and D. K. Kim, "The design of CNN architectures for optimal six basic emotion classification using multiple physiological signals," *Sensors*, vol. 20, no. 3, pp. 1–17, 2020.
[54] J. R. Machado Fernández and L. Anishchenko, "Mental stress detection using bioradar respiratory signals," *Biomed. Signal Process. Control*, vol. 43, pp. 244–249, 2018.
[55] A. N. Khan, A. A. Ihalage, Y. Ma, B. Liu, Y. Liu, and Y. Hao, "Deep learning framework for subject-independent emotion detection using wireless signals," pp. 1–13, 2020.
[56] M. Zhao, F. Adib, and D. Katabi, "Emotion recognition using wireless signals," *Commun. ACM*, vol. 61, no. 9, pp. 91–100, 2018.
[57] U. R. Acharya, K. P. Joseph, N. Kannathal, C. M. Lim, and J. S. Suri, "Heart rate variability: A review," *Med. Biol. Eng. Comput.*, vol. 44, no. 12, pp. 1031–1051, 2006.
[58] W. von Rosenberg, T. Chanwimalueang, T. Adjei, U. Jaffer, V. Goverdovsky, and D. P. Mandic, "Resolving ambiguities in the LF/HF ratio: LF-HF scatter plots for the categorization of mental and physical stress from HRV," *Front. Physiol.*, vol. 8, no. JUN, pp. 1–12, 2017.
[59] T. Adjei, W. Von Rosenberg, T. Nakamura, T. Chanwimalueang, and D. P. Mandic, "The ClassA framework: HRV based assessment of SNS and PNS dynamics without LF-HF controversies," *Front. Physiol.*, vol. 10, no. APR, pp. 1–15, 2019.
[60] G. Strauss-Blasche, M. Moser, M. Voica, D. R. McLeod, N. Klammer, and W. Marktl, "Relative timing of inspiration and expiration affects respiratory sinus arrhythmia," *Clin. Exp. Pharmacol. Physiol.*, vol. 27, no. 8, pp. 601–606, 2000.
[61] R. Jerath and C. Beveridge, "Respiratory rhythm, autonomic modulation, and the spectrum of emotions: The future of emotion recognition and modulation," *Front. Psychol.*, vol. 11, 2020.
[62] P. Philippot, G. Chapelle, and S. Blairy, "Respiratory feedback in the generation of emotion," *Cogn. Emot.*, vol. 16, no. 5, pp. 605–627, 2002.
[63] K. L. Lichstein, B. W. Riedel, and S. L. Richman, "The Mackworth clock test: a computerized version.," *J. Psychol.*, vol. 134, no. 2, pp. 153–161, Mar. 2000.
[64] G. Stoet, "PsyToolkit: a novel web-based method for running online questionnaires and reaction-time experiments," *Teach. Psychol.*, vol. 44, no. 1, pp. 24–31, 2017.
[65] G. Stoet, "PsyToolkit: a software package for programming psychological experiments using Linux," *Behav. Res. Methods*, vol. 42, no. 4, pp. 1096–1104, 2010.
[66] C. Ding and H. Peng, "Minimum redundancy feature selection from microarray gene expression data," *J. Bioinform. Comput. Biol.*, vol. 3, no. 2, pp. 185–205, 2005.
[67] P. Sharma and E. C. Kan, "Sleep scoring with a UHF RFID tag by near field coherent sensing," in *IEEE MTT-S Int. Microw. Symp. Dig.*, 2018, pp. 1419–1422.
[68] L. Pecchia, R. Castaldo, L. Montesinos, and P. Melillo, "Are ultra-short heart rate variability features good surrogates of short-term ones? State-of-the-art review and recommendations," *Healthc. Technol. Lett.*, vol. 5, no. 3, pp. 94–100, 2018.
[69] M. R. Esco and A. A. Flatt, "Ultra-short-term heart rate variability indexes at rest and post-exercise in athletes: evaluating the agreement with accepted recommendations," *J. Sports*

Sci. Med., vol. 13, no. 3, p. 535—541, Sep. 2014.
[70] L. Salahuddin, J. Cho, M. G. Jeong, and D. Kim, "Ultra Short Term Analysis of Heart Rate Variability for Monitoring Mental Stress in Mobile Settings," in *IEEE Engineering in Medicine and Biology*, 2007, pp. 4656–4659.
[71] J. M. Yentes, N. Hunt, K. K. Schmid, J. P. Kaipust, D. McGrath, and N. Stergiou, "The appropriate use of approximate entropy and sample entropy with short data sets.," *Ann. Biomed. Eng.*, vol. 41, no. 2, pp. 349–365, Feb. 2013.
[72] R. W. Picard, E. Vyzas, and J. Healey, "Toward machine emotional intelligence: Analysis of affective physiological state," *IEEE Trans. Pattern Anal. Mach. Intell.*, vol. 23, no. 10, pp. 1175–1191, 2001.
[73] M. Azarnoosh, A. L. I. M. Nasrabadi, M. R. Mohammadi, and M. Firoozabadi, "Evaluating nonlinear variability of mental fatigue behavioral indices during long-term attentive task," *Complexity*, vol. 17, no. 6, pp. 7–16, 2012.
[74] C. Li, C. Xu, and Z. Feng, "Analysis of physiological for emotion recognition with the IRS model," *Neurocomputing*, vol. 178, pp. 103–111, 2016.

Appendix I

(PDF downloaded from Science) X. Hui and E. C. Kan, “No-touch measurements of vital signs in small conscious animals”, *Science Advances*, vol. 5, art: eaau0169, Feb. 2019. (Featured in *AAAS News*)

RESEARCH METHODS

No-touch measurements of vital signs in small conscious animals

Xiaonan Hui* and Edwin C. Kan

Copyright © 2019 The Authors, some rights reserved; exclusive licensee American Association for the Advancement of Science. No claim to original U.S. Government Works. Distributed under a Creative Commons Attribution NonCommercial License 4.0 (CC BY-NC).

Measuring the heartbeat and respiration of small conscious animals is important for assessing their health and behavior, but present techniques such as electrocardiogram (ECG), ultrasound, and auscultation rely on close skin contact with the animal. These methods can also require surface preparation, cause discomfort or stress to animals, and even require anesthetic administration, especially for birds, reptiles, and fish. Here, we show that radio frequency near-field coherent sensing (NCS) can provide a new solution to animal vital sign monitoring while ensuring minimal pain and distress. We first benchmarked NCS with synchronous ECG on an anesthetized rat. NCS was then applied to monitor a conscious hamster from outside its cage, and was further extended to a parakeet, Russian tortoise, and betta fish in a noninvasive manner. Our system can revolutionize vital sign monitoring of small conscious animals in their laboratory living quarters or natural habitats.

INTRODUCTION

In this paper, we demonstrate a new touchless method to measure the vital signs of small conscious animals, where the near-field coherent sensing (NCS) principle is applied to previously unachievable sensing ability and testing convenience. Our setup has minimal interference to the daily rhythms of the animal under test; most subjects will likely not even notice the ongoing real-time measurement. With this work, we not only provide an innovative tool to facilitate small-animal studies but also promote refinement in animal laboratory procedures against invasive, risky, and sometimes inhumane techniques such as anesthetization, hair/scale removal, forceful body stretch, intramuscular electrode insertion, and surgical implants.

Difficulties in present methods

Current approaches to measuring vital signs in animals with various body coverings often involve complicated and invasive preparation procedures (*1*, *2*) and cause major distress to the animals, even requiring that they be anesthetized or heavily restrained to prevent motion that could disrupt the measurement setup. For example, an electrocardiogram (ECG) (*2*–*5*) for heartbeat waveforms requires skin electrodes with stable electrical contact and is therefore difficult to be applied to mammals with thick fur, reptiles with scutes or shells, birds with feathers, and fish with scales. Bare skin areas such as soles and lips often have insufficient electrical signals and can be sensitive to touch. Intramuscular electrodes are typically performed with anesthetization. Similarly, the body surface condition also causes intricacy in photoplethysmography (PPG) (*6*, *7*), which limits its application to animals. Auscultation (*8*, *9*) and ultrasound (*10*, *11*) need tight skin touch or impedance-matching gels to obtain clear signals, which require high degrees of animal handling. Radio frequency (RF) methods such as Doppler far-field backscattering (*12*–*16*) of minute skin motion have nonspecific wireless channels and can be potentially interfered by ambient motion covered by the same beam lobe, although beamforming by large antenna arrays can improve directivity at the cost of system complexity. To be sufficiently sensitive to the vital signs of small animals, raising the carrier frequency to the millimeter-wave level was proposed (*17*, *18*), which not only increases the system cost but also reduces the operational distance. Respiration can often be the dominant signal and become a major interference to accurate heartbeat detection. RF methods based on the transmission line model (*19*–*21*) again require good impedance matching of the skin electrodes and hence the associated surface preparation. Small animals pose further challenges for most of these previous RF methods because of their limited signal sensitivity.

Experimental setups

Our recently proposed NCS method (*22*) by near-field modulation of the antenna characteristics on multiplexed radio signals has very high signal-to-noise ratio (SNR) but does not require restraint or even contact with the animal (*23*). NCS thus offers an effective solution to long-term vital sign monitoring for small conscious animals with various body coverings. The schematics for two possible NCS setups are shown in Fig. 1. The wireless sensing in Fig. 1A uses the harmonic RFID (radio frequency identification) architecture (*24*), where the passive sensing tags are inexpensive and maintenance free, but a specific multiplexing reader (*25*) is required. This version can be appropriate for deployment in natural habitats with weather-proof passive tags, and the vital signs are collected from a nearby reader on the operator or fixture. To retrieve accurate vital signs of small animals, the system SNR and sensitivity are critical because of the weak signal strength from a very small motion source. The conventional RFID system uses the same frequency band for the transmitter (Tx) and receiver (Rx). Thus, the Tx-to-Rx leakage, the antenna reflection caused by antenna impedance mismatch, and the ambient reflection from nearby large objects are received and amplified by the Rx chain together with the intended signals carrying the vital signs. Considering the double-trip path loss and available scavenged power of the passive tag, not only is the amplitude of the tag signal at Rx weak but also the sideband frequency offset is small, with low base bandwidth. The backscattering from tags can be easily overwhelmed by the phase noise skirt of the Tx leakage or the reflected carrier signal to render poor SNR and signal sensitivity.

The use of the harmonic system reduces self-jamming by separating the bands of Tx and Rx and improves both SNR and signal sensitivity. The NCS signal impinged on the animal body is estimated

School of Electrical and Computer Engineering, Cornell University, Ithaca, NY 14853, USA.
*Corresponding author. Email: xh273@cornell.edu

Downloaded from http://advances.sciencemag.org/ on February 13, 2019

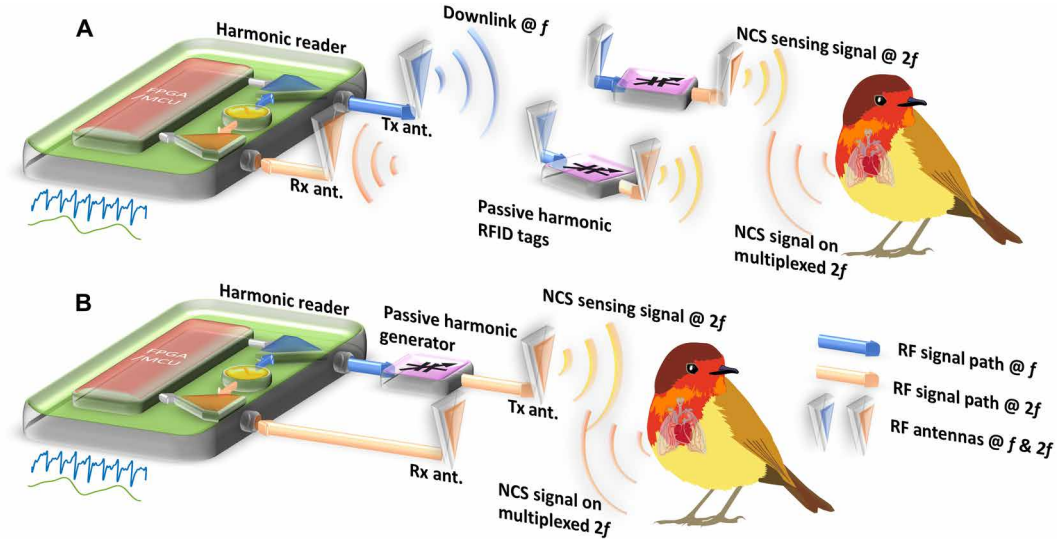

Fig. 1. Two setups of NCS for vital signs of small conscious animals. The signal is collected by the harmonic reader with digital baseband processing by the field-programmable gate array (FPGA) and microcontroller (MCU). (**A**) The wireless NCS system is realized by the harmonic RFID system with passive harmonic sensing tags. (**B**) The wired NCS system replaces the wireless links between the reader and the harmonic tag by RF cables for reduced interference and convenient indoor laboratory deployment.

to be much lower than 0.1 mW/cm^2 and 0.15 W/kg to comply with the health and safety standards in the human and rodent models (*26*). In Fig. 1A, the harmonic reader by Ettus X310 Software Defined Radio (SDR) transmits the downlink signal at *f* around 950 MHz (the blue wave) through the reader Tx antenna. The downlink signal powers up the passive harmonic RFID tags and is then converted to the second-harmonic frequency at 2*f* as the NCS sensing signal (the yellow waves) in the vicinity of the target animal body. As long as the vital signals are within the near-field range (typically about one-third of the used wavelength) of the sensing tag antenna, motion on and inside the animal body can be coupled to the backscattered signal (the orange wave) to be received by the reader Rx antenna. The overall tag antenna motion relative to the reader Rx will be mostly represented by phase modulation, which can be naturally separated from the magnitude modulation out of the dielectric boundary motion relative to the tag antenna in the near field. The signal originated from the sensing tag can contain a unique identification code to achieve code-division multiple access (CDMA) (*25*), which improves channel isolation against nonspecific interference and enables simultaneous reading of multiple sensing tags. Manufacturing of the passive sensing tag is similar to the conventional RFID tag, which gives low-cost production (*27*) and flexible substrate choices (*28*) in addition to convenient deployment without need of maintenance.

Alternatively, the setup in Fig. 1B replaces the reader-to-tag channels with RF cables, which reduces interferences and can be appropriate for convenient deployment in an indoor laboratory with heavy operator traffic or with other interfering sources. The reader Tx antenna transmits the NCS sensing signal (the yellow wave) directly at 2*f* and is in the near-field range of the animal under test. Then, the NCS signal modulated by the vital signs (the orange wave) is received by the reader Rx antenna, which can be deployed according to the application under consideration. The use of 2*f* here is mainly to reduce the Tx-to-Rx leakage inside the SDR. When sufficient Tx-to-Rx isolation can be achieved by improved transceiver design, the harmonic scheme to separate Tx and Rx bands becomes optional. Because the ambient interference is reduced and no tag circuit needs to be supported by scavenged power, the Tx NCS signal to couple into the animal body can be further decreased to eliminate any health concerns of RF radiation.

RESULTS AND DISCUSSION

Benchmarks on an anesthetized rat

To compare the NCS vital signals on small animals for cardio waveforms, we first performed synchronized NCS and ECG measurements on an established rodent model, which not only is important for pharmaceutical trials but also has much fainter and faster heartbeats than humans, providing a more challenging test. A Long-Evans laboratory rat (*Rattus norvegicus*), coded #110, was anesthetized with complete belly hair removal by razors and Veet gel cream for ECG electrode deployment, as shown in Fig. 2A. We also tried out alligator clips and conductive sticker pads on both paws, but the ECG signal was much weaker and noisier. The sensing tag antenna with the architecture in Fig. 1B was placed near the back of the neck area by a rubber harness without hair removal. Other antenna placements, including along the tail, in front of the chest, and along the back leg, were also attempted with reasonable NCS signal strength. A representative 5-min recording is shown in Fig. 2A, and the inset shows the waveform details within half a second within the third minute. The cardiogram waveforms of ECG and NCS in Fig. 2B rendered very similar beat-to-beat intervals (*26*), as shown in Fig. 2C. However, the detailed waveforms, for example, the NCS feature points in comparison with the ECG S and T feature points, will need further characterization. In view of heart rate comparison, NCS is sufficiently accurate to replace ECG for behavior studies based on heart rate variation (HRV). The breath waveforms were synchronously collected by NCS with an additional 0.5- to 2.5-Hz low-pass filtering in Fig. 2D, allowing further cardiopulmonary analyses not achievable by ECG alone.

NCS measures the tag antenna characteristics modulated by the near-field dielectric boundary movement changes, while ECG measures the body potential differences induced by the minute skin

Downloaded from http://advances.sciencemag.org/ on February 13, 2019

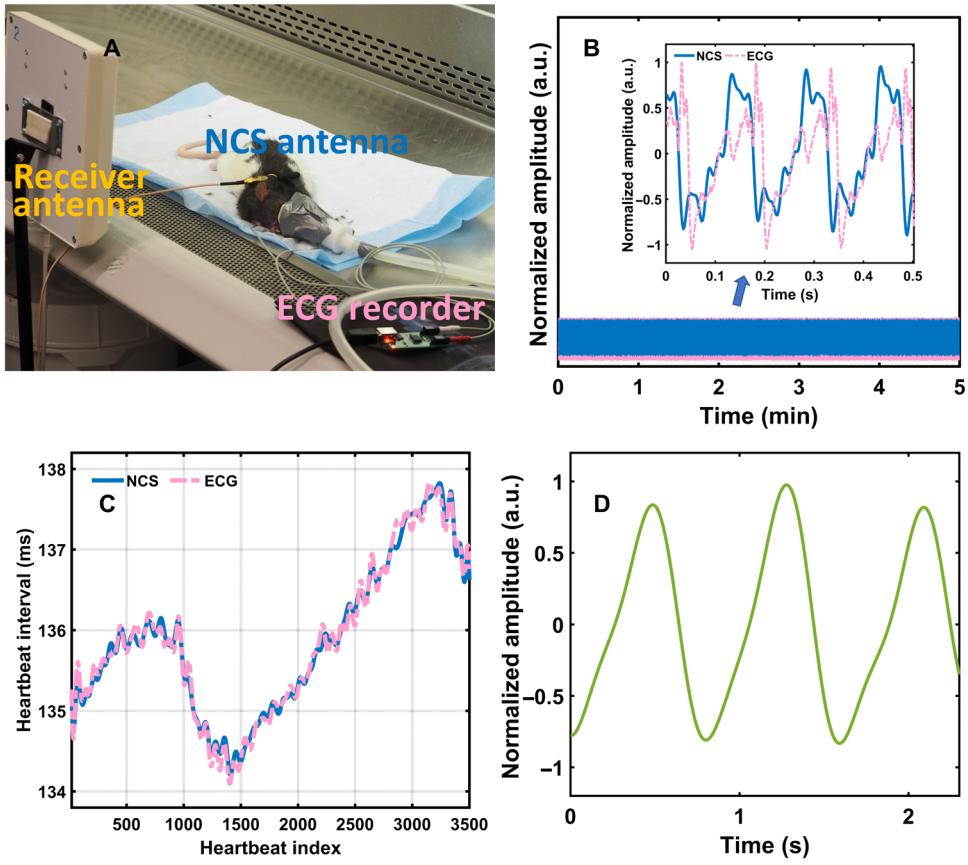

Fig. 2. The vital sign monitoring of a laboratory rat by synchronous NCS and ECG measurements. (**A**) Experimental setup with the anesthetized rat for ECG electrode placement. (**B**) Data recording (5 min) of NCS and ECG. The inset shows waveform details at a selected half-second duration. a.u., arbitrary units. (**C**) Heartbeat interval extracted from NCS and ECG showing very close match. (**D**) Representative respiration signals demodulated from the phase of the NCS signal around from the third to the fourth second. (The picture was taken by Xiaonan Hui, School of Electrical and Computer Engineering, Cornell University, Ithaca, NY 14853, USA.)

current further induced by the electrical heart stimulation and blood flow. In this perspective, NCS has a waveform transducing the heart internal and external mechanical motion, which is related to the mechanical information in ballistocardiogram (BCG) (*29*) and seismic cardiography (SCG) (*30*). In addition, NCS is much less subjected to variations from skin preparation steps and resulting surface conditions in comparison with ECG.

Other small conscious animals

After confirming the cardiopulmonary signals on the anesthetized rat, we next demonstrated the possible noninvasive NCS setups on several other species of small conscious animals, for which other monitoring methods such as ECG have been difficult, if not impossible (see Figs. 3 and 4). A pet golden hamster (*Mesocricetus*), named "Timo," was monitored in its cage sleeping quarter, as shown in Fig. 3A. Both wireless and wired NCS architectures in Fig. 1 were applied outside the cage. For the wireless version, the passive harmonic tag was powered up by the downlink signal, part of which was converted to the second harmonic as the NCS sensing signal coupled into the hamster body. The reader Rx antenna was about 1.5 m away from the tag. For the wired version, the sensing antenna was mounted on the right side of the sleeping quarter, which transmitted the NCS sensing signal directly. In Fig. 3B, the waveforms for respirations and heartbeats were acquired without the hamster being aware of the device. The amplitudes of the vital signals were normalized to the maximum values of the entire recording period. The inset shows the heartbeat waveform details around the ninth second. The waveform features were similar not only for each heartbeat during the recording but also to those in the anesthetized rat in Fig. 2B. The negative minimums of the waveform were extracted for the heartbeat interval, as shown in Fig. 3C, after applying moving average with a window size of 20. The hamster heartbeat interval was about 20% longer than that of the rat.

We then continued the measurements when the hamster was running on the exercise wheel, as shown in Fig. 3D. The NCS sensing antenna was placed to the back of the wheel outside the cage, and the reader antenna is about 1.5 m away. The raw data from the demodulated NCS signal are shown as the red curve in Fig. 3E. From around 0 to 4 s and 12 to 20 s, the hamster was running on the wheel but otherwise took an intermittent rest without large body motion. After the bandpass filtering of 1 to 30 Hz, the time-domain signal is shown as the green curve in Fig. 3E, and the corresponding spectrum is shown in Fig. 3F. Because of the high heartbeat rate of the hamster, the heartbeat peak (blue arrow) and the derived heart rate can often be distinguished from the major body motion interference with different spectral content (black arrow). The second and third harmonic components of the heartbeat are also shown in the spectrum, indicated by the red and green arrows. An equalized peak

Downloaded from http://advances.sciencemag.org/ on February 13, 2019

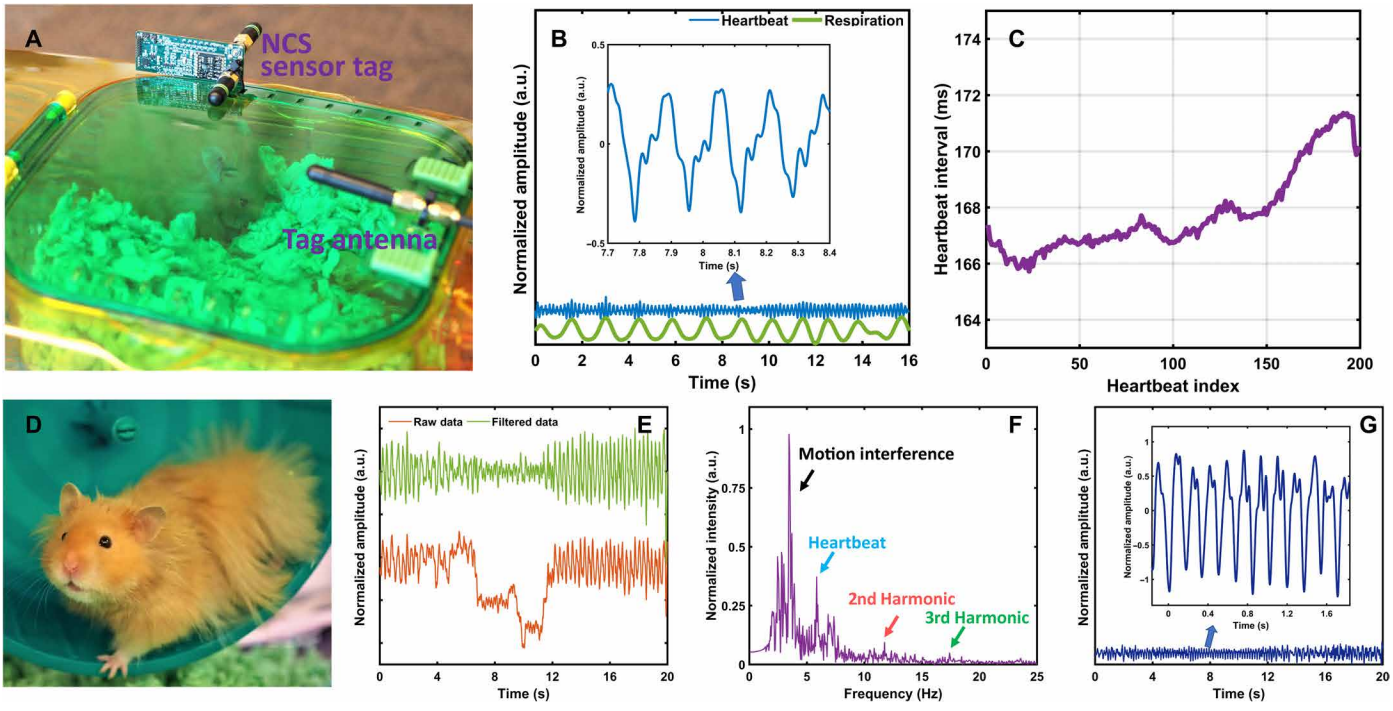

Fig. 3. The vital sign monitoring of a conscious pet hamster. (**A**) Illustrations of the experimental setup when the hamster was in its sleeping quarter. (**B**) Heartbeat (blue) and respiration (green) signals demodulated from NCS. The inset shows the heartbeat waveform details around the ninth second. (**C**) Heartbeat interval extraction for about 30 s. (**D**) Experimental setup when the hamster was running in the exercise wheel during the measurements. The NCS tag antenna was placed at the back of the wheel outside the wire cage. (**E**) Demodulated NCS raw data (red) and data after bandpass filtering (green) for 20 s. (**F**) The spectrum of the NCS signal indicates the frequency components of the body motion and the heartbeat as well as its harmonics. (**G**) Reconstructed time-domain heartbeat waveform after the equalized comb filtering. The inset shows the waveform details when the hamster was under the intermittent rest with less motion interference. (The pictures were taken by Xiaonan Hui, School of Electrical and Computer Engineering, Cornell University, Ithaca, NY 14853, USA.)

comb filter was then applied to recover the time-domain heartbeat waveform, as shown in Fig. 3G (21). The inset of Fig. 3G shows the waveform around the eighth second, when the hamster was under the intermittent rest. The sharp negative peaks can be detected for accurate heartbeat interval calculation. The heartbeat waveforms during the period of running still contained distortion from the strong motion artifact, where more advanced signal-processing methods are needed to obtain clearer results. Comb filtering can also be unreliable as a way to get rid of the NCS body motion interference when the motion in the near-field region has similar spectral content. In comparison, ECG had been attempted for free-moving conscious rodents by three paw pads (*31*). Recording is only valid when at least two pads are in touch with bare paws or body parts, which makes the pad design strongly dependent on the body shape and size. The rodent under test also needs to be moved from its habitat to the heated pad setup.

In addition to rodents, our touchless NCS method can be broadly administered to many other small conscious animals with various sizes, shapes, and body coverings. To demonstrate NCS applicability to small birds, we measured a pet fancy parakeet (*Melopsittacus undulates*, also known as budgies), named "Banana," as shown in Fig. 4 (A to C). Noninvasive monitoring of vital signs of conscious avian species will enable new capabilities in behavior studies, as well as health screening. Figure 4A demonstrates the wired experimental setup. The harmonic Tx antenna was fixed on the perch and transmitted the NCS sensing signal, which was coupled into the parakeet body. The harmonic Rx antenna was also integrated to the perch and was able to acquire detailed features of both heartbeat and respiration, as shown in Fig. 4B, with the extracted heartbeat intervals in Fig. 4C. Movie S1 shows the real-time experiment. The blue and green curves on the screen represent the heartbeat and the breath waveforms, respectively. The antenna deployment was very convenient for the wired NCS setup. After simple observation of the parakeet behavior, we identified several positions on the perch where the bird usually stood. We chose the most frequent one and mounted the antenna pair. During the NCS measurement, there was no interference to the circadian rhythm of the parakeet.

The next demonstration was made on a pet Russian tortoise (*Agrionemys horsfieldii*, also known as Horsfield's tortoise or Central Asian tortoise), named "Blimp," as shown in Fig. 4 (D to F). Russian tortoises were the first vertebrate species to reach the moon orbits (*32*) and are important for studies of long space travels because of their sub-hibernation capability, which makes the continuous long-term recording of the vital signs even more scientifically important. Tortoises have a body structure of a hard shell and soft body tissues separated by small air gaps. Vital sign acquisition by ECG and ultrasound is only feasible with neck or intramuscular probes (*5*), both of which cause major discomfort to the animal. The physiological features of the shell and being ectothermic, together with the lack of proper diagnostic methods, have thus made chelonian critical care very difficult (*33*). The hearts of birds and rodents have four chambers with two atria and two ventricles, similar to human, and thus, the NCS waveforms in Figs. 2B, 3B, and 4B have similar features. In comparison, tortoises have a three-chamber heart consisting of two

Downloaded from http://advances.sciencemag.org/ on February 13, 2019

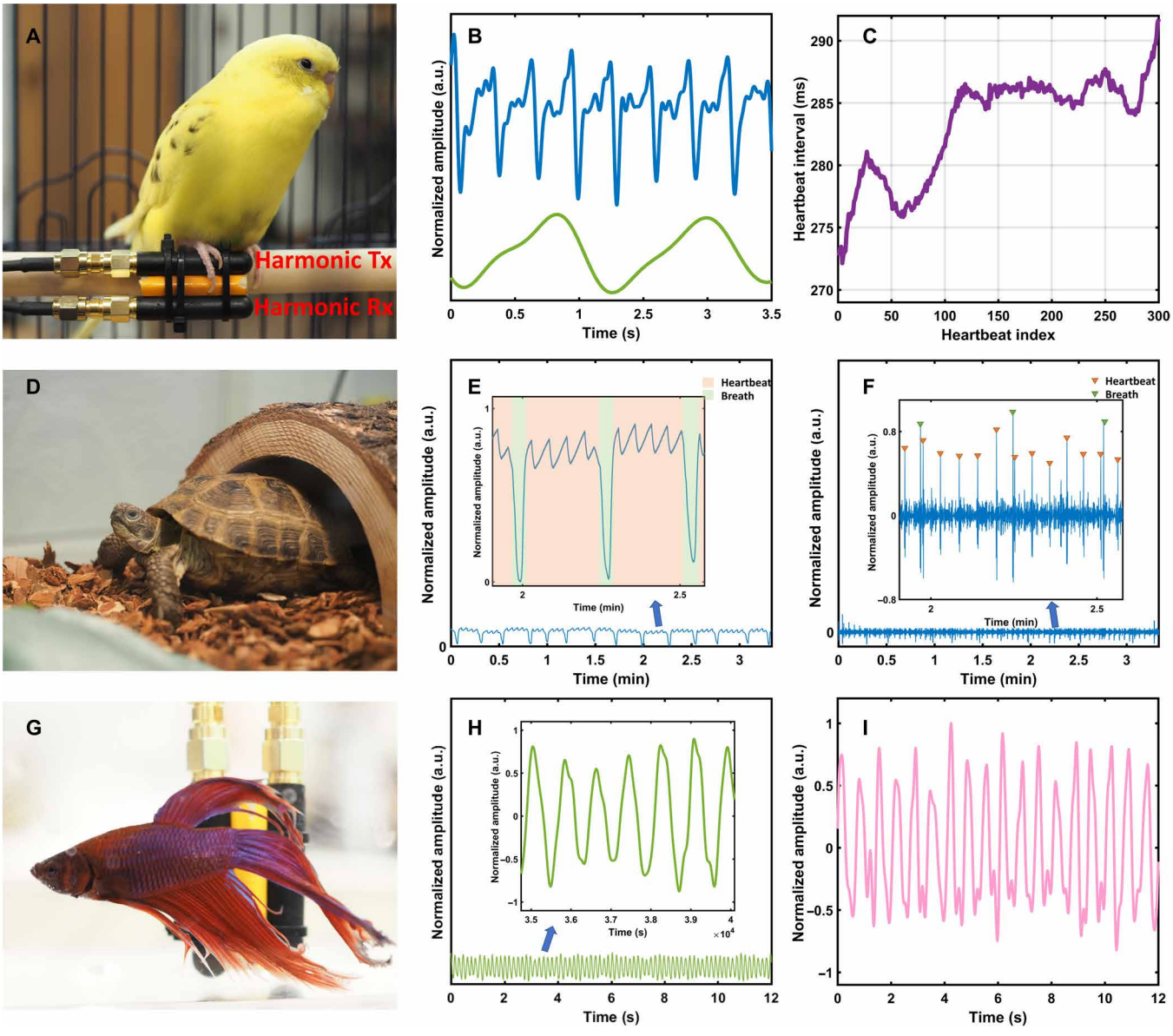

Fig. 4. The vital sign monitoring of small conscious animals with noninvasive NCS setups. (**A**) Wired NCS setup for the parakeet. (**B**) Heartbeat (blue) and respiration (green) signals demodulated from NCS. (**C**) Extracted heartbeat intervals for about 1.5 min. (**D**) NCS setup for the Russian tortoise similar to Fig. 3A, where the antennas are under the wood chip flooring. (**E**) Normalized raw amplitude of the NCS signal for 3 min, which represents both breaths and heartbeats due to the shell structure. The inset shows the waveform details of the overlapped signals. The pink shaded sections indicate the heartbeats, while the green shaded sections indicate the breaths. The strong breath signal will overwhelm the heartbeat signal during the overlap. (**F**) The online processed signals during the same period as (E) by continuous wavelet transform (CWT) show clear separation of heartbeats and breaths for accurate rate estimation. The inset shows the extracted waveform details, indicating every peak in heartbeats and breaths. (**G**) NCS setup similar to Fig. 3A for the betta fish. The Tx and Rx antennas are deployed in the water close to the fish. (**H**) Demodulated NCS phase signal caused by the pectoral fin movement, where the inset shows the waveform details. (**I**) Demodulated NCS magnitude signal possibly caused by the heartbeat. (The pictures were taken by Xiaonan Hui, School of Electrical and Computer Engineering, Cornell University, Ithaca, NY 14853, USA.)

atria and one ventricle, and the NCS cardiogram has different features, although the heart rate can still be accurately retrieved. The NCS setup is shown in Fig. 4D. A similar antenna pair in Fig. 4A was placed under the cedarwood chips outside the glass cage. Due to the body structure, respiration and heartbeat signals were both embedded in the raw data of the NCS amplitude in Fig. 4E because there was no shell surface movement during breath. The heartbeat signal could sometimes be clear (as shown in the pink shaded regions in the inset) but would be overwhelmed by the strong breath signal during the respiration movement (the green shaded regions) because of the relatively larger volume of the lungs. To separate the two overlapped signals for accurate rate estimation, the continuous wavelet transform (CWT) was used to extract the peak features of both waveforms in Fig. 4F. We have also tried the antenna placement directly on the vertebral shell and plastron, where the NCS heartbeat and respiration signals can be clearly recorded as well.

Last but not least, RF signals lower than a few gigahertz can propagate a short range in water with reasonably low attenuation,

Downloaded from http://advances.sciencemag.org/ on February 13, 2019

especially for near-field coupling. Although ECG telemetry has been previously demonstrated (*34*), the instrument implant procedure is only suitable for larger fish with a week-long recovery period before unbiased measurements can be performed. Thus, ichthyologists have long sought after other noninvasive solutions to retrieve physiological information for behavior studies and evolution biology in small fish. We demonstrated the vital sign measurements of a pet betta splendens (*Betta channoides*, also known as Siamese fighting fish), named "Glee," in Fig. 4 (G to I). The demodulated NCS phase signal was interpreted as pectoral fin movement in Fig. 4G, which had a periodic waveform with frequency matched with the unsynchronized video recording. We hypothesized that the demodulated NCS magnitude signal in Fig. 4I represented the periodical waveform originated from the heartbeat. Because of the lack of other direct measurements for comparison, further studies are needed to confirm the motion source.

CONCLUSION

Here, we demonstrate a novel noninvasive method to measure the vital signs of small conscious animals, including furry mammals, birds, tortoises, and fish. Our NCS system with convenient setup not only provides the previously unachievable sensing capability but also improves the animal testing protocols with no harm to their welfare or interference to their circadian rhythms. Previous preparation methods for vital sign monitoring such as anesthetization, hair removal, alligator clips, intramuscular probe insertion, shell hole drilling, and body implant can all be avoided. Our demonstrations can be further adapted to other species and laboratory settings to provide more humane study, care, and assessment of animals; our method also provides measurement of unbiased vital signs of animals monitored in their natural state.

MATERIALS AND METHODS

Hardware configuration

As shown in Fig. 1, the harmonic reader is implemented by an SDR consisting of Ettus USRP X310 and UBX 160 MHz RF daughterboards (*35*). Ettus USRP B200/210 can also be configured as the harmonic reader for this application, but X310 has higher data sampling rates for high resolution of waveform details. To function as a coherent harmonic transceiver in Fig. 1, the Tx chain (the blue triangle) and the Rx chain (the orange triangle) share the same RF clock source (the yellow circle). The synthesizer in the Rx chain configures the local oscillator (LO) frequency at two times of the Tx LO frequency. The Tx baseband (the gray arrow) is generated by the field-programmable gate array (FPGA), while the Rx baseband is fed into FPGA to be demodulated for data recording and display.

Both wireless and wired versions in Fig. 1 can be applied for NCS. In the wireless version in Fig. 1A, the passive harmonic tag (*36*) was modified from the wireless identification and sensing platform (WISP) (*37*), with the addition of the nonlinear transmission line (NLTL) and data modulation on the second-harmonic backscattering signal (*38*). NLTL is a ladder structure of inductors and varactors, so the varactor symbol is chosen to represent the harmonic tag and harmonic generator. The harmonic tags were operated under harvested RF power and can be readily deployed in large quantities (*25*) on many sensing targets or on multiple points of the same target (*22*). Alternatively, for single-point monitoring, the wired version in Fig. 1B is easier to apply to indoor animal laboratories. The harmonic generator here can still be NLTL as before to provide high-conversion efficiency over a broad band (*38*). The low-pass filter at the input port isolates the direct harmonic reflection from NLTL to the reader, and the high-pass filter at the output port of the NLTL damps out the signal at the fundamental frequency to the Tx antenna. Unlike the tight power constraint in the passive tag, any active or passive frequency doubler with proper frequency response can replace the NLTL in the wired version. During the experiments, we tried the custom diodes and commercial passive doubler (CRYSTEK CPPD-0.85-2) as the harmonic generator, both of which provided satisfactory performance. The wired NCS system can also be extended for multiple points with the reader CDMA technique (*39*), but the system cost will increase proportionally. The benefits of the harmonic system were demonstrated in our pervious works (*22*, *24*, *25*). In short, the harmonic system provides much better isolation between Tx and Rx, so the Rx noise floor can be much lower to improve both SNR and reader Rx sensitivity. In turn, the Tx power can also be tuned lower to still maintain sufficient SNR for the vital sign sensing, which eliminates any further health concern about the RF power impinging to live tissues.

Software configuration

The SDR is controlled by the computer with LabVIEW. The sampling rates of the DAC (digital-to-analog converter) and ADC (analog-to-digital converter) are both configured at 10 MSps (mega-samples per second). The frequency of the baseband output from the DAC is 1 MHz. When the Tx LO frequency is 950 MHz, the signal output from the Tx is 951 MHz. After the harmonic conversion, the center frequency of the Rx signal will be around 1902 MHz. The Rx LO at 1900 MHz is set to be two times of the Tx LO. Hence, the Rx baseband frequency is 2 MHz to be sampled by the ADC. The digitized baseband signal is down-converted and down-sampled in LabVIEW to an NCS sampling rate of 5 kSps (kilo-samples per second).

SUPPLEMENTARY MATERIALS

Supplementary material for this article is available at http://advances.sciencemag.org/cgi/content/full/5/2/eaau0169/DC1

Movie S1. Real-time heartbeat and breath monitoring of the parakeet.

REFERENCES AND NOTES

1. P. P. Pereira-Junior, M. Marocolo, F. P. Rodrigues, E. Medei, J. H. M. Nascimento, Noninvasive method for electrocardiogram recording in conscious rats: Feasibility for heart rate variability analysis. *An. Acad. Bras. Cienc.* **82**, 431–437 (2010).
2. R. H. Wolf, N. D. Lehner, E. C. Miller, T. B. Clarkson, Electrocardiogram of the squirrel monkey, *Saimiri sciureus*. *J. Appl. Physiol.* **26**, 346–351 (1969).
3. E. Lepeschkin, B. Surawicz, The measurement of the Q-T interval of the electrocardiogram. *Circulation* **6**, 378–388 (1952).
4. P. Kligfield, L. S. Gettes, J. J. Bailey, R. Childers, B. J. Deal, E. W. Hancock, G. van Herpen, J. A. Kors, P. Macfarlane, D. M. Mirvis, O. Pahlm, P. Rautaharju, G. S. Wagner, Recommendations for the standardization and interpretation of the electrocardiogram: Part I: The electrocardiogram and its technology: A scientific statement from the American Heart Association Electrocardiography and Arrhythmias Committee, Council on Clinical Cardiology; the American College of Cardiology Foundation; and the Heart Rhythm Society endorsed by the International Society for Computerized Electrocardiology. *Circulation* **115**, 1306–1324 (2007).
5. A. E. Bowles, S. Eckert, L. Starke, E. Berg, L. Wolski, *Effects of Flight Noise From Jet Aircraft and Sonic Booms on Hearing, Behavior, Heart Rate and Oxygen Consumption of Desert Tortoises* (Gopherus agassizii) (United States Air Force Research Laboratory, 1999).
6. J. Allen, Photoplethysmography and its application in clinical physiological measurement. *Physiol. Meas.* **28**, R1–R39 (2007).
7. T. Tamura, Y. Maeda, M. Sekine, M. Yoshida, Wearable photoplethysmographic sensors—Past and present. *Electronics* **3**, 282–302 (2014).

Downloaded from http://advances.sciencemag.org/ on February 13, 2019

8. J. R. Kindig, T. P. Beeson, R. W. Campbell, F. Andries, M. E. Tavel, Acoustical performance of the stethoscope: A comparative analysis. *Am. Heart J.* **104**, 269–275 (1982).
9. H. Liang, S. Lukkarinen, I. Hartimo, Heart sound segmentation algorithm based on heart sound envelogram, *Proceedings of the 1997 IEEE Computers in Cardiology*, Lund, Sweden, 7 to 11 September 1997.
10. P. J. A. Frinking, A. Bouakaz, J. Kirkhorn, F. J. Ten Cate, N. de Jong, Ultrasound contrast imaging: Current and new potential methods. *Ultrasound Med. Biol.* **26**, 965–975 (2000).
11. J. S. Mattoon, T. G. Nyland, *Small Animal Diagnostic Ultrasound* (Elsevier Health Sciences, 2014).
12. J. C. Lin, Noninvasive microwave measurement of respiration. *Proc. IEEE* **63**, 1530 (1975).
13. C. Li, V. M. Lubecke, O. Boric-Lubecke, J. Lin, A review on recent advances in Doppler radar sensors for noncontact healthcare monitoring. *IEEE Trans. Microwave Theory Techn.* **61**, 2046–2060 (2013).
14. C. Li, Z. Peng, T.-Y. Huang, T. Fan, F.-K. Wang, T.-S. Horng, J.-M. Muñoz-Ferreras, R. Gómez-García, L. Ran, J. Lin, A review on recent progress of portable short-range noncontact microwave radar systems. *IEEE Trans. Microw. Theory Tech.* **65**, 1692–1706 (2017).
15. F. Adib, H. Mao, Z. Kabelac, D. Katabi, R. C. Miller, Smart homes that monitor breathing and heart rate, *CHI '15 Proceedings of the 33rd Annual ACM Conference on Human Factors in Computing Systems*, Seoul, Korea, 18 to 23 April 2015.
16. F. Pfanner, T. Allmendinger, T. Flohr, M. Kachelrieß, Modelling and simulation of a respiratory motion monitor using a continuous wave Doppler radar in near field, *Proceedings of the Medical Imaging 2013: Physics of Medical Imaging, International Society for Optics and Photonics*, Lake Buena Vista, FL, 6 March 2013.
17. T.-Y. Huang, J. Lin, L. F. Hayward, Non-invasive measurement of laboratory rat's cardiorespiratory movement using a 60-GHz radar and nonlinear Doppler phase modulation, *Proceedings of the 2015 IEEE MTT-S International Microwave Workshop Series on RF and Wireless Technologies for Biomedical and Healthcare Applications (IMWS-BIO)*, Taipei, Taiwan, 21 to 23 September 2015.
18. T.-Y. Huang, L. F. Hayward, J. Lin, Noninvasive measurement and analysis of laboratory rat's cardiorespiratory movement. *IEEE Trans. Microw. Theory Tech.* **65**, 574–581 (2017).
19. A. Serra, R. Reggiannini, R. Massini, P. Nepa, RF sensor for non-invasive cardiopulmonary monitoring, *Proceedings of the International Conference on Wireless Mobile Communication and Healthcare*, Paris, France, 21 to 23 November 2012.
20. R. R. G. Perron, M. F. Iskander, T. B. Seto, G. C. Huang, D. A. Bibb, Electromagnetics in medical applications: The cardiopulmonary stethoscope journey, in *World of Applied Electromagnetics* (Springer, 2017), pp. 443–479.
21. N. Celik, R. Gagarin, G. C. Huang, M. F. Iskander, B. W. Berg, Microwave stethoscope: Development and benchmarking of a vital signs sensor using computer-controlled phantoms and human studies. *IEEE. Trans. Biomed. Eng.* **61**, 2341–2349 (2014).
22. X. Hui, E. C. Kan, Monitoring vital signs over multiplexed radio by near-field coherent sensing. *Nat. Electron.* **1**, 74–78 (2018).
23. X. Hui, E. C. Kan, Mitigation of body movement interference in near-field coherent sensing for heartrate monitoring, *Proceedings of the IEEE 15th International Conference on Wearable and Implantable Body Sensor Networks (BSN) 2018*, Las Vegas, NV, 4 to 7 March 2018.
24. Y. Ma, X. Hui, E. C. Kan, 3D real-time indoor localization via broadband nonlinear backscatter in passive devices with centimeter precision, *Proceedings of the 22nd Annual International Conference on Mobile Computing and Networking (MobiCom'16)*, New York City, NY, 3 to 7 October 2016.
25. X. Hui, Y. Ma, E. C. Kan, Code division multiple access in centimeter accuracy harmonic RFID locating system. *IEEE J. Radio Freq. Identif.* **1**, 51–58 (2017).
26. National Research Council, Animal and human studies addressing health effects, in *An Assessment of Potential Health Effects from Exposure to PAVE PAWS Low-Level Phased-Array Radiofrequency Energy* (The National Academies Press, 2005), chap. 7.
27. M. Bolić, D. Simplot-Ryl, I. Stojmenović, *RFID Systems: Research Trends and Challenges* (Wiley, 2010).
28. P. H. Gordon, R. Chen, H. Park, E. C. Kan, Embroidered antenna characterization for passive UHF RFID tags. arXiv:1710.02237 [eess.SP] (5 October 2017).
29. E. Pinheiro, O. Postolache, P. Girão, Theory and developments in an unobtrusive cardiovascular system representation: Ballistocardiography. *Open Biomed. Eng. J.* **4**, 201–216 (2010).
30. O. T. Inan, P.-F. Migeotte, K.-S. Park, M. Etemadi, K. Tavakolian, R. Casanella, J. Zanetti, J. Tank, I. Funtova, G. K. Prisk, M. Di Rienzo, Ballistocardiography and seismocardiography: A review of recent advances. *IEEE J. Biomed. Health Inform.* **19**, 1414–1427 (2015).
31. ECGenie Video, How to record ECG non-invasively in conscious mice; https://mousespecifics.com/heart-monitoring/ECGenie-video.
32. A. C Madrigal, "Who was first in the race to the moon? The tortoise," *The Atlantic*, 27 December 2012.
33. T. M. Norton, Chelonian emergency and critical care. *Semin. Avian Exot. Pet. Med.* **14**, 106–130 (2005).
34. V. J. T. van Ginneken, P. Snelderwaard, R. van der Linden, N. van der Reijden, G. E. E. J. M. van den Thillart, K. Kramer, Coupling of heart rate with metabolic depression in fish: A radiotelemetric and calorimetric study. *Thermochim. Acta* **414**, 1–10 (2004).
35. USRP X310 and UBX-160 daughterboard, products of Ettus Research (2018); https://www.ettus.com/product.
36. Y. Ma, X. Hui, E. C. Kan, Harmonic-WISP: A passive broadband harmonic RFID platform, *Proceedings of the 2016 IEEE MTT-S International Microwave Symposium (IMS)*, San Francisco, CA, 22 to 27 May 2016.
37. D. J. Yeager, A. P. Sample, J. R. Smith, WISP: A passively powered UHF RFID tag with sensing and computation, in *RFID Handbook: Applications, Technology, Security, and Privacy* (CRC Press, 2008), pp. 261–278.
38. F. Yu, K. G. Lyon, E. C. Kan, A novel passive RFID transponder using harmonic generation of nonlinear transmission lines. *IEEE Trans. Microw. Theory Tech.* **58**, 4121–4127 (2010).
39. X. Hui, E. C. Kan, Collaborative reader code division multiple access in the harmonic RFID system. *IEEE J. Radio Freq. Identif.* **2**, 86–92 (2018).

Acknowledgments: The animal experiments are under Cornell IACUC Protocol 2018-0034. We wish to thank C. Cammarata and A. K. Anderson for help in the experiment of the anesthetized rat, as well as J. Kan and A. Kan for help in handling and care of the hamster, tortoise, and parakeet. We also wish to thank E. Berliner for providing feedback from the viewpoint of a veterinary doctor. **Funding:** This project was supported by U.S. Department of Energy (DoE) under Advanced Research Projects Agency—Energy (ARPA-E) project numbers DE-AR0000528 and DE-AR0000946. **Author contributions:** X.H. conducted all experiments and data analyses. E.C.K. supervised the project and participated in the design of experiments. They both contributed to the manuscript preparation. **Competing interests:** X.H. and E.C.K. are inventors on a provisional patent related to this work filed by Cornell Research Foundation (no. PCT/US18/38121, filed on 18 June 2018). The authors declare no other competing interests. **Data and materials availability:** All data needed to evaluate the conclusions in the paper are present in the paper and/or the Supplementary Materials. The data that support the plots within this paper and other findings of this study are available from the corresponding author upon reasonable request.

Submitted 27 April 2018
Accepted 3 January 2019
Published 13 February 2019
10.1126/sciadv.aau0169

Citation: X. Hui, E. C. Kan, No-touch measurements of vital signs in small conscious animals. *Sci. Adv.* **5**, eaau0169 (2019).

Downloaded from http://advances.sciencemag.org/ on February 13, 2019

ScienceAdvances

No-touch measurements of vital signs in small conscious animals

Xiaonan Hui and Edwin C. Kan

Sci Adv **5** (2), eaau0169.
DOI: 10.1126/sciadv.aau0169

ARTICLE TOOLS http://advances.sciencemag.org/content/5/2/eaau0169

SUPPLEMENTARY MATERIALS http://advances.sciencemag.org/content/suppl/2019/02/11/5.2.eaau0169.DC1

REFERENCES This article cites 21 articles, 2 of which you can access for free
http://advances.sciencemag.org/content/5/2/eaau0169#BIBL

PERMISSIONS http://www.sciencemag.org/help/reprints-and-permissions

Use of this article is subject to the Terms of Service

Science Advances (ISSN 2375-2548) is published by the American Association for the Advancement of Science, 1200 New York Avenue NW, Washington, DC 20005. 2017 © The Authors, some rights reserved; exclusive licensee American Association for the Advancement of Science. No claim to original U.S. Government Works. The title *Science Advances* is a registered trademark of AAAS.

Downloaded from http://advances.sciencemag.org/ on February 13, 2019

Appendix J

(PDF downloaded from IEEE) J. Zhou, P. Sharma, X. Hui and E. C. Kan, “Wireless wearable RF sensor for long-term vital-sign monitoring on chelonians”, *IEEE J. Electromagnetics, RF and Microwaves in Medicine and Biology*, doi: 10.1109/JERM.2020.2998761, 2020.

A Wireless Wearable RF Sensor for Brumation Study of Chelonians

Jianlin Zhou, Pragya Sharma, Xiaonan Hui and Edwin C Kan, *Senior Member, IEEE,*

***Abstract*—We present a low-power wireless radio-frequency (RF) sensor to perform continuous vital-sign monitoring for chelonians in various stages of brumation. Due to their unique body structure, vital signs of chelonians cannot be recorded without substantial animal handling in previous methods, which would severely bias the brumation condition. In contrast, our sensor on harness can couple significant RF energy into various body parts to evaluate the heartbeat, respiration and activity levels. The self-contained unit is lightweight for ease of wearable deployment and low power to avoid unnecessary heat generation as well as frequent battery replacement. We recorded the shell temperature, heart rate, respiration rate and activity levels of a Russian tortoise during the entire brumation cycle and found that the heart rate correlated with the ambient temperature well, while the breath rate did not significantly reduce during brumation. This experimental study is minimally invasive and thus least biased.**

***Keywords*—vital-sign monitoring; radio frequency; wearable sensors; chelonians.**

I. Introduction

LONG-TERM monitoring of vital signs of animals not only helps us better understand their circadian rhythms, behavior and wellness, but also clarifies some important ecological implications. Heart and respiratory rates are most often used as the key parameters to evaluate animal metabolism and their adaption to environmental changes [1]–[3] such as hibernation for endotherms and brumation for ectotherms [4]–[6]. In this depressed-metabolism state, animals enter into an inactive or dormant mode for energy conservation [7], as reflected by lower heart and respiratory rates [8]. Meanwhile, many researchers also suggested a correlation among the metabolic rate, body temperature and lifespan [9], [10], which may explain the longer lifespan for chelonians [11]. However, we do not have sufficient data on the vital signs during the phases of entering and waking up from brumation, and hence retrieval of the mechanistic transition of brumation remains difficult. Researches on hibernation and brumation also have an impact on comparative physiology applications [12]. In present clinical practices, controlled hypothermia is widely used in cardiac surgery and acute brain trauma to reduce metabolism [13], where the process management is critical to minimize collateral damages. For deep space traveling, a hibernation induction chamber is considered as one of the most critical projects [14]–[16]. Furthermore, the mechanistic understanding of brumation can help the study of circadian-rhythm control. However, vital signs for animals with different body surface coverings were difficult to measure in a non-invasive manner. Substantial preparation procedures are often required for many veterinarian vital-sign sensing procedures. Electrocardiogram (ECG) and ultrasound need direct contact with the skin with good electrical or acoustic impedance match. The surface preparation may include shaving hair, fur, scales, or feathers. Reptiles, especially chelonians with shells, are even more difficult due to their body structure of the hard shell, air gap, and soft tissues. In veterinarian practice, to retrieve the heart rate, ECG is often administered by implanted subdermal electrodes in the muscle or inside plastron. Alternatively, esophageal stethoscope or a Doppler probe can be placed in the region of the thoracic inlet [17]–[19]. For respiratory monitoring, a thermistor or an airflow detector can be placed on the endotracheal tube [20]. Anesthesia is often required before the sensor setup and can cause a serious bias to the metabolic parameters. Without anesthesia, the discomfort and distress are also serious concerns in addition to animal cruelty. To overcome such drawbacks, researchers have attempted many touchless vital-sign monitoring methods [21]–[23], such as the Doppler radar [24], [25], frequency-modulated continuous-wave (FMCW) radar [26]–[28], impulse response ultra-wideband (IR-UWB) radar [29]–[31], and stepped-frequency continuous-wave (SFCW) radar [32], [33]. However, most radar-based vital-signs monitoring methods are based on the line-of-sight (LoS) reflection from body surface motion, and can be difficult to apply to animals whose heartbeat and breathing do not show body surface motion or whose motion makes LoS alignment to specific body parts difficult . For chelonians in brumation when most vital organs are hidden away from LoS, these far-field radio-frequency (RF) methods become ineffective.

In this work, we followed a new touchless vital-sign sensing method based on the near-field coherent sensing (NCS) principle [34]. Its main difference from the radar-based method is that the internal dielectric (tissue) motion can be coupled as an antenna characteristic variation which performs as a modulation onto the RF signal. Thus, for sensing objects like chelonians whose vital-signs do not render surface motion, this method can still be applicable [35]. In the previous experiments, a software-defined radio (SDR) platform based on universal software radio peripheral (USRP) was employed, which has a large size, high cost, and high power consumption as well as noticeable heat generation. This platform for long-term wearable sensing is thus limited by the deployment options and temperature concerns. Wearable tethering on harness or clothing also allows free motion for the subject under tests and is desirable for long-term operations. Minimal heat generation can avoid disturbance to the animal under test, especially

J. Zhou, P. Sharma, X. Hui and E. C. Kan are with the School of Electrical and Computer Engineering, Cornell University, Ithaca, NY 14853, USA. E-mails: jz899; ps847; xh273; eck5@cornell.edu.

for brumation study. In this paper, we present a low-power wireless wearable NCS sensor to monitor the entire brumation cycle of a conscious Russian tortoise (Agrionemys horsfieldii, also known as Horsfield's tortoise or Central Asian tortoise). We integrated sensing of the shell temperature, heartbeat, respiration, and activity levels which were indicative parameters on tortoise metabolism. Sensor design and system benchmark experiments on human with known comparative vital signs are described in Sec. II. Section III discusses the experimental protocol and setup including the ambient control. Section IV presents the vital-sign acquisition algorithm. Section V shows the experimental results and analyses of the entire brumation cycle. Conclusion and some future work are summarized in Sec. VI.

II. System Design and Verification

A. RF Sensor Design

The overall block diagram of the NCS vital-sign monitoring system, as shown in Fig. 1, includes three main modules. Two CC1310 SimpleLink sub-1 GHz ultra-low-power wireless microcontrollers are used as the sensing transmitter (Tx) and receiver (Rx). Each CC1310 contains one main ARM Cortex-M3 CPU and one ARM Cortex-M0 RF core. The M3 core handles the main digital threads and the M0 core processes the RF samples. The Tx and Rx transceivers employed quadrature I/Q modulation, where two channels of 12-bit I and Q samples were sampled at 1.6 kHz and accumulated into one 150-bytes cyclic buffer at the sensor Rx. Once the I/Q buffer was filled, the Rx M3 core would bundle the I and Q samples with the temperature reading to send to the Bluetooth Low Energy (BLE) module (TI CC2640R2F) through a module of universal asynchronous receiver/transmitter (UART). The temperature sensor is implemented by Texas Instrument TMP112 and is connected by the inter-integrated-circuits (I2C) serial protocol. The BLE NCS sensor is manufactured on a 4-layer printed circuit board (PCB), including two signal layers, one ground layer, and one power layer, as shown in Fig. 2. The system characteristics are summarized in Table. I

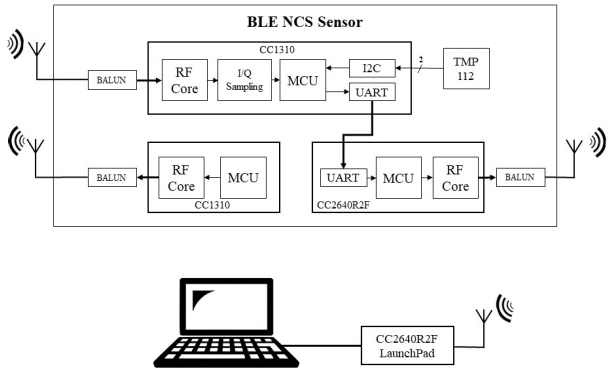

Fig. 1. Block diagram of the low-power wireless RF sensor.

B. System Verification

As there is no other sensor that can retrieve the cardiopulmonary recording of the conscious free-moving tortoise, we opt to verify our sensor on human where a physiological measurement system of BIOPAC MP36R (Biopac Systems Inc, Santa Barbara, California, USA) is used as the reference during system verification. The BIOPAC system collects the respiration signals by the torso belts (SS5LB) and the cardiogram by a three-electrode ECG. The real-time clock (RTC) on the host computer is used for synchronization between BIOPAC and our BLE NCS sensor. In the benchmark experiments, the BLE NCS sensor was mounted inside a 3D-printed case, which was secured on the chest by an elastic belt. The battery and antennas were mounted on the case using Velcro stickers, as shown in Fig. 3. Two sensing PCB antennas (Taoglas PC91) were used for NCS, and a ceramic patch antenna (Taoglas WLP.25) for BLE. The heartbeat and respiration signals from BIOPAC were sampled at 2 kHz. In post-processing, both NCS and BIOPAC signals are down-sampled to 500 Hz after an anti-aliasing low-pass filter. All procedures involving human subjects were approved by the Cornell Institutional Review Board (IRB). A representative 2-min recording is shown in Fig. 4, where the inset shows a detailed comparison of the heartbeat signal between BIOPAC ECG and NCS for 12 seconds. The user performed two types of activities: normal breathing and breath-holding. In Fig. 4, breathing patterns from BIOPAC and NCS were very similar with a correlation coefficient of $r = 0.87$, and the cardiogram

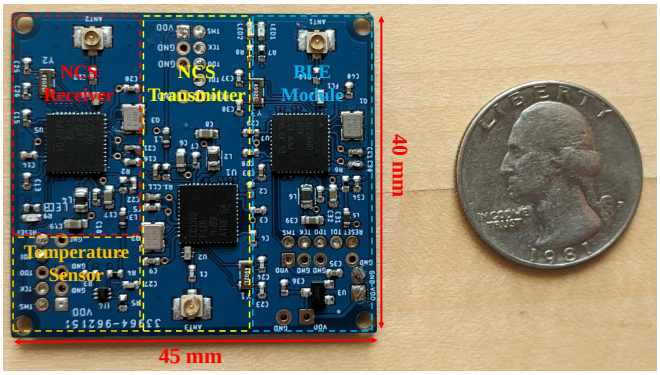

Fig. 2. Photo of the low-power BLE NCS sensor PCB.

Parameters	Value
PCB size	4.5 × 4 mm
Weight (board)	30 g
Weight (total)	69 g
Supply voltage	3.7 V
Average current consumption (LED off)	24 mA
NCS sensor carrier frequency	779 MHz
NCS sensor transmitting power (tunable)	$\leq$ 10 dBm
NCS sensor sampling rate (tunable)	$\geq$ 1600 Sps

TABLE I
SUMMARY OF THE NCS SENSOR SYSTEM CHARACTERISTICS

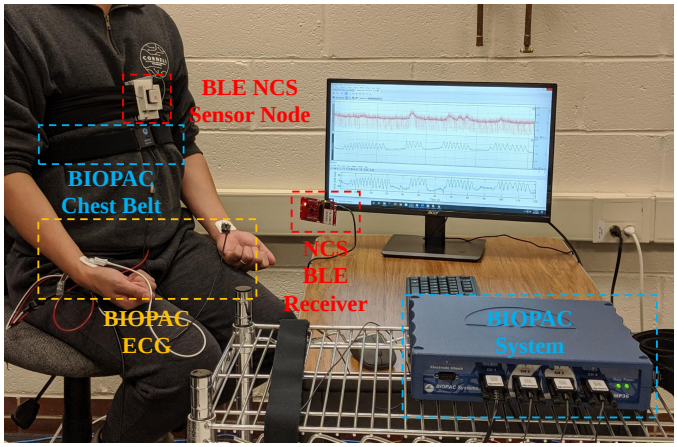

Fig. 3. Photo of the BLE NCS sensor for human benchmark experiments.

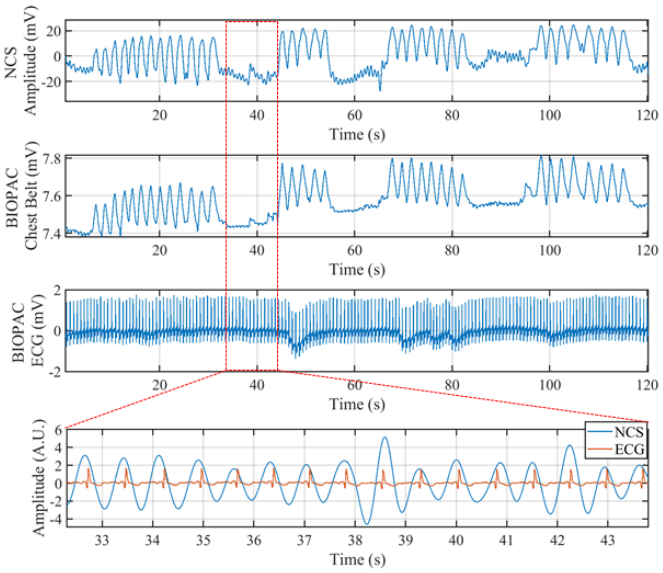

Fig. 4. Synchronized NCS and BIOPAC vital-sign signals on a human participant for sensor benchmarking.

waveforms from ECG and NCS gave very similar beat-to-beat intervals.

III. Experimental Protocol

A 6-day experiment on a Russian tortoise is designed to demonstrate our long-term vital-sign monitoring capability on the physiological response of chelonians to temperature variations. Our brumation protocol contains three phases: pre-brumation, in-brumation, and post-brumation, which take 1.5 days, 3days and 1.5 days long, respectively. A BLE NCS sensor was mounted in a 3D-printed case and placed on top of the tortoise shell secured by a leather tortoise harness (Asocea). The sensing antenna pair was fixed with rubber bands on the front part of the shell, as shown in Figure. 5 (A). In pre-brumation and post-brumation phases, the tortoise under test stayed in a wooden habitat (Zoo Med) at the room temperature (25.7 °C). The habitat box has two compartments: the large room has a steel screen with a top heat lamp and the small room has wood siding to let the tortoise feel secure. The

(A)

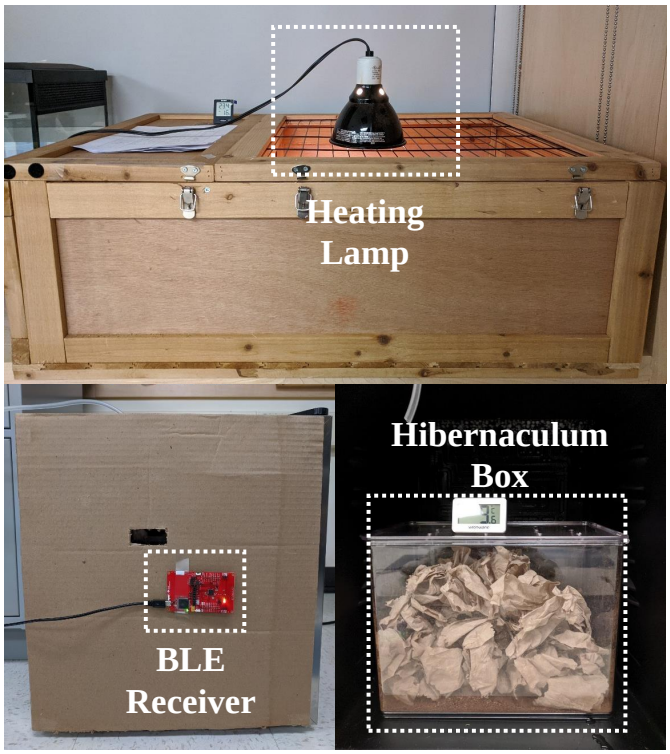

(B)

Fig. 5. (A) Photo of the sensor setup on tortoise; (B) Photo of the regular habitat and the hibernaculum box.

habitat floor is covered with wood chips, and the heating lamp was on during the daytime for 12 hours. When the tortoise is basking directly under the heat lamp, the shell temperature can reach nearly 40 °C. During the in-brumation phase, the tortoise was kept in a plastic hibernaculum box which has ventilation holes on the lid and filled with soil and paper strips, as shown in Figure. 5(B). The hibernaculum box is placed inside a refrigerator with ventilation by an air pump. The cooling temperature was first set to 10 °C on the first in-brumation day and 5 °C for the remaining 2 days.

In the pre-brumation phase, only water but no food was provided for the tortoise, which would allow the tortoise to pass out the remaining food in its gastrointestinal tract to reduce possible harm caused by food residuals during brumation

[36]. At the start of the post-brumation phase, the tortoise was taken out from the hibernaculum box and soaked in warm water for 30 minutes to induce the tortoise out of brumation. All procedures involving animal subjects were approved by the Cornell Institutional Animal Care and Use Committee (IACUC). During the 6-day process, a CC2640R2F LauchPad BLE receiver was mounted on the wood box or inside the refrigerator for data recording. A real-time MATLAB routine was used for continuous data visualization and processing.

IV. Data Processing and Algorithms

A. The Signal Model

Motions of the body surface and internal organs in the near-field region are modulated onto the NCS Rx signal and can be demodulated as the baseband data. CC1310 has a built-in patch function that provides raw I/Q quadrature signal samples. Quadrature signals are given by:

$$I_{RX}(t) = A(t)\cos(2\pi f_{Baseband} + \theta(t)) \tag{1}$$

$$Q_{RX}(t) = A(t)\sin(2\pi f_{Baseband} + \theta(t)) \tag{2}$$

The NCS signal here is the baseband amplitude which can be retrieved from:

$$AMP_{NCS}(t) = \sqrt{I_{RX}(t)^2 + Q_{RX}(t)^2} \tag{3}$$

Respiration and heartbeat waveforms can be readily extracted by a simple bandpass filtering to remove the high-frequency noise and DC drifting [37].

From previous ultrasound and airflow sensors [19], [20], both heart and respiration rates of the Russian tortoise are estimated to be below 1 Hz. Thus, to increase the processing speed and decrease data redundancy, the NCS amplitude signal is first processed by a 6th-order low-pass Butterworth filter with a cutoff of 2 Hz, and then down-sampled to 10 samples per second (Sps) in the pre-processing stage.

B. Motion Detection and Activity Level

In terms of the total surface area, body motion causes a larger NCS amplitude change than that from internal organ motion, as shown in Fig. 6. Thus, it is critical to detect body motion and annotate these periods before extracting heart and respiration rates. Meanwhile, the period with significant body motion can be applied for activity estimate. The parameter of the activity level (AL) is defined as:

$$AL = \frac{T_{motion}}{T_{segment}} \tag{4}$$

where T_{motion} is the total motion period appeared in a given data segment and $T_{segment}$ is chosen here as 15 minutes.

Segmented NCS signals are normalized with the root mean square (RMS) of the signal sequence and then separated into epochs of 30-s duration, where the line length, signal energy, average RMS, largest power spectrum density, kurtosis, skewness, entropy, mean and zero crossings of the first derivative of the signal, maximum amplitude, mean curve length, mean level 1 wavelet coefficient (db10), mean amplitude and amplitude variance are calculated [37].

Three support vector machine (SVM) classifiers with radial basis function kernels are adopted to detect motion using the above 134 statistical and time-frequency domain features. Three 16-hour labeled signal sequences from each phase are used to train each SVM classifier and 6-fold cross-validation is then performed on each classifier. Finally AL can be calculated by the SVM classifiers. An example of a 15-min signal segment with motion detection is shown in Fig. 6

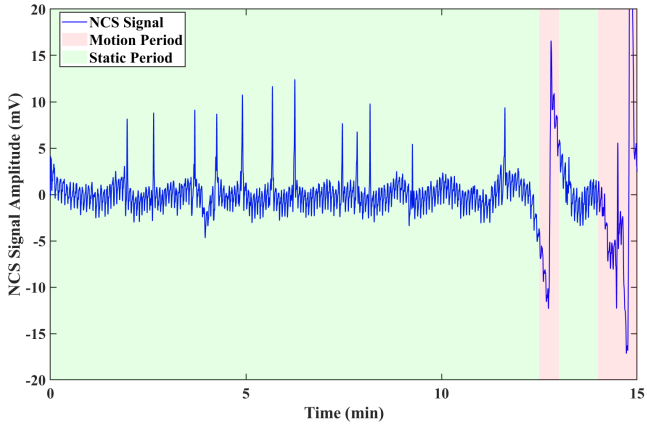

Fig. 6. Vital signs and motion classification. The low-amplitude cyclic signals around 3mV peak-to-peak are from the heartbeat and the spikes around 10mV are from respiration. The detected motion is in the shaded pink region.

C. Heartrate Calculation

Heartbeat signals have the lowest magnitude and can be seriously distorted by motion, while breath can also cause minor interference. Thus, the peak detection in heartbeats has to exclude periods where motion is strong in each signal segment. To maximize the number of samples in heartrate calculation, we set an AL threshold of 0.7, where the entire segment will be rejected for calculation of heart and respiration rates. A wavelet-based peak detection method by the 1-D decomposition coefficient is applied for heart rate estimation. Simultaneously, a method based on selected-band spectral peak detection is used for comparison and possible correction. During the in-brumation phase, our approach starts from the level-7 1-D decomposition coefficient using the Daubechies 6 wavelet (db6), which results in maximum correlation with the heartbeat signal upon reconstruction. In the pre-brumation and post-brumation phases, we apply Daubechies 10 wavelet (db10) for 1-D wavelet decomposition. When the shell temperature is higher than 28 °C, the level-4 coefficients had the maximum correlation with the heartbeat signal, while the level-5 coefficients were most correlated at the room temperature.

D. Breath Peak Detection

As the tortoise with the sensor on harness was allowed to move freely, the RF environment kept changing. This leads to variation of the NCS coupling strength and variable signal-to-noise ratio (SNR). Therefore, simple thresholding on signal amplitude is not applicable for breath peak detection.

Meanwhile, the heartbeat can also cause ambiguous peak detection on slow or shallow breathing signals. Simple filtering is problematic as respiration can be voluntary such as sniffing and may not be cyclic. Further analysis is needed to extract breaths unambiguously and to rid of heartbeats and other interferences. [37] To improve signal processing accuracy for breathing, we propose a multi-stage thresholding peak detection (MTPD) algorithm.

The same motion rejection is used for breathing peak detection when AL is higher than 0.7 in each segment. The NCS signal is first low-pass filtered with cut-off at 0.03Hz for the in-brumation phase and 0.15 Hz for the pre- and post-brumation phases. The signal is then normalized by RMS and fed to MTPD input: $S_{Input}(t) = S_{filtered}(t)/RMS(S_{filtered}(t))$. MTPD algorithm has four-stage thresholding on the time-domain signal pattern, and the parameter tuning is based on prior knowledge [35].

In *Stage One*, we first performed a local maximum detection based on the absolute value of the first derivative to identify all potential peaks. Then two times of the RMS is used to threshold and reject the small peaks:

$$ABS(S_{Input}(t_{stage1})) > 2 * S_{RMS}, \quad t_{stage1} \in [0, T_{segement}],$$

where t_{stage1} represents the time stamp of the detected peak after the first thresholding.

In *Stage Two*, to avoid duplicated counting on the same breathing peak which appeared in the adjacent segments, we rejected the edge peaks which appear in the last two seconds of the time segment. Furthermore, to accommodate the NCS coupling strength variation and remove miscounted heartbeat as beathing peak, further thresholding needs to be performed on the potential peaks. From our previous observation, we found breathing and heartbeat signals not only had different amplitude but also different duration for different brumation phases. Thus, we threshold the slope points at 0.5s, 1s, 2s and 3s of the suspected breathing peaks during in-brumation and at 0.125s, 0.25s, 0.5s and 0.75s during pre-brumation and post-brumation with the signal RMS:

$$ABS(S_{Input}(t_{stage2} + T_{slope})) > S_{RMS}, \tag{5}$$

where $t_{stage2} \in t_{stage1}, 2 < t_{stage2} < (T_{segement} - 2)$ and $T_{slope} \in \{\pm 0.5, \pm 1, \pm 2, \pm 3\}$ for the in-brumation phase, $T_{slope} \in \{\pm 0.125, \pm 0.25, \pm 0.5, \pm 0.75\}$ for the pre- and post-brumation phases.

In *Stage Three*, to further remove spurious peaks which appeared very closely, we perform another thresholding assuming the tortoise breathing interval is no less than 5 seconds . Even though tortoise is also known to sniff, in our entire brumation circle, we did not observe two breathings appeared within 5 seconds. Therefore, for all the detected peaks whose timestamps are within 5 seconds, we only keep the maximum peak in that period at t_{stage3}.

In *Stage Four*, we will remove the peaks caused by undetected motion artifact as well as by baseline discontinuity after motion epoch removal and signal recombination. Since breathing patterns are similar and consistent in each time segment, we first subtracted the time-domain signal within ± 2 seconds of the detected peak. Statistic-based thresholding were then applied to reject inconsistent and abnormal patterns. The mean $S_{mean}(t)$ and variances $S_{variance}(t)$ of all the time-domain patterns were calculated from the absolute values of the detected peaks from *Stage Three*, $ABS(S_{Input}(t))$, where $(T_{peak3} - 2) < t < (T_{peak3} + 2), T_{peak3} \in t_{stage3}$. We then recorded the peaks t_{stage4} which met the following conditions:

$$0.5 \times median(S_{mean}(t_{stage3})) < S_{mean}(t_{stage4}) < 5 \times median(S_{mean}(t_{stage3}));$$

$$0.6 \times median(S_{variance}(t_{stage3})) < S_{variance}(t_{stage4}) < 3 \times median(S_{variance}(t_{stage3})).$$

t_{stage4} are the final output timestamps of breathing peaks by MTPD. For illustration, peaks detected in a 15-min segment during in-brumation is shown in Fig. 7

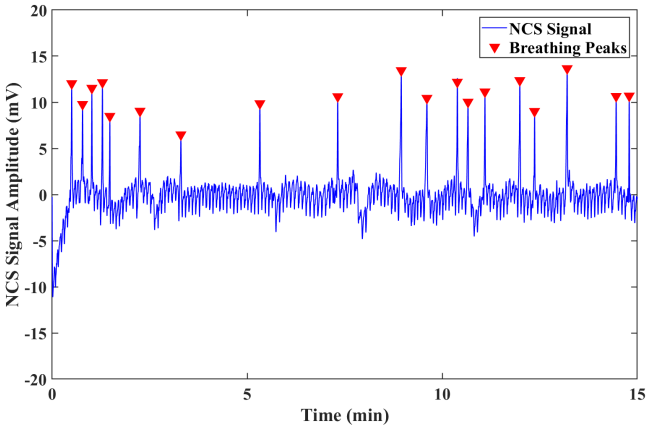

Fig. 7. The demodulated NCS signal where the heartbeats and breathing peaks can be identified. Notice that the heart intervals are reasonably constant, while the breath intervals have large irregularity.

V. Experimental Results

We present one example of 15-min NCS signal segment for each phases of pre-, in- and post-brumaton, as shown in Fig. 9. Breathing peaks and heartbeats can be clearly seen in each plot which indicates that our sensor and signal processing can be applied in various phases. During the in-brumation phase in a low-temperature environment, the time intervals between heartbeats and between breaths become longer than those in pre- and post- brumation conditions. The breath intervals have much higher variation than the heart intervals in all phases, although the breath rate during the in-brumation phase is relatively stable. Larger NCS signal magnitude in the post-brumation phase does not necessarily imply stronger heartbeats or larger breath efforts, as the tortoise may have move to a different position with different NCS coupling strength.

The extracted AL, heart rate, breathing rate and shell temperature vs. time over the entire brumation cycle are shown in Fig. 8, according to the algorithms in the previous section. The correlation coefficients between vital-signs and temperature

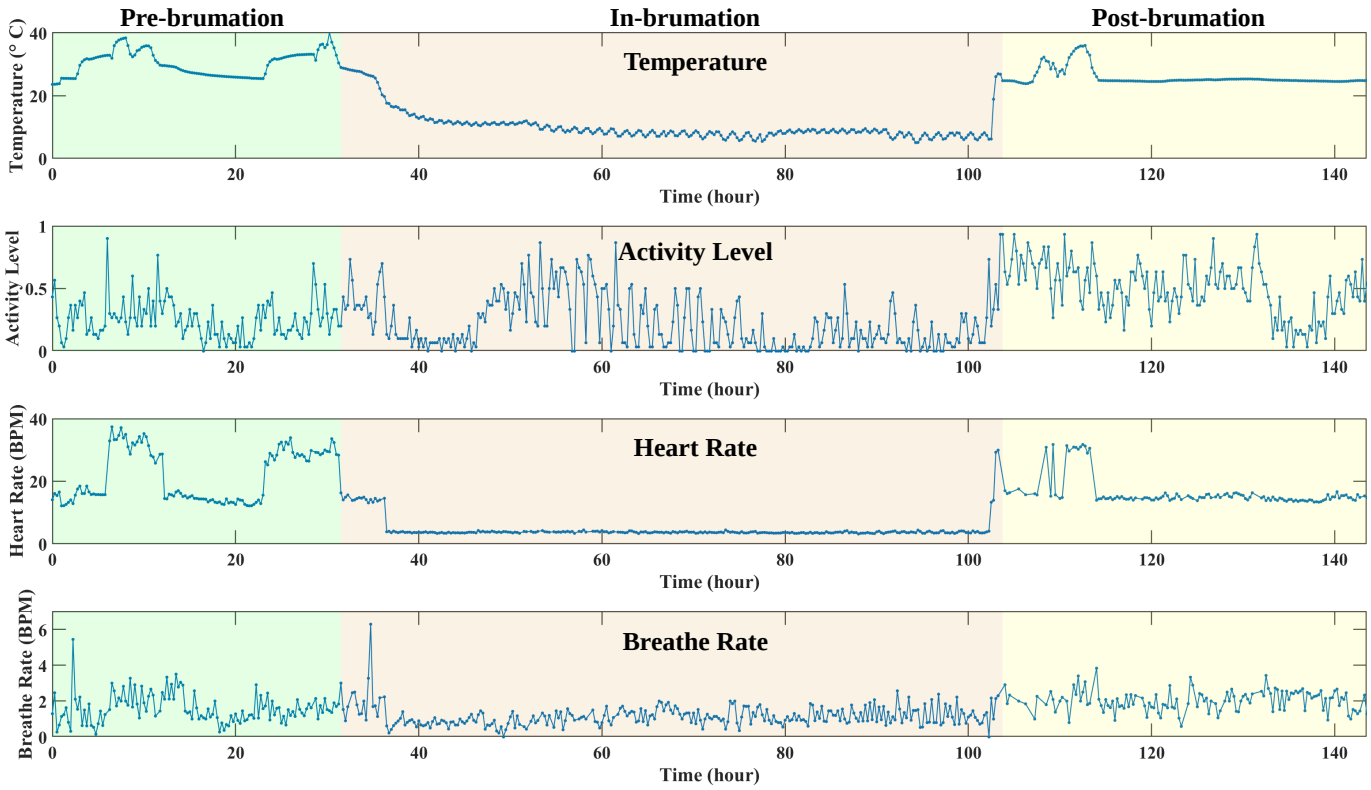

Fig. 8. The shell temperature, activity level, heart and breathe rates over the entire brumation cycle. The green, beige and yellow regions indicate the pre-, in- and post-brumation phases, respectively.

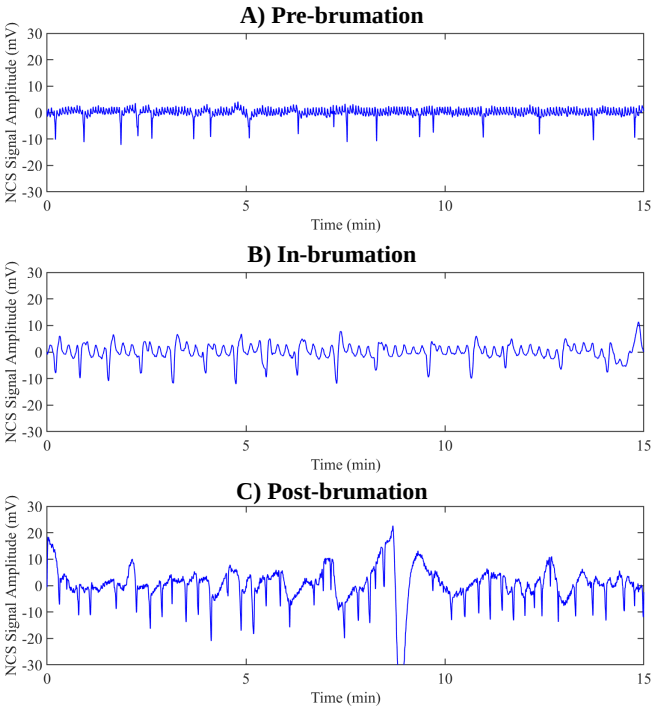

Fig. 9. 15-min vital-sign recording during (A) pre-brumation; (B) in-brumation; (C) post-brumation

are shown in Table. II. We can see that AL does not strongly depend on temperature which renders a low correlation value. During brumation, the tortoise was not in the motionless deep-sleep status, as in mammal hibernation cases [6]. It can wake up instantly and move a little, when it needs water or get stimulated by noise, smell or contact. We can also observe that the heart rate is strongly correlated to the temperature and can change significantly from 37 beats per minute (BPS) when the temperature is around 38 °C, and stays at 3 to 4 BPS during brumation when the temperature is below 10 °C. However, the correlation between the respiration rate and the temperature is not as strong, as shown in Table. II, although we can still observe a lower average respiration rate during brumation from Figure. 8. This could be because the normal respiration rate is already low, or because all chambers are ventilated without CO_2 control. Moreover, neither the breath rate nor heart rate correlates strongly to AL, with the correlation coefficients of 0.29 and 0.33, respectively.

Furthermore, we took a 24-hour heart and breath rate recording from in-brumation (60^{th} to 84^{th} hour) and post-brumation (120^{th} to 144^{th} hour) and calculated their mean and standard deviation (STDev), as shown in Table. III. We can see that the tortoise has a higher average heart and breath rates in post-brumation than in-brumation. The breath rate has a larger relative variation than the heart rate for both in- and post-brumation. However, both heart and breath rates have a relative stable variation during the in- and post-brumation. This indicates that this vital-sign variation does not have a strong dependence on temperature. Thus, we can apply some smoothing method to reduce the variation especially for the breath rate. After applying a 4-point moving average on the

Vital-sign	Correlation coefficient
Activity level	0.34
Heart rate	0.92
Breath rate	0.45
Breathe rate with 4-point moving average	0.60

TABLE II
CORRELATION COEFFICIENTS BETWEEN THE SHELL TEMPERATURE AND VITAL-SIGNS FOR THE ENTIRE BRUMATION CYCLE

Vital-sign	In-brumation		Post-brumation	
	Mean	STDev	Mean	STDev
Breath rate (BPM)	1.21	0.40	2.03	0.57
Heart rate (BPM)	3.64	0.21	14.71	0.82

TABLE III
MEAN AND STANDARD DEVIATION FOR THE HEART AND BREATH RATES DURING THE PERIODS OF 60^{TH} - 84^{TH} HOUR AND 120^{TH} - 144^{TH} HOUR

breath rate, we can see a larger correlation between the breath rate and temperature, as shown in Table. II.

VI. CONCLUSION

In this paper, a wireless wearable vital-sign sensor based on NCS is presented for long-term continuous monitoring of a tortoise with a unique body structure. This sensor is light-weight and low-power, and thus would cause the least disturbance to chelonian brumation cycles. The system can be potentially applied to other small animals, especially reptiles, which is a new capability to study the circadian rhythm entering to, remaining in and waking up from brumation. The long-term continuous vital-sign recording on the entire brumation cycle here has never been presented before. Experimental results also showed that the tortoise heart rate has a higher correlation to temperature than the breath rate or activity level does. Future work will include further sensor miniaturization, more robust algorithms to detect breathing peaks accurately, and to measure motion directly with accelerometers. Also, more testing cases are needed to solidify the statistical conclusion.

ACKNOWLEDGMENT

The animal experiments are under Cornell IACUC Protocol 2018-0034. This project is supported by US Army Discovery Award through the CDMRP Program PR182496 and by US Department of Energy ARPA-E Project DE-AR0000946.

REFERENCES

[1] C. M. Williams, A. Szejner-Sigal, T. J. Morgan, A. S. Edison, D. B. Allison, and D. A. Hahn, "Adaptation to low temperature exposure increases metabolic rates independently of growth rates," *Integrative and comparative biology*, vol. 56, no. 1, pp. 62–72, 2016.

[2] W. Zuo, M. E. Moses, G. B. West, C. Hou, and J. H. Brown, "A general model for effects of temperature on ectotherm ontogenetic growth and development," *Proc. Royal Society B: Biological Sciences*, vol. 279, no. 1734, pp. 1840–1846, 2012.

[3] T. D. Clark, P. Butler, and P. B. Frappell, "Factors influencing the prediction of metabolic rate in a reptile," *Functional Ecology*, vol. 20, no. 1, pp. 105–113, 2006.

[4] J. F. Staples, "Metabolic flexibility: hibernation, torpor, and estivation," *Comprehensive Physiology*, vol. 6, no. 2, pp. 737–771, 2011.

[5] M. Jastroch, S. Giroud, P. Barrett, F. Geiser, G. Heldmaier, and A. Herwig, "Seasonal control of mammalian energy balance: recent advances in the understanding of daily torpor and hibernation," *J. neuroendocrinology*, vol. 28, no. 11, 2016.

[6] C. P. Lyman, *Hibernation and torpor in mammals and birds*. Elsevier, 2013.

[7] P. K. Theil, A. E. Coutant, and C. R. Olesen, "Seasonal changes and activity-dependent variation in heart rate of roe deer," *J. mammalogy*, vol. 85, no. 2, pp. 245–253, 2004.

[8] S. Els, T. Erasmus, and P. Winter, "Heating and cooling rates and their effects upon heart rate in the angulate tortoise, chersina angulata," *South African J. Zoology*, vol. 23, pp. 231–234, 01 1988.

[9] S. B. Munch and S. Salinas, "Latitudinal variation in lifespan within species is explained by the metabolic theory of ecology," *Proc. National Academy of Sciences*, vol. 106, no. 33, pp. 13 860–13 864, 2009.

[10] A. I. Petrov and M. V. Razuvaeva, "Effect of temperature on metabolism and lifespan in several homeothermic animals," *Technical Physics*, vol. 63, no. 10, pp. 1410–1414, 2018.

[11] J. R. Speakman, "Body size, energy metabolism and lifespan," *J. Experimental Biology*, vol. 208, no. 9, pp. 1717–1730, 2005.

[12] J. Nowack, C. Stawski, and F. Geiser, "More functions of torpor and their roles in a changing world," *J. Comparative Physiology B*, vol. 187, no. 5-6, pp. 889–897, 2017.

[13] M. Luscombe and J. C. Andrzejowski, "Clinical applications of induced hypothermia," *Continuing Education in Anaesthesia Critical Care & Pain*, vol. 6, no. 1, pp. 23–27, 2006. [Online]. Available: https://doi.org/10.1093/bjaceaccp/mki064

[14] M. Braddock, "Concepts for deep space travel: from warp drives and hibernation to world ships and cryogenics," *Current Trends in Biomedical Engineering & Biosciences*, vol. 12, no. 5, 2018.

[15] C. A. Nordeen and S. L. Martin, "Engineering human stasis for long-duration spaceflight." *Physiology (Bethesda, Md.)*, vol. 34, no. 2, pp. 101–111, 2019.

[16] M. Schaffer, J. Bradford, and D. Talk, "A feasible, near-term approach to human stasis for long-duration deep space missions," in *67th International Astronautical Congress (IAC), Guadalajara, Mexico*, 2016, pp. 1–17.

[17] D. Malley, "Reptile anaesthesia and the practising veterinarian," *In Practice*, vol. 19, no. 7, pp. 351–368, 1997. [Online]. Available: https://inpractice.bmj.com/content/19/7/351

[18] M. Kirchgessner and M. Mitchell, *Chelonians*. Elsevier Inc., 12 2009, pp. 207–249.

[19] T. M. Norton, "Chelonian emergency and critical care," *Seminars in Avian and Exotic Pet Medicine*, vol. 14, no. 2, pp. 106 – 130, 2005.

[20] B. P. Monitoring, "Monitoring vital signs in clinical and research animals," *Current Separations*, vol. 16, no. 2, p. 44, 1997.

[21] C. Li, Z. Peng, T. Huang, T. Fan, F. Wang, T. Horng, J. Muñoz-Ferreras, R. Gómez-García, L. Ran, and J. Lin, "A review on recent progress of portable short-range noncontact microwave radar systems," *IEEE Transactions on Microwave Theory and Techniques*, vol. 65, no. 5, pp. 1692–1706, May 2017.

[22] J.-M. Muñoz-Ferreras, Z. Peng, R. Gómez-García, and C. Li, "Review on advanced short-range multimode continuous-wave radar architectures for healthcare applications," *IEEE J. Electromagnetics, RF and Microwaves in Medicine and Biology*, vol. 1, no. 1, pp. 14–25, 2017.

[23] J. C. Lin, "Noninvasive microwave measurement of respiration," *Proc. IEEE*, vol. 63, no. 10, pp. 1530–1530, Oct 1975.

[24] X. Ma, Y. Wang, X. You, J. Lin, and L. Li, "Respiratory pattern recognition of an adult bullfrog using a 100-ghz cw doppler radar transceiver," in *2019 IEEE MTT-S International Microwave Biomedical Conference (IMBioC), Nanjing, China*, vol. 1, May 2019, pp. 1–3.

[25] T. Huang, L. F. Hayward, and J. Lin, "Noninvasive measurement and analysis of laboratory rat's cardiorespiratory movement," *IEEE Transactions on Microwave Theory and Techniques*, vol. 65, no. 2, pp. 574–581, Feb 2017.

[26] G. Wang, J.-M. Muñoz-Ferreras, C. Gu, C. Li, and R. Gómez-García, "Linear-frequency-modulated continuous-wave radar for vital-sign monitoring," in *2014 IEEE Topical Conference on Wireless Sensors and*

Sensor Networks (WiSNet), Newport Beach, CA, USA, Jan 2014, pp. 37–39.
[27] Z. Peng, J. Muñoz-Ferreras, Y. Tang, R. Gómez-García, and C. Li, "Portable coherent frequency-modulated continuous-wave radar for indoor human tracking," in *2016 IEEE Topical Conference on Biomedical Wireless Technologies, Networks, and Sensing Systems (BioWireleSS), Austin, TX, USA*, Jan 2016, pp. 36–38.
[28] F. Adib, H. Mao, Z. Kabelac, D. Katabi, and R. C. Miller, "Smart homes that monitor breathing and heart rate," in *Proc. 33rd Annual ACM Conference on Human Factors in Computing Systems, Seoul, Republic of Korea*, 2015, pp. 837–846.
[29] B. Schleicher, I. Nasr, A. Trasser, and H. Schumacher, "Ir-uwb radar demonstrator for ultra-fine movement detection and vital-sign monitoring," *IEEE Transactions on Microwave Theory and Techniques*, vol. 61, no. 5, pp. 2076–2085, 2013.
[30] A. Lazaro, D. Girbau, and R. Villarino, "Analysis of vital signs monitoring using an ir-uwb radar," *Progress In Electromagnetics Research*, vol. 100, pp. 265–284, 2010.
[31] S. K. Leem, F. Khan, and S. H. Cho, "Vital sign monitoring and mobile phone usage detection using ir-uwb radar for intended use in car crash prevention," *Sensors*, vol. 17, no. 6, p. 1240, 2017.
[32] L. Ren, H. Wang, K. Naishadham, Q. Liu, and A. E. Fathy, "Noninvasive detection of cardiac and respiratory rates from stepped frequency continuous wave radar measurements using the state space method," in *2015 IEEE MTT-S International Microwave Symposium, Phoenix, AZ, USA*. IEEE, 2015, pp. 1–4.
[33] L. Ren, L. Kong, F. Foroughian, H. Wang, P. Theilmann, and A. E. Fathy, "Comparison study of noncontact vital signs detection using a doppler stepped-frequency continuous-wave radar and camera-based imaging photoplethysmography," *IEEE Transactions on Microwave Theory and Techniques*, vol. 65, no. 9, pp. 3519–3529, 2017.
[34] X. Hui and E. C. Kan, "Monitoring vital signs over multiplexed radio by near-field coherent sensing," *Nature Electronics*, vol. 1, no. 1, pp. 74–78, 2018.
[35] X. Hui and E. C. Kan, "No-touch measurements of vital signs in small conscious animals," *Science Advances*, vol. 5, no. 2, p. eaau0169, 2019.
[36] C. Leone. How to brumate a tortoise. [Online]. Available: http://www.reptilesmagazine.com/How-To-Brumate-A-Tortoise/
[37] P. Sharma and E. C. Kan, "Sleep scoring with a uhf rfid tag by near field coherent sensing," in *2018 IEEE/MTT-S International Microwave Symposium - IMS, Philadelphia, PA, USA*, June 2018, pp. 1419–1422.

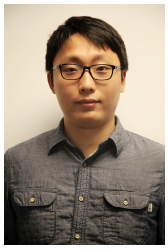

Jianlin Zhou received the B.S. degree in electronics and information engineering from Nanjing University of Science and Technology, Nanjing, China in 2013, and the M.S. degree in electrical and computer engineering from Northeastern University, Boston, MA in 2016. He is currently pursuing the Ph.D. degree in electrical and computer engineering at Cornell University, Ithaca, NY, USA.

He has previously worked as a research support associate on ingestible electronics design for drug delivery and bio-sensing in Robert Langer Lab at Massachusetts Institute of Technology from November 2016 to May 2018. His research interests include radio frequency, vital signs monitoring, wearable biomedical sensor design and electromagnetic near-field coupling system optimization

Pragya Sharma received the B.Tech. degree in electrical engineering from Indian Institute of Technology (IIT) Kharagpur, India, in 2015. She is currently pursuing the Ph.D. degree in electrical engineering at Cornell University, Ithaca, NY, USA.

Xiaonan Hui received the B.S. degree from Northeastern University, China in 2012, and the M.S. degree from Zhejiang University, China in 2015, all in electrical engineering. He is currently pursuing the Ph.D. degree in electrical and computer engineering at Cornell University, Ithaca, NY, USA.

Edwin C Kan received the B.S. degree from National Taiwan University in 1984, and the M.S. and Ph.D. degrees from the University of Illinois at Urbana Champaign in 1988 and 1992, respectively, all in electrical engineering. In 1992, he joined Dawn Technologies as a Principal CAD Engineer. He was then with Stanford University, as a Research Associate from 1994 to 1997. Since 1997, he has been a Professor with the School of Electrical and Computer Engineering, Cornell University, Ithaca, NY, USA.

Appendix K

(PDF downloaded from IEEE) X. Hui, J. Zhou and E. C. Kan, “High-volume parallel mouse vital-sign monitoring with near-field coherent sensing”, *IEEE Antenna and Wireless Propagation Letters*, doi: 10.1109/ LAWP.2020.2992055, 2020.

This article has been accepted for publication in a future issue of this journal, but has not been fully edited. Content may change prior to final publication. Citation information: DOI 10.1109/LAWP.2020.2992055, IEEE Antennas and Wireless Propagation Letters

High-Volume Parallel Mouse Vital-Sign Monitoring with Near-Field Coherent Sensing

Xiaonan Hui, *Student Member, IEEE*, Jianlin Zhou and Edwin C. Kan, *Senior Member, IEEE*

***Abstract*—Mouse vital signs such as the heartbeat and respiration rates are critical observables for the current biomedical and pharmaceutical researches. The number of mice going through the measurement pipeline often needs to be massive to derive statistically significant correlation. However, present mouse vital-sign monitoring methods require substantial individual handling and have limited throughput per setup. In this work, we demonstrated for the first time a parallel mouse vital-sign reading system, which can simultaneously retrieve the respiration and heartbeat rates for multiple mice in individual chambers with minimal non-invasive handling. The cardio signal quality is high enough to estimate the stress states by the heart rate variation analyses. Our system utilizes the multiplexed radio frequency (RF) signal around 1.8 GHz to detect the vital signs by near-field coherent sensing (NCS). The cross-chamber interference is minimized by the locality of near fields, frequency division and radar absorbing materials. The isolation can be readily more than 20 dB within a compact system volume. Our scalable design clearly shows how to achieve a high-throughput system for mouse vital-sign monitoring.**

***Index Terms*— Animal vital signs; biomedical signal processing; cardiography; microwave sensors.**

I. Introduction

MONITORING of mouse vital signs such as the respiration and heartbeat rates are critical for the behavioral, biomedical and pharmaceutical researches where mice are used as the mammal model. Statistically reliable results often require a plethora of measurements to derive conclusions with high confidence, where the overall testing throughput becomes an important cost factor. Conventional electrocardiogram (ECG) and photo-plethysmography (PPG) for the heart rate are however problematic to apply to animals with various surface coverings, especially for the small laboratory mice. To adapt ECG and PPG to a mouse, its body hair often needs to be removed to provide good skin access [1,2], or small areas of the ventral soles are accessed by conducting gels or by chance [3]. Furthermore, anesthesia is commonly applied to reduce the motion interference in order to increase the yield rate and improve the signal quality [4,5]. The discomfort after hair removal and neural disruption from anesthetics would inevitably introduce biases in the heart rate [6,7] with an unknown interference effect to the factor under investigation. Alternatively, the sensing electrodes or probes can be implanted, which will further complicate the procedure and increase the cost [5,8]. In researches involving vaccine and therapeutics development for highly restricted pathogens, any additional procedures to the animal will significantly raise the risk and overall experimental difficulties [9,10]. Breath rates can be estimated by optical or infrared cameras [11,12], as long as the mouse can remain motionless to reduce motion artifact and the camera sampling rate is higher than about 40 Hz to avoid aliasing of the respiration signal around 2 – 6 Hz. To counter these difficulties, non-contact vital-sign acquisition methods such as various kinds of radar systems had been developed [13,14]. In order to capture the minute heartbeat motion of the rodent, the millimeter-wave system was employed, although it is only sensitive enough for the larger rats [14,15]. Nevertheless, the parallel cost-effective measurement of vital signs remains unavailable.

In this work, we demonstrate an ultra-high-frequency (UHF) radio-frequency (RF) system for vital-sign monitoring of multiple mice in parallel based on commercial software-defined radios (SDR). The heartbeat and respiration waveforms can be simultaneously retrieved from different mice with minimal interference in the compact setup. The present 4-chamber configuration can be scaled up in the future to satisfy the need in high-throughput testing systems.

II. System Design and Simulation

The vital-sign sensor is based on the principle of near-field coherent sensing (NCS) [16,17]. When the sensing antenna is deployed closely to the target area within the chosen near field, a substantial amount of RF energy will be coupled into the living tissue. The internal organ motion such as heartbeat and respiration can be thought as part of the antenna characteristics and will be modulated on the amplitude of the received RF signal, which can be multiplexed in frequency and/or in code division to reduce interference [18,19]. The transceiver schematic is shown in Fig. 1(a), which is implemented by a commercial SDR (Ettus B210). The transmitter (Tx) of the SDR is connected to the Tx sensing antenna built in the mouse restrainer box. The modulated RF signal is then received by the receiver (Rx) antenna also built in the box, feeding to the SDR Rx through a bandpass filter (BPF). The Tx baseband signal is formulated in the field-programmable gate array (FPGA) and then converted by the digital-to-analog converter (DAC), which

This project is supported by the Department of Defense of the United States through Office of the Congressionally Directed Medical Research Programs (CDMRP) Discovery Award PR-182496.

X. Hui, J. Zhou and E. C. Kan are with Cornell University, Ithaca, NY 14853, USA. E-mails: {xh273, jz899, eck5}@cornell.edu.

1536-1225 (c) 2020 IEEE. Personal use is permitted, but republication/redistribution requires IEEE permission. See http://www.ieee.org/publications_standards/publications/rights/index.html for more information.
Authorized licensed use limited to: Cornell University Library. Downloaded on July 03,2020 at 23:04:54 UTC from IEEE Xplore. Restrictions apply.

This article has been accepted for publication in a future issue of this journal, but has not been fully edited. Content may change prior to final publication. Citation information: DOI 10.1109/LAWP.2020.2992055, IEEE Antennas and Wireless Propagation Letters

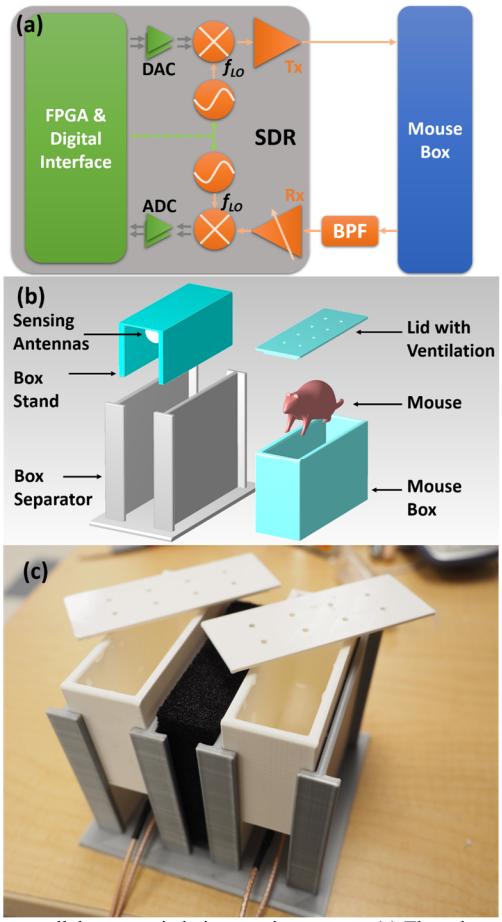

Fig. 1. The parallel mouse vital-sign sensing system. (a) The schematics of the RF sensing unit. (b) The assembly view of the mouse restrainer box. (c) The picture of the two-chamber unit with in-between RF isolation.

is further mixed up with the local oscillating (LO) signal f_{LO} at 1.8 GHz and amplified to 0 dBm. At the Rx end, the received signal is first amplified by the tunable-gain low-noise amplifier (LNA), down-converted by the same LO, and then sampled by the analog-to-digital converter (ADC). The digital signal is processed by FPGA to formulate the sensing data, which are finally downloaded to the computer through the universal serial bus (USB) port. The assembly view of the mouse restrainer box is shown in Fig. 1(b), and the picture of a two-chamber unit with radar-absorbing material (RAM) isolation in Fig. 1(c). The sensing antennas are housed underneath the box stand, which is inserted into the box separator. Two monopole antennas (Taoglas TG.19.0112) are mounted on a 3D-printed holder as the sensing antenna pair [20] which is directly under the mouse chamber. The overall dimensions are 69 × 17 × 11 mm (W × L× D). The operating frequency is around 1.82 GHz with a bandwidth of 40 MHz. One of the monopole antennas is connected to Tx of the transceiver and the other is connected to Rx to receive the vital-sign modulated RF signal. We use the monopole antennas with broad bandwidth here, so that the system will have better tolerance to the antenna frequency shift caused by the presence of the mouse in the near field. The box assembly is 3D-printed (Ultimaker 3) with the polylactic acid (PLA) material. The mice under test will be put inside the individual chambers with the ventilated lid cover. The internal dimensions of the mouse box are 93×30×60 mm (L×W×H). The

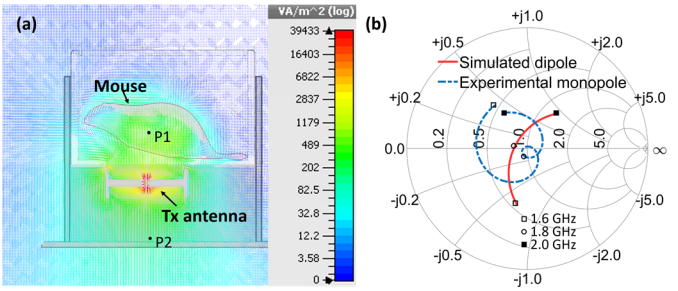

Fig. 2. (a) The CST simulation of the RF power flow in the mouse box with a single dipole Tx antenna. The presence of the mouse makes the power distribution to be asymmetric in the positions of P1 and P2. (b) Antenna S_{11} with respect to the frequency in the Smith chart. The red curve is from CST simulation for the single dipole Tx antenna, and the blue curve is the measurement of the Tx antenna reflection when two monopole antennas are used for Tx and Rx.

setup geometry is imported into CST Microwave Studio [21] to verify the near-field coupling. Fig. 2 shows the simulation results of the RF power flow from a dipole Tx antenna as an illustration of near-field coupling into living tissues. The electromagnetic material properties are configured according to the CST library. The mouse is simulated by a homogeneous tissue model with an approximate geometry. As shown in Fig. 2(b), the simulated Tx dipole antenna operates at 1.8 GHz with 100 MHz bandwidth where the antenna S_{11} (red curve) is less than −15 dB with consideration of the ambient dielectric properties [22]. In the simulation the antenna is fed by the discrete port in CST Studio with the default 1 W^{-2} input and 50-Ohm impedance match. From the simulation results in Fig. 2, significant amount of RF power is coupled into the mouse body in comparison with outside the box. For example, the power flow at Point 1 (P1) is at 482 VA/m^2, which is much higher than that of Point 2 (P2) at 72 VA/m^2, especially considering the symmetric radiation pattern of the dipole antenna in free space. As the antenna characteristics are more dominated by the dielectric ambient with higher energy coupling, the dielectric boundary motion inside the living tissue will dominate over motion outside the box in the NCS operation. S_{11} of the Tx antenna of the experimental monopole antenna pair (blue curve) was measured by the vector network analyzer (Keysight E5063A), where we can see that the antenna remained well matched around 1.8 GHz in the presence of the mouse. When the mouse respiration and heartbeats are represented by the dielectric boundary motion within the near-field path of the Tx-to-Rx signal, the phase of that part of the signal will be modulated. The total Rx signal will contain both the modulated and unmodulated parts from the same Tx, and hence its magnitude can be used to derive the vital-sign information after carrier demodulation [16]. In comparison with the far-field radar sensing system which mostly depends on the body surface reflection, the near-field energy in NCS directly couple into the internal organ motion and hence can give higher sensitivity and signal-to-noise ratio (SNR) at the same RF band.

The black foam inserted between the two chambers in Fig. 1(c) is the lossy RAM (Mast Technologies, MF22-0009-00), which can provide around 43 dB insertion loss at the UHF band. The SDR by Ettus B210 used in this work has 2 Tx and 2 Rx ports, which can support two vital-sign sensors simultaneously. Frequency division multiple access (FDMA) is used to provide

1536-1225 (c) 2020 IEEE. Personal use is permitted, but republication/redistribution requires IEEE permission. See http://www.ieee.org/publications_standards/publications/rights/index.html for more information.
Authorized licensed use limited to: Cornell University Library. Downloaded on July 03,2020 at 23:04:54 UTC from IEEE Xplore. Restrictions apply.

This article has been accepted for publication in a future issue of this journal, but has not been fully edited. Content may change prior to final publication. Citation information: DOI 10.1109/LAWP.2020.2992055, IEEE Antennas and Wireless Propagation Letters

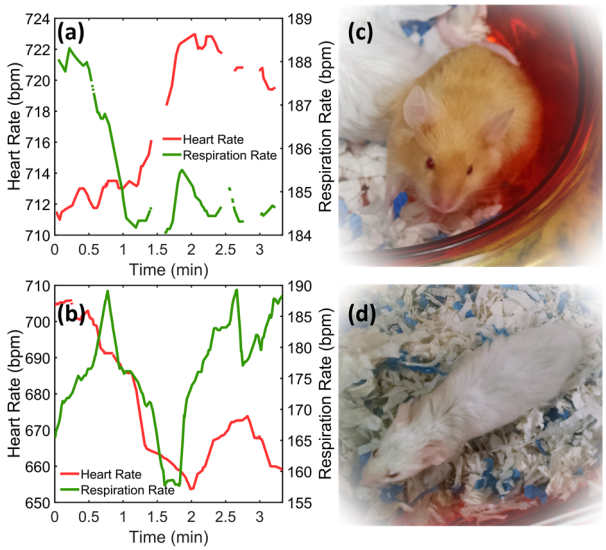

Fig. 3. The recording of the heartbeat and respiration rates from the 2-channel sensing system for two mice. (a) The heartbeat (red) and respiration (green) rates of Mouse 1. (b) The vital signs of Mouse 2. (c) The photo of Mouse 1. (d) The photo of Mouse 2.

isolation between the channels [17,18], and code division multiple access (CDMA) can be employed for larger systems [19,23]. Because the two Tx of the SDR share the same LO, FDMA can only be implemented by applying different baseband frequencies rather than two independent carriers by different f_{LO}. In order to reduce the digital data bandwidth, the sampling rate of 2 MSps (million samples per second) is applied to both DACs and ADCs. The baseband frequencies are set at 377 kHz and 531 kHz for the two sensing channels, respectively. The baseband frequency selection should consider the LO phase noise, the DAC and ADC jitters, and the frequency separation for the digital filter design [24].

III. Experimental Results

Two mice are put into their individual boxes. When the mice calmed down and stayed reasonably stable after about 1 minute, their vital signs are recorded and analyzed for the next period around 3 minutes. The signals are processed in LabVIEW in real-time. Because FDMA is used to distinguish the two sensing channels, two 3rd-order infinite impulse response (IIR) digital filters with 10 kHz bandwidth and the center frequencies of 377 kHz and 531 kHz are employed as the demultiplexer to extract the corresponding signals. The baseband signals are then down sampled to 20 kSps, followed by a low-pass filter with the cut-off frequency of 200 Hz and then further down sampled to 2 kSps. After a bandpass filter with 2–25 Hz passband, the signals go through the windowed fast Fourier transform (FFT). The 20 kSps sampled signals are recorded as the raw data for analysis and the 2 kSps sampled signals are for the waveform display. A 10-second square sliding window is chosen to calculate the heart rate (red) and the respiration rate (green), as shown in Fig. 3. The results in Figs. 3(a) and 3(b) were from Mouse 1 in Fig. 3(c) and Mouse 2 in Fig. 3(d), respectively. The averaged heart rate and respiration rate of Mouse 1 are 715.4 beats per minute (bpm) and 186.3 breaths per minute (bpm), and Mouse 2 are 670.1 bpm and 173.2 bpm, respectively. Estimation of both rates can be interrupted by fast strong body motion, which resulted in the discontinuities on the curves shown in Fig. 3. When the real-time algorithm detects strong interferences based on the spectrum clarity and number of peaks, the polluted period will be annotated with the associated data disregarded. In the algorithm the signals need to meet two criteria to be regarded as valid. First, the number of the spectral peaks above a certain threshold within the bands of respiration and heartbeat needs to be equal to or less than two. Second, the standard deviation of the time-domain signals within the sliding window needs to be below the thresholds of the stable signals after removal of the DC biases. The two threshold values are dynamically tuned according to the signal strength.

NCS couples more RF energy to the sensing area of interest by the near-field effect. At the selected UHF frequency, our system can retrieve not only the heart and respiration rates, but also their waveforms in the time domain when the motion interference is not dominant. Fig. 4 shows an example of the 1-second heartbeat and respiration waveforms around the end of the 1st minute, where Fig. 4(a) corresponds to Mouse 1 and Fig. 4(b) to Mouse 2. The recoil after the main peak caused by ventricles and atriums motions on the heartbeat waveform in Fig. 4(a) can be repeatedly observed. Comparing to extracting the heart rate from FFT or other spectrum-based methods such as wavelets [21,25], time-domain cardiograms require higher system SNR and can be used to evaluate the intervals of individual heartbeats and the heart rate variability (HRV), which can potentially offer more physiological and emotional information [26,27]. We employed the root mean square of the successive differences (RMSSD) to calculate HRV [28], where the HRV is 2 ms of the heartbeat data in Fig. 3(a) and 4.5 ms of the heartbeat data in Fig. 3(b). Furthermore, the low-frequency (LF) and high-frequency (HF) bands in HRV, which are related to the sympathetic (SNS) and parasympathetic (PNS) nervous system activities, can be applied to interpret the stress level

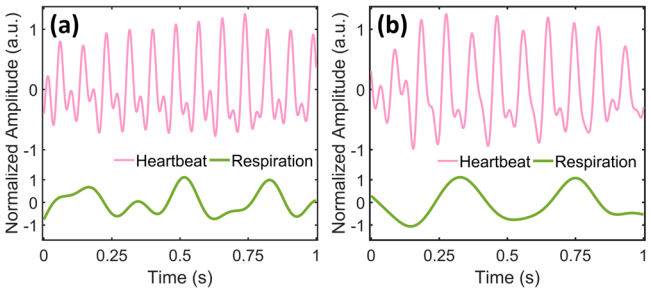

Fig. 4. The cardiogram and respiration waveforms of (a) Mouse 1 and (b) Mouse 2.

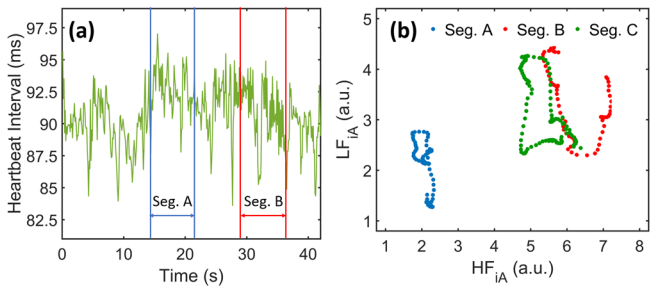

Fig. 5. (a) The heartbeat interval of Mouse 2 around 1.5 minutes in Fig. 3(b). (b) The stress evaluation scatter points of Mouse 2 by LF and HF bands.

1536-1225 (c) 2020 IEEE. Personal use is permitted, but republication/redistribution requires IEEE permission. See http://www.ieee.org/publications_standards/publications/rights/index.html for more information.
Authorized licensed use limited to: Cornell University Library. Downloaded on July 03,2020 at 23:04:54 UTC from IEEE Xplore. Restrictions apply.

This article has been accepted for publication in a future issue of this journal, but has not been fully edited. Content may change prior to final publication. Citation information: DOI 10.1109/LAWP.2020.2992055, IEEE Antennas and Wireless Propagation Letters

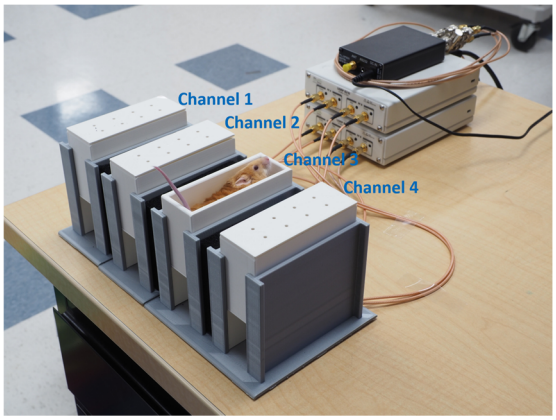

Fig. 6. The 4-channel parallel mice vital-sign acquisition system with two SDRs driven by the same external clock source for synchronization.

[29]. The heartbeat intervals of Mouse 2 around 1.5 minutes in Fig. 3(b) are extracted in Fig. 5(a). The heart rate was smoothly decreasing during this period, but the respiration rate changed dramatically. Segment A and Segment B were chosen for stress evaluation by the following steps. The heartbeat interval is decomposed by empirical mode decomposition (EMD) [30,31], where the first two intrinsic-mode functions are regarded as the HF and LF signals, where are further processed by the Hilbert transform. The instantaneous amplitudes of HF (HF_{iA}) and LF (LF_{iA}) are then employed to construct the scatter plot of Fig. 5(b) for stress evaluation [28]. The blue points are derived from Segment A and the red points from Segment B. The data from the two segments are less than 10 seconds apart, but the scatter points are well separated, which implies that SNS and PNS interacted during these periods. We also conduct the same procedure to another data set denoted as Segment C around 2.5 minutes in Fig. 3(b). The results are shown as the green points in Fig. 5(b), where the stress status can be identified to be close to that of Segment B.

Because NCS is more sensitive to the local area within the near-filed zone of the sensing antennas, the system can be further expanded with compact size and low cross-chamber interference. For scaling demonstration, we built a 4-chamber system as shown in Fig. 6. Four sensing channels are built by two Ettus B210 SDRs, which are synchronized by an external reference clock (the black module on top by BG7TBL-GPSDO), providing a 10-MHz signal for carrier synchronization and 1 pulse-per-second (PPS) signal for baseband synchronization. In this implementation, carrier synchronization is not essential, but baseband synchronization is recommended for better system timing accuracy, especially for further scaling or multi-modal sensor recording. For example, when CDMA is chosen to expand the number of parallel measurements, high baseband synchronization is important to reduce cross-channel interference. We measured the channel isolation performance in the 4-channel setup where a mouse was put into Chamber 3 as shown in Fig. 6. The box lid remained closed during the measurements. Other boxes were left empty. The 4-channel data were recorded and analyzed simultaneously, where all spectra were plotted in Fig. 7 after applying a bandpass filter of 2 – 25 Hz. The result with the RAM isolation is in Fig. 7(a), and without in Fig. 7(b). In Fig. 7(a), the spectral peaks of the respiration (4.3 Hz) and the

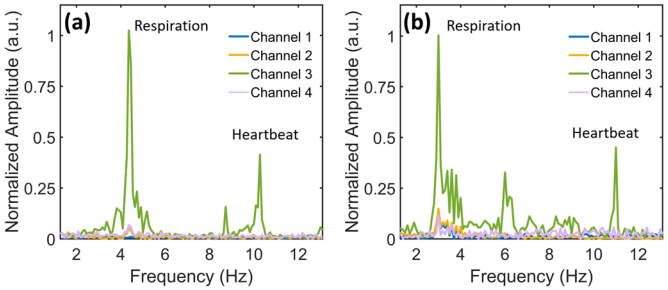

Fig. 7. Multi-channel crosstalk in the 4-channel system when a mouse was put in Chamber 3 and other chambers were empty: (a) With the RAM isolation between the chambers; (b) Without the RAM isolation.

heartbeat (10.1 Hz) are clear from Channel 3 (green). The respiration motion is strong to cause nonlinearity in modulation, and its 2nd harmonic has shown a peak around 8.6 Hz. The results from the adjacent channels, Channels 2 (yellow) and 4 (purple), show very small crosstalk from the respiration of the mouse in Chamber 3 by more than 20 dB reduction, and the heartbeat crosstalk is below the noise floor. The crosstalk from Channel 1 (blue) is negligible even for respiration. Not only FDMA in this system provides effective channel isolation, but also near-filed coupling is weaker when the sensing area is further away. When the RAM isolation is removed, the crosstalk in Channels 2 and 4 increases to −16 dB but remains tolerable, as shown in Fig. 7(b). The heartbeat interference is still unobservable.

IV. Discussion and Conclusion

We have used the monopole antenna pair in the experimental demonstration. The patch antennas with narrower beams had also been investigated, as intuitively the focused beam can improve cross-chamber isolation and provide higher gain. The result was however a mixed trade-off instead of direct benefit. The high-gain patch antenna also often has a narrower bandwidth which can be more vulnerable to antenna detuning. As the mouse position inside the chamber is not strictly fixed, the change in position can result in significant gain variation which makes the waveform processing for rate evaluation more ambiguous. Hence, the better isolation across the chambers from the focused beam actually comes at the price of reliable data retrieval. Since our design already has very good cross-chamber isolation as shown in Fig. 7, we opt to use the antenna with broader bandwidth in the practical system design.

In this work, we demonstrated for the first time a scalable sensing system with the capability of parallel vital-sign recording of multiple mice without complicated preparation procedures. We utilized the NCS operation, which not only provided better SNR performance, but also the necessary isolation between the mouse boxes. The high signal quality enables nearly continuous extraction of the heartbeat and respiration rates, as well as extraction of HRV for stress evaluation. Our system does not employ the high-frequency millimeter wave to improve the sensitivity, and can be implemented cost effectively in large commercial systems with high testing throughput.

1536-1225 (c) 2020 IEEE. Personal use is permitted, but republication/redistribution requires IEEE permission. See http://www.ieee.org/publications_standards/publications/rights/index.html for more information.
Authorized licensed use limited to: Cornell University Library. Downloaded on July 03,2020 at 23:04:54 UTC from IEEE Xplore. Restrictions apply.

This article has been accepted for publication in a future issue of this journal, but has not been fully edited. Content may change prior to final publication. Citation information: DOI 10.1109/LAWP.2020.2992055, IEEE Antennas and Wireless Propagation Letters

REFERENCES

[1] P. P. Pereira-Junior *et al.*, "Noninvasive method for electrocardiogram recording in conscious rats: feasibility for heart rate variability analysis," *Anais da Academia Brasileira de Ciências*, vol. 82, pp. 431–437, June 2010.

[2] J. Allen, "Photoplethysmography and its application in clinical physiological measurement," *Physiological Measuremen*t, vol. 28, pp. R1, Feb. 2007.

[3] Online: https://mousespecifics.com/heart-monitoring/ecgenie/

[4] L. Tilley and N. Burtnick, *ECG for the small animal practitioner*, Teton NewMedia, 2009.

[5] D. Ho *et al.*, "Heart rate and electrocardiography monitoring in mice," *Current Protocols in Mouse Biology*, vol. 1, pp. 123–139, Mar. 2011.

[6] C. Constantinides, R. Mean and B. J. Janssen, "Effects of isoflurane anesthesia on the cardiovascular function of the C57BL/6 mouse," *ILAR journal/National Research Council, Institute of Laboratory Animal Resources*, vol. 52, pp. e21, 2011.

[7] A. A. Chaves *et al.*, "Age and anesthetic effects on murine electrocardiography. Life sciences," *Life Sciences*, vol. 72, pp. 2401–2412, Apr. 2003.

[8] N. Cesarovic *et al.*, "Implantation of radiotelemetry transmitters yielding data on ECG, heart rate, core body temperature and activity in free-moving laboratory mice," *J. Visualized Experiments*, vol. 57, pp. e3260, Nov. 2011.

[9] A. Marzi and H. Feldmann, "Ebola virus vaccines: an overview of current approaches," *Expert Review of Vaccines*, vol. 13, pp. 521–531, Apr. 2014.

[10] I. S. Lukashevich, "The search for animal models for Lassa fever vaccine development," *Expert Review of Vaccines*, vol. 12, pp. 71–86, Jan. 2013.

[11] K. Mutlu, J. E. Rabell, P. M. Del Olmo and S. Haesler, "IR thermography-based monitoring of respiration phase without image segmentation," *J. Neuroscience Methods*, vol. 301, pp. 1–8, 2018.

[12] J. Grimaud and V. N. Murthy, "How to monitor breathing in laboratory rodents: a review of the current methods," *J. Neurophysiology*, vol. 120, pp. 624–232, 2018.

[13] F. Pfanner, T. Allmendinger, T. Flohr and M. Kachelrieß, "Modelling and simulation of a respiratory motion monitor using a continuous wave Doppler radar in near field," *Proc. Medical Imaging 2013: Physics of Medical Imaging, International Society for Optics and Photonics*, Lake Buena Vista, FL, 6 Mar. 2013.

[14] C. Li *et al.,* "A review on recent progress of portable short-range noncontact microwave radar systems," *IEEE Trans. Microw. Theory Tech.* vol. 65, no. 5, pp. 1692–1706, Jan. 2017.

[15] T. Huang, J, Lin and L. Hayward, "Non-invasive measurement of laboratory rat's cardiorespiratory movement using a 60-GHz radar and nonlinear Doppler phase modulation," *IEEE MTT-S 2015 International Microwave Workshop Series on RF and Wireless Technologies for Biomedical and Healthcare Applications*, 2015.

[16] X. Hui and E. C. Kan, "Monitoring vital signs over multiplexed radio by near-field coherent sensing," *Nat. Electron.,* vol. 1, no. 1, pp. 74, Jan. 2018.

[17] X. Hui and E. C. Kan, "No-touch measurements of vital signs in small conscious animals," *Sci. Adv.,* vol. 5, no. 2, art. eaau0169, Feb. 2019.

[18] X. Hui and E. C. Kan "Seat integration of RF vital-sign monitoring," in *Proc. 2019 IEEE Int. Microw. Bio. Conf. (IMBioC),* Mar. 2019.

[19] X. Hui, Y. Ma and E. C. Kan, "Code division multiple access in centimeter accuracy harmonic RFID locating system," *IEEE J. Radio Freq. Identif.,* vol. 1, no. 1, pp. 51–58, Aug. 2017.

[20] X. Hui, T. B. Conroy and E. C. Kan, "Multi-point near-field RF sensing of blood pressures and heartbeat dynamics," under review.

[21] CST Studio, [Online]. Available: https://www.3ds.com/products-services/simulia/products/cst-studio-suite/

[22] X. Hui, P. Sharma and E. C. Kan, "Microwave stethoscope for heart sound by near-field coherent sensing," in *Proc. Microw. Symp. (IMS), 2019 IEEE MTT-S Int.*, Boston, MA, USA, June 2019.

[23] X. Hui and E. C. Kan, "Collaborative reader code division multiple access in the harmonic RFID system," *IEEE J. Radio Freq. Identif.,* vol. 2, no. 2, pp. 86–92, July 2018.

[24] X. Hui and E. C. Kan, "Radio ranging with ultrahigh resolution using a harmonic radio-frequency identification system," *Nat. Electron.,* vol. 2, no. 3, pp. 125, Mar. 2019.

[25] P. Sharma and E. C. Kan, "Sleep scoring with a UHF RFID tag by near-field coherent sensing", *IEEE MTT 2018 International Microwave Symp. (IMS)*, Philadelphia, Pennsylvania, June 10 – 15, 2018.

[26] R. E. Kleiger, *et al.*, "Time domain measurements of heart rate variability," *Cardiology Clinics*, vol. 10, no. 3, pp.487–498, Aug. 1992.

[27] K. H. Kim, S. W. Bang and S. R. Kim, "Emotion recognition system using short-term monitoring of physiological signals," *Medical and Biological Engineering and Computing*, vol. 42, no. 3, pp. 419–427, May 2004.

[28] G. G. Berntson, D. L. Lozano and Y. J. Chen, "Filter properties of root mean square successive difference (RMSSD) for heart rate," Psychophysiology, vol. 42, pp 246 – 252, Mar. 2005.

[29] W. von Rosenberg, T. Chanwimalueang, T. Adjei, U. Jaffer, V. Goverdovsky and D. P. Mandic, "Resolving ambiguities in the LF/HF ratio: LF-HF scatter plots for the categorization of mental and physical stress from HRV," *Frontiers in Physiology*, vol. 8, pp. 360, 2017.

[30] N. E. Huang, *Hilbert-Huang Transform and Its Applications*, World Scientific, Singapore, 2014.

[31] J. C. Echeverria, J. A. Crowe, M. S. Woolfson and B. R. Hayes-Gill, "Application of empirical mode decomposition to heart rate variability analysis," *Medical and Biological Engineering and Computing*, vol. 39, pp. 471–479, July 2001.

1536-1225 (c) 2020 IEEE. Personal use is permitted, but republication/redistribution requires IEEE permission. See http://www.ieee.org/publications_standards/publications/rights/index.html for more information.
Authorized licensed use limited to: Cornell University Library. Downloaded on July 03,2020 at 23:04:54 UTC from IEEE Xplore. Restrictions apply.